8-22-2016

# Design of a Passive Intensity Modulation Device for Bolus Electron Conformal Therapy

Erin Leanne Chambers
*Louisiana State University and Agricultural and Mechanical College*

# DESIGN OF A PASSIVE INTENSITY MODULATION DEVICE FOR BOLUS ELECTRON CONFORMAL THERAPY

A Thesis

Submitted to the Graduate Faculty of the
Louisiana State University and
Agricultural and Mechanical College
in partial fulfillment of the
requirements for the degree of
Master of Science

in

The Department of Physics and Astronomy

by
Erin Chambers
B.S., Tennessee Technological University, 2013
December 2016

# ACKNOWLEDGMENTS

I would like to acknowledge the many people who made this thesis possible. First of all, I'd like to thank my advisor, Robert Carver, who was always available when I had questions or problems. I would like to thank my committee (Kenneth Hogstrom, Jonas Fontenot, and James Matthews) for their valuable input and flexibility. I'd also like to thank the staff at Mary Bird who were always willing to answer questions, and my fellow students who were open to discussions during long stretches at the desk. In particular, I'd like to thank Susan Hammond, who made lunches a particularly looked-forward-to time of day, for all of the sass and the support. I would also like to thank my family for their unswerving confidence and encouragement.

This research was funded in part by .decimal, Inc (Sanford, FL).

# TABLE OF CONTENTS

# LIST OF TABLES

# LIST OF FIGURES

# ABSTRACT

**Purpose**: To develop a process that can design an island block matrix that produces an intensity distribution (70-100%), which acceptably matches one planned for an intensity modulated (IM) bolus electron conformal therapy (ECT) patient. The intensity modulator concept is that electrons laterally scatter behind hexagonally-packed, small-diameter island blocks such that local intensity equals the fractional unblocked area.

**Methods**: A pencil beam algorithm (PBA) was used to calculate the modulated electron intensity created by varying diameter ($d$) of island blocks in a hexagonal array (separation $r$). Accuracy of the PBA model was assessed by comparing with Monte Carlo (MC) calculations. PBA calculations determined acceptability of $(r, d)$ values for achieving clinical intensity reduction factors (70%≤IRF≤100%) at 100 and 103 cm SSD and 0.5 and 2.0 cm water depths for 7-20 MeV electron beams. Intensity distributions were calculated beneath a half-blocked 20x20 cm$^2$ field for $r$=0.5-1.5cm and IRF=0.70-0.95, for which d=0.117-0.863cm. $(r, d)$ values were acceptable if intensity was within 2% of the IRF. A C++ algorithm (Modulator Generator), which generated a map of $d$ values that produced the desired intensity distribution, was tested for a buccal mucosal patient for whom Kudchadker *et al* (2002) generated a 20-MeV IM bolus ECT plan.

**Results**: PBA and MC calculations agreed within ±5%. At 103 cm SSD PBA results showed $r \leq$0.5 cm and 0.75 cm at 0.5 cm and 2.0 cm depths, respectively, acceptable for 7-20 MeV electrons; larger $r$ values were acceptable for lower energies. Although larger $r$ require fewer blocks, smaller $r$ decreased the distance to transition to the desired IRF, helping achieve intensity distributions with sharp gradients. The Modulator Generator required <5sec (r=0.5cm) to produce clinically-acceptable distributions for the buccal mucosa patient (>99% of points within 3% of planned intensity).

**Conclusions**: The PBA model was sufficient to study the impact of island block parameters $(r, d)$ on achieving desired IRFs for differing conditions (energy, SSD, depth); however, PBA-MC agreement should be improved for patient use. The primary objective

was achieved; electron intensity modulators comprised of island blocks of variable diameter can be designed to deliver a desired intensity distribution of clinical complexity (70-100%) with an accuracy of ±3% for 95% of modulated points.

# 1 INTRODUCTION

## 1.1 Background and significance

### 1.1.1 Clinical utility of electron beam therapy

Electron beam therapy has been a standard modality in cancer treatment for over sixty years. Electron beams are characterized by high surface dose, relatively uniform dose plateau, sharp distal dose falloff, and low exit x-ray dose. For clinical energies between 6-20 MeV ($R_{90} \approx$ 1.8-6.0 cm), these characteristics have allowed superficial cancers within 6 cm of surface to be treated while minimizing dose to underlying critical structures (Hogstrom and Almond, 2006). Figure 1.1 shows how the electron depth-dose changes with increasing energy for Elekta Infinity electron treatment beams. Above 20 MeV, (1) the falloff region becomes progressively broader due to increased range straggling, (2) the fraction of bremsstralung contamination arising form the dual scattering foil system in the beam increases, and (3) the lateral falloff (c.f. Figure 1.2) becomes increasingly large due to increased multiple Coulomb scattering. These characteristics make electron beam therapy less suitable for tumors requiring beams above 20 MeV, which corresponds to a depth of approximately 6 cm.

Historically, electrons have been the modality of choice for [1] the treatment of skin, lip, and head and neck tumors, [2] boost doses to superficial lymph nodes, and [3] post-mastectomy chest wall irradiation (Haas *et al*, 1954; Tapley, 1976; Vaeth and Meyer, 1991; Khan *et al*, 1991; Khan, 2010). Electron therapy planning generally requires only a single beam of energy sufficient to deliver a uniform dose to the deepest part of the target, while minimizing dose to tissue distal to the planning target volume (PTV). Typically, maximum PTV depth is just less than $R_{90}$ of the electron beam. However, implementation in sites in the head and neck and post-mastectomy chest wall is often complicated by the presence of internal heterogeneities and irregular patient surface. Also, variable depth of distal surface of the PTV may result in overdosing of distal structures when utilizing a single energy

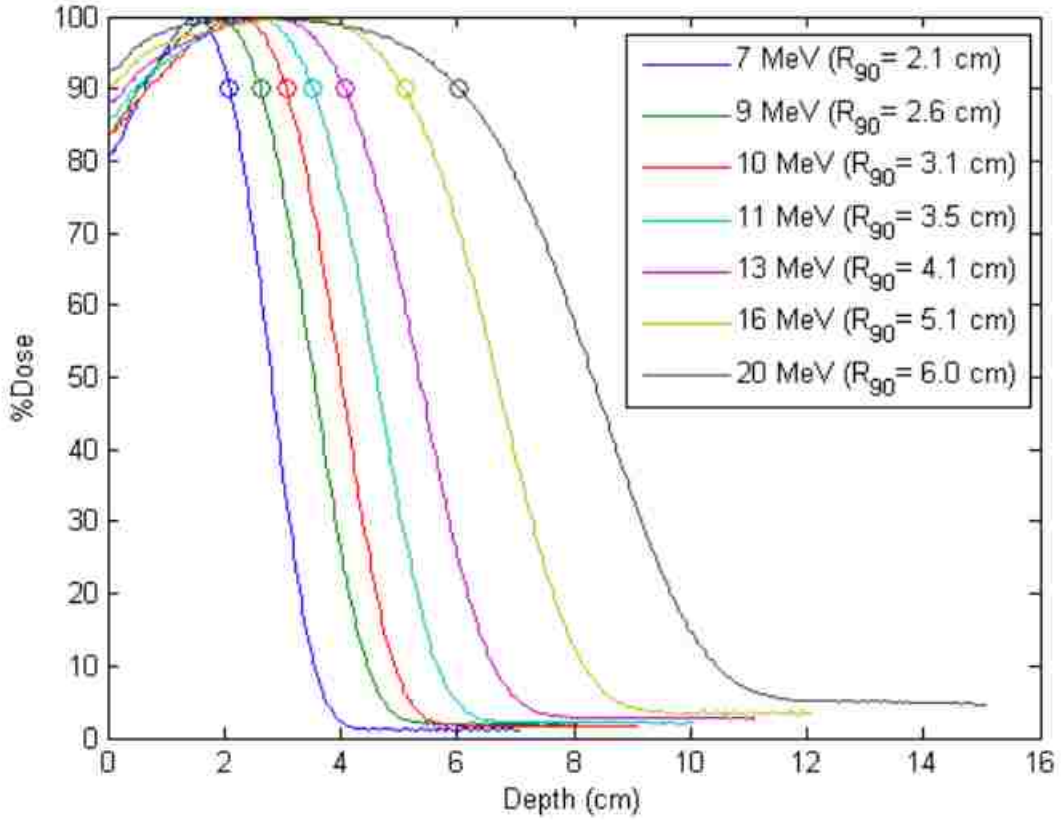


Figure 1.1: Percent depth-dose curves for Elekta Infinity MLCi3 beams (10x10 $cm^2$) in water. Electron depth-dose curves are characterized by a high-dose plateau followed by a sharp dose falloff to the practical range and a low-dose x-ray tail. Depth of distal 90% dose ($R_{90}$) and nominal beam energy in key. From McLaughlin (2010).

beam, as illustrated in Figure 1.2, in which case some form of electron conformal therapy (ECT) to contour the dose plateau to the distal surface of the PTV is desirable.

### 1.1.2 Electron conformal therapy

The goal of electron conformal therapy is to conform the distal 90% dose surface to the distal surface of the PTV, provide a homogeneous or prescribed heterogeneous dose to the PTV, and maximize dose sparing of critical structures deep to the PTV (Hogstrom *et al*, 2003). Two methods for electron conformal therapy have been used in the clinic: segmented-field ECT and bolus ECT. Figure 1.3 illustrates a transverse slice of a chest wall treatment field using each method.

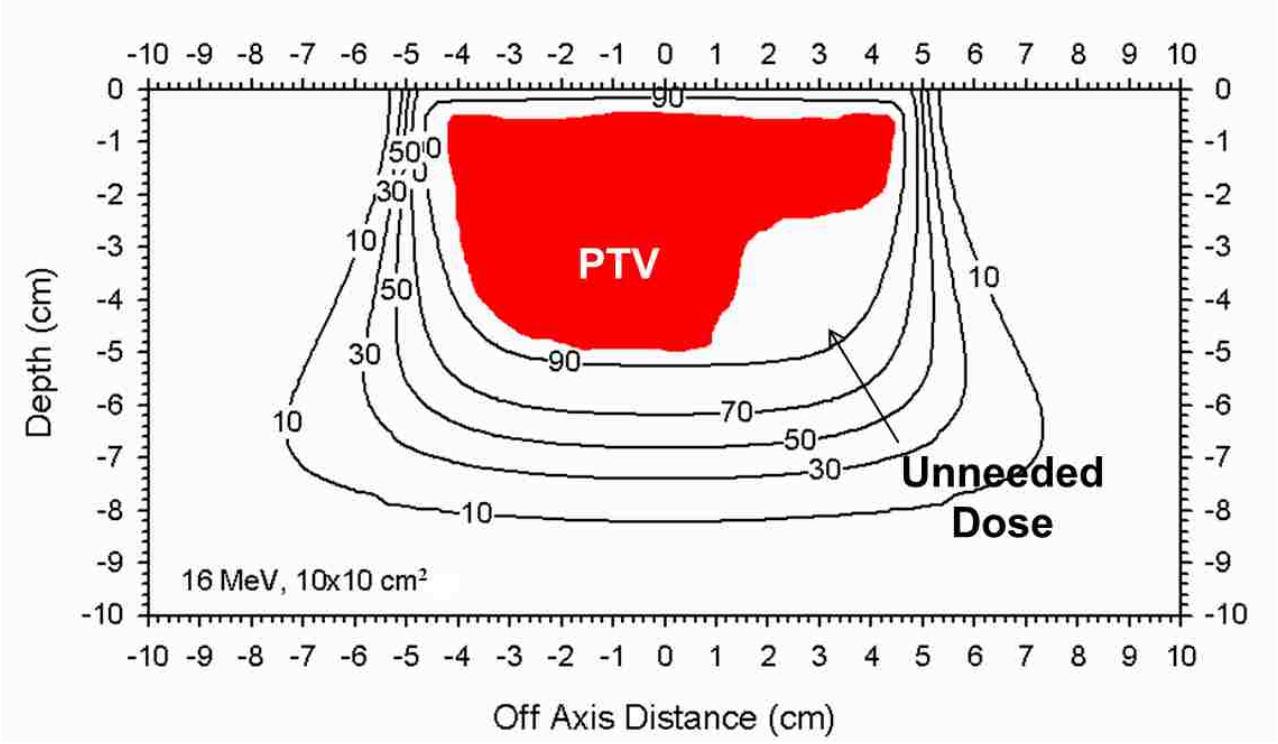


Figure 1.2: Schematic PTV with irregular distal surface in water. The distal 90% dose surface of a single 16 MeV electron beam conforms well to the deepest depth of the PTV, given in red, but delivers a large volume of unneeded dose where the PTV does not extend as deep.

Segmented-field ECT uses multiple beams of one or more energies and/or beam weightings having the same virtual source to conform the distal 90% dose surface to the tumor volume. Abutment of electron beams of different energies causes the formation of hot and cold spots in the target volume due to differing penumbral widths (Million et al 1991). For this reason, segmented-field ECT needs the use of specialized delivery techniques, such as edge feathering (Eley *et al* 2011) or variable source-to-collimator distance (Richert *et al* 2007) to match penumbra and deliver a uniform dose in the PTV, neither of which are provided by industry. Delivery of segmented-field ECT is also cumbersome due to the large number of irregularly-shaped fields, a limitation that requires either a number of Cerrobend cutouts (requiring numerous trips into the room during treatment) or specialized technologies such as an electron multileaf collimator (only available from third-party).

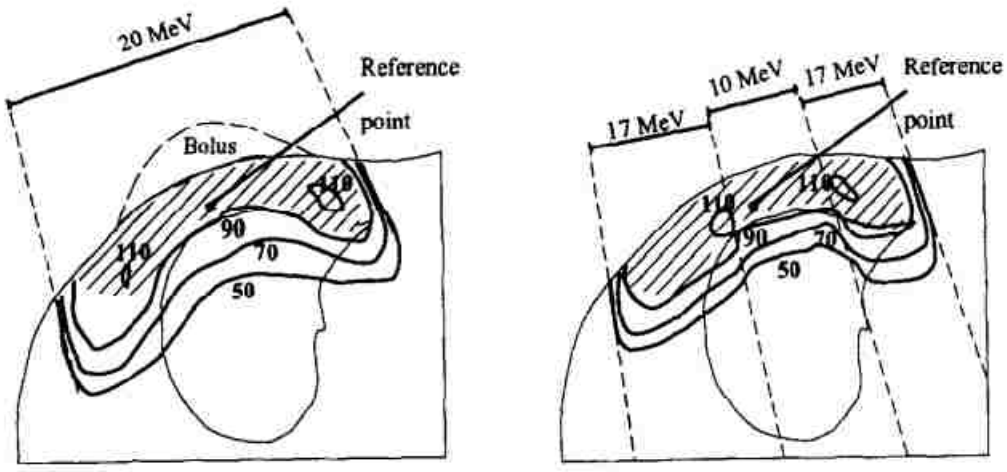


Figure 1.3: Illustration of two clinical techniques for electron conformal therapy (modified from Zackrisson and Karlsson 1996). At left, bolus ECT: the PTV is treated with a single 20 MeV beam and variable-thickness bolus. At right, segmented-field ECT: the PTV is treated with three beams of 10 and 17 MeV. PTV is demarcated by hatched lines. Both plans shape the distal 90% dose surface to the distal PTV surface; both also produce hot spots in the PTV of 110%.

Bolus ECT is defined by Hogstrom *et al* (2003) as "the use of a single energy electron beam to deliver a dose distribution that conforms the 90% dose surface to the distal surface of the PTV." This is accomplished by using variable-thickness bolus, a nearly water-equivalent material which is placed on the patient surface. An algorithm for bolus generation was created by Low *et al* (1992); it projected ray lines from the electron virtual source to the distal margin of the PTV and applied a succession of bolus operators to generate a bolus structure. Three types of operators are used by the algorithm: creation, modification, and extension operators. Creation operators provide the initial bolus shape using physical or effective depth to match the distal 90% dose surface of the electron beam to that of the PTV. Modification operators improve the initial design by adjusting thickness to improve distal matcing and by smoothing the bolus surface to reduce dose heterogeneities due to multiple Coulomb scatter from the irregular proximal surface of the bolus. Extension operators extend the bolus to outside the projected PTV and field size.

Figure 1.4 illustrates how bolus ECT contours the 90% dose surface to the PTV for a parotid patient.

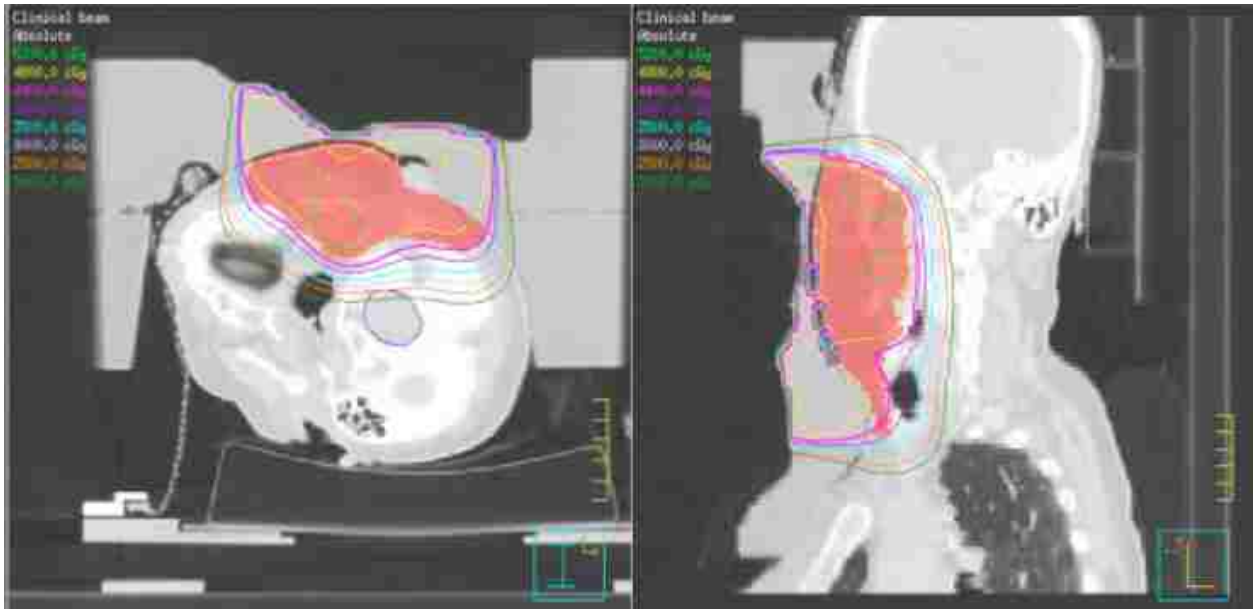

Figure 1.4: Isodose distribution with bolus ECT using a 20 MeV beam for a parotid patient. From Kudchadker *et al* (2003).

Boluses have been readily available to clinics since the introduction in 2009 of bolus design software (p.d BolusECT®) and milling technology, available only from .decimal, LLC (Sanford, FL, http://dotdecimal.com/products/electrons/bolusect/). Patient structures, CT data, and an electron beam plan are transferred from an institution's treatment planning system (TPS) to p.d BolusECT®. Bolus is designed using selected Low *et al* (1992) and .decimal operators and a pencil beam redefinition algorithm for dose calculations (Shiu and Hogstrom, 1991; Boyd *et al*, 1998; Boyd *et al*, 2001; Carver *et al*, 2013). Subsequently, the bolus structure is exported to the clinic's TPS, where the dose is recalculated using the TPS electron dose algorithm. When deemed acceptable, the bolus design is electronically forwarded to the manufacturer for production (milling machineable wax). The patient is typically given a new computed tomography (CT) scan with the machined bolus in place, which is used to perform a final dose calculation, providing quality assurance on the bolus. A typical setup for a head and neck patient is shown in Figure 1.5. Typically, the patient

is secured with a facemask and the blue, machineable wax bolus in place. One side of the bolus has a shape that conforms to the patient's face, while the other side varies thickness to conform the 90% dose surface to the distal PTV surface.

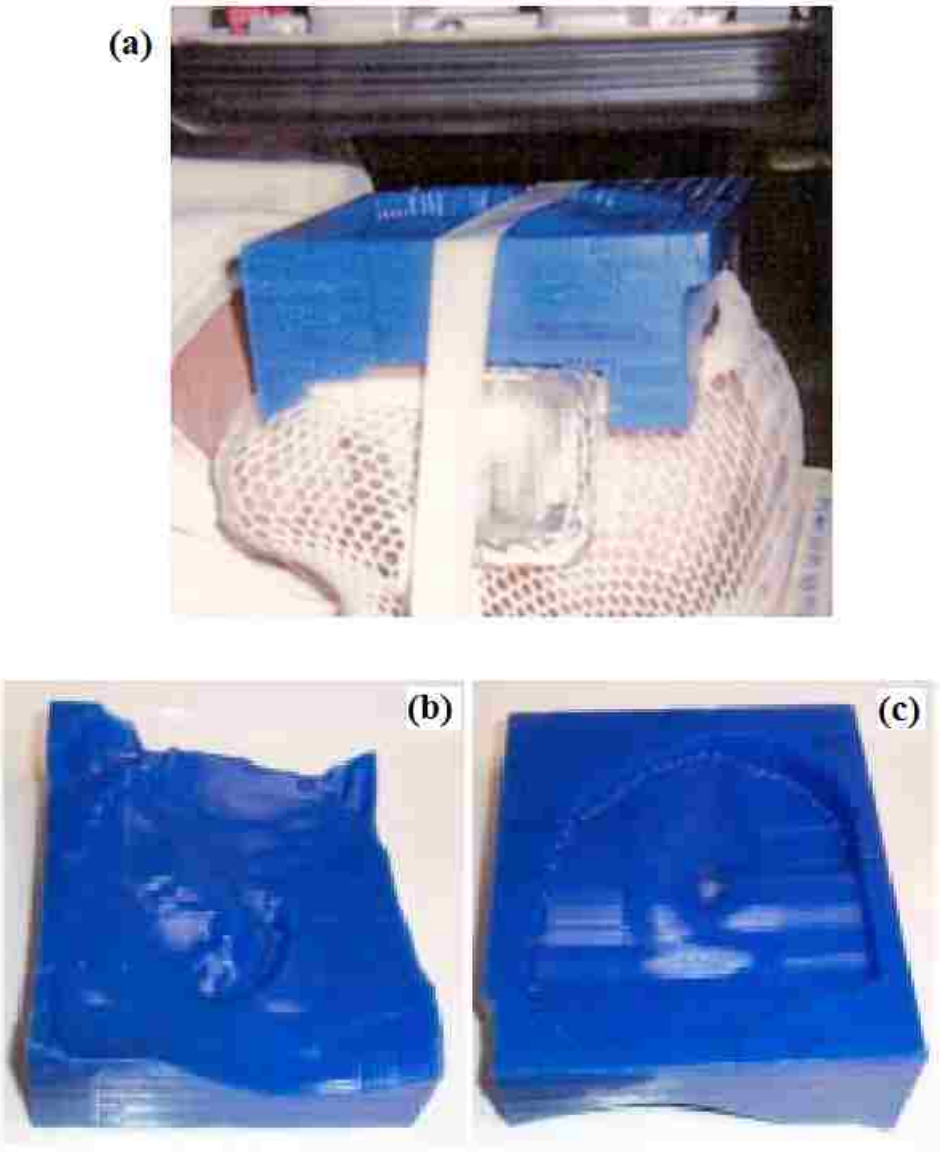


Figure 1.5: Bolus ECT patient for treatment of ear concha. (a) The blue, machineable wax bolus has been securely positioned and attached to the face and facemask of a patient. (b) Distal bolus surface, which conforms to the patient's face, and (c) proximal bolus surface, which varies thickness to shape the 90% dose surface to conform to and enclose the distal PTV surface. Modified from Kudchadker *et al* (2003).

Bolus ECT has been used for multiple sites, which include paraspinal muscles (Low *et al*, 1995; Kudchadker *et al*, 2002), post-mastectomy chest wall (Kudchadker *et al*, 2002; Perkins *et al*, 2005; Kim *et al*, 2012; Opp *et al*, 2013), ear, parotid, and buccal mucosa (Kudchadker *et al* 2002 and 2003), nose (Zeidan *et al*, 2011), and foot (Su *et al*, 2014). Bolus ECT, as compared to segmented-field ECT, has the advantage of continuous energy (range) modulation, which allows for highly conformal dose distributions, requiring only a single beam. However, the distal conformity can lead to the creation of hot and cold spots in the treatment volume as a result of the irregular proximal bolus surface necessary to achieve that conformity. As a result, for some patients the use of bolus ECT could be precluded on account of unacceptably high dose heterogeneity in the the target. In these cases, it was shown by Kudchadker *et al* (2002) that the use of intensity modulation with bolus ECT can produce a clinically acceptable dose distribution in the patient. One such case is shown in Figure 1.6. The original bolus ECT dose distribution with no intensity modulation conforms the distal 90% dose surface to the PTV, but produces a 120% dose hotspot. A modified bolus for use with a modulated intensity distribution also conforms the 90% dose surface to the PTV, but the hotspot has been moved outside the patient and has a significantly reduced magnitude of 106%. The required intensity modulation is modest (70-100%), and the PTV dose-volume histograms show how intensity modulation reduces the dose spread from approximately 30% to 10%.

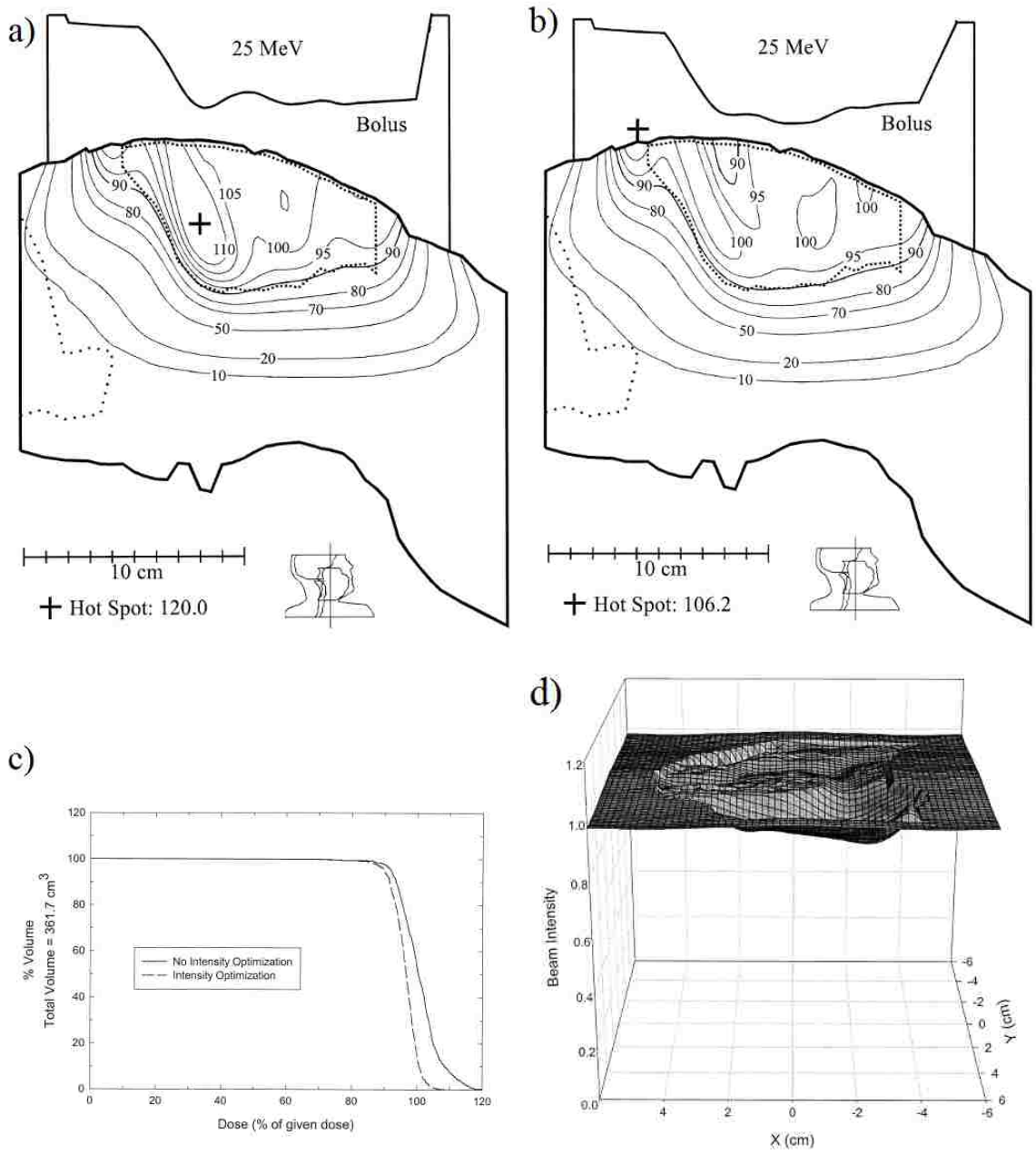


Figure 1.6: Dose distributions for buccal mucosa PTV with bolus ECT. The PTV is indicated by the closely dotted line. (a) The original bolus ECT dose distribution with no intensity modulation conforms the distal 90% dose surface to the PTV, but produces a 120.0% hotspot. (b) A modified bolus with use with a modulated intensity distribution also conforms the 90% dose surface to the PTV, and the hotspot, which has moved out of the patient, has a reduced magnitude of 106.2%. (c) The PTV dose-volume histograms show how intensity modulation reduces the dose spread from approximately 30% to 10%. (d) Intensity plot shows that the required intensity modulation is modest (70-100%). Modified from Kudchadker *et al* (2002).

### 1.1.3 Electron intensity modulation

While several methods have been proposed to implement electron intensity modulation, none of these are practically viable for clinical use with bolus ECT. Electron beams shaped with x-ray MLC have excessive penumbra width due to air scatter at standard SSDs. Work by various groups suggests an SSD in the range of 65-70 cm is required for acceptable penumbra (du Plessis *el al* 2006, Klein *et al* 2009), which might be impractical. Scanned electron beams are no longer available on clinically used accelerators and for lower energies have unacceptably large dose kernel width (Hogstrom *et al* 2003). Electron MLCs (Hogstrom *et al* 2004, Eley *et al* 2011) are ideal for the purpose but are not supported by accelerator manufacturers, requiring the purchase of a bulky, costly add-on from a single third-party supplier (EUROMECHANICS medical GmbH). Also, TPS software for eMLCs is not available. Lastly, a series of Cerrobend block cutouts could be used, at the cost of increased treatment time, increased leakage dose, and other risks associated with multiple room entries to exchange cutouts.

Under ideal conditions, the insertion of a high-density block of sufficient thickness at some position (x,y) in the treatment field will remove from the beam all electrons incident on the block. For example, a small cylindrical block ($\approx$1 cm diameter) has been previously used to treat retinoblastoma by sparing the lens of the eye while electrons scatter behind the block, delivering a reduced dose to the retina (Kirsner *et al* 1987, Steenbakkers *et al* 1997), and a sawtooth cutout edge has been used to broaden the penumbra (Kalend *et al* 1985). Recently, researchers at Mary Bird Perkins Cancer Center (private communication: Drs. Kenneth Hogstrom and Robert Carver) have built upon these concepts by proposing a new technology for electron intensity modulations that uses a matrix of variable small-diameter, high-density "island" blocks, as shown in Figure 1.7. The matrix should closely produce the desired intensity modulation while the beam energy remains relatively unchanged.

The concept of electron intensity modulation is illustrated as follows. In an unmodulated beam, an area in the central portion of the beam would be in side-scatter equilibrium,

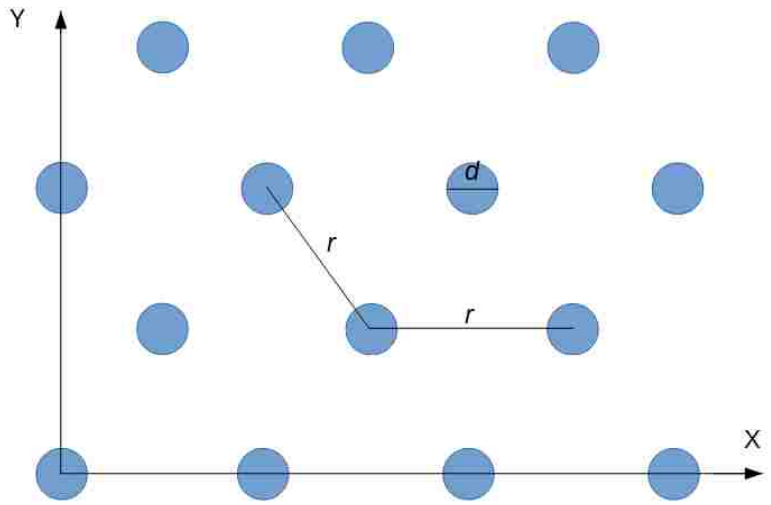


Figure 1.7: Beam's eye view of a sample hexagonally-packed matrix of island blocks with relevant parameters (r, d).

with electrons scattering equally in and out. The addition of a block removes out-scatter but still allows in-scatter electrons. Thus, the electrons retain the original beam energy while reducing overall intensity. This effect is depicted in Figure 1.8. A high density block intercepts the beam some distance above patient surface. The resulting blocked portion of the beam is gradually filled by scattered particles from the surrounding beam. Using a matrix of such blocks, a uniform decrease in intensity can be achieved.

The degree of decreased intensity (modulation) will be directly proportional to the fraction of beam area covered by island blocks in the region overlying the field locally. Hexagonal packing is one possible geometric arrangement that allows for simple calculations of the degree of intensity modulation. The intensity reduction factor (IRF), defined as the fraction of the unblocked intensity, under hexagonal packing is calculated using packing radius $r$ and block diameter $d$, and is given by:

$$IRF(r,d) = 1 - \left(\frac{\pi}{2\sqrt{3}}\right)(d/r)^2. \tag{1.1}$$

By modifying the block diameter in the matrix, i.e. d=d(x,y), the intensity can become modulated, i.e. IRF=IRF(x,y).

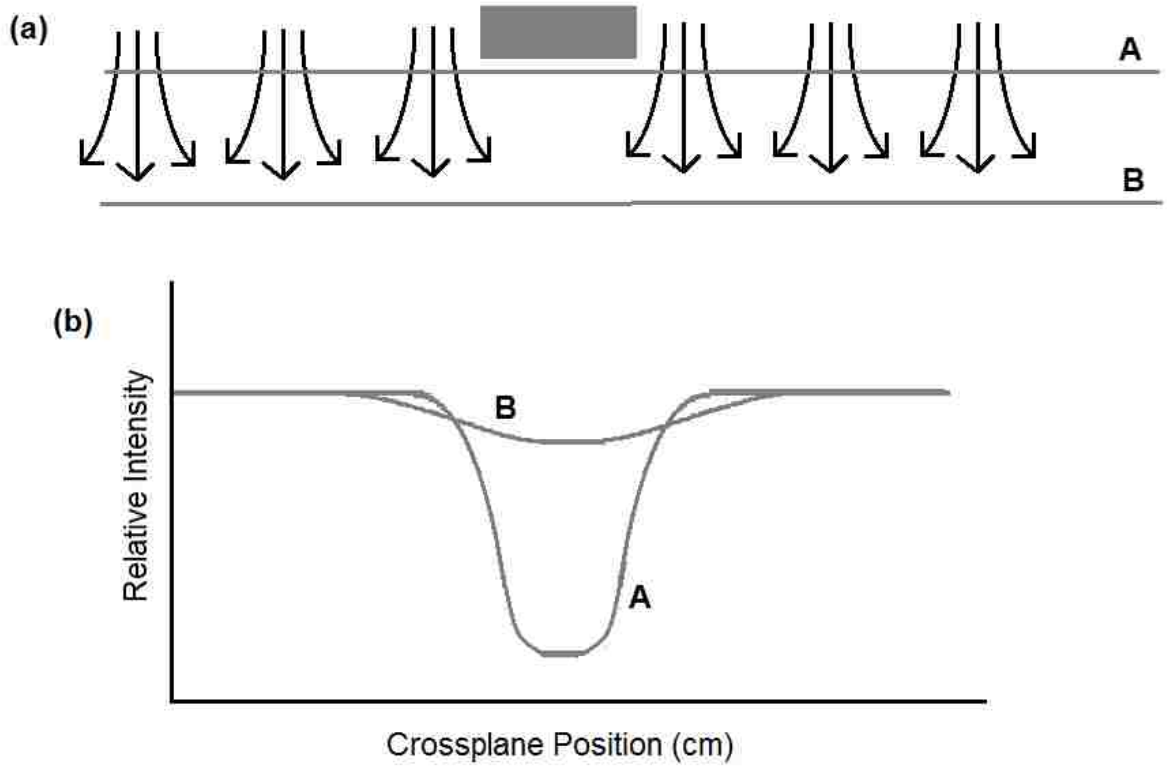


Figure 1.8: Intensity reduction shadow effect schematic. (a) A high density island block (shaded gray) intercepts the beam some distance above patient surface. The resulting gap in the beam is gradually filled by scattered particles from the surrounding beam. (b) Two relative intensity profiles corresponding to positions A and B. At A, a deep gap in intensity is present distal to the block position. At B, the gap has been mostly filled by in-scatter.

To demonstrate this concept, Carver and Hogstrom (private communication) built a prototype intensity modulator by inserting lead pins of diameter 0.2 cm and thickness 2.0 cm into a piece of styrofoam in a regular hexagonal pack with a packing radius of 0.5 cm (Figure 1.9). The block matrix consisted of five rows and seven columns of pins, with the central pin located at central axis. Dose measurements were mode along x=0 (in-plane) with a 16 MeV electron beam and 10x10 $cm^2$ field at 2.0 cm depth on the Elekta Infinity accelerator at Mary Bird Perkins Cancer Center. The modulator was inserted into the lowest level of the applicator (on top of final trimmer) and aligned using the light field. The measurement was done using a diode in a scanning water tank. The PBA with

intensity modulation was used to calculate dose under identical conditions. The relative dose profiles for measurement and calculation are compared in Figure 1.10. The results showed agreement within approximately 1% in the modulated area x=[-3,3].

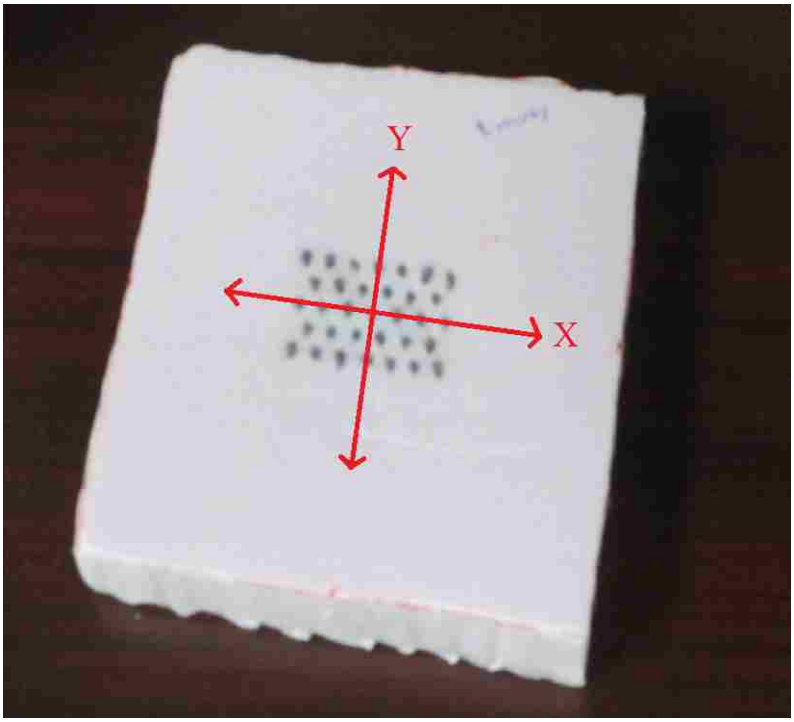


Figure 1.9: Prototype intensity modulator. Lead pins (d=0.2cm) were embedded in a block of styrofoam in a hexagonal pack (r=0.5cm) having 5 rows and 7 columns centered on central axis.

Mary Bird Perkins Cancer Center in collaboration with .decimal, LLC, who markets bolus ECT technology, has proposed to develop treatment planning software and a delivery device for passive electron intensity modulation consisting of a regular matrix of high-density cylindrical island blocks embedded in a low-density slab. The device, henceforth referred to as an electron intensity modulator, is a custom, patient-specific addition, which will be attached to the electron beam-defining collimating insert (cutout) and used in concert with existing bolusECT®technology. By careful optimization of block diameter and separation, the device should produce a smoothly varying intensity distribution incident on the bolus surface, restoring the dose spread in the PTV to approximately 10%.

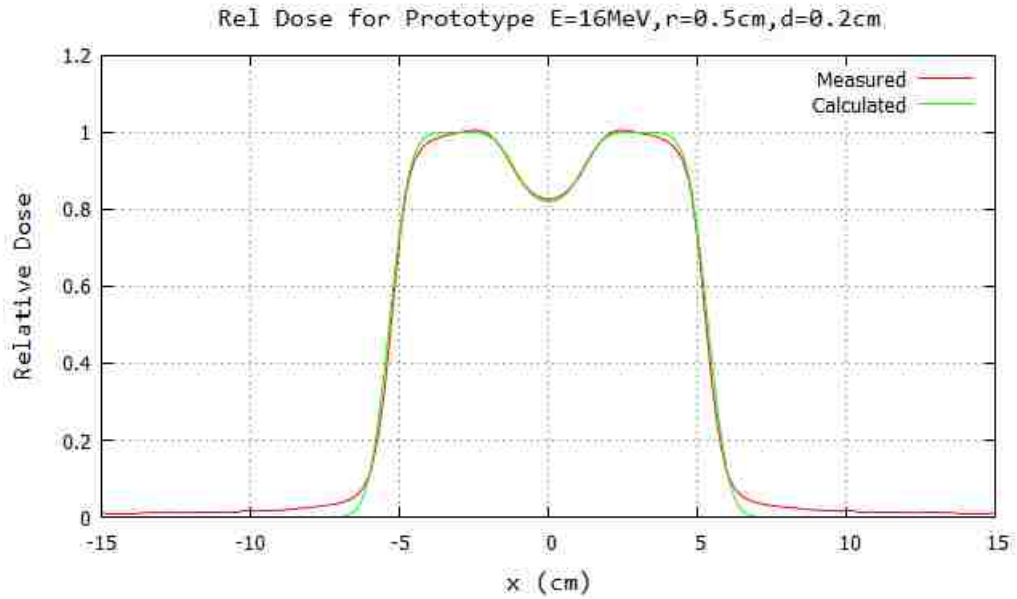


Figure 1.10: Comparison of relative dose measurement and calculation for prototype intensity modulation device. Good agreement is shown within the modulated area.

## 1.2 Purpose

The purpose of this research is to develop a process that will generate an island block matrix arrangement sufficient to deliver a given intensity distribution in the range of 70-100% for bolus electron conformal therapy, which is accurate within a clinically-acceptable margin.

## 1.3 Hypothesis and specific aims

**Hypothesis**: Passive electron intensity modulators comprised of a matrix of island blocks of variable diameter can be designed to deliver a desired intensity distribution of clinically-representative complexity (70-100%) with an accuracy of $\pm 3\%$ for 95% of modulated points (IRF$<$1).

**Aim 1, Suitability of pencil beam algorithm for modulated electron intensity distribution**: Develop a pencil beam algorithm for calculating intensity distributions resulting from intensity modulation (70-100%) with island blocks for 7-20 MeV electron beams, and evaluate its accuracy compared to Monte Carlo calculations.

**Aim 2, Dependence of intensity reduction on island block diameter and packing radius**: Using a pencil beam algorithm for electron dose calculations, determine island block geometries (combinations of diameter and packing radius) for passive electron intensity reduction (70-95%) that minimize Distance of Transition ($d_T$) and Ripple Intensity ($\Delta I_R$) for electron energies ranging from 7-20 MeV.

**Aim 3, Algorithm for design of intensity modulation using island blocks**: Develop a pencil beam-based design tool for generating electron intensity modulators for an objective intensity distribution, beam energy, and SSD that is accurate to within 3% for 95% of modulated points (IRF<1) for a clinically-applicable intensity distribution.

# 2 AIM 1: SUITABILITY OF PENCIL BEAM ALGORITHM FOR MODULATED ELECTRON INTENSITY DISTRIBUTION CALCULATIONS

Develop a pencil beam algorithm for calculating intensity distributions resulting from intensity modulation (70-95%) with island blocks for 7-20 MeV electron beams, and evaluate its accuracy compared to Monte Carlo calculations.

## 2.1 Research methods

### 2.1.1 Calculating intensity reduction using block geometry

From geometry, the reduction in electron intensity under a given regular packing (matrix) of blocks can be estimated by calculating the ratio of unblocked area to the total area. This ratio is henceforth referred to as the intensity reduction factor (IRF). The ratio can be achieved by altering the size of the blocks, local variation of block proximity, or both. The specific block geometry chosen for this project is hexagonal packing (matrix) of cylindrical blocks. In this case, the IRF, which is a function of the individual block diameter (d) and the packing radius (r) as shown in Figure 2.1, is given by

$$IRF(r,d) = 1 - \frac{\pi d^2}{2\sqrt{3}r^2} \ . \tag{2.1}$$

For the purposes of this project, a uniform packing radius was used throughout the field. Given a particular packing radius and IRF, Equation 2.1 can be solved for the necessary block diameter, i.e.

$$d(r,IRF) = r\left[\frac{2\sqrt{3}}{\pi}(1-\mathrm{IRF})\right]^{1/2} . \tag{2.2}$$

In this study, a range of packing radii from 0.5-1.5 cm (with 0.25 cm increments) and a range of IRFs from 0.70-0.95 (with 0.05 increments) were explored.

### 2.1.2 Calculating electron intensity using a pencil beam algorithm

The relative electron intensity (normalized to the central-axis value, x=y=0, with no island blocks) at depth z in water can be written as the intensity distribution for a field

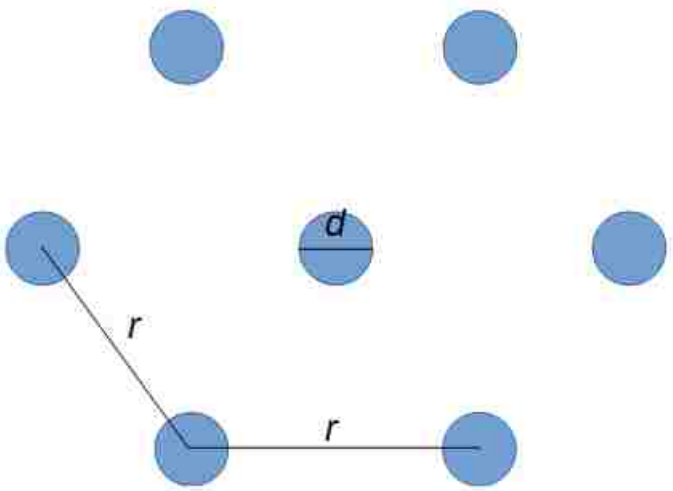


Figure 2.1: Schematic for hexagonal packing of island blocks. A subset of the hexagonal grid shows the two key geometry parameters for intensity reduction, block diameter (d) and packing radius (r).

WX by WY without the island blocks less the sum of intensity distribution removed by each of the N island blocks, i.e.

$$I^{WX,WY}_{\text{with blocks}}(x,y,z) = I^{WX,WY}_{\text{no block}}(x,y,z) - \sum_{i=1}^{N} I_{block,i}(x,y,z;x_i,y_i,s_i), \tag{2.3}$$

where the relative electron intensity for a field of dimension WX by WY with no island blocks for a non-diverging beam is given by Fermi-Eyges pencil beam dose calculation (Hogstrom *et al*, 1981)

$$I^{WX,WY}_{\text{no block}}(x,y,z) = \frac{1}{4}\left(\text{erf}\frac{WX/2-x}{\sqrt{2}\sigma} + \text{erf}\frac{WX/2+x}{\sqrt{2}\sigma}\right) \times \left(\text{erf}\frac{WY/2-y}{\sqrt{2}\sigma} + \text{erf}\frac{WY/2+y}{\sqrt{2}\sigma}\right), \tag{2.4}$$

and where the intensity for a small square field centered at $(x_i, y_i)$ and of dimensions $s_i$ such that its area equals that of a circle of the ith island block diameter $d_i$ ($s_i = d_i\sqrt{\pi}/2$)

is given by

$$I_{block,i}(x,y,z;x_i,y_i,s_i) = \frac{1}{4}\left[\mathrm{erf}\left(\frac{(x_i+s_i/2)-x)}{\sqrt{2}\sigma}\right) - \mathrm{erf}\left(\frac{(x_i-s_i/2)-x)}{\sqrt{2}\sigma}\right]$$
$$\times\left[\mathrm{erf}\left(\frac{(y_i+s_i/2)-y)}{\sqrt{2}\sigma}\right) - \mathrm{erf}\left(\frac{(y_i-s_i/2)-y)}{\sqrt{2}\sigma}\right)\right]. \quad (2.5)$$

The rms ($\sigma$) of the projected spatial spread of a point beam traveling from the collimation plane to the plane of calculation is given by

$$\sigma^2(z) = \sigma_{\theta_x}^2(L_0+z)^2 + \frac{1}{2}a_2(z), \quad (2.6)$$

where as in Figure 2.2, $L_0$ is the air gap from the collimation plane to the water surface and z is the depth in water. $\sigma_{\theta_x}^2$ is the rms of the projected angular-spread of electrons at any point in the collimating plane, and $a_2(z)$ is the second moment of the scattering power in water, which according to Fermi-Eyges theory is given by

$$a_2(z) = \int_0^z dz'(z-z')^2 T(z'), \quad (2.7)$$

where T(z′) is the linear angular scattering power in water at depth z′. T(z) (radians$^2$cm$^{-1}$) is approximated by the Werner *et al* (1982) power law approximation $\mathrm{T(z)} = 4.525E(MeV)^{-1.78}$, where the energy at depth z is given by

$$E(z) = E_{p,0}(1 - z/R_p), \quad (2.8)$$

where $E_{p,0}$ is the most probable energy at the water surface and $R_p$ is the practical range (ICRU Report 35). The two are related by

$$E_{p,0}(MeV) = 0.22 + 1.98R_p(cm) + 0.0028R_p^2(cm). \quad (2.9)$$

Unless otherwise noted in the text, all beam energies refer to the most probable energy at the surface ($E_{p,0}$). An empirical formula derived from commissioning data for the Elekta Infinity accelerator at Mary Bird Perkins Cancer Center (private communication) was used to calculate $\sigma_{\theta_x}$:

$$\sigma_{\theta_x}(\text{radians}) = \sqrt{0.15064 * [E_{p,0}(MeV)]^{-1.78}} \tag{2.10}$$

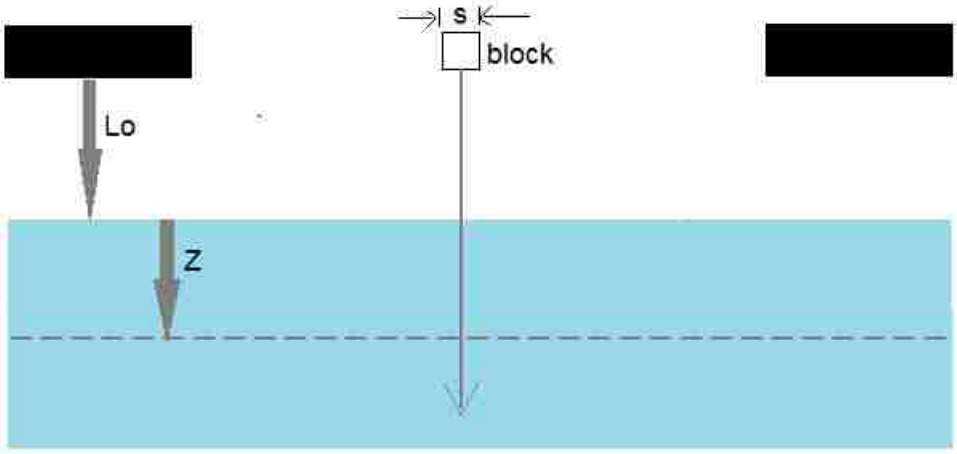


Figure 2.2: Schematic of electron beam incident on patient surface in X-Z plane.

### 2.1.3 Secondary effects from electron-block interactions

#### 2.1.3.1 Simulation geometry

The MC model used was based on the Elekta Infinity accelerator model developed by Guy Harris, MS, using the EGSnrc/BEAMnrc Monte Carlo software (Harris, 2012), with some project-specific modifications. Figure 2.3 shows the accelerator's treatment head as modeled by the BEAMnrc visualization software. All calculations were done using a 25x25 $cm^2$ applicator (field size defined at bottom of applicator) with 95 cm source to collimator distance SCD (source located 100 cm from isocenter). A cylindrical block component module, which consisted of a 2.0 cm thick lead block, was inserted immediately below the lowest level applicator along the central axis. This thickness was approximately 1.0 cm greater than that required to stop electrons up to 20 MeV (Khan *et al*, 1991). Placing the bottom of the block 2.0 cm below the applicator, which differed slightly from the intended

physical implementation of the intensity modulator (bottom even with the bottom of the applicator), was necessary based on the limitations of BEAMnrc component modules. The air gap between the applicator and water surface was adjusted to 7.0 cm to account for the 2.0 cm thick block, keeping a 5.0 cm gap ($L_0$) between the bottom of the block and the surface of the water.

#### 2.1.3.2 Incident electron beam

The electron beam exiting the accelerator and incident upon the accelerator exit window was assumed to be an elliptical Gaussian centered on central axis with a full-width half maximum of 2 mm in the Y (in-plane) and 1 mm in the cross-beam directions (Harris, 2012). The accelerator's polyenergetic spectrum beam was modeled as a monoenergetic beam with incident energy $E_{p,i}$ to better match the conditions of the pencil beam algorithm. Calculations were performed for $E_{p,i}$ values of 9, 13, and 17 MeV.

The energy used in PBA calculations for comparison was the most probable energy at the surface or $E_{p,0}$. The relation between $E_{p,i}$, $E_{p,0}$, and $\sigma_{\theta_x}$ for each energy is given in Table 2.1. $E_{p,0}$ was determined from $E_{p,i}$ accounting for the energy loss in the treatment head using the dual-foil scattering system simulator of Carver *et al* 2014. $\sigma_{\theta_x}$ was determined using a fit to Elekta Infinity accelerator commissioning data (c.f. Equation 2.10).

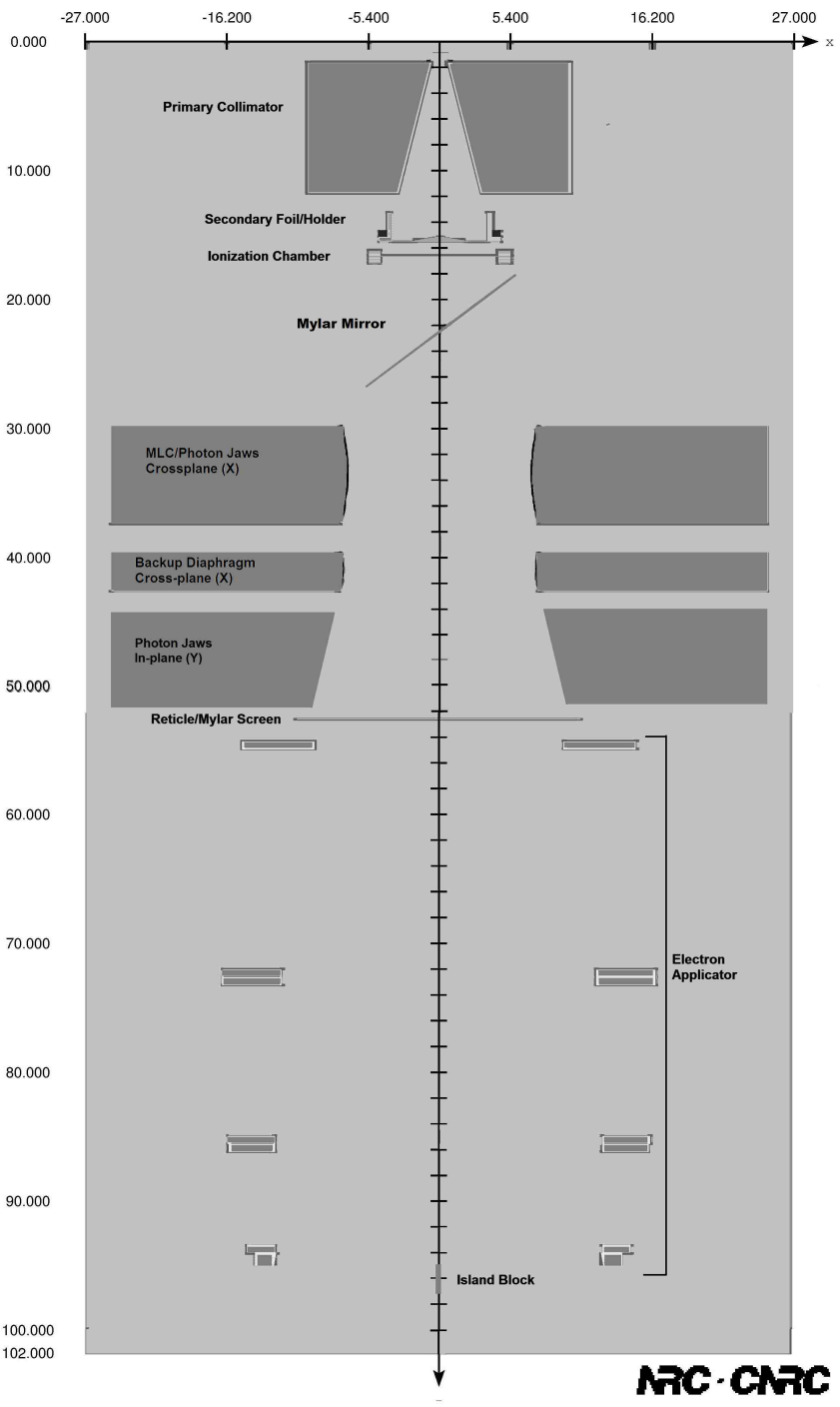


Figure 2.3: Elekta Infinity BEAM accelerator model. Harris' original model for a 25x25 $cm^2$ applicator was adjusted with the addition of a cylindrical component module directly beneath the lowest applicator level and the use of a monoenergetic beam.

Table 2.1: Summary of nominal energy, energy incident on the accelerator exit window ($E_{p,i}$), most probable energy at surface ($E_{p,0}$), and electron angular spread ($\sigma_{\theta_x}$).

| Nominal E (MeV) | $E_{p,i}$ (MeV) | $E_{p,0}$ (MeV) | $\sigma_{\theta_x}$ |
|---|---|---|---|
| 9 | 9 | 8.31 | 0.060 |
| 13 | 13 | 12.20 | 0.042 |
| 17 | 17 | 15.91 | 0.033 |

#### 2.1.3.3 Monte Carlo calculations

The MC simulations computed dose per incident electron in a water phantom. Each MC simulation used a single cylindrical block along the central axis of the beam, with each simulation using one billion histories and a voxel size of 0.2 cm. Simulations were done using the SuperMike II computer cluster at Louisiana State University. MC data were converted from dose per incident electron to relative dose by normalizing to the dose per incident electron over a central 1x1 $cm^2$ of the open beam. Relative intensity was assumed equal to relative dose. Radial profiles were generated from MC data in planes located at depth 0.5 cm and 2.0 cm. The standard error of voxel dose values was approximately 0.6%, which was reduced to 0.2% by averaging radial profiles every 30°. This was permitted since the MC geometry was radially symmetric about central axis with the exception of 25x25 $cm^2$ applicator's collimating geometry, whose edges were sufficiently far from central axis to neglect their effect.

Central axis island block calculations were done for select island block diameters (0.117, 0.288, 0.352, 0.508, 0.719, 0.863 cm) for each energy. This set of island block diameters was selected to model secondary effects within the range of clinically-viable geometries for the range of $r$ (0.50-1.50 cm) and IRF (0.70-0.95) studied (c.f. Section 3.2).

#### 2.1.3.4 Comparison with PBA calculations for single block

Because the PBA assumed a uniform incident beam, to compare MC results to those of the PBA, the MC profiles were flattened (both blocked and unblocked fields) to be unity for the unblocked beam within the region $|x|$ <10cm, where side-scatter equilibrium exists,

i.e.

$$I_{block}(x,0,z;d) = I_{block}^{unflattened}(x,0,z;d) * WF \tag{2.11}$$

and

$$I_{\text{no block}}(x,0,z;d) = I_{\text{no block}}^{unflattened}(x,0,z;d) * WF, \tag{2.12}$$

where the weighting factor WF was given by

$$WF(x,0,z;d=0) = \frac{1}{I_{\text{no block}}^{unflattened}(x,0,z;d=0)}. \tag{2.13}$$

Block kernels, defined as the relative intensity removed from or added to the beam due to the presence of the island block, were calculated by taking the difference in relative intensity between the Monte Carlo (or PBA) calculated open beam and the beam with a single central axis island block, i.e.

$$K(x,0,z;d) = I_{\text{no block}}(x,0,z;d=0) - I_{block}(x,0,z;d). \tag{2.14}$$

These kernels were used to evaluate secondary interaction effects on the intensity distribution. The calculation difference kernel (MC kernel - PBA kernel) also equals the difference in $I_{block}$ (MC - PBA) because the unblocked beam in both cases was normalized and flattened to unity in the central region being investigated, i.e.

$$CDK(x,0,z;d) = I_{block}^{MC}(x,0,z;d) - I_{block}^{PBA}(x,0,z;d). \tag{2.15}$$

Also, because the PBA model presented earlier was a parallel beam, the field width of calculation was the applicator width (25.0 cm) at the SCD times the geometry factor that accounts for the divergence at the SSD plus depth of calculation, i.e.

$$WXZ(SSD,z) = 25.0 \text{ cm} * \left(\frac{SSD+z}{SCD}\right). \tag{2.16}$$

The effect of beam divergence on effective island block size and position was neglected. For single, central axis island block calculations the effect was a slight, insignificant underestimation of reduced dose in the block penumbra for PBA compared to MC calculations.

#### 2.1.3.5 Comparison with PBA calculations for arrays of multiple blocks

Although calculation difference kernels can have magnitudes up to 30%, this does not translate into a large of error for intensity modulated beams, because many nearby difference kernels contribute to the intensity distribution. Therefore, using Equation 2.3 the intensity distribution was calculated for a parallel beam collimated to 20x20 $cm^2$ and modulated with hexagonally packed island blocks all of equal spacing (r) and diameter (d). Both PBA and MC calculations were performed so that the composite effect of the PBA could be evaluated.

The first set of calculations selected the geometry for which PBA approximations would be expected to be worse: smallest block diameter (d=0.117cm) and shallower depth (z=0.5cm). The calculations were done for the 9, 13, and 17 MeV beams. Calculations were done for IRF=0.95 (r=0.5cm) and IRF=0.69 (r=0.2cm). A second, more practical set of calculations were also done for 9, 13, and 17 MeV beams, having a depth of z=2.0cm with r=0.5 cm for which d=0.117 cm (IRF=0.95) and d=0.288 cm (IRF=0.70).

## 2.2 Results and discussion

### 2.2.1 Comparison of PBA-based and MC-based kernels for singular central axis blocks

Figure 2.4 shows the crossplane profile for a 17 MeV open beam, the same beam for a 0.863 cm diameter central axis block, and the block kernel for a depth of 0.5 cm and 5.0 cm air gap. As shown by the kernel profile, differences are restricted to the region x=[-2,2]. The shape of the kernel's dose distribution is expected due to (1) dose removed by the presence of the block, (2) scatter of electrons just lateral to the block, and (3) x-rays penetrating or created in the block. The peak under the block represents the intensity, predominantly electrons, removed by the block; the penumbra is due to multiple Coulomb

scatter of electrons from the block edges back into the beam. Block scatter effects are indicated by the small negative intensity values in the kernel. They are seen in the regions x=±1.2-1.6 cm and have a maximum contribution of 0.4% of the total dose at that point. X-ray contributions from the block are not readily identifiable.

The flattened MC calculations for a single block on central axis were compared to respective PBA calculations. Figure 2.5 compares the crossplane profiles of MC and PBA calculations for a 17 MeV beam and a central axis island block of diameter 0.863 cm. Differences inside the field were small and restricted to the region x=[-2,2]. Large differences in the low dose region outside the field, due to the PBA not including x-ray contamination, are of little relevance to the effects of the central island block being studied. Finally, Figure 2.6 shows the calculation difference kernel between these MC and PBA calculations.

Figures 2.7, 2.8, and 2.9 show central axis block profiles and kernels for 17 MeV with 0.352cm diameter, 13 MeV with a 0.352 cm diameter, and 13 MeV with a 0.863 cm diameter, respectively. Comparison of PBA and MC-calculated intensity profiles at 9, 13, and 17 MeV for block diameters of 0.117, 0.288, 0.352, 0.508, 0.719, and 0.863 cm are found in Appendix A. For each condition, the difference kernels are shown. Figure 2.10 summarizes these results by plotting at 9, 13, and 17 MeV, the resulting difference kernel (MC-PBA) for each block diameter.

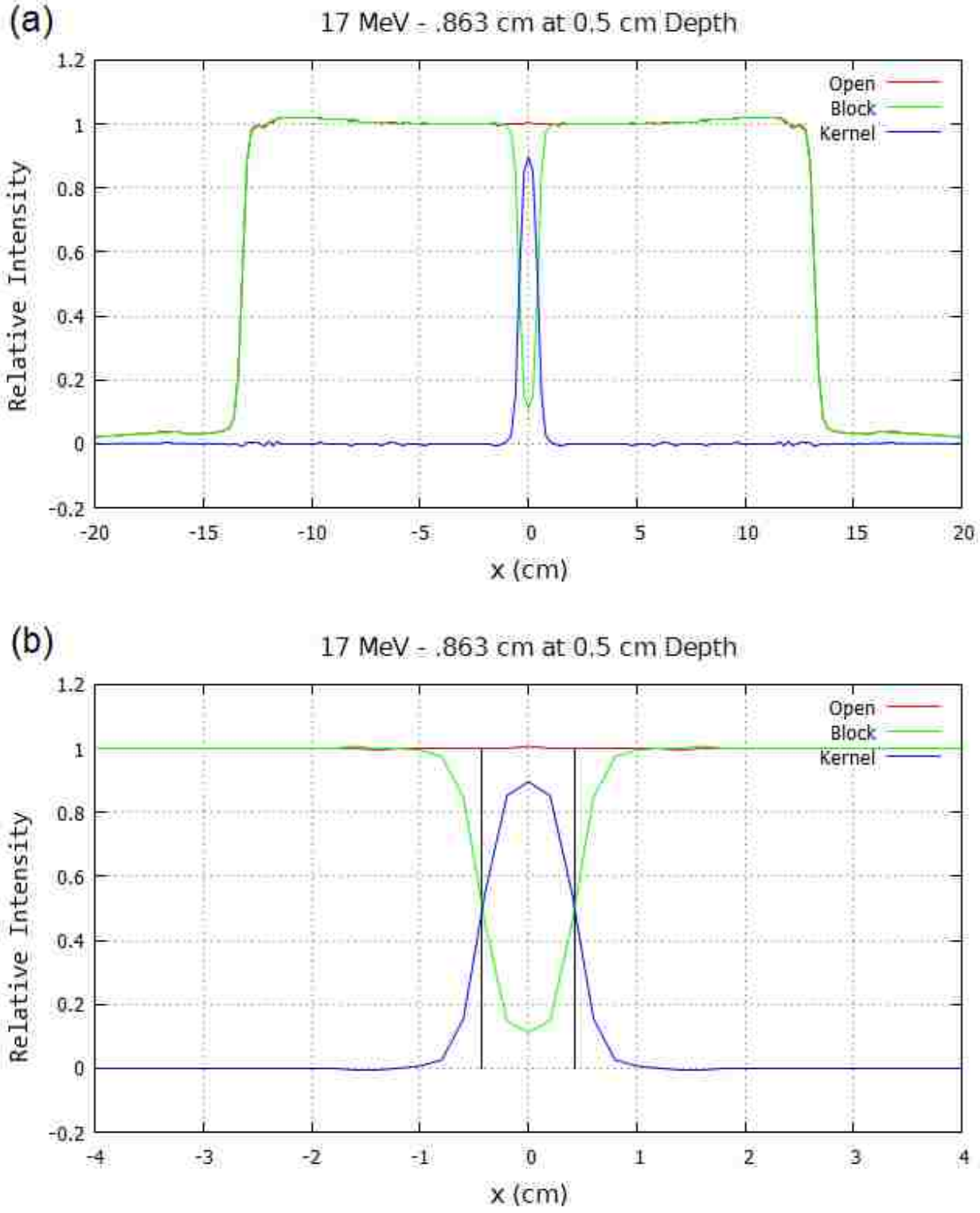


Figure 2.4: Monte Carlo central axis block profile and kernel: monoenergetic 17 MeV beam with a central axis block of diameter d=0.863cm at depth z=0.5cm with air gap g=5.0 cm. (a) Crossplane intensity profile (y=0) for open beam and 0.863 cm CAX block, overlaid by the block kernel. (b) The scale of the x-axis has been magnified to provide greater detail. Vertical black lines indicate the edges of the block.

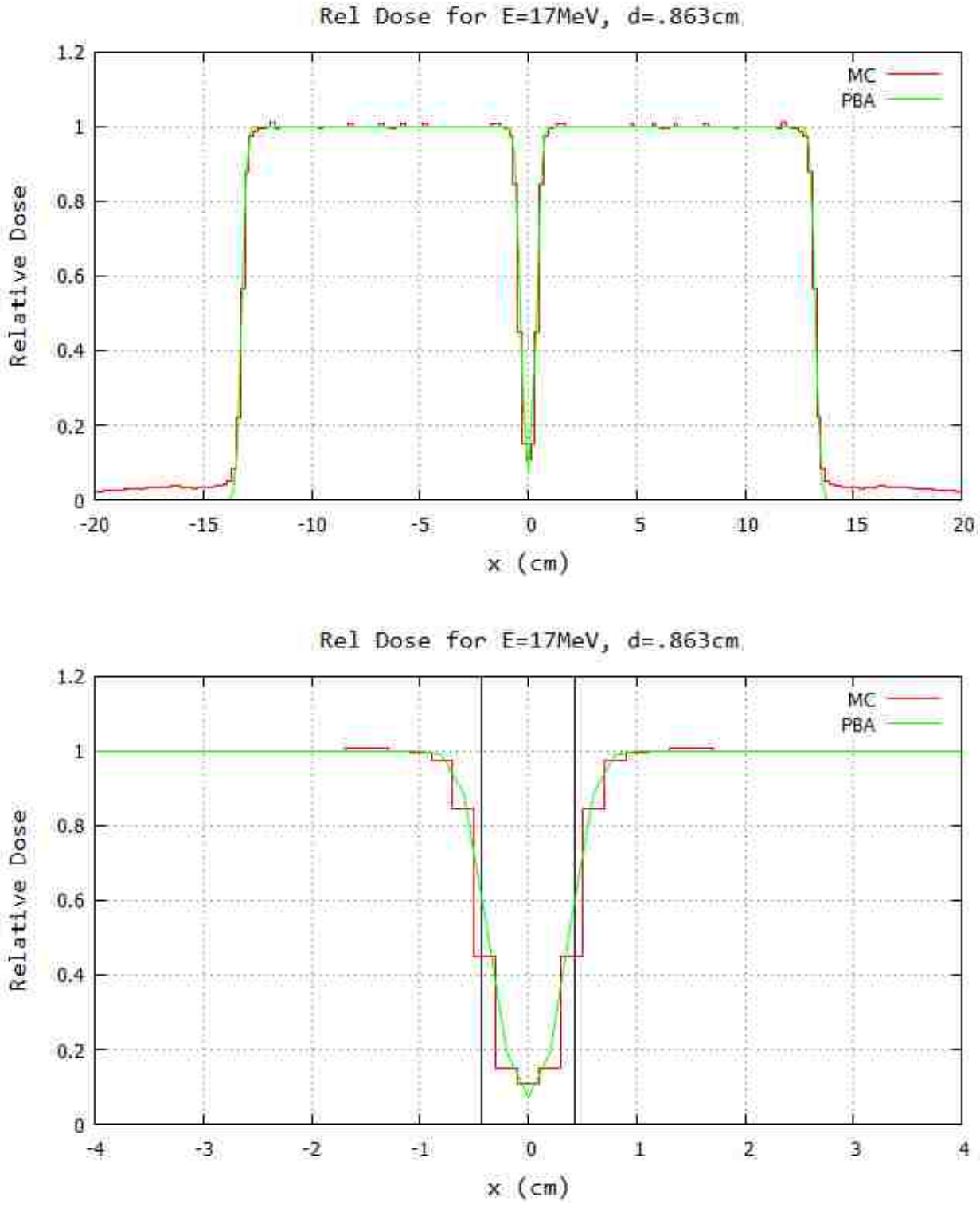


Figure 2.5: PBA/MC profiles comparisons for a monoenergetic 17 MeV beam with a central axis block of diameter d=0.863cm at depth z=0.5cm with air gap g=5.0 cm. (a) Relative intensity profile (y=0) for Monte Carlo and pencil-beam algorithm calculations, and (b), zoomed in version for detail. Vertical black lines indicate the position of the block.

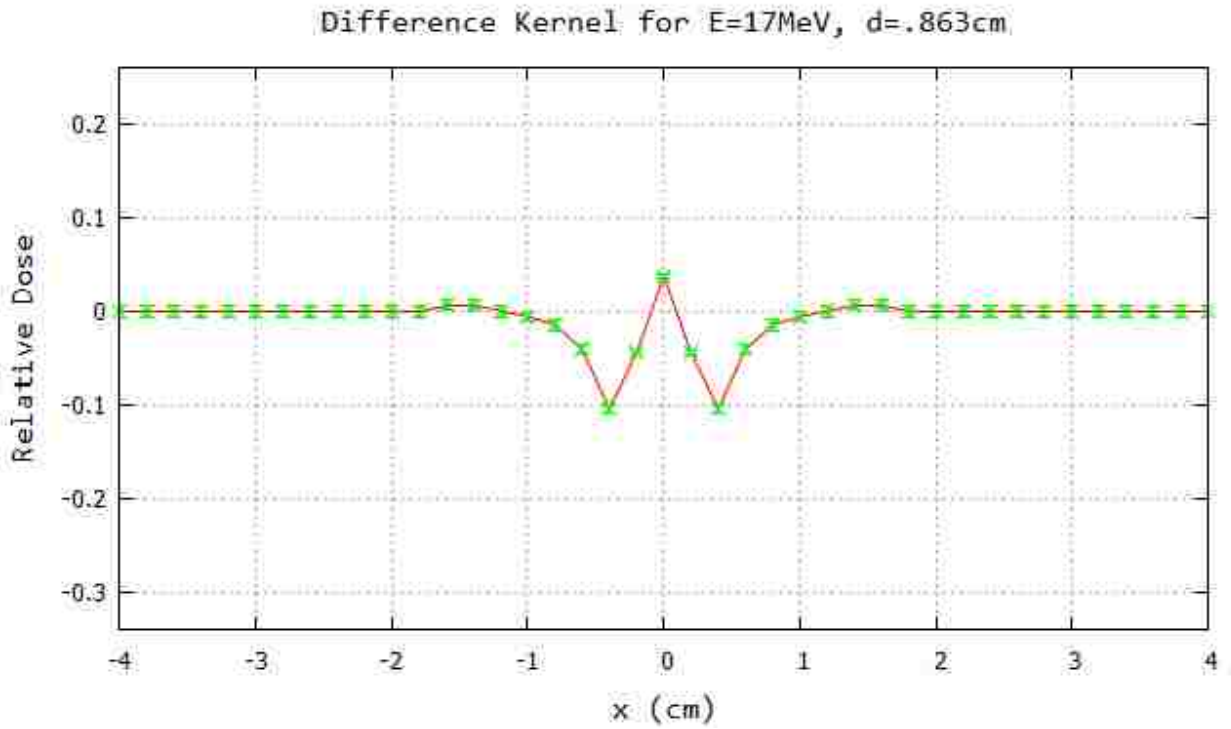


Figure 2.6: Absolute (MC-PBA) difference kernel for 17 MeV, d=0.863cm, z=0.5cm, and $L_0$=5cm.

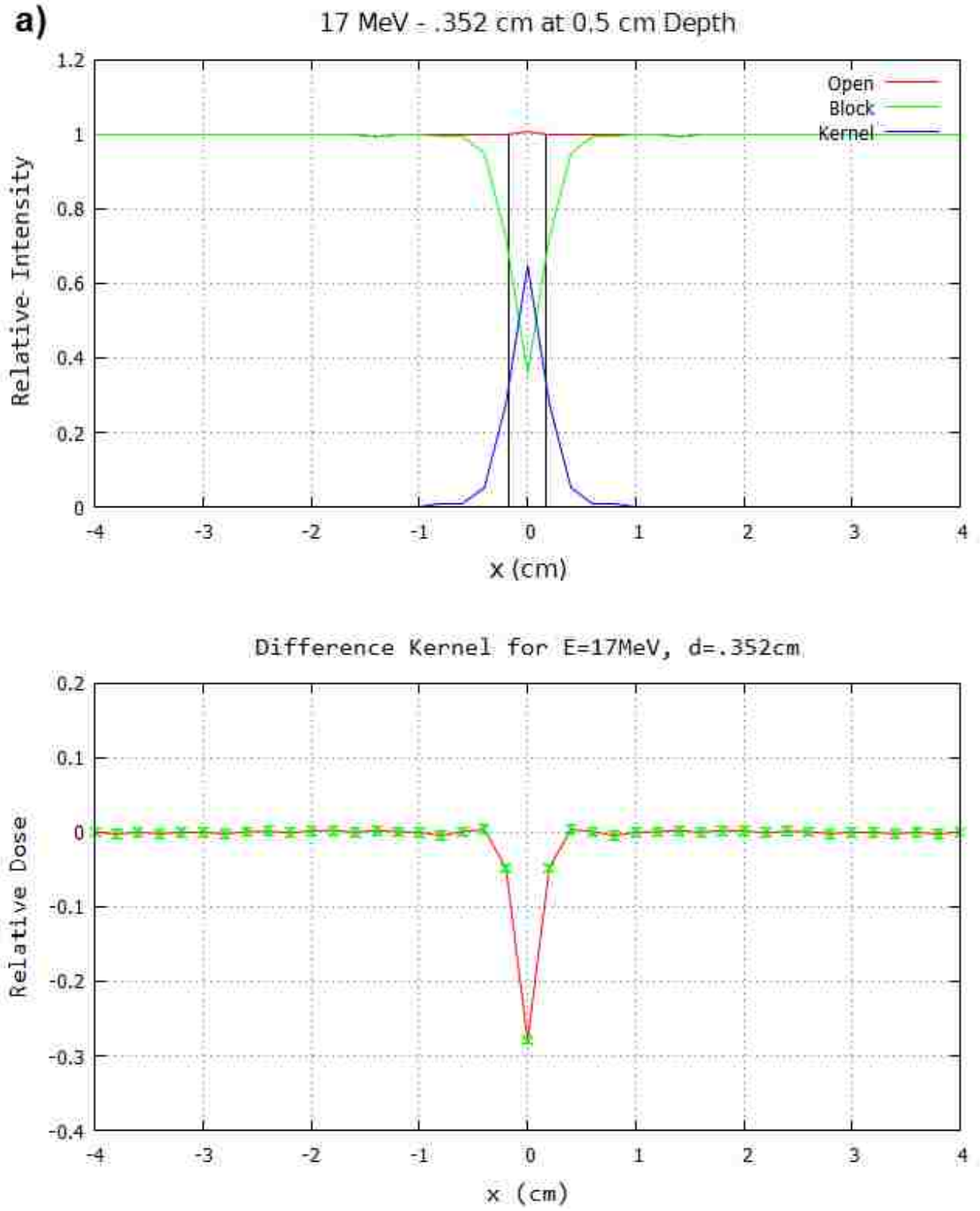


Figure 2.7: Monte Carlo central axis block profile and kernel: monoenergetic 17 MeV beam with a central axis block of diameter d=0.352cm at depth z=0.5cm with air gap g=5.0 cm. (top) Crossplane intensity profile (y=0) for MC and PBA. Vertical black lines indicate the edges of the block. (b) MC-PBA difference kernel for 17 MeV, d=0.352cm, z=0.5cm, and $L_0$=5cm

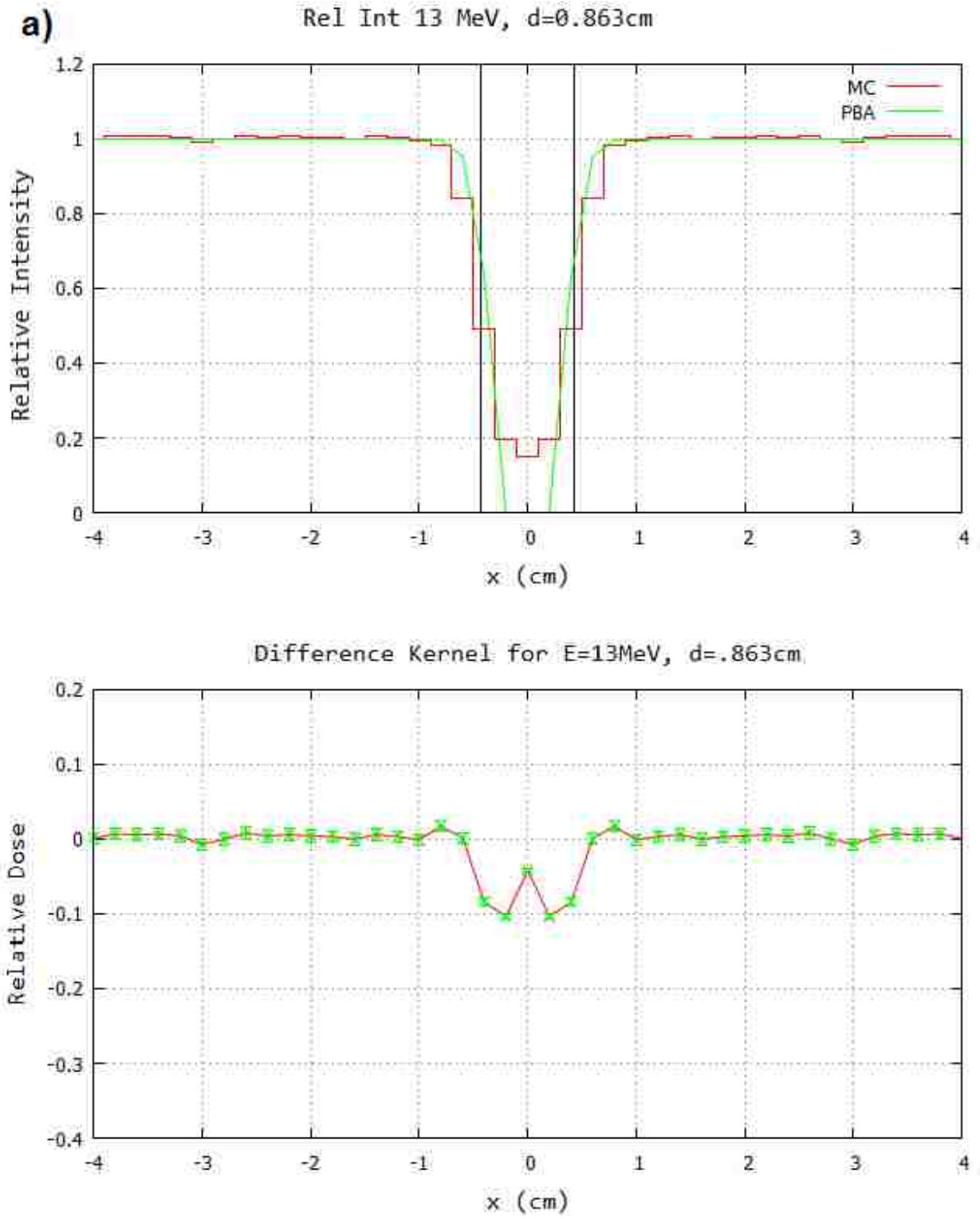


Figure 2.8: Monte Carlo central axis block profile and kernel: monoenergetic 13 MeV beam with a central axis block of diameter d=0.863cm at depth z=0.5cm with air gap g=5.0 cm. (a) Crossplane intensity profile (y=0) for MC and PBA. Vertical black lines indicate the edges of the block. (b) MC-PBA difference kernel for 13 MeV, d=0.863cm, z=0.5cm, and $L_0$=5cm

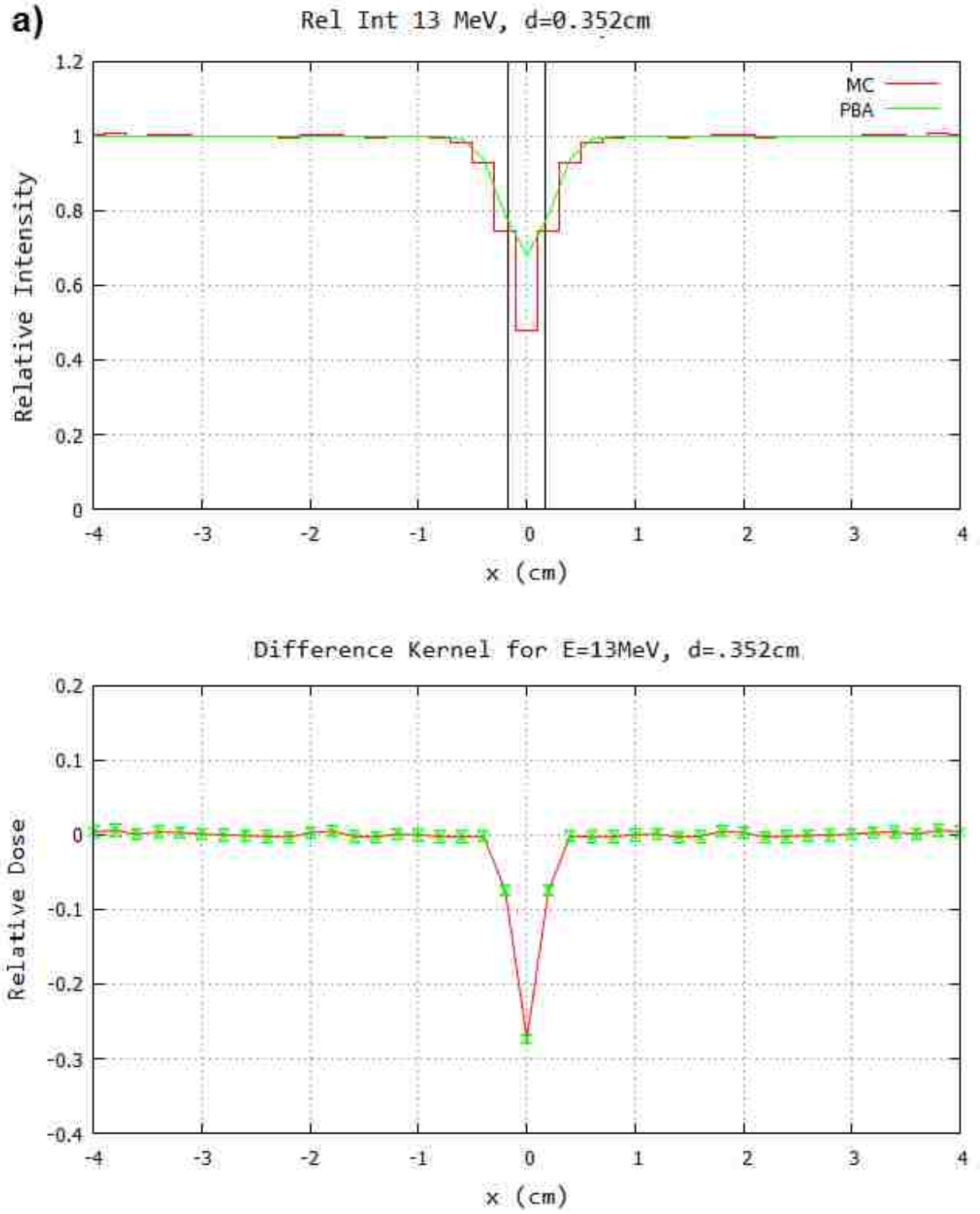


Figure 2.9: Monte Carlo central axis block profile and kernel: monoenergetic 13 MeV beam with a central axis block of diameter d=0.352cm at depth z=0.5cm with air gap g=5.0 cm. (a) Crossplane intensity profile (y=0) for MC and PBA. Vertical black lines indicate the edges of the block. (b) MC-PBA difference kernel for 13 MeV, d=0.352cm, z=0.5cm, and $L_0$=5cm

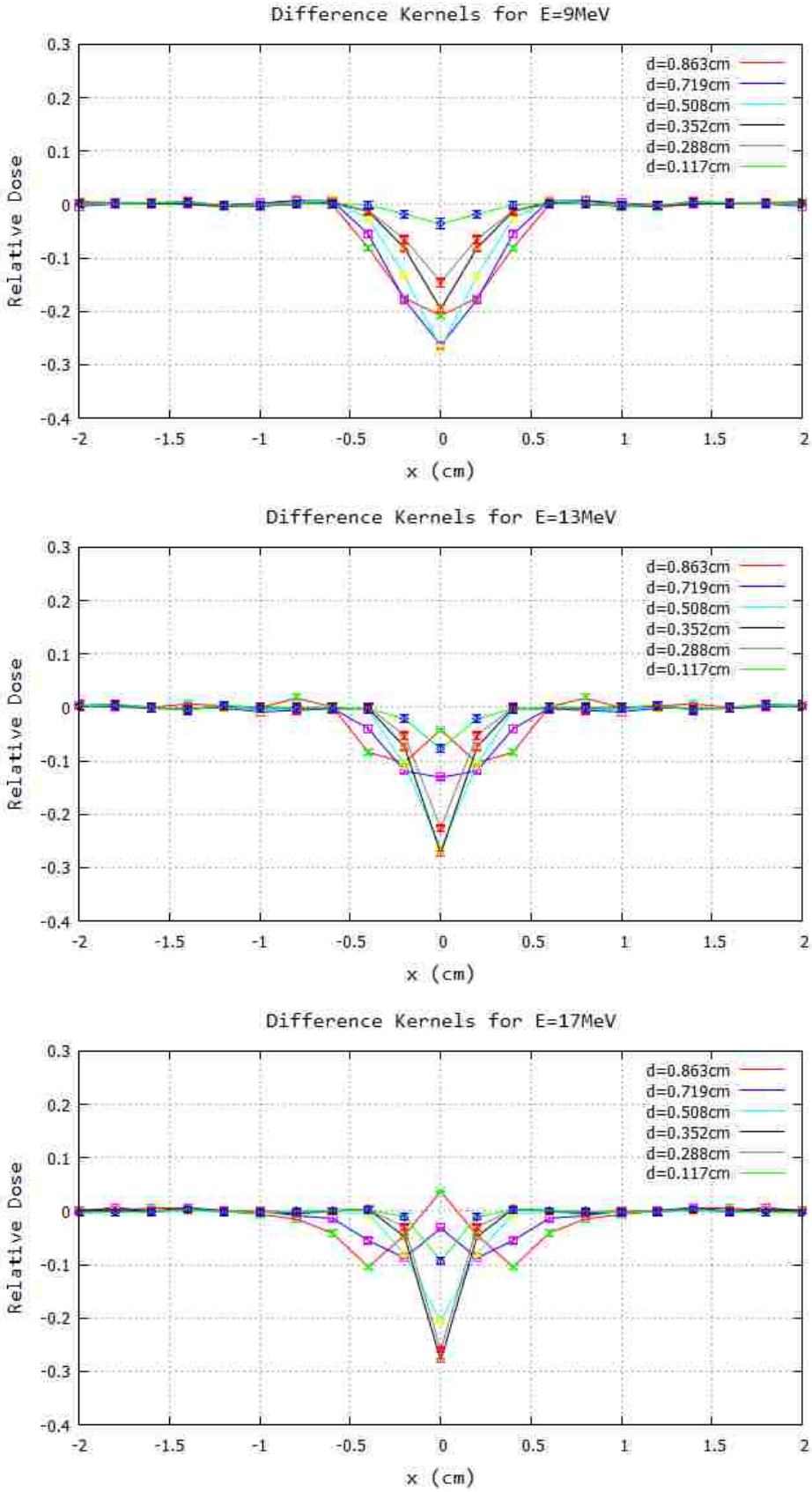


Figure 2.10: Calculation difference kernels (MC - PBA) for each diameter at 9, 13, and 17 MeV.

All but one of the plots show the difference kernel (MC - PBA) (1) to be negative, typically greatest on the central axis (approximately -0.05 to -0.30), (2) to have a full-width half maximum (FWHM) that increases slightly with block diameter, and (3) to have a small energy dependence. These differences are believed primarily due to (1) small differences in multiple Coulomb scattering calculations in MC and PBA, since varying the $\sigma_{\theta_x}$ values can generate better agreement, and (2) approximating the circular block area as a square.

Of particular importance is the impact of electrons scattered off of the block. There appears to be a small effect in the region (d/2) + 0.04 cm $\leq |x| \leq$ 2.0 cm, although its magnitude <1% is of the order of the error bar. Because the effects extends laterally up to 2 cm, the scatter from several blocks could be significant for a dose under a matrix of island blocks.

### 2.2.2 Comparison of composite effect of PBA-based and MC-based kernels for an array of island blocks

Intensity distributions for multi-block arrays were calculated using Monte Carlo-based kernels and compared to distributions calculated using the equivalent square block pencil beam-based kernels. Figure 2.11 shows the results in the uniform region for a block diameter of 0.117cm using packing radii of 0.5cm (IRF=0.95) and 0.2cm (IRF=0.69), with nominal beam energies of 9, 13, and 17 MeV respectively. At 9 MeV, Figure 2.11.a shows that PBA underestimate MC calculations by 2% for an IRF of 0.95 and by 5% at an IRF of 0.69. At 13 MeV, Figure 2.11.b shows that PBA and MC calculations agree to within 1% for both IRFs. At 17 MeV, Figure 2.11.c, the calculations agree to within 2% neglecting the points at block central axes, where differences are as much as 5%.

Figure 2.12 shows the results in the uniform region for a slightly different, more practical case, using a set r=0.5cm and using two diameters d=0.117cm (IRF=0.95) and d=0.288cm (IRF=0.70) for 100 cm SSD and 2.0 cm depth. At 9 MeV, Figure 2.12.a shows that PBA overestimates MC calculations by up to 5% for an IRF of 0.95 and underestimates by 3%

at an IRF=0.70. At 13 MeV, Figure 2.12.b shows that PBA and MC calculations agree to within 3% for both IRFs. At 17 MeV, Figure 2.12.c, the calculations agree to within 2% for IRF=0.95 and 4% for IRF=0.70.

## 2.3 Conclusions and discussion

In this aim, the objective was to evaluate the accuracy of PBA intensity calculations compared to Monte Carlo calculations. This was done by comparing PBA and MC calculations for a single central axis block in a 25x25 $cm^2$ field and for a subset of beam energies and block diameters. Additionally, intensity distributions were calculated for composite block arrays (20x20 $cm^2$ field filled with a regular hexagonal grid of identical blocks) using PBA- and MC-based intensity reduction kernels. For a single central-axis island block, differences under island block showed the PBA kernels overcalculated the MC calculation by as much as 30%. Of equal importance, intensity lateral to the block showed differences less than 1%, but still significant due to lateral extension (d/2) + 0.04 cm $\leq |x| \leq$ 2.0 cm. The net impact of these differences was seen in the differences of the composite dose distributions under a matrix of island blocks. Differences ranged ±5%. Based on these differences, it was concluded that it was acceptable to use the PBA for our qualitative study of the impact of island block parameters, beam energy, source to surface distance, air gap, and depth on achieving desired IRFs; however, the comparisons in this aim could be improved by the following:

1. Modeling the block as a circle, not a square,
2. Including the photon dose model in the PBA,
3. Improving MC statistics by increasing the radial sampling from every 30° to 0.2 cm along a circumference,
4. Performing MC calculations at a more clinical SSD (103 cm).

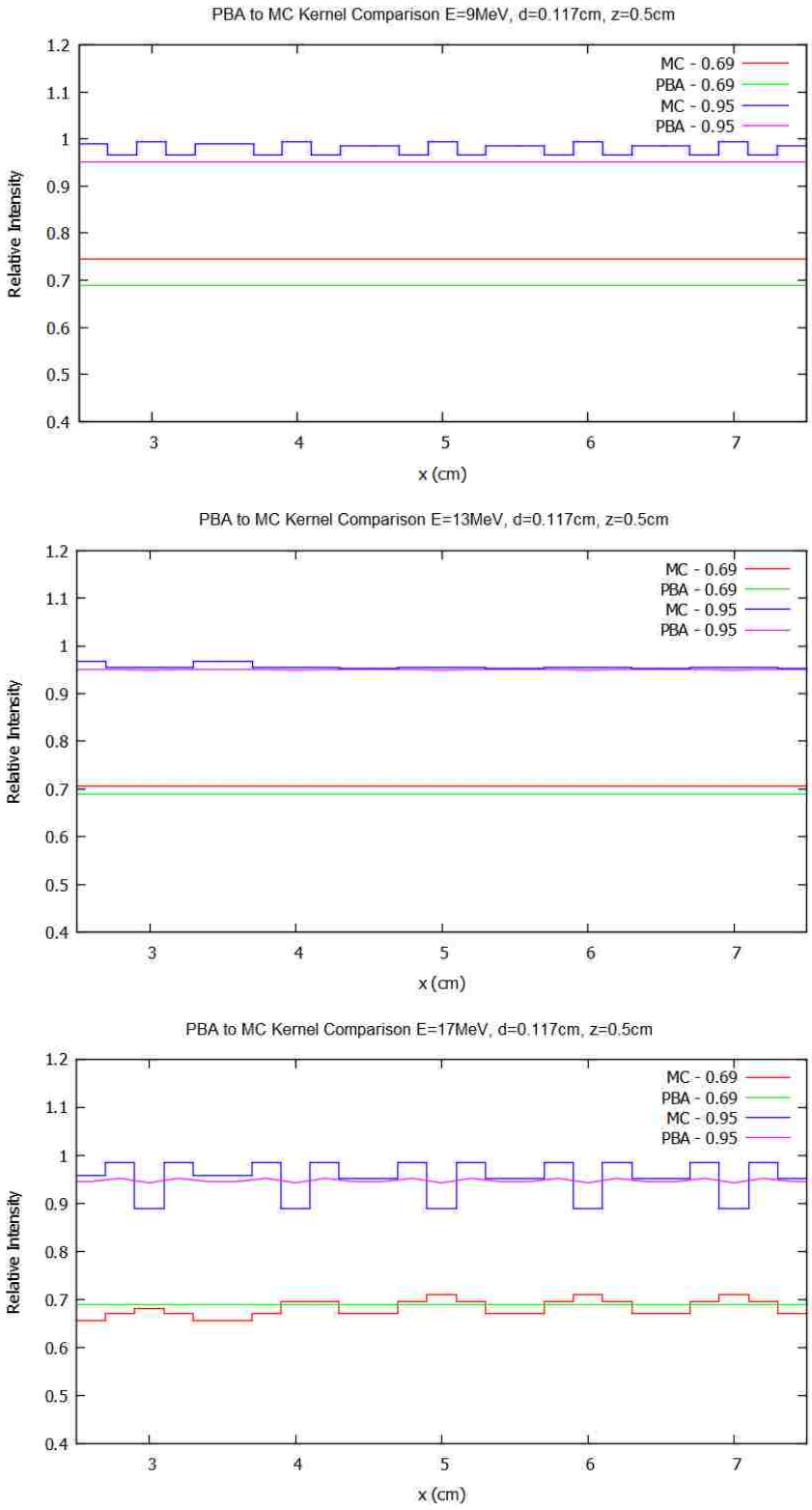


Figure 2.11: Off-axis profile for 9, 13, and 17 MeV beam at 100 cm SSD, IRF=0.95 (r=0.5cm) and IRF=0.69 (r=0.2cm), through y=0cm of a 20x20 $cm^2$ half-blocked field.

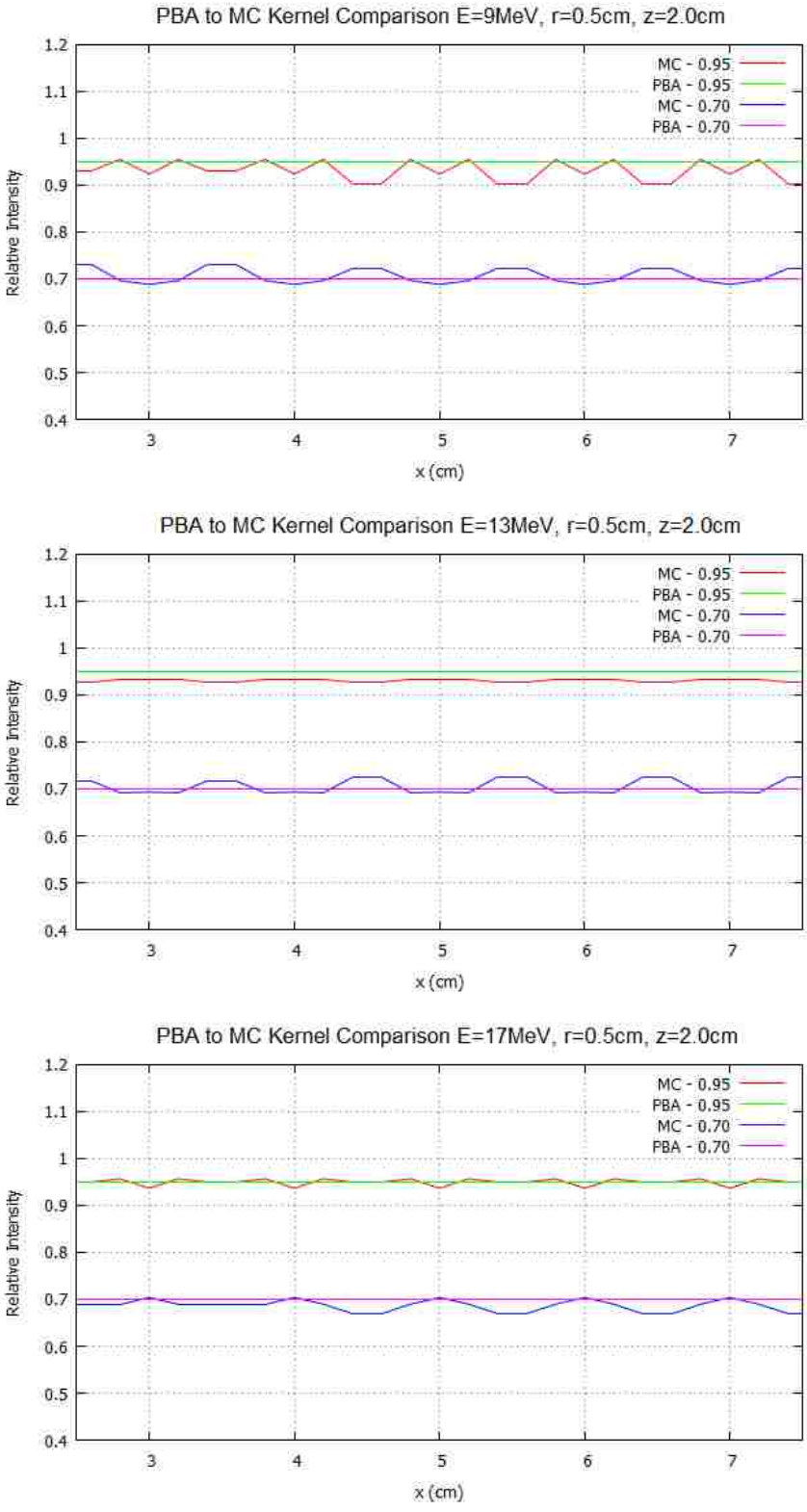


Figure 2.12: Off-axis profile for 9, 13, and 17 MeV beam at 100 cm SSD, IRF=0.95 (d=.117cm) and IRF=0.70 (d=.288cm), through y=0cm of a 20x20 $cm^2$ half-blocked field.

# 3 AIM 2: DEPENDENCE OF INTENSITY REDUCTION ON ISLAND BLOCK DIAMETER AND PACKING RADIUS

Using a pencil beam algorithm for electron dose calculations, determine island block geometries (diameter and packing radius) for passive electron intensity reduction (70-95%) that minimize Distance of Transition ($d_T$) and Ripple Intensity ($\Delta I_R$) for electron energies ranging from 7-20 MeV.

## 3.1 Research methods

### 3.1.1 Determining clinical acceptability for block combinations (r,d) at therapeutic energies using PBA

Equation 2.3 was used with the pencil beam algorithm (PBA) to determine which block geometries ($r$ and $d$) produce intensity distributions (70-95%) acceptable for clinical use. Calculations were performed for monoenergetic beams of energies 7, 9, 10, 11, 13, 16, and 20 MeV using a 20x20 cm$^2$ field at depths of 0.5 cm and 2.0 cm. The PBA assumed a parallel beam with $\sigma_{\theta_x}$ given by Equation 2.10. The collimating plane to water surface distances (air gaps) were taken to be 5 cm and 8 cm, corresponding to a 100 cm and 103 cm SSD, respectively, for a clinically divergent beam. The latter corresponds to setting the patient skin surface at 105 cm SSD and placing an average bolus thickness of 2 cm, typical of a clinical setup. At the depth of calculation $z$, relative intensity was calculated using a point spacing of 0.2 cm in $x$ and $y$.

Half of the 20x20 cm$^2$ field was covered with an array of identical cylindrical island blocks in a hexagonal packing formation with packing radius $r$ and block diameter $d$. A schematic of one such block matrix is shown in Figure 3.1.

Calculated relative intensity distributions were evaluated using two metrics: Average Blocked Intensity ($I_{avg}$) and Ripple Intensity ($\Delta I_R$). $I_{avg}$ was the average intensity for $|y|<7.5$ cm and $2.5 \leq |x| \leq 7.5$ cm. Ripple Intensity was defined as the difference between the maximum and minimum intensities within the blocked region, defined by $|y|<7.5$ cm

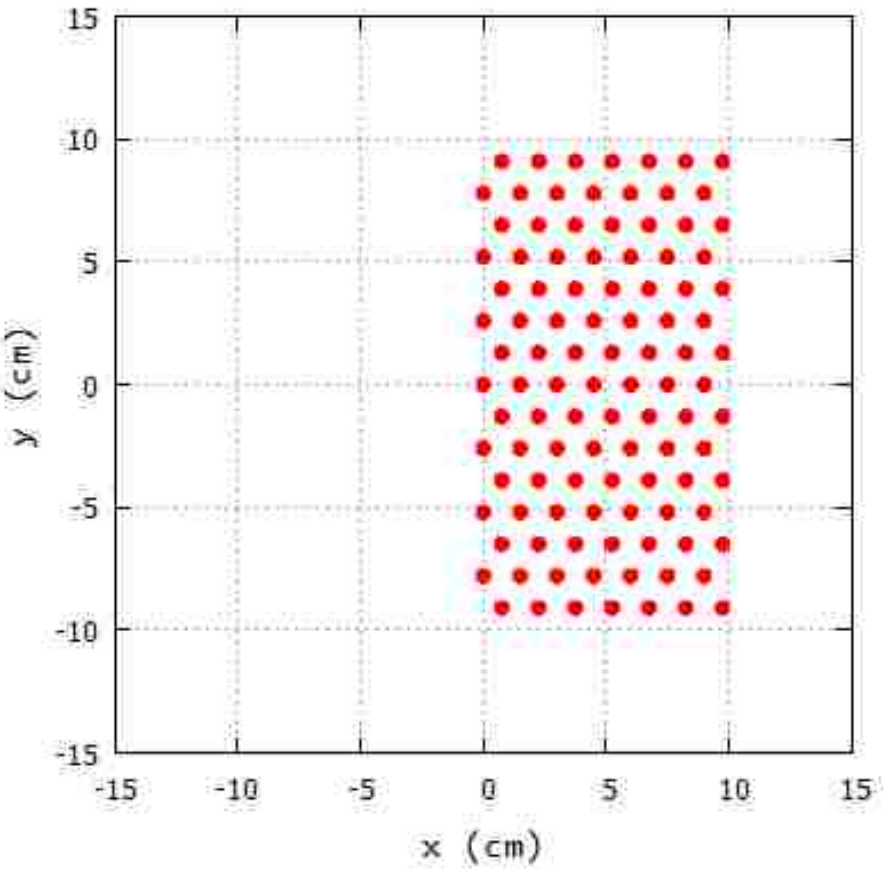


Figure 3.1: Sample island block matrix used to determine acceptable (r,d) combinations. For this particular example, blocks with (r,d)=(1.50cm,0.498cm), having an IRF=0.90, are hexagonally packed over the field in the +x plane at the positions indicated by the red circles. Circle diameters on the image are proportionally correct with the true value.

and $2.5 \leq |x| \leq 7.5$ cm. A block configuration ($r$,$d$) for each energy, was considered unacceptable if $I_{avg}$ differed from the intended IRF by more than 2% or if $\Delta I_R$ was greater than 4%. In addition, a third metric called Distance of Transition ($d_T$) was calculated for all combinations. Distance of Transition was defined as the average straight-line distance along the $x$-axis from relative intensities 0.99 to IRF +0.01 for each $y$-coordinate between [-7.5,7.5]. This distance is a measure of the spatial resolution of the specific IRF. Figure 3.2 illustrates these three metrics.

These metrics were studied for 6 IRF values (0.70, 0.75, 0.80, 0.85, 0.90, and 0.95) and 5 packing radius ($r$) values (0.5, 0.75, 1.0, 1.25, and 1.5 cm). For each of the 30

geometries, the island block diameter d(IRF,r) was computed using Equation 2.2. For each geometry the metrics were calculated for 7 energies (7-20 MeV), 2 SSDs (100 cm and 103 cm), and 2 depths ($z$=0.5 cm and $z$=2.0 cm). These 28 combinations resulted in 840 different conditions for which calculations were performed.

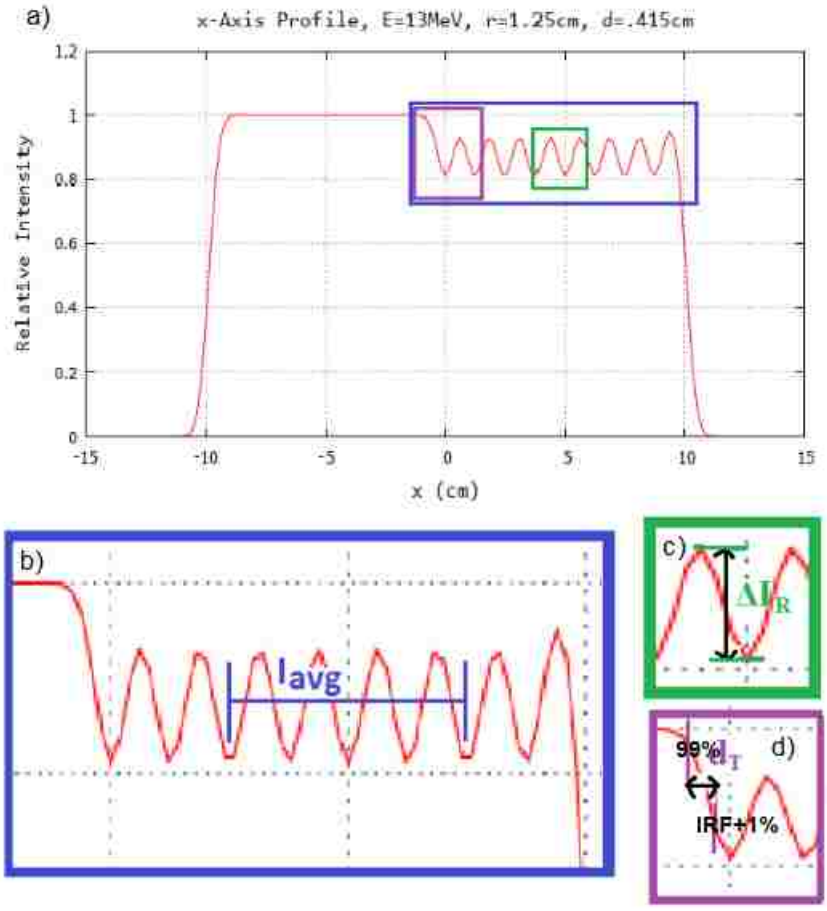


Figure 3.2: Illustrations of the assessment metrics. (a) A single x-axis profile (y=0cm) for E=13MeV, FS=20x20cm$^2$, SSD=100cm, z=2.0cm is plotted for a matrix of island blocks at locations shown in Figure 3.1, with island blocks defined by r=1.25cm, and d=.415cm (IRF=.85). Outlined regions corresponding to the assessment metrics: $I_{avg}$ are given in blue (b), $\Delta I_R$ in green (c), and $d_T$ in purple (d).

### 3.2 Results

This section provides results for half-beam intensity modulation computed by the PBA. Results are presented for 7 energies, 2 SSDs, 2 depths (z) in water, 5 packing radii, and

6 IRFs ranging from 0.70-0.95 using a total of 30 island block diameters calculated using Equation 2.2 (c.f. Table 3.1).

Table 3.1: Diameters in cm used for the range of island block combinations (IRF,r) calculated using Equation 2.2. Resulting diameter values ranged from 0.117-0.863 cm.

| **IRF** | **r=0.5cm** | **r=0.75cm** | **r=1.0cm** | **r=1.25cm** | **r=1.5cm** |
|---|---|---|---|---|---|
| 0.95 | 0.117 | 0.176 | 0.235 | 0.294 | 0.352 |
| 0.90 | 0.166 | 0.249 | 0.332 | 0.415 | 0.498 |
| 0.85 | 0.203 | 0.305 | 0.407 | 0.508 | 0.610 |
| 0.80 | 0.235 | 0.352 | 0.470 | 0.587 | 0.704 |
| 0.75 | 0.263 | 0.394 | 0.525 | 0.656 | 0.788 |
| 0.70 | 0.288 | 0.431 | 0.575 | 0.719 | 0.863 |

### 3.2.1 Off-axis profiles under island block arrays for uniform half-beam intensity modulation

For 10 MeV, Figures 3.3, 3.4, and 3.5 show off-axis profiles taken at y=0 for packing radii r=0.5, 1.0, and 1.5 cm respectively for each IRF (0.70, 0.75, 0.80, 0.85, 0.90, and 0.95) at calculation depths of z=0.5cm and z=2.0cm for 103 cm SSD. Similar results at 16 MeV are shown in Figures 3.6, 3.7, and 3.8, respectively. The complete set of y=0 profiles for all $r$ (0.5, 0.75, 1.0, 1.25, and 1.5 cm) and IRF (0.70, 0.75, 0.80, 0.85, 0.90, and 0.95) combinations at all energies (7, 9, 10, 11, 13, 16, and 20 MeV), both SSDs (100 and 103 cm), and both depths (0.5 and 2.0 cm) is given in Appendix B.

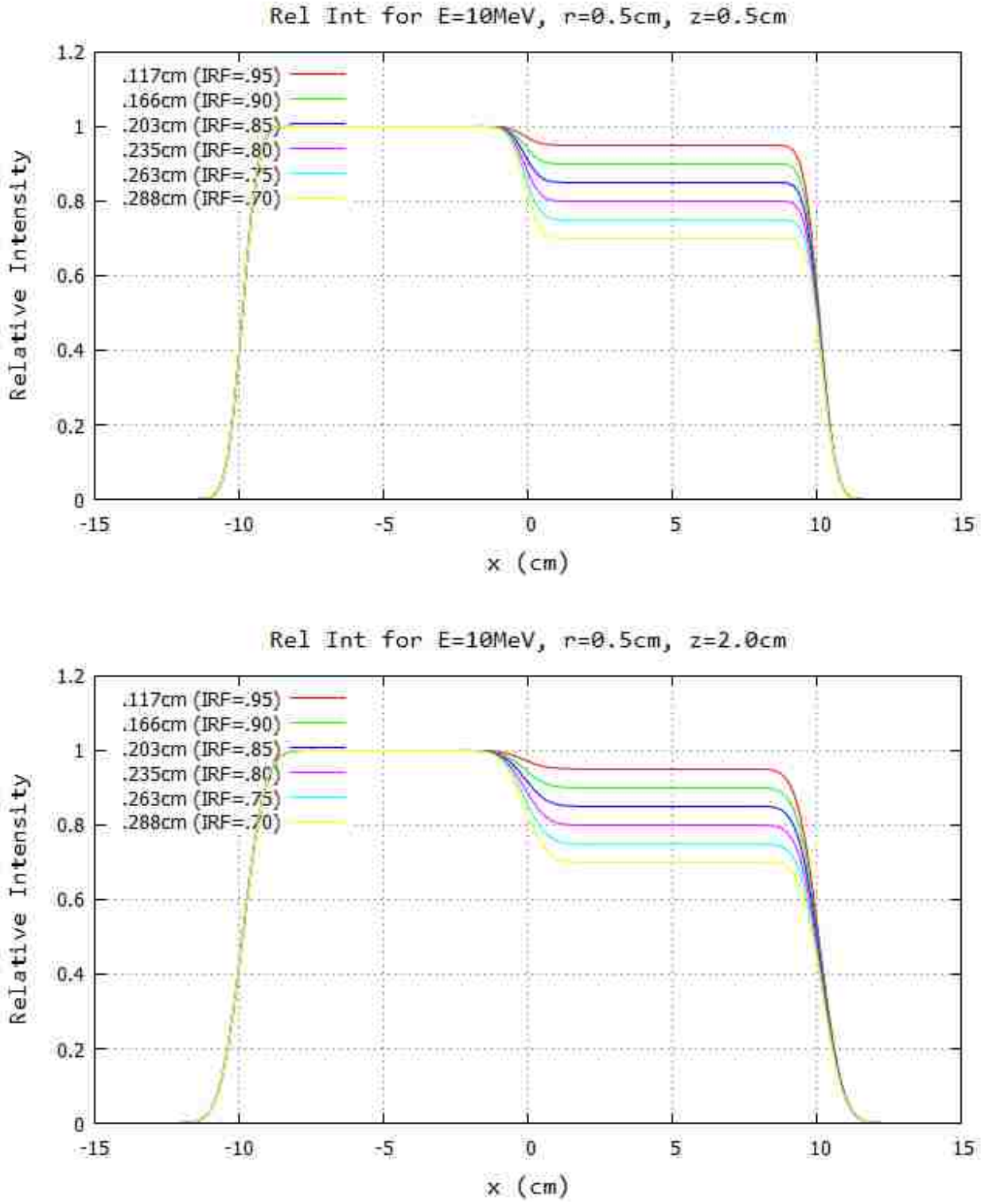


Figure 3.3: Profiles at y=0cm for 10 MeV, 20x20 half-blocked field (r=0.5cm), 100 cm SSD: z=0.5cm (top) and z=2.0cm (bottom). The computed island block diameter for 0.70, 0.75, 0.80, 0.85, 0.90, and 0.95 IRF values are listed in each plot's inserted key.

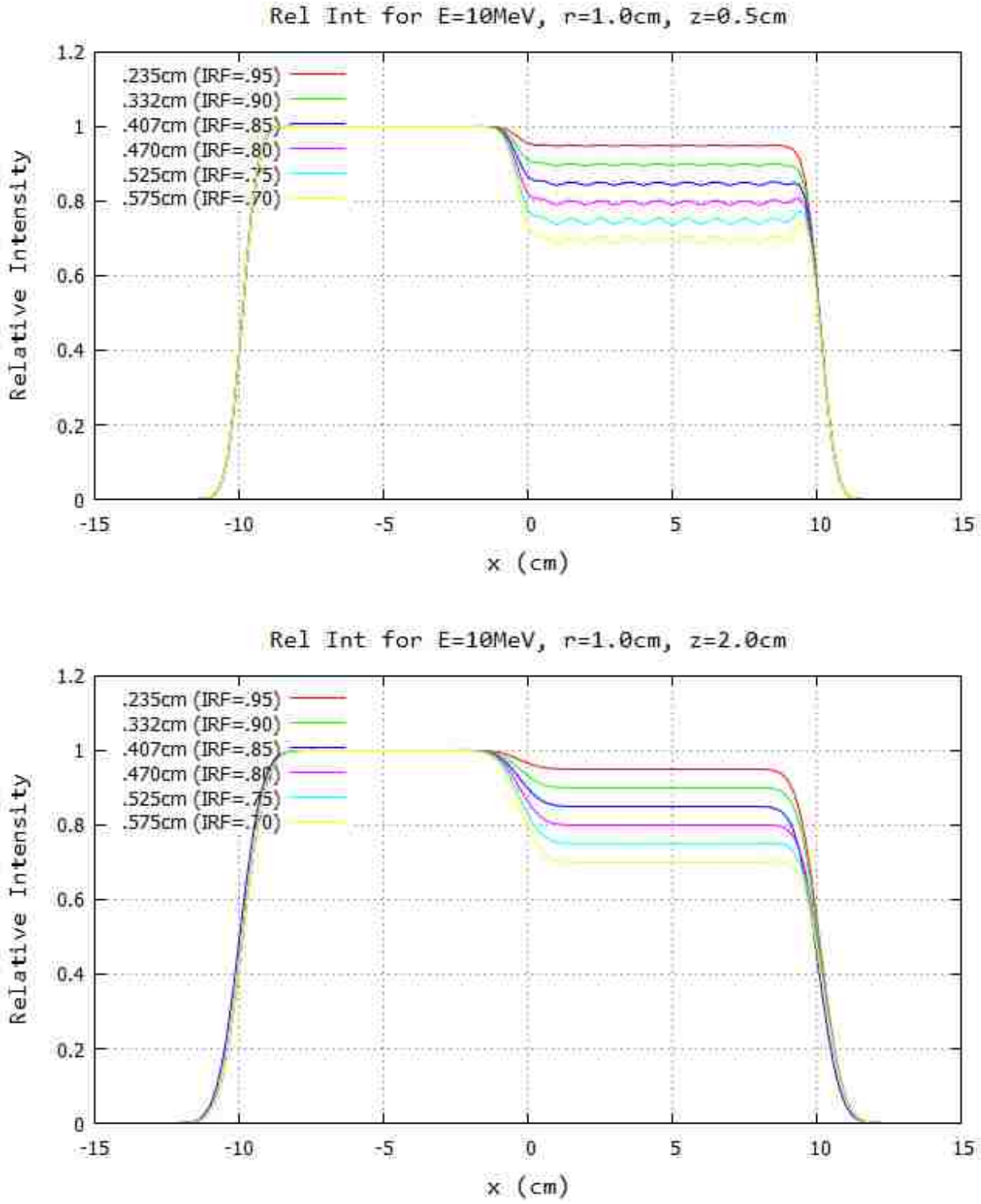


Figure 3.4: Profiles at y=0cm for 10 MeV, 20x20 half-blocked field (r=1.0cm), 100 cm SSD: z=0.5cm (top) and z=2.0cm (bottom). The computed island block diameter for 0.70, 0.75, 0.80, 0.85, 0.90, and 0.95 IRF values are listed in each plot's inserted key.

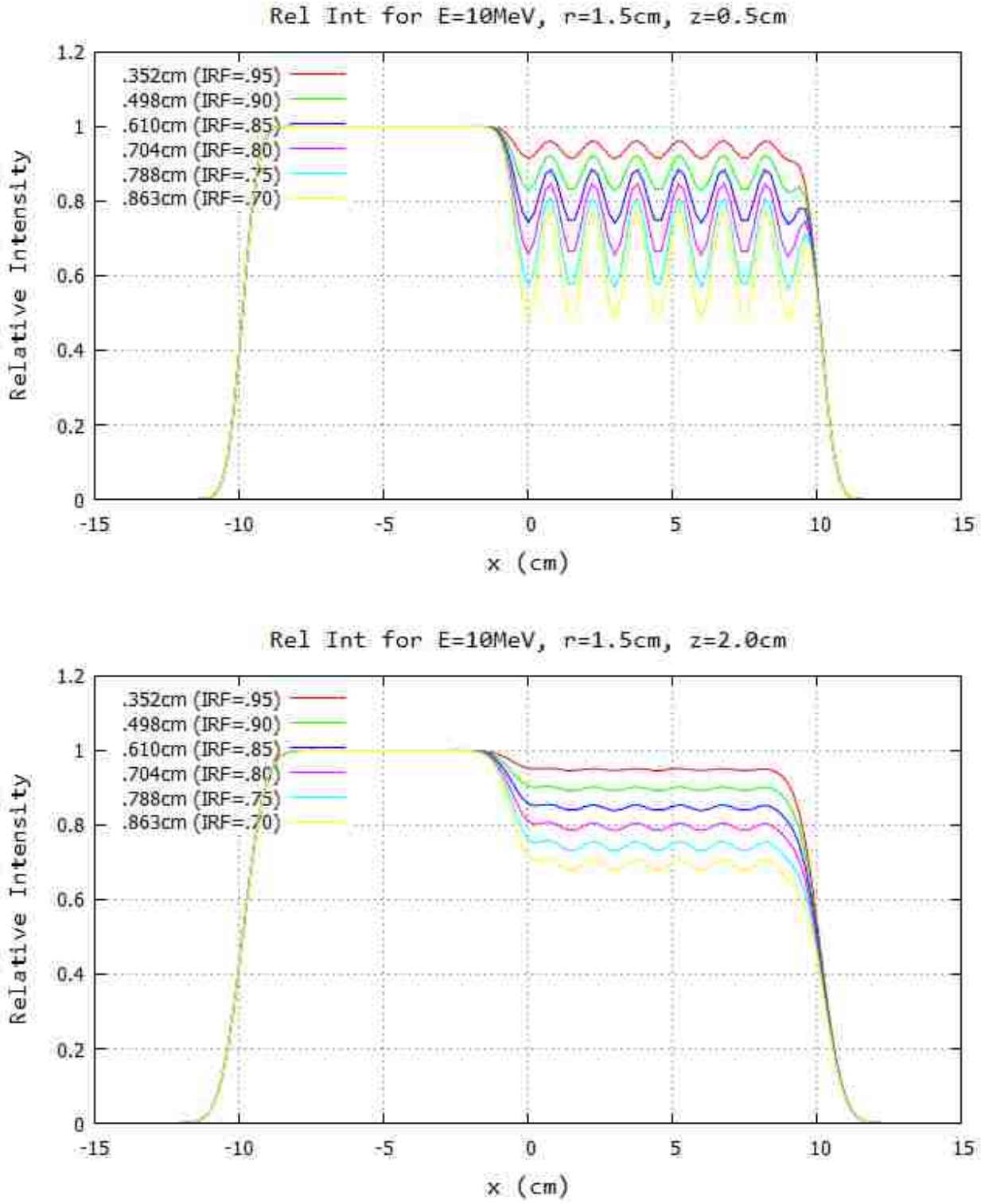


Figure 3.5: Profiles at y=0cm for 10 MeV, 20x20 half-blocked field (r=1.5cm), 100 cm SSD: z=0.5cm (top) and z=2.0cm (bottom). The computed island block diameter for 0.70, 0.75, 0.80, 0.85, 0.90, and 0.95 IRF values are listed in each plot's inserted key.

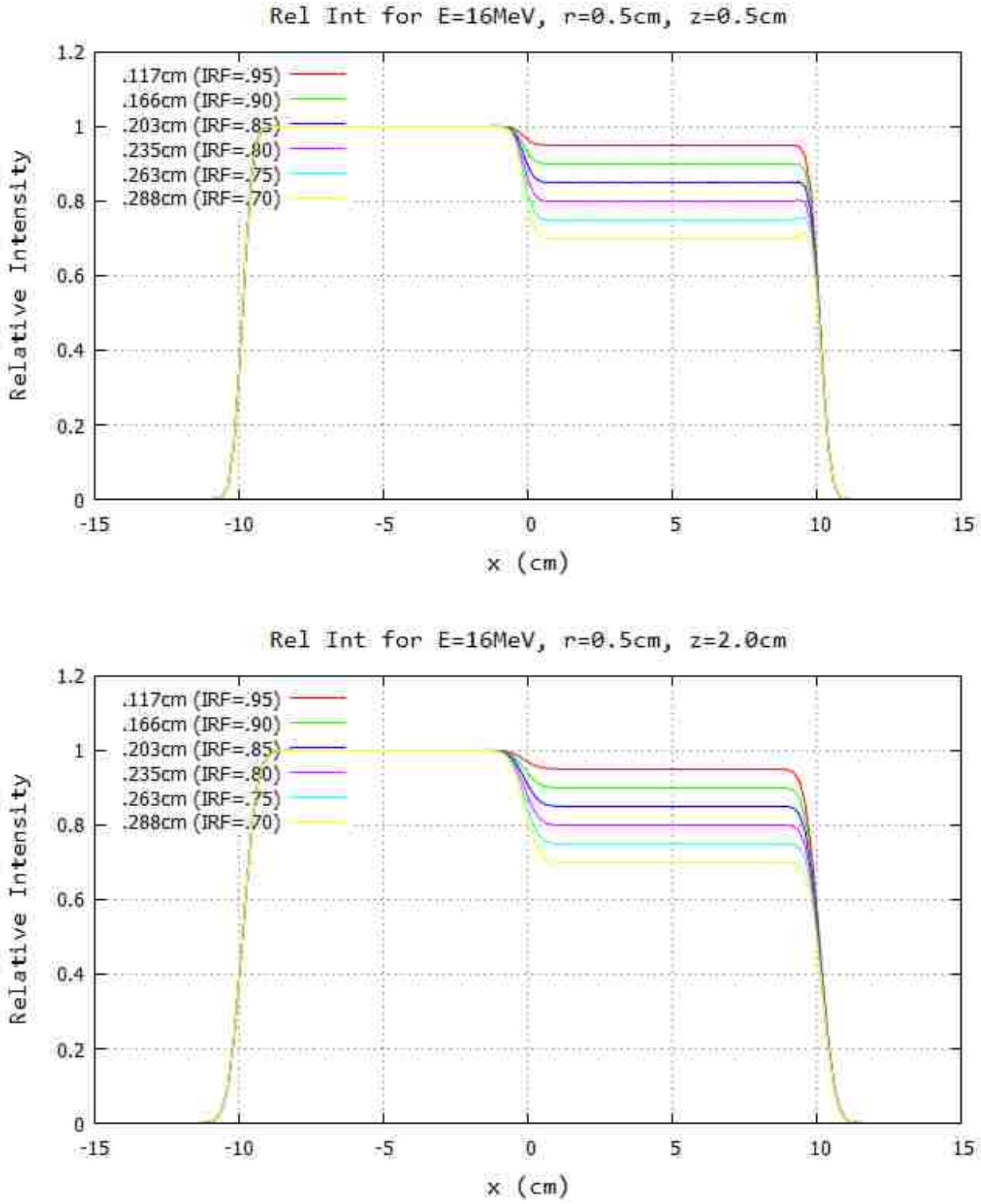


Figure 3.6: Profiles at y=0cm for 16 MeV, 20x20 half-blocked field (r=0.5cm), 100 cm SSD: z=0.5cm (top) and z=2.0cm (bottom). The computed island block diameter for 0.70, 0.75, 0.80, 0.85, 0.90, and 0.95 IRF values are listed in each plot's inserted key.

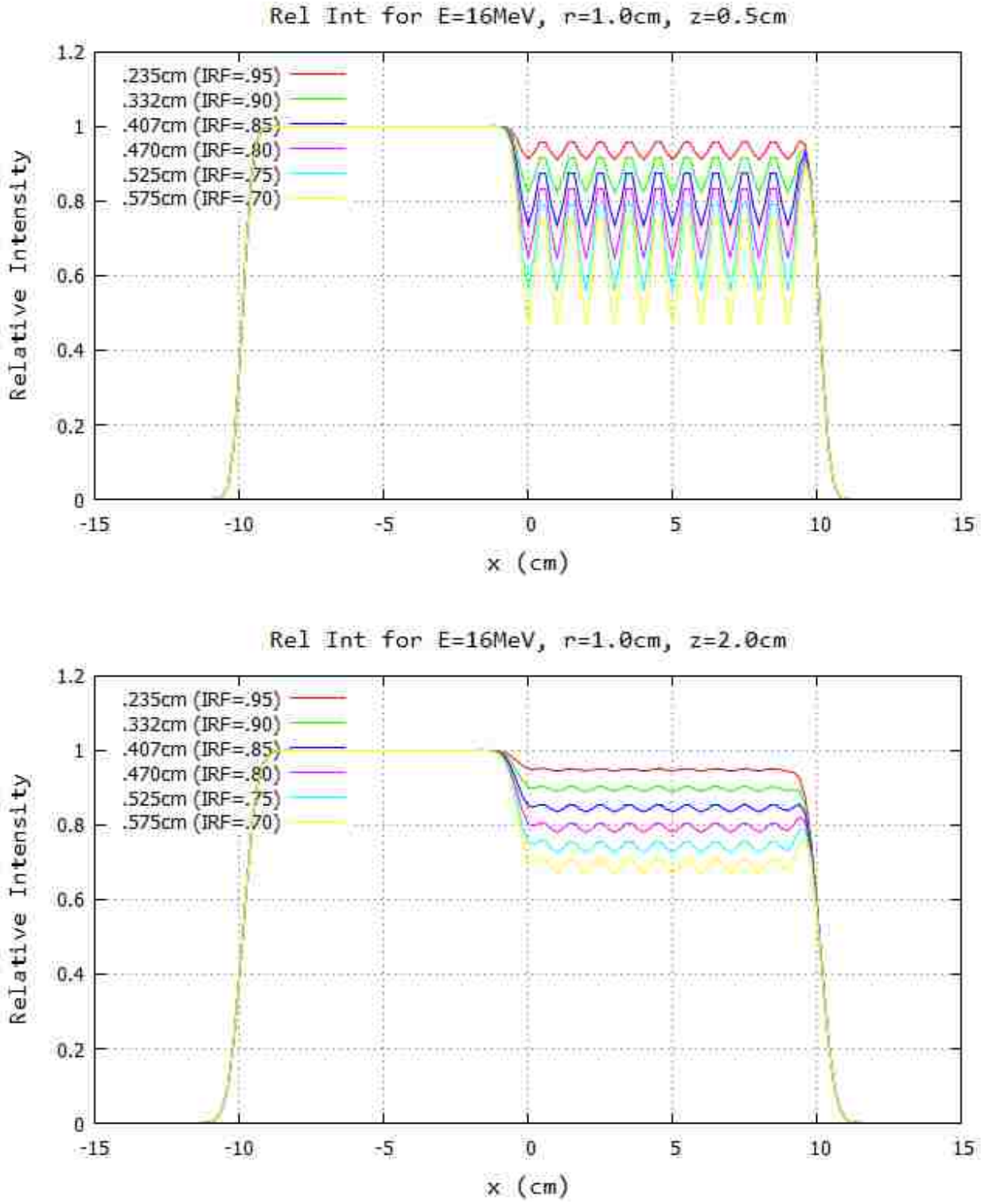


Figure 3.7: Profiles at y=0cm for 16 MeV, 20x20 half-blocked field (r=1.0cm), 100 cm SSD: z=0.5cm (top) and z=2.0cm (bottom). The computed island block diameter for 0.70, 0.75, 0.80, 0.85, 0.90, and 0.95 IRF values are listed in each plot's inserted key.

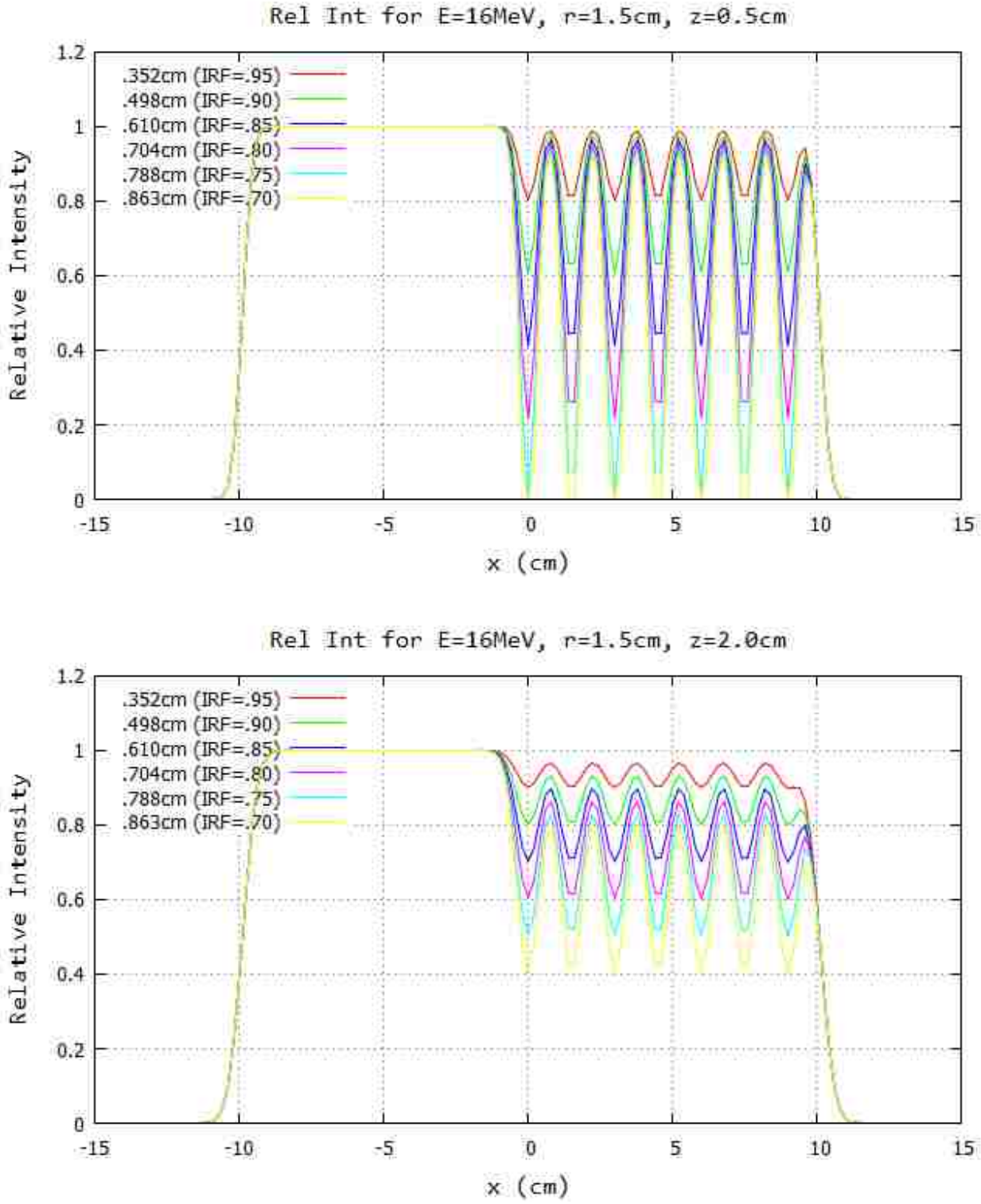


Figure 3.8: Profiles at y=0cm for 16 MeV, 20x20 half-blocked field (r=1.5cm), 100 cm SSD: z=0.5cm (top) and z=2.0cm (bottom). The computed island block diameter for 0.70, 0.75, 0.80, 0.85, 0.90, and 0.95 IRF values are listed in each plot's inserted key.

### 3.2.2 Evaluation of acceptability metrics for uniform half-beam intensity modulation using island blocks

These PBA-calculated, relative electron intensity distributions were scored and evaluated using the three metrics $I_{avg}$, $\Delta I_R$, and $d_T$, described in Section 3.1.1. Tables 3.2 and 3.3 show the scoring values for the 10 MeV and 16 MeV distributions, respectively, at 103 cm SSD. Tables for all 7 energies and 2 SSDs can be found in Appendix C.

#### 3.2.2.1 Evaluation of $I_{avg}$

For all combinations of beam energy, SSD, $z$, $r$, and IRF having $\Delta I_R$ values less than 0.10, well outside the acceptable criteria of 0.04, $I_{avg}$ agrees within 0.001 of the intended values (0.70, 0.75, 0.80, 0.85, 0.90, and 0.95). Hence, the $I_{avg}$ acceptance criteria is redundant and unnecessary. This is not an unexpected outcome, as $I_{avg}$ should equal the fraction of the beam unblocked by the island blocks. Although $I_{avg}$ may not hold any value for assessing treatment parameters for a half-field uniform modulation, the agreement between calculated intensity for an actual patient $IRF_{calc}$ and the objective intensity $IRF_{obj}$ will remain important.

#### 3.2.2.2 Evaluation of $\Delta I_R$

Ripple Intensity $\Delta I_R$ trends smaller for reduced energy, reduced packing radius, and IRFs nearer to 1.0. Another way to look at the data is to evaluate what are the acceptable $r$ values for a specific set of conditions, namely energy, SSD, and IRF, the latter being the minimum value for a specific patient's planned intensity distribution. The largest acceptable $r$ values are advantageous because they require (1) the smallest total number of blocks and (2) the largest block diameter, both desirous from a fabrication perspective. Therefore, it is preferred to select the largest $r$ value that keeps $\Delta I_R \leq 4\%$ at z=2.0cm. Data for z=0.5cm produce substantially greater $\Delta I_R$ values, which require progressively smaller $r$ values if the shallow depth oscillations are in the patient, as opposed to in the bolus. Further analysis of results will be restricted to 103 cm SSD, since this is typical of the clinic.

Table 3.2: Metrics summary for 10 MeV at 103 cm SSD at y=0cm 20x20 half-blocked field for z=0.5cm (left) and z=2.0cm (right).

| r (cm) | IRF | d (cm) | $d_T$ | $\sigma_{d_T}$ | $I_{avg}$ | $\Delta I_R$ | $d_T$ | $\sigma_{d_T}$ | $I_{avg}$ | $\Delta I_R$ |
|---|---|---|---|---|---|---|---|---|---|---|
| | 0.95 | 0.117 | 0.63 | 0.02 | 0.950 | 0.000 | 1.05 | 0.03 | 0.950 | 0.000 |
| | 0.90 | 0.166 | 1.03 | 0.02 | 0.900 | 0.000 | 1.66 | 0.03 | 0.900 | 0.000 |
| 0.50 cm | 0.85 | 0.203 | 1.42 | 0.02 | 0.851 | 0.000 | 1.87 | 0.03 | 0.851 | 0.000 |
| | 0.80 | 0.235 | 1.42 | 0.02 | 0.800 | 0.000 | 2.07 | 0.03 | 0.800 | 0.000 |
| | 0.75 | 0.263 | 1.43 | 0.02 | 0.749 | 0.000 | 2.26 | 0.03 | 0.749 | 0.000 |
| | 0.70 | 0.288 | 1.62 | 0.02 | 0.699 | 0.000 | 2.27 | 0.03 | 0.699 | 0.000 |
| r (cm) | IRF | d (cm) | $d_T$ | $\sigma_{d_T}$ | $I_{avg}$ | $\Delta I_R$ | $d_T$ | $\sigma_{d_T}$ | $I_{avg}$ | $\Delta I_R$ |
| | 0.95 | 0.176 | 0.79 | 0.02 | 0.950 | 0.000 | 1.15 | 0.03 | 0.950 | 0.000 |
| | 0.90 | 0.249 | 1.16 | 0.02 | 0.900 | 0.000 | 1.67 | 0.03 | 0.900 | 0.000 |
| 0.75 cm | 0.85 | 0.305 | 1.22 | 0.02 | 0.850 | 0.000 | 2.02 | 0.03 | 0.850 | 0.000 |
| | 0.80 | 0.352 | 1.42 | 0.02 | 0.800 | 0.000 | 2.07 | 0.03 | 0.800 | 0.000 |
| | 0.75 | 0.394 | 1.58 | 0.02 | 0.750 | 0.000 | 2.81 | 0.03 | 0.750 | 0.000 |
| | 0.70 | 0.431 | 1.62 | 0.02 | 0.701 | 0.001 | 2.44 | 0.02 | 0.701 | 0.000 |
| r (cm) | IRF | d (cm) | $d_T$ | $\sigma_{d_T}$ | $I_{avg}$ | $\Delta I_R$ | $d_T$ | $\sigma_{d_T}$ | $I_{avg}$ | $\Delta I_R$ |
| | 0.95 | 0.235 | 0.67 | 0.02 | 0.950 | 0.004 | 1.04 | 0.03 | 0.950 | 0.000 |
| | 0.90 | 0.332 | 1.03 | 0.02 | 0.900 | 0.007 | 1.61 | 0.03 | 0.900 | 0.000 |
| 1.00 cm | 0.85 | 0.407 | 1.24 | 0.02 | 0.850 | 0.011 | 1.53 | 0.08 | 0.850 | 0.000 |
| | 0.80 | 0.470 | 1.30 | 0.02 | 0.800 | 0.015 | 2.03 | 0.03 | 0.800 | 0.000 |
| | 0.75 | 0.525 | 1.47 | 0.03 | 0.750 | 0.019 | 2.17 | 0.03 | 0.750 | 0.000 |
| | 0.70 | 0.575 | 1.64 | 0.03 | 0.700 | 0.022 | 2.26 | 0.03 | 0.700 | 0.000 |
| r (cm) | IRF | d (cm) | $d_T$ | $\sigma_{d_T}$ | $I_{avg}$ | $\Delta I_R$ | $d_T$ | $\sigma_{d_T}$ | $I_{avg}$ | $\Delta I_R$ |
| | 0.95 | 0.294 | 0.69 | 0.04 | 0.950 | 0.021 | 0.98 | 0.03 | 0.950 | 0.001 |
| | 0.90 | 0.415 | 1.98 | 0.06 | 0.900 | 0.042 | 1.59 | 0.02 | 0.900 | 0.002 |
| 1.25 cm | 0.85 | 0.508 | 2.27 | 0.07 | 0.850 | 0.063 | 1.78 | 0.03 | 0.850 | 0.002 |
| | 0.80 | 0.587 | 2.20 | 0.06 | 0.800 | 0.084 | 2.02 | 0.02 | 0.800 | 0.003 |
| | 0.75 | 0.656 | 2.24 | 0.05 | 0.750 | 0.104 | 2.12 | 0.02 | 0.750 | 0.004 |
| | 0.70 | 0.719 | 2.26 | 0.05 | 0.700 | 0.125 | 2.19 | 0.02 | 0.700 | 0.005 |
| r (cm) | IRF | d (cm) | $d_T$ | $\sigma_{d_T}$ | $I_{avg}$ | $\Delta I_R$ | $d_T$ | $\sigma_{d_T}$ | $I_{avg}$ | $\Delta I_R$ |
| | 0.95 | 0.352 | 2.5 | 0.1 | 0.950 | 0.053 | 0.95 | 0.03 | 0.950 | 0.006 |
| | 0.90 | 0.498 | 2.51 | 0.08 | 0.901 | 0.106 | 1.43 | 0.04 | 0.900 | 0.011 |
| 1.50 cm | 0.85 | 0.610 | 2.65 | 0.07 | 0.851 | 0.159 | 1.94 | 0.05 | 0.850 | 0.017 |
| | 0.80 | 0.704 | 2.50 | 0.08 | 0.802 | 0.212 | 2.18 | 0.04 | 0.800 | 0.022 |
| | 0.75 | 0.788 | 2.42 | 0.09 | 0.752 | 0.266 | 2.61 | 0.05 | 0.750 | 0.028 |
| | 0.70 | 0.863 | 2.45 | 0.09 | 0.702 | 0.319 | 2.74 | 0.07 | 0.700 | 0.034 |

Figure 3.9 plots $\Delta I_R$ versus $r$ (cm) for multiple combinations of energies (11, 13, 16, and 20 MeV) and IRF values (0.70, 0.80,and 0.90). These plots were used to estimate $r$ values for which $\Delta I_R$=0.04, which are plotted versus IRF for the highest three energies in

Table 3.3: Metrics summary for 16 MeV at 103 cm SSD at y=0cm 20x20 half-blocked field for z=0.5cm (left) and z=2.0cm (right).

| r (cm) | IRF | d (cm) | $d_T$ | $\sigma_{d_T}$ | $I_{avg}$ | $\Delta I_R$ | $d_T$ | $\sigma_{d_T}$ | $I_{avg}$ | $\Delta I_R$ |
|---|---|---|---|---|---|---|---|---|---|---|
| | 0.95 | 0.117 | 0.56 | 0.01 | 0.950 | 0.042 | 0.63 | 0.02 | 0.950 | 0.000 |
| | 0.90 | 0.166 | 0.61 | 0.01 | 0.900 | 0.007 | 1.03 | 0.02 | 0.900 | 0.000 |
| 0.50 cm | 0.85 | 0.203 | 0.94 | 0.01 | 0.851 | 0.001 | 1.22 | 0.02 | 0.851 | 0.000 |
| | 0.80 | 0.235 | 1.00 | 0.00 | 0.800 | 0.000 | 1.42 | 0.02 | 0.800 | 0.000 |
| | 0.75 | 0.263 | 1.00 | 0.00 | 0.749 | 0.001 | 1.42 | 0.02 | 0.749 | 0.000 |
| | 0.70 | 0.288 | 1.00 | 0.00 | 0.699 | 0.001 | 1.42 | 0.02 | 0.699 | 0.000 |
| r (cm) | IRF | d (cm) | $d_T$ | $\sigma_{d_T}$ | $I_{avg}$ | $\Delta I_R$ | $d_T$ | $\sigma_{d_T}$ | $I_{avg}$ | $\Delta I_R$ |
| | 0.95 | 0.176 | 0.44 | 0.01 | 0.950 | 0.024 | 0.68 | 0.02 | 0.950 | 0.000 |
| | 0.90 | 0.249 | 0.73 | 0.02 | 0.900 | 0.031 | 1.03 | 0.02 | 0.900 | 0.001 |
| 0.75 cm | 0.85 | 0.305 | 1.38 | 0.08 | 0.850 | 0.033 | 1.22 | 0.02 | 0.850 | 0.001 |
| | 0.80 | 0.352 | 1.55 | 0.10 | 0.800 | 0.044 | 1.25 | 0.02 | 0.800 | 0.001 |
| | 0.75 | 0.394 | 2.35 | 0.09 | 0.750 | 0.056 | 1.39 | 0.02 | 0.750 | 0.001 |
| | 0.70 | 0.431 | 1.90 | 0.06 | 0.700 | 0.067 | 1.48 | 0.02 | 0.701 | 0.002 |
| r (cm) | IRF | d (cm) | $d_T$ | $\sigma_{d_T}$ | $I_{avg}$ | $\Delta I_R$ | $d_T$ | $\sigma_{d_T}$ | $I_{avg}$ | $\Delta I_R$ |
| | 0.95 | 0.235 | 1.17 | 0.06 | 0.950 | 0.056 | 0.59 | 0.03 | 0.950 | 0.007 |
| | 0.90 | 0.332 | 0.86 | 0.06 | 0.900 | 0.113 | 1.23 | 0.04 | 0.900 | 0.014 |
| 1.00 cm | 0.85 | 0.407 | 1.43 | 0.08 | 0.850 | 0.169 | 1.37 | 0.03 | 0.850 | 0.021 |
| | 0.80 | 0.470 | 1.68 | 0.07 | 0.800 | 0.226 | 1.55 | 0.03 | 0.800 | 0.029 |
| | 0.75 | 0.525 | 1.50 | 0.09 | 0.751 | 0.282 | 1.90 | 0.05 | 0.750 | 0.036 |
| | 0.70 | 0.575 | 1.50 | 0.07 | 0.701 | 0.338 | 2.21 | 0.07 | 0.700 | 0.043 |
| r (cm) | IRF | d (cm) | $d_T$ | $\sigma_{d_T}$ | $I_{avg}$ | $\Delta I_R$ | $d_T$ | $\sigma_{d_T}$ | $I_{avg}$ | $\Delta I_R$ |
| | 0.95 | 0.294 | 1.19 | 0.08 | 0.950 | 0.122 | 1.07 | 0.07 | 0.950 | 0.032 |
| | 0.90 | 0.415 | 1.29 | 0.08 | 0.901 | 0.243 | 2.09 | 0.07 | 0.900 | 0.064 |
| 1.25 cm | 0.85 | 0.508 | 1.43 | 0.08 | 0.851 | 0.363 | 1.98 | 0.05 | 0.850 | 0.095 |
| | 0.80 | 0.587 | 1.50 | 0.09 | 0.801 | 0.485 | 2.10 | 0.05 | 0.800 | 0.127 |
| | 0.75 | 0.656 | 1.55 | 0.08 | 0.752 | 0.606 | 2.17 | 0.06 | 0.751 | 0.159 |
| | 0.70 | 0.719 | 1.56 | 0.08 | 0.702 | 0.728 | 2.17 | 0.06 | 0.700 | 0.191 |
| r (cm) | IRF | d (cm) | $d_T$ | $\sigma_{d_T}$ | $I_{avg}$ | $\Delta I_R$ | $d_T$ | $\sigma_{d_T}$ | $I_{avg}$ | $\Delta I_R$ |
| | 0.95 | 0.352 | 0.67 | 0.07 | 0.951 | 0.191 | 2.2 | 0.1 | 0.951 | 0.071 |
| | 0.90 | 0.498 | 0.69 | 0.05 | 0.903 | 0.382 | 2.48 | 0.07 | 0.901 | 0.143 |
| 1.50 cm | 0.85 | 0.610 | 0.97 | 0.06 | 0.854 | 0.573 | 2.40 | 0.07 | 0.852 | 0.214 |
| | 0.80 | 0.704 | 0.97 | 0.06 | 0.806 | 0.763 | 2.60 | 0.06 | 0.802 | 0.285 |
| | 0.75 | 0.788 | 0.99 | 0.06 | 0.757 | 0.955 | 2.54 | 0.06 | 0.752 | 0.357 |
| | 0.70 | 0.863 | 0.98 | 0.06 | 0.712 | 0.967 | 2.41 | 0.08 | 0.703 | 0.428 |

Figure 3.10. Now based on energy and minimum required IRF, a maximum island block packing radius $r$ value can be selected.

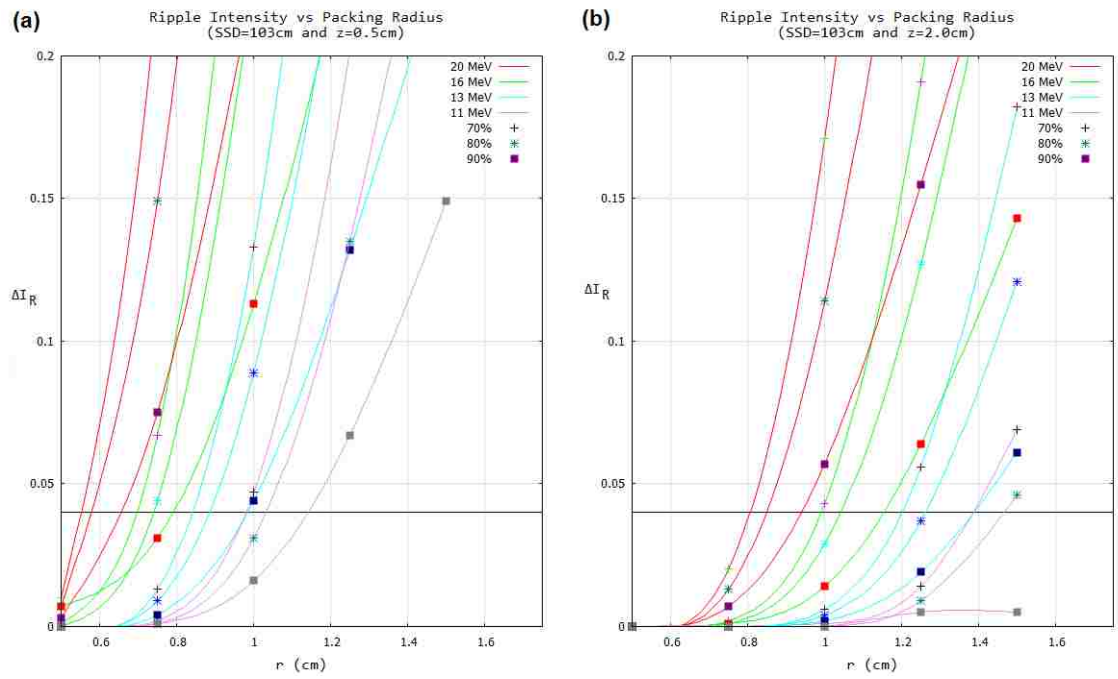


Figure 3.9: $\Delta I_R$ versus packing radius for clinical energies used in bolus ECT. Beam energy is given by line color and minimum IRF by point type in key. $\Delta I_R$ acceptability threshold (0.04) is illustrated with a horizontal black line. Results are plotted for (a) z=0.5cm and (b) z=2.0cm.

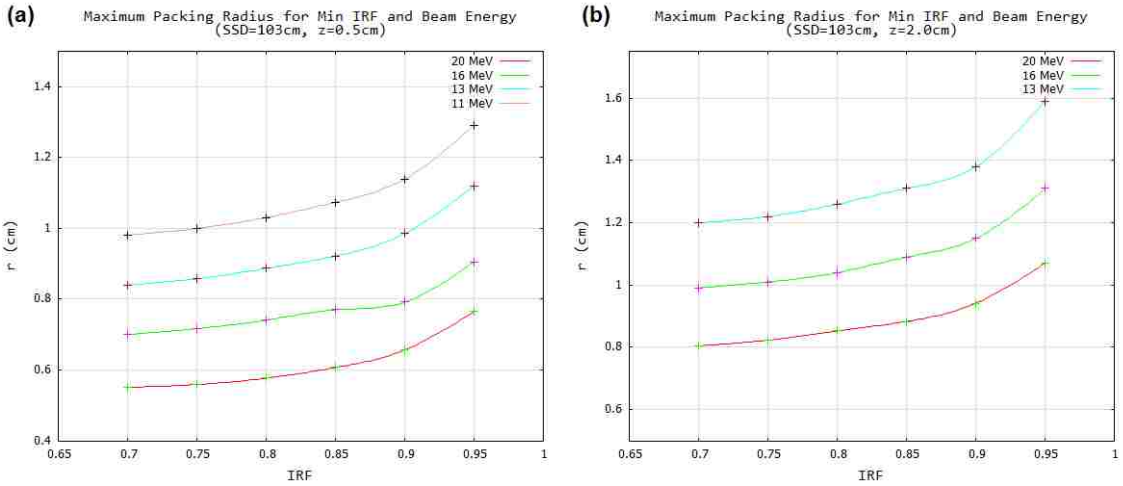


Figure 3.10: Reference plot for determination of packing radius for intensity modulators designed for 103 cm SSD and average bolus thickness 2 cm. Results are plotted for (a) z=0.5cm and (b) z=2.0cm.

#### 3.2.2.3 Evaluation of $d_T$

Though Distance of Transition $d_T$ had no formal pass/fail limit, for clinical use the smallest $d_T$ is preferred. Table 3.4 gives a summary of $d_T$ values for a representative subset of all studied geometries at 103 cm SSD. From these results, it can be concluded that $d_T$ trends smaller for higher energy and IRFs nearer to 1.0. Dependence of $d_T$ on beam energy, depth, packing radius, and IRF were further analyzed.

Table 3.4: Summary of results for Distance of Transition $d_T$ in cm for 103 cm SSD at matching depth z=0.5cm (left) and z=2.0cm (right). $d_T$ trends smaller for higher energy and IRFs nearer to 1.0. $d_T$ values have error of 0.05 cm or less. Clinically viable combinations (shown in Table 3.6) are bolded for clarity.

z=0.5cm

| 7 MeV | | | |
|---|---|---|---|
| IRF | r=0.5cm | r=1.0cm | r=1.5cm |
| 0.90 | **1.49** | **1.56** | **1.33** |
| 0.80 | **1.90** | **1.95** | **2.61** |
| 0.70 | **2.26** | **2.18** | 2.98 |

| 13 MeV | | | |
|---|---|---|---|
| IRF | r=0.5cm | r=1.0cm | r=1.5cm |
| 0.90 | **1.00** | 1.68 | 2.00 |
| 0.80 | **1.05** | 1.82 | 1.86 |
| 0.70 | **1.26** | 1.85 | 1.82 |

| 20 MeV | | | |
|---|---|---|---|
| IRF | r=0.5cm | r=1.0cm | r=1.5cm |
| 0.90 | **0.64** | 0.92 | 0.88 |
| 0.80 | **0.73** | 1.06 | 1.13 |
| 0.70 | **0.89** | 1.21 | 0.74 |

z=2.0cm

| 7 MeV | | | |
|---|---|---|---|
| IRF | r=0.5cm | r=1.0cm | r=1.5cm |
| 0.90 | **2.19** | **2.18** | **2.12** |
| 0.80 | **2.85** | **2.84** | **2.77** |
| 0.70 | **3.24** | **3.22** | **3.11** |

| 13 MeV | | | |
|---|---|---|---|
| IRF | r=0.5cm | r=1.0cm | r=1.5cm |
| 0.90 | **1.26** | **1.24** | 2.50 |
| 0.80 | **1.65** | **1.58** | 2.70 |
| 0.70 | **1.83** | **1.75** | 2.70 |

| 20 MeV | | | |
|---|---|---|---|
| IRF | r=0.5cm | r=1.0cm | r=1.5cm |
| 0.90 | **0.89** | 1.27 | 1.79 |
| 0.80 | **1.00** | 1.54 | 1.75 |
| 0.70 | **1.20** | 1.61 | 1.66 |

Distance of Transition monotonically decreased with energy, following an approximately 1/E dependence, similar to that of $\sigma_{\theta_x}$. This is illustrated by Figure 3.11, which plots results at z=0.5 and 2.0 cm for r=0.5 cm and IRF=0.80. The values at z=0.5 cm are about 70% of those of z=2.0 cm.

Not surprisingly, $d_T$ was approximately constant with variation in $r$ (0.5-1.5 cm), so long as $\Delta I_R$ (variation in IRF) was less than 2%. For example, for an IRF of 0.80 at 11

MeV and for z=0.5 cm and z=2.0 cm, $d_T$ remained within 0.1 cm of an average of 1.32 and 1.89 cm, respectively.

Figure 3.12 plots $d_T$ versus IRF for SSD=103 cm and r=0.5 cm at E=10 and 16 MeV for depths z=0.5 and 2.0 cm. It shows that $d_T$ monotonically increased as IRF decreased, but was fairly constant for IRF values below 0.80.

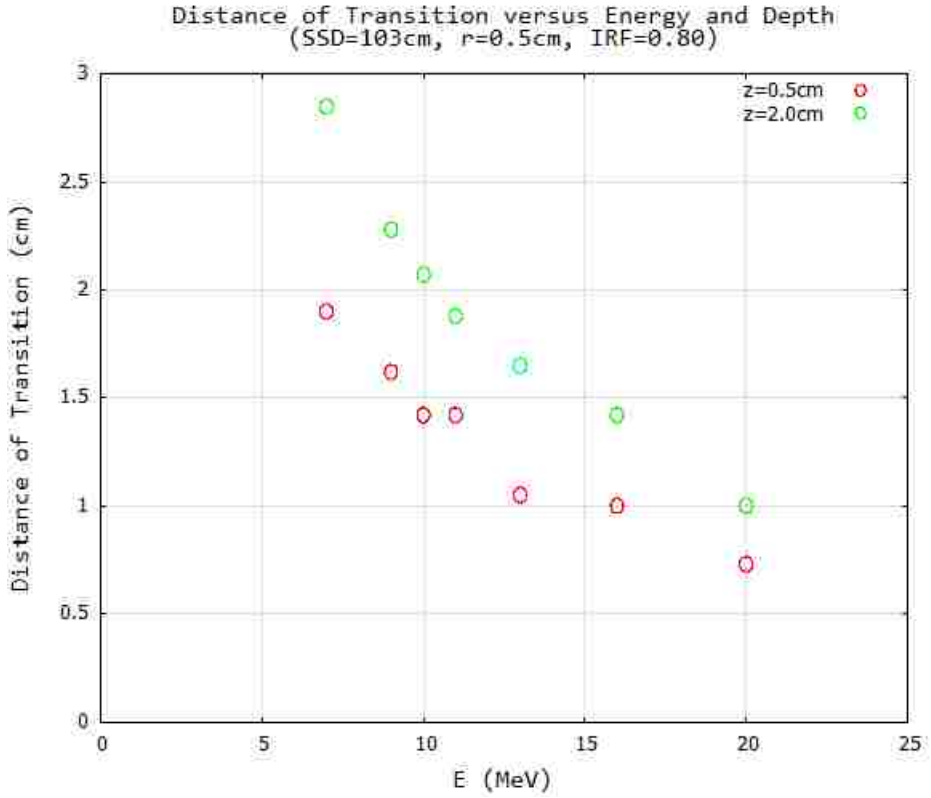


Figure 3.11: Distance of transition versus beam energy and depth for 103 cm SSD, r=0.5cm, and IRF=0.80. For a given IRF and at both depths, $d_T$ monotonically decreased with increased energy, following an approximately 1/E dependence.

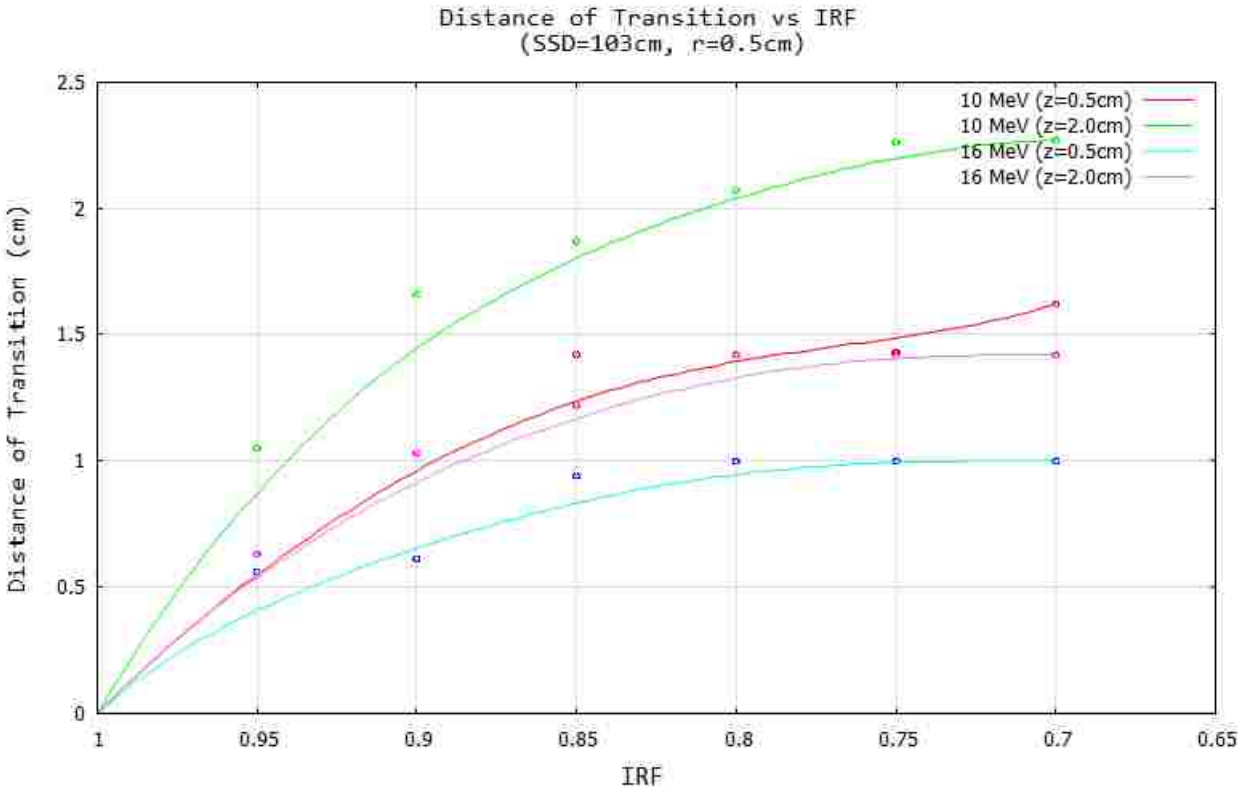


Figure 3.12: Distance of transition versus IRF for 103 cm SSD and r=0.5cm. For 10 and 16 MeV beams at depths of 0.5 and 2.0 cm, $d_T$ monotonically increased as IRF decreased, but was fairly constant for IRF values below 0.80.

### 3.2.3 Combinations (r,d) suitable for clinical use

Table 3.5 summarizes the scoring results at 100 cm SSD for all combinations (E, r) at depths z=0.5cm and z=2.0cm for all IRF 0.70-0.95, respectively. Combinations with a check denote passing all criteria for all IRF. These combinations are acceptable for intensity modulator design. For partial passes, the minimum permissible IRF is given, and where no modulation (IRF $\geq$ 0.70) is possible, the combination is given as N/A.

At shallow depths (z=0.5cm), the results show that beam energies above 13 MeV do not exhibit enough scatter to produce clinically acceptable intensity distributions for the entire range of IRFs under consideration. In particular, 20 MeV beams may not be used under any conditions, and 16 MeV is limited to a minimum IRF of 0.85. This places

limitations on treatment volume depth and size of island blocks. For a deeper matching depth (z=2.0cm), beam energies up to and including 20 MeV can be used.

Table 3.5: Summary of (E, r) combinations which pass for all block diameters at depths z=0.5cm (top) and z=2.0cm (bottom) and 100 cm SSD. Passes are denoted by check marks and partial passes by minimum IRFs. All others are N/A.

| E0 (MeV) | r=0.5cm | r=0.75cm | r=1.0cm | r=1.25cm | r=1.5cm |
|---|---|---|---|---|---|
| 7 | ✓ | ✓ | 0.80 | 0.95 | N/A |
| 9 | ✓ | ✓ | 0.95 | N/A | N/A |
| 10 | ✓ | 0.85 | N/A | N/A | N/A |
| 11 | ✓ | 0.95 | N/A | N/A | N/A |
| 13 | ✓ | N/A | N/A | N/A | N/A |
| 16 | 0.85 | N/A | N/A | N/A | N/A |
| 20 | N/A | N/A | N/A | N/A | N/A |

| E0 (MeV) | r=0.5cm | r=0.75cm | r=1.0cm | r=1.25cm | r=1.5cm |
|---|---|---|---|---|---|
| 7 | ✓ | ✓ | ✓ | ✓ | ✓ |
| 9 | ✓ | ✓ | ✓ | ✓ | 0.85 |
| 10 | ✓ | ✓ | ✓ | 0.75 | 0.95 |
| 11 | ✓ | ✓ | ✓ | 0.90 | N/A |
| 13 | ✓ | ✓ | 0.80 | 0.95 | N/A |
| 16 | ✓ | ✓ | 0.95 | N/A | N/A |
| 20 | ✓ | 0.90 | N/A | N/A | N/A |

Table 3.6 summarizes the scoring results at 103 cm SSD for all combinations (E, r) at depths z=0.5cm and z=2.0cm for all IRF 0.70-0.95, respectively. At this more clinical SSD, beam energies from 7-20 MeV have acceptable geometries for all IRF. In general, the 103 cm SSD allows larger block diameters, which as previously mentioned, have advantages.

Table 3.6: Summary of (E, r) combinations which pass for all block diameters at depths z=0.5cm and z=2.0cm and 103 cm SSD. Passes are denoted by check marks and partial passes by minimum IRFs. All others are N/A.

| E0 (MeV) | r=0.5cm | r=0.75cm | r=1.0cm | r=1.25cm | r=1.5cm |
|---|---|---|---|---|---|
| 7 | ✓ | ✓ | ✓ | ✓ | 0.80 |
| 9 | ✓ | ✓ | ✓ | 0.85 | 0.95 |
| 10 | ✓ | ✓ | ✓ | 0.95 | N/A |
| 11 | ✓ | ✓ | 0.75 | 0.95 | N/A |
| 13 | ✓ | ✓ | 0.95 | N/A | N/A |
| 16 | ✓ | 0.85 | N/A | N/A | N/A |
| 20 | ✓ | 0.95 | N/A | N/A | N/A |

| E0 (MeV) | r=0.5cm | r=0.75cm | r=1.0cm | r=1.25cm | r=1.5cm |
|---|---|---|---|---|---|
| 7 | ✓ | ✓ | ✓ | ✓ | ✓ |
| 9 | ✓ | ✓ | ✓ | ✓ | ✓ |
| 10 | ✓ | ✓ | ✓ | ✓ | ✓ |
| 11 | ✓ | ✓ | ✓ | ✓ | 0.85 |
| 13 | ✓ | ✓ | ✓ | 0.80 | 0.95 |
| 16 | ✓ | ✓ | 0.75 | 0.95 | N/A |
| 20 | ✓ | ✓ | 0.95 | N/A | N/A |

### 3.3 Conclusions and discussion

In this aim, the objective was to determine combinations for block diameter and packing radius which could be used to produce clinically acceptable intensity distributions while minimizing Ripple Intensity $\Delta I_R$ and Distance of Transition $d_T$.

A pencil beam algorithm was used to calculate the intensity distribution beneath a half-blocked 20x20 $cm^2$ field (blocks on positive x-axis) for a range of packing radii from r=0.5-1.5 cm and IRFs from 0.70-0.95 (i.e, diameters d=0.117-0.863 cm) at depths of

z=0.5cm and z=2.0cm. This was done both at SSD=100cm (air gap, g=5cm) and extended SSD=103cm (g=8cm) for beam energies ranging from 7-20 MeV.

In conclusion: (1) the average intensity agreed with the intended intensity within 0.001 so long as $\Delta I_R$ was within a clinically acceptable range (0.04) and (2) ripple intensity $\Delta I_R$ was clinically acceptable in limited regions of E, SSD, r, IRF, and z space. For example, the use of 20 MeV beams was precluded at 100 cm SSD and shallow depth (z=0.5cm), and the 16 MeV beam was limited to cases with IRF $\geq$ 0.85. However, using a more clinical 103 cm SSD, $\Delta I_R$ was acceptable for all energies (7-20 MeV) and depths (z=0.5 and 2.0 cm).

Although selecting solutions with the largest block separation (r) and thus the largest diameter blocks may have some fabrication advantages, this comes with the disadvantage of increased distance of transition ($d_T$), which could limit the gradient of sharply varying intensity modulating patterns. These competing effects should be properly balanced in the planning process, which will depend on the wide range of data computed in this aim.

# 4 AIM 3: ALGORITHM FOR DESIGN OF INTENSITY MODULATION USING ISLAND BLOCKS

Develop a pencil beam-based design tool for generating electron intensity modulators for an objective intensity distribution, beam energy, and SSD that is accurate to within 3% for 95% of modulated points (IRF <1) for a clinically-applicable intensity distribution.

## 4.1 Research methods

A software design tool was developed which generates a block matrix schematic for an electron intensity modulator that will deliver a user-specified intensity distribution for a given energy and SSD. The initial block matrix was determined from the user specified energy, SSD, and intensity distribution. The intensity distribution for this initial block matrix was calculated at depths 0.5 cm and 2.0 cm using the pencil beam algorithm described in Aim 1. The PBA-calculated relative intensity distributions were compared to a user specified relative intensity distribution (henceforth the objective intensity distribution) and scored according to local and global acceptance criteria. Local failures forced optimization of individual blocks, while global failure forced complete matrix redesign. Once a block matrix passes acceptance criteria, the final block matrix geometry, the calculated relative intensity distribution, and the relative intensity difference distribution (objective - calculation) are provided to the user. The overall algorithm workflow is summarized in Figure 4.1.

The software tool, called the Modulator Generator (final version ModGenV2.cpp) was created using procedural C++ using the Code::Blocks integrated development environment. Intensity distribution input and a list of available production island block diameters (both assumed to be ASCII files with file extension .txt) are required in the directory of the application for the Modulator Generator to run. In all cases studied in this work, Modulator Generator runtime on an Intel Core i7 processor was less than 5 seconds to completion.

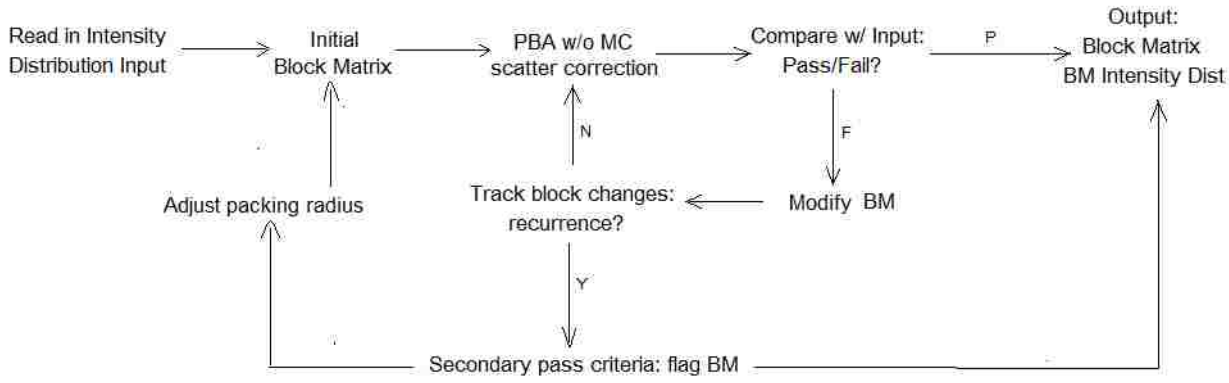


Figure 4.1: Workflow for the electron intensity modulator generator software. An initial guess block matrix is generated and tested using pre-established criteria. Points of failure are improved iteratively until criteria are met or minimized.

### 4.1.1 Initial block matrix

The initial block matrix starts with a uniform hexagonally packed grid covering the given field size with a block on the central axis. The packing radius for the initial guess is the largest size producing clinically acceptable distributions for all IRF (0.70-0.95) for the specified beam energy, as determined from the results of Aim 2 (Tables 3.5-3.6). The objective intensity distribution is represented as a list of modulation points ($x_i$, $y_i$, IRF). For each block position in the initial block matrix $(x_b, y_b)_{b=1,\text{number of blocks}}$, a linear search algorithm checks the objective intensity distribution for its nearest neighbor. The nearest neighbor is defined as the point for which the distance $\Delta$ is minimized, where $\Delta$ is given by:

$$\Delta_i = \sqrt{(x_b - x_i)^2 + (y_b - y_i)^2}. \tag{4.1}$$

The intensity reduction factor (IRF) given by the nearest neighbor is used to determine the diameter for that block point using Equation 2.2. No physical limitations are placed on the choice of block diameter, but results are rounded to the nearest 0.01 cm. If the IRF=1, no block is placed. Block parameters and calculated intensity are stored in memory as lists of $(x_b, y_b, d_b)_{b=1,\text{number of blocks}}$ and $(x_t, y_t, IRF_{test})_{t=1,\text{number of intensity points}}$, respectively.

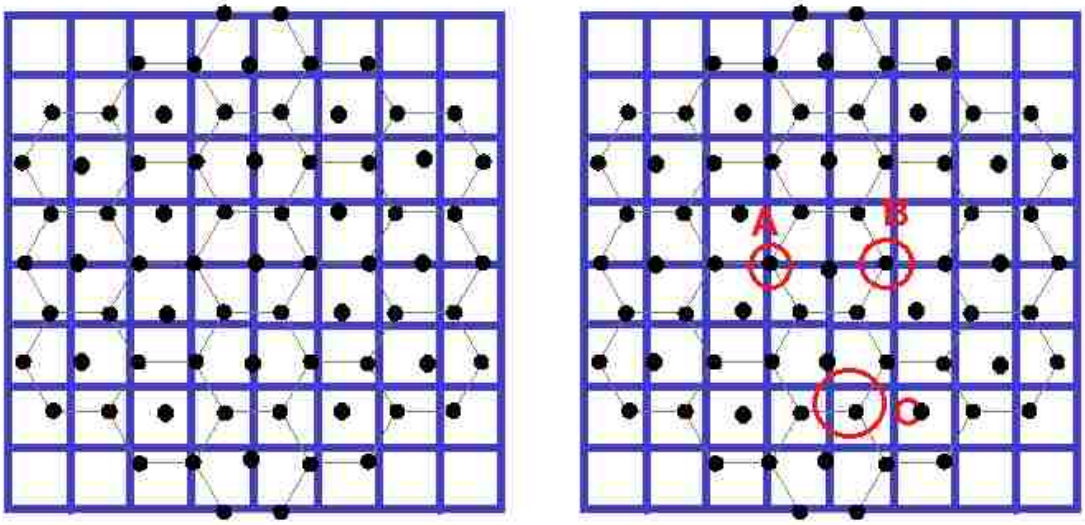


Figure 4.2: Nearest neighbor initialization example. On left, a black hexagonal grid and blue square grid are overlapped. The hexagonal grid (solid black points) represent the block matrix. The blue square grid represents the intensity distribution. At right, red circles contain block positions and their nearest intensity neighbor. The two grids are very close at points A and B. By contrast, the nearest neighbor for point C is more poorly matched.

As the block matrix is based on a hexagonal geometry and the objective intensity distribution is rectangular, there may not be an exact match between the block position and its nearest neighbor. Figure 4.2 shows a schematic diagram of the process, using hexagonal and square grids of different sizes. The two grids are very close at points A and B. By contrast, the nearest neighbor for point C is poorly matched. Initial guesses of the block diameters ($d_b$) will be modified during optimization.

### 4.1.2 Acceptance criteria

Once a block matrix has been generated, it is used for calculating intensity at depth with the PBA described in Aim 1. Intensity is calculated over the given field size using a grid size of 0.2 cm in $x$ and $y$. The calculated intensity distribution ($IRF_{test}$) is compared to the objective intensity distribution ($IRF_{obj}$), by comparing each test point to its nearest neighbor in the input intensity distribution. The results are used to decide if the matrix is acceptable or requires further optimization.

Block matrix acceptance is based on two criteria: the *local fail fraction* (LFF) and the *standard deviation of modulated points* ($\mathrm{SD}_{calc}$). These criteria consider only modulated points (IRF <1.0). A test point ($x_t$, $y_t$, $IRF_{test}$) is considered to fail if the difference between the desired and calculated intensity at that point is greater than 0.03 ($|IRF_{obj} - IRF_{test}| > 0.03$). Both the LFF and $\mathrm{SD}_{calc}$ must be less than 0.05. The LFF criteria is motivated by intensity modulated photon therapy quality assurance standards and corresponds to a 95% pass rate with points agreeing to within 3%. The LFF is defined as the ratio of failure points ($N_F$) to modulated points ($N_M$) on the intensity grid, given by:

$$\text{Local Fail Fraction } = \frac{N_F}{N_M} \tag{4.2}$$

The $\mathrm{SD}_{calc}$ is defined as the sum of the differences between the desired and calculated intensity at each modulated point divided by $N_M$:

$$SD_{calc} = \frac{1}{N_M}\sqrt{\sum_{i=1}^{N_M}(IRF_{obj,i} - IRF_{test,i})^2}\ . \tag{4.3}$$

In cases where the LFF is preventing acceptance but the $\mathrm{SD}_{calc}$ is acceptable (e.g., a large number of very near failures), secondary pass criteria (LFF $\leq 0.15$) may be used to determine matrix acceptability. In this case the block matrix will be flagged as having passed the looser secondary criteria.

### 4.1.3 Block matrix optimization

For each failing test point, the position and intensity difference ($\Delta I = I_{obj} - I_{test}$) is logged for use by the optimization protocol. For each block in the matrix, the algorithm searches for a fail point within the packing radius (a 'local fail'). Once a local fail is found, the search continues until it is determined that the given fail point is the nearest neighbor to the block position. Afterward, the diameter of the block is modified to a new target IRF, i.e. $IRF_{new} = IRF_{prev} + \Delta I$. If no local fail exists, the block is left unchanged. Figure

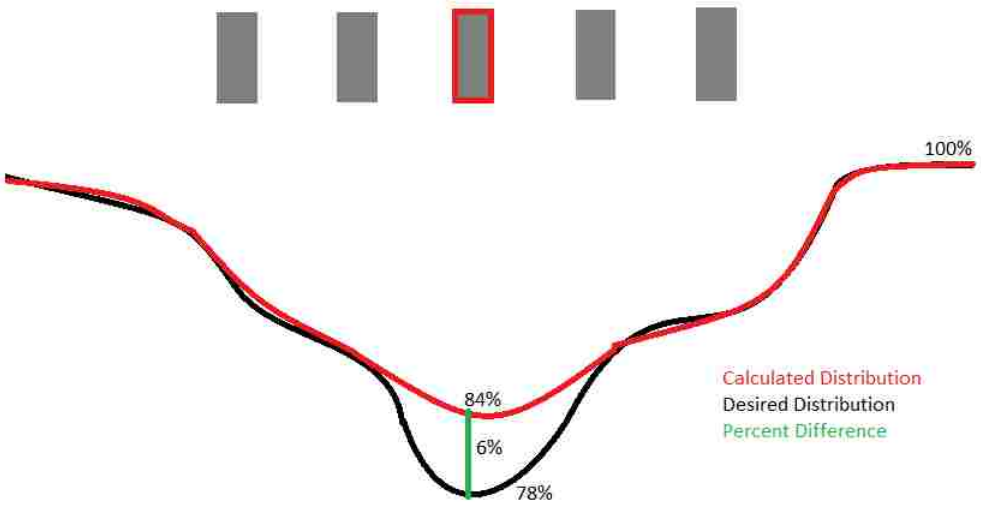


Figure 4.3: Block optimization logic visualization. The block outlined in red is assessed: the current percent relative intensity difference at its position is 6%, which makes it a local failure. The IRF will be adjusted by this difference and the block diameter reassigned to match.

4.3 demonstrates the optimization method for the block outlined in red. The intensity difference ($\Delta IRF$) between $IRF_{prev}$ and $IRF_{test}$ is -6% (-0.06), which makes the point a local fail for the block. The block's initial IRF is 78% (0.78), so the new IRF becomes 0.72, and the block will be assigned the diameter corresponding to the new IRF using Equation 2.2.

Once all blocks have been evaluated, the revised block matrix is used to recalculate intensity and scored again as described in the previous section. This optimization loop repeats this process until acceptance criteria are met.

### 4.1.4 Evaluation of algorithm using clinical test case

The software (Modulator Generator) for designing a matrix of island blocks to generate a desired electron intensity distribution was tested using a clinical case for which bolus ECT was used to treat the buccal mucosa (Kudchadker *et al* 2002). Kudchadker *et al* (2002) showed that modest intensity modulation (70-100%) with bolus ECT can deliver a sharply conformal, homogeneous dose distribution in the PTV. Lacking access to the intensity values for the original intensity data matrix plotted in Figure 4.4.a, an approximation of

Table 4.1: Acceptance criteria for clinical case block matrices for the initial block matrix (left) and the final result (right). Each matching depth was reproduced with LFF and $SD_{calc}$ well below acceptance criteria.

Initial Block Matrix

| **Match Depth** | **LFF** | **$SD_{calc}$** |
|---|---|---|
| 0.5 cm | 0.131 | 0.037 |
| 2.0 cm | 0.165 | 0.014 |

Final Block Matrix

| **Match Depth** | **LFF** | **$SD_{calc}$** |
|---|---|---|
| 0.5 cm | 0.000 | 0.007 |
| 2.0 cm | 0.011 | 0.008 |

the intensity matrix was generated by manual digitization of the published distribution. The resulting manually-digitized intensity distribution is shown in Figure 4.4.b.

Next, the initial packing radius and block diameters were geometrically determined by the Modulator Generator. This was done for incident energy E=20MeV, field size 15x15 $cm^2$, and matching depths of z=0.5cm and z=2.0cm for 103 cm SSD (8 cm air gap). The packing radius was r=0.50cm. Then the blocks were modified using the Modulator Generator's block matrix modification algorithm.

## 4.2 Results

### 4.2.1 Clinical test case

The block matrices for the initial and final designs for depths of 0.5 cm and 2.0 cm are shown in Figure 4.5. The corresponding intensity difference maps (objective - calculated) are given in Figure 4.6. The designed block matrices were very similar, regardless of matching depth. Calculated isointensity plots for the finalized block matrix at both depths are compared to the objective intensity distribution in Figure 4.7. The results are similar for both depths, with the objective intensity distribution reproduced to within 1% $SD_{calc}$ over the modulated area with less than 2% LFF (Table 4.1), well within the range considered clinically acceptable.

Program runtime was less than five seconds for each design. The largest error was at matching depth z=2.0cm for both LFF and $SD_{calc}$. Failures are primarily seen in the lower left quadrant, visibly reduced in the final block matrix heatmap compared to the the initial block matrix.

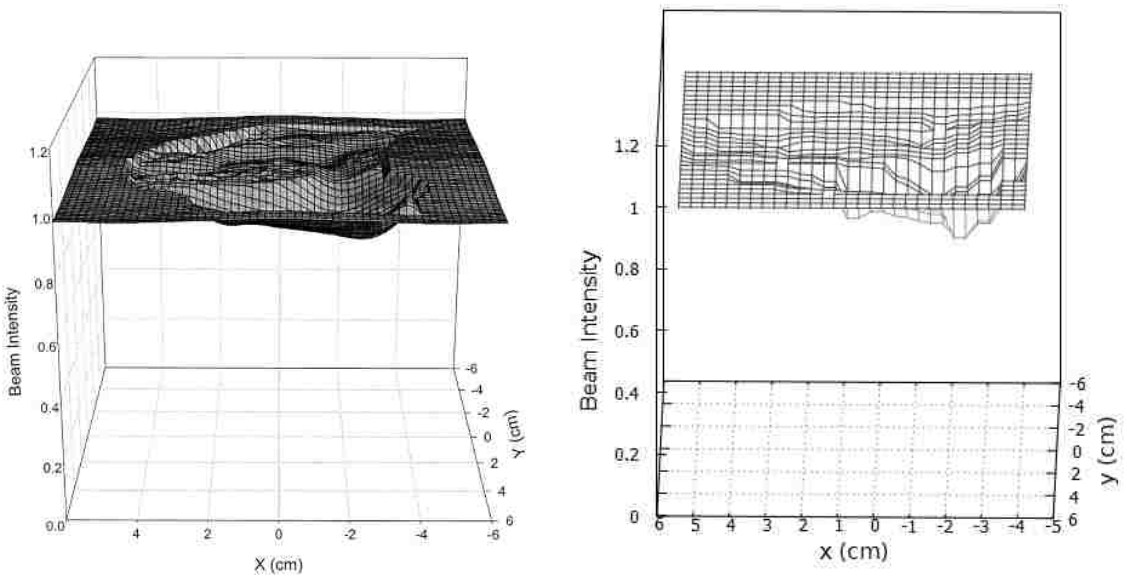


(a) (b)

Figure 4.4: Comparison of published and manually digitized intensity distributions for clinical test case. (a) For a buccal mucosa PTV the beam intensity distribution determined by Kudchadker (2002), also described in Figure 1.6. (b) Intensity distribution resulting from manual digitization.

### 4.3 Summary and conclusions

In this aim, the objective was to create a software design tool capable of taking a user-specified objective intensity distribution and select treatment beam information and using it to generate a schematic for building a passive electron intensity modulator. The design tool, called the Modulator Generator, generated the initial design based on the principles and data gathered in Aims 1 and 2. Adjustments were made to the design using a block-by-block optimization algorithm.

A clinically-applicable objective intensity distribution was used to test the design tool using a 20 MeV beam, considering two possible matching depths (0.5cm and 2.0cm) at 103 cm SSD. This intensity distribution was based on the buccal mucosa field found in Kudchadker *et al* (2002). At both depths the calculated intensity distribution was found to be clinically acceptable. The worst case yielded a local fail fraction (LFF) of 1% and standard deviation of modulated points ($SD_{calc}$) of 0.8%, both well within the primary

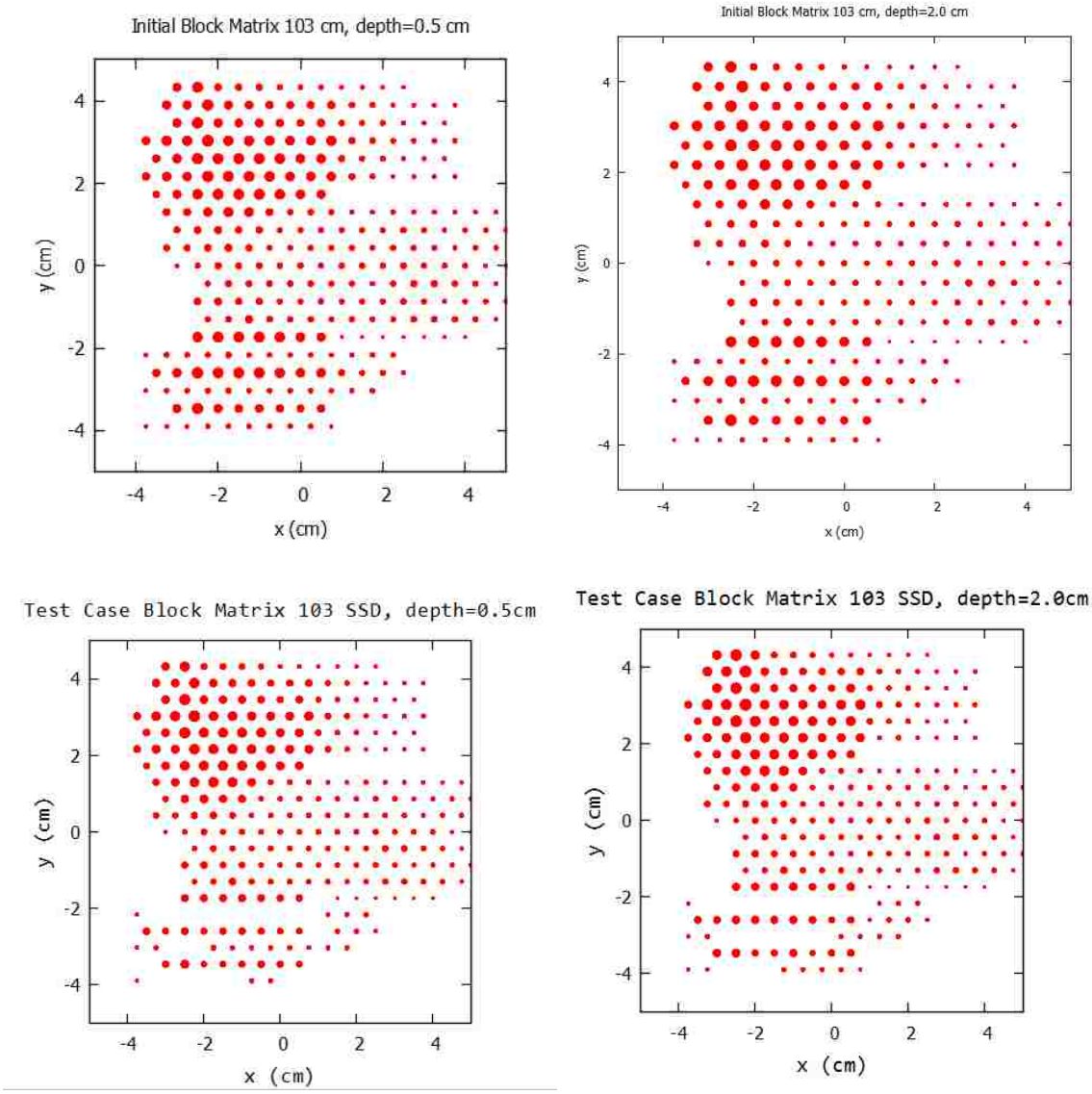


Figure 4.5: Beam-eye-view of initial (top) and final (bottom) block matrices. Intensity matching was done at a depth z=0.5cm (left) and z=2.0cm (right) respectively, showing similar block matrices. Note that the initial block matrices for z=0.5 cm and z=2.0 cm are identical.

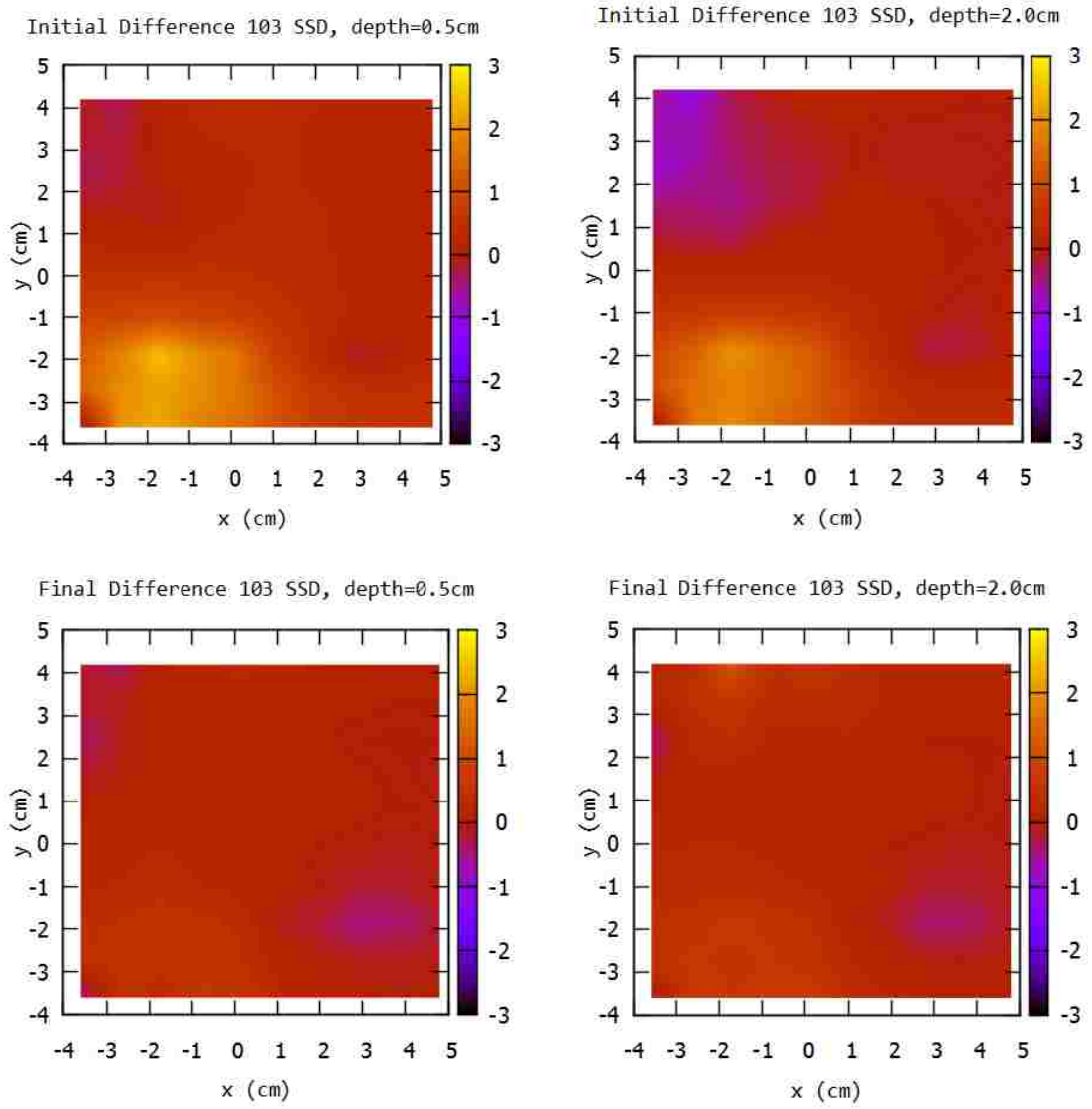


Figure 4.6: Model-calculation intensity difference heatmap. (top) Initial intensity difference maps (objective - initial calculated) at depths of z=0.5 cm (L) and z=2.0 cm (R). Note differences as great as ±3%. (bottom) Final intensity difference maps (objective - final calculated) at depths of z=0.5 cm (L) and z=2.0 cm (R). Note differences are within ±2%.

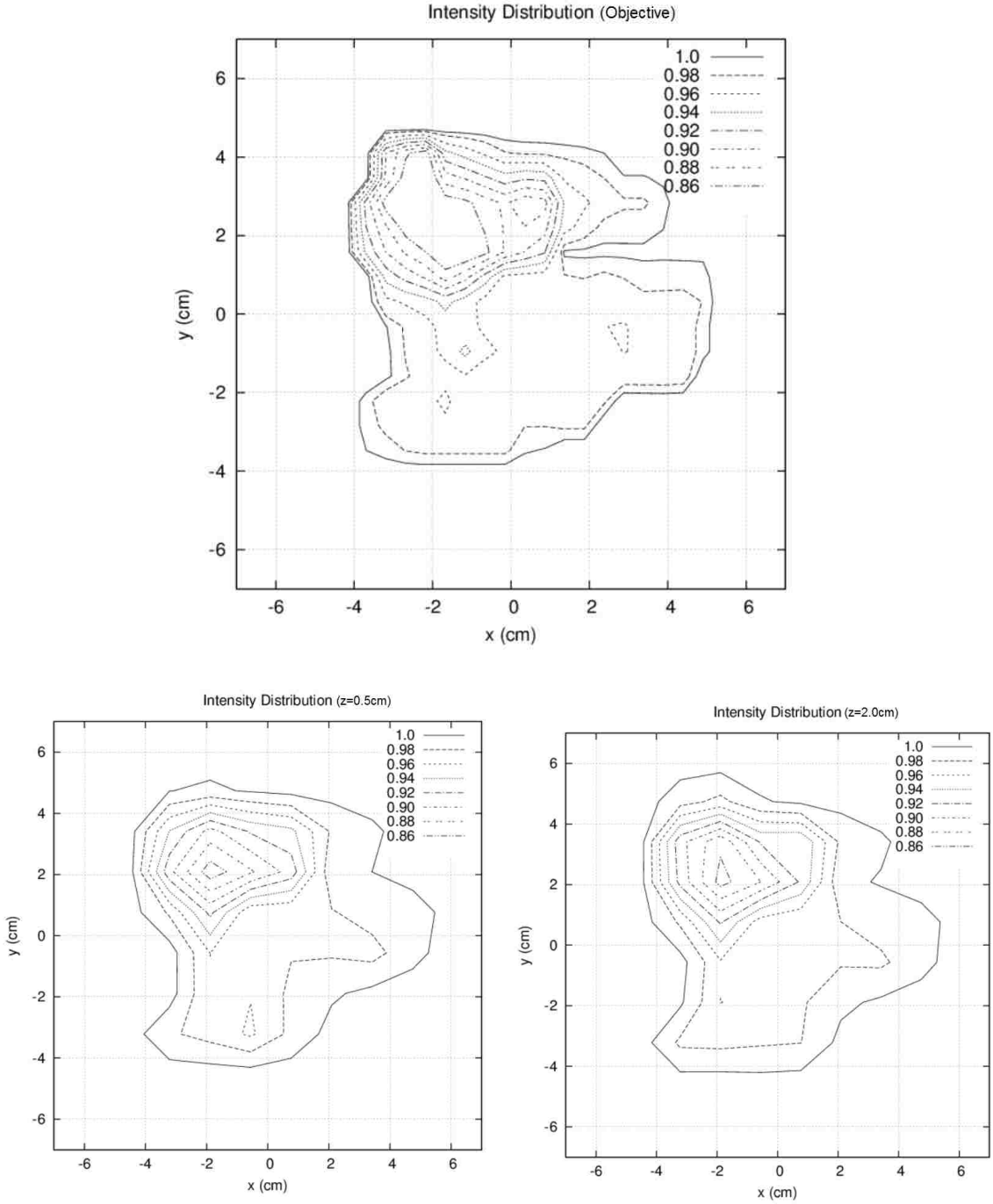


Figure 4.7: Isointensity plots for objective and calculated intensity distributions using final block matrix at matching depth of z-0.5cm and z=2.0cm.

acceptance criteria of 5% in each assessment metric. Program runtime remained under five seconds for all cases studied.

Based on these results, the Modulator Generator is suitable for further investigations that determine island block matrices for delivering a specified intensity distribution (70-100%) for intensity modulated bolus electron conformal therapy.

# 5 CONCLUSIONS

## 5.1 Aim 1: Suitability of pencil beam algorithm for modulated electron intensity distribution

### 5.1.1 Summary of results

Relative intensity calculations under a matrix of island blocks of clinical nature (0.70 $\leq$ IRF $\leq$ 0.95) showed PBA-based calculations differed from MC-based calculations no more than $\pm$5%. Differences were attributed to (1) selected approximations made in the PBA modeling (island block modeled as equivalent square and neglecting x-ray dose component), (2) MC statistics (number of particles and not taking full advantage of azimuthal symmetry), and (3) innate PBA characteristics (Gaussian approximation to Moliere multiple Coulomb scattering and modeling neither electron scattering from edges of island blocks nor photons and electrons originating in the block).

### 5.1.2 Conclusions

It was concluded that the PBA model was sufficiently accurate to study in Aim 2 the impact of island block parameters, beam energy, source to surface distance, air gap, and depth on achieving desired intensity reduction factors (IRFs). However, prior to using the PBA model for intensity calculations under island blocks of patient intensity modulators, the agreement between PBA-based and MC-based calculations should be improved.

### 5.1.3 Recommendations for future work

Improve the comparison of PBA-based and MC-based calculations by (1) including the x-ray dose component and comparing dose rather than intensity distributions under the matrix of island blocks, (2) perform the comparison in water at a more clinical, 103 cm SSD, (3) model the island blocks to be circular in the PBA, and (4) improve statistics of individual MC calculations and improve azimuthal averaging by selecting dose at spacings along a circumference equal to the 0.2 cm voxel dimension.

## 5.2 Aim 2: Dependence of intensity reduction on island block diameter and packing radius

### 5.2.1 Summary of results

Small values of packing radius (e.g. r <0.5 cm) increase the number of island blocks, while decreasing their diameters, likely making the manufacturing process more complex while increasing electron scatter from the block edges. Contrastingly, Table 3.4 showed decreasing packing radius decreases the distance to transition ($d_T$). With these competing preferences for packing radii, this aim studied the acceptable range of (r, IRF) combinations within 0.5-1.5 cm and 0.70-0.95 intervals, respectively, for multiple energies (7-20 MeV) at two depths in water (0.5 and 2.0 cm) and two SSDs (100 and 103 cm). Results at 103 cm SSD (Table 3.6 and Figure 3.10) show acceptable ranges for $r$ as a function of IRF and energy.

### 5.2.2 Conclusions

At a 103 cm treatment SSD, block separations of 0.5 to 1.0 cm have ripple intensity less than <2% of planned intensity for IRF values 0.70-1.00 at depths of 0.5 and 2.0 cm. Some restrictions, which occur for the higher energies, larger block separations, smaller IRFs, and shallower depths, can be determined using Table 3.6.

### 5.2.3 Clinical utility

Table 3.6 provides important data for the planning process by providing the planner with limits for specific objective intensities. Table 3.4 provides valuable data on the variation of distance to transition ($d_T$) with energy, IRF, and block separation, which is useful if the optimizer has difficulty in achieving intensity distributions with sharp gradients.

### 5.2.4 Recommendations for future work

Although not expected to have significant impact, the data provided in this thesis should be recalculated following any significant changes made to the PBA, e.g. modeling the island blocks with circular in lieu of equivalent square blocks.

## 5.3 Aim 3: Algorithm for design of intensity modulation using island blocks

### 5.3.1 Summary of results

A software optimization algorithm Modulator Generator was developed for determining a suitable matrix of hexagonally-packed (0.5-1.5 cm spacing) island blocks of variable diameters that produce a planned, patient intensity distribution specified at depths of 0.5 and 2.0 cm in water. The algorithm was tested using a replication of the intensity pattern designed by Kudchadker *et al* (2002) for a buccal mucosa patient treated using bolus electron conformal therapy with a 20 MeV beam. Results at depths of 0.5 and 2.0 cm in water at 103 cm SSD showed the objective and optimized intensity distributions to agree within 1% $SD_{calc}$ and $LFF$.

### 5.3.2 Conclusions

The results of this aim proved true the hypothesis "Passive electron intensity modulators comprised of island blocks of variable diameter can be designed to deliver a desired intensity distribution of clinically-representative complexity (70-100%) with an accuracy of ±3% for 95% of the modulated points (IRF <1)."

### 5.3.3 Clinical utility

The Modulator Generator is a C++ computer algorithm that can be implemented as a tool in a treatment planning system capable of intensity modulated (IM) bolus electron conformal therapy (ECT). The algorithm quickly converges to a solution, as exemplified by a run time of less than 5 seconds for the buccal mucosa test case. Based on these results, the Modulator Generator is suitable for further investigations that determine island block matrices for delivering a specified intensity distribution (70-100%) for IM bolus ECT.

### 5.3.4 Recommendations for future work

Future work should include (1) incorporating the Modulator Generator into a treatment planning system for IM bolus ECT, (2) designing intensity modulators (hexagonal matrix of variable island block diameters) for patients at multiple sites for which IM bolus ECT is useful, and (3) validating the design of the intensity modulator by constructing it,

calculating the dose to a water phantom under it (SSD=103 cm, depths of 0.5 and 2.0 cm), and measuring dose in the calculation geometry.

### 5.4 Recommendations for related projects

Exclusive of the recommendations for future work related to Aims 1, 2, and 3 of the present study, two other major projects are needed. First, there must be a practical, commercially-available method of designing and fabricating a patient-specific intensity modulator. It must be able to be produced at a reasonable cost in a reasonable time, and there must be methods for quality assurance by both the manufacturer at the factory and by the medical physicist at the cancer treatment center. Such a project is planned to be the subject of an upcoming joint effort of .decimal LLC and Mary Bird Perkins Cancer Center. Second, the clinical utility of IM bolus ECT needs evaluated by multiple treatment planning studies for multiple sites that build on the initial study of Kudchadker *et al* (2002). Such a retrospective study is presently being planned for left-sided postmastectomy radiotherapy patients as the subject of a masters thesis of LSU graduate student John Doiron.

# REFERENCES


Boyd, RA, Hogstrom, KR and Rosen, II. 'Effect of using an initial polyenergetic spectrum with the pencil-beam redefinition algorithm for electron-dose calculations in water.' *Medical Physics* **25** 2176 (1998).

Boyd, RA, Hogstrom, KR, and Starkschall, G. 'Electron pencil-beam redefinition algorithm dose calculations in the presence of heterogeneities.' *Med. Phys.* **28** 2096 (2001).

Carver RL, Hogstrom KR, Chu C, Fields RS, Sprunger CP. 'Accuracy of pencil-beam redefinition algorithm dose calculations in patient-like cylindrical phantoms for bolus electron conformal therapy.' *Med Phys.* **40** 071720 (2013).

Carver RL, Hogstrom KR, Price MJ, LeBlanc JD, Pitcher GM. 'Real-time simulator for designing electron dual scattering foil systems.' *Journal of Applied Clinical Medical Physics* **15** (2014).

du Plessis FCP, Leal A, Stathakis S, Xiong W, and Ma C-M. 'Characterization of megavoltage electron beams delivered through a pMLC.' *Phys. Med. Biol.* **51** 2113-2129 (2006).

Eley JG, Hogstrom KR, Matthews KL, Parker BC, Price MJ. 'Potential of discrete Gaussian edge feathering method for improving abutment dosimetry in eMLC-delivered segmented-field electron conformal therapy.' *Medical Physics.* **38** 6610-22 (2011).

Giarratano JC, Duerkes RJ, and Almond PR. 'Lead shielding thickness for dose reduction of 7- to 28-MeV electrons.' *Medical Physics* **2** 336-337 (1975).

Haas, LL, Harvey, RA, Laughlin, JS, Beattie, JW, and Henderson, WJ. 'Medical aspects of high energy electron beams.' *Am J Roentgenol Radium Ther Nucl Med.* **72** 250-9 (1954).

Harris, GM. *Development and validation of an electron Monte Carlo model for the Elekta Infinity accelerator.* Master's thesis, Louisiana State University, Baton Rouge, Louisiana. (2012).

Hogstrom, KR and Almond, PR. 'Review of electron beam therapy physics.' *Phys. Med. Biol.* **51** R455-R489 (2006).

Hogstrom KR, Antolak JA, Kudchadker RJ, Ma CM, Leavitt DD. 'Modulated electron therapy.' *Intensity Modulated Radiation Therapy, The State of the Art: Proc. 2003 AAPM Summer School.* Editors J Palta and R Mackie (Madison, WI: Medical Physics Publishing) 749-789 (2003).

Hogstrom KR, Boyd RA, Antolak JA, Svatos MM, Faddegon BA and Rosenman JG. 'Dosimetry of a prototype retractable eMLC for fixed-beam electron therapy.' *Med. Phys.* **31** 443 (2004).

Hogstrom, KR, Mills, MD, and Almond, PR. 'Electron beam dose calculations.' *Phys. Med. Biol.* **26** 445 (1981).

*Quantitative Concepts and Dosimetry in Radiobiology.* ICRU Report 30. Issued 15 April. 1979.

*Radiation Dosimetry: Electron Beams with Energies Between 1 and 50 MeV.* ICRU Report 35. Issued 15 September. 1984.

Kalend AM, Zwicker RD, Wu A, and Sternick ES. 'A beamedge modifier for abutting electron fields.' *Medical Physics* **12** 793 (1985).

Khan, FM. *The physics of radiation therapy, 4th Ed.* Philadelphia: Lippincott Williams & Wilkins (2010).

Khan, FM, Doppke KP, *et al.* 'Clinical electron-beam dosimetry: report of AAPM Radiation Therapy Committee Task Group No. 25.' *Medical Physics* **18** 73-109 (1991).

Kim MM, Kudchadker RJ, Kanke JE, Zhang S, Perkins GH. 'Bolus electron conformal therapy for the treatment of recurrent inflammatory breast cancer: a case report.' *Med Dosim.* **37** 20813 (2012).

Kirsner SM, Hogstrom KR, Kurup RG, and Moyers MF. 'Dosimetric evaluation in heterogeneous tissue of anterior electron beam irradiation for treatment of retinoblastoma.' *Med. Phys.* **14** 772 (1987).

Klein EE, Mamalui-Hunter M, and Low DA. 'Delivery of modulated electron beams with conventional photon multi-leaf collimators.' *Phys. Med. Biol.* **54** 327-339 (2009).

Kudchadker RJ, Antolak JA, Morrison WH, Wong PF, Hogstrom KR. 'Utilization of custom electron bolus in head and neck radiotherapy.' *J. Applied Clinical Med. Phys.* **4** 4 (2003).

Kudchadker RJ, Hogstrom KR, Garden AS, McNeese MD, Boyd RA, and Antolak JA. 'Electron conformal radiotherapy with bolus and intensity modulation.' *Int. J. Radiation Oncology Biol. Phys.* **53** 1023-1037 (2002).

Low DA, Starkschall G, Bujnowski SW, Wang LL, Hogstrom KR. 'Electron bolus design for radiotherapy treatment planning: Bolus design algorithms.' *Medical Physics* **19** 115 (1992).

Low DA, Starkschall G, Sherman NE, Bujnowski SW, Ewton JR, Hogstrom KR. 'Computer-aided design and fabrication of an electron bolus for treatment of the paraspinal muscles.' *Int J Radiat Oncol Biol Phys.* **33** 1127-38 (1995).

McLaughlin, D. J. *Energy spectra comparisons for matched clinical electron beams on Elekta linear accelerators using a permanent magnet spectrometer.* Master's thesis, Louisiana State University, Baton Rouge, Louisiana (2010).

Million, R. R., J. T. Parsons, F. J. Bova, and K. J. Kalbaugh. 'Electron Beam: The Management of Head and Neck Cancer.' *The Role of High Energy Electrons in the Treatment of Cancer: 25th Annual San Francisco Cancer Symposium.* Editors J. M. Vaeth and J. L. Meyer (San Francisco, CA: Frontiers of Radiation Therapy and Oncology) 107127 (1991).

Opp D, Forster K, Li W, Zhang G, and Harris EE. 'Evaluation of bolus electron conformal therapy compared with conventional techniques for the treatment of left chest wall postmastectomy in patients with breast cancer.' *Medical Dosimetry* **38** 448453 (2013).

Perkins GH, McNeese MD, Antolak JA, Buchholz TA, Strom EA, Hogstrom KR. 'A custom three-dimensional electron bolus technique for optimization of postmastectomy irradiation.' *Int J Radiat Oncol Biol Phys.* **51** 1142-1151 (2001).

Richert, J. D. 2006. *Improved abutment dosimetry in segmented field electron conformal therapy.* Master's thesis, Louisiana State University, Baton Rouge, Louisiana (2006). http://etd.lsu.edu/docs/available/etd-07132006-154808/.

Richert, J. D., K. R. Hogstrom, R. S. Fields, K. L. Matthews, and R. A. Boyd. 'Improvement of field matching in segmented-field electron conformal therapy using variable-SCD applicator.' *Physics in Medicine and Biology* **52** 2459-2481 (2007).

Shiu, AS and Hogstrom, KR. 'Pencil-beam redefinition algorithm for electron dose distributions.' *Medical Physics* **18** 7-18 (1991).

Steenbakkers RJHM, Altschuler, MD, D'Angio, GJ, Goldwein, JW, Kassaee, A. 'Optimized lens-sparing treatment of retinoblastoma with electron beams.' *Int J Radiat Oncol Biol Phys.* **39** 589-594 (1997).

Su S, Moran K, Robar JL. 'Design and production of 3D printed bolus for electron radiation therapy.' *Journal of Applied Clinical Medical Physics* **15** 4 (2014).

Tapley N, ed. *Clinical Applications of the Electron Beam.* New York, NY: John Wiley & Sons; 1976.

Vaeth JM, Meyer JL, eds. 'The Role of High Energy Electrons in the Treatment of Cancer.' *Front Radiat Ther Oncol.* Basel, Karger, bf 25 (1991).

Werner, B. L., Khan F. M., and Deibel F. C. 'A model for calculating electron beam scattering in treatment planning.' *Medical Physics* **9** 180 (1982).

Zackrisson B and Karlsson M. 'Matching of electron beams for conformal therapy of target volumes at moderate depths.' *Radiotherapy and Oncology* **39** 261-270 (1996).

Zeidan OA, Chauhan BD, Estabrook WW, Willoughby TR, Manon RR, and Meeks SL. 'Image-guided bolus electron conformal therapy a case study.' *Journal of Applied Clinical Medical Physics* **12** 1 (2011).

# APPENDIX A
# OFF-AXIS PROFILES AND MC/PBA DIFFERENCE KERNELS

For all figures, the top plot compares Monte Carlo and pencil-beam algorithm calculated off-axis relative dose profiles, and the bottom plots the difference kernel (MC-calculated less PBA-calculated relative dose) for the following geometries:

| Plot | Energy (MeV) | Diameter (cm) |
|---|---|---|
| A.1 | 9 | 0.117 |
| A.2 | 9 | 0.288 |
| A.3 | 9 | 0.352 |
| A.4 | 9 | 0.508 |
| A.5 | 9 | 0.719 |
| A.6 | 9 | 0.863 |
| A.7 | 13 | 0.117 |
| A.8 | 13 | 0.288 |
| A.9 | 13 | 0.352 |
| A.10 | 13 | 0.508 |
| A.11 | 13 | 0.719 |
| A.12 | 13 | 0.863 |
| A.13 | 17 | 0.117 |
| A.14 | 17 | 0.288 |
| A.15 | 17 | 0.352 |
| A.16 | 17 | 0.508 |
| A.17 | 17 | 0.719 |
| A.18 | 17 | 0.863 |

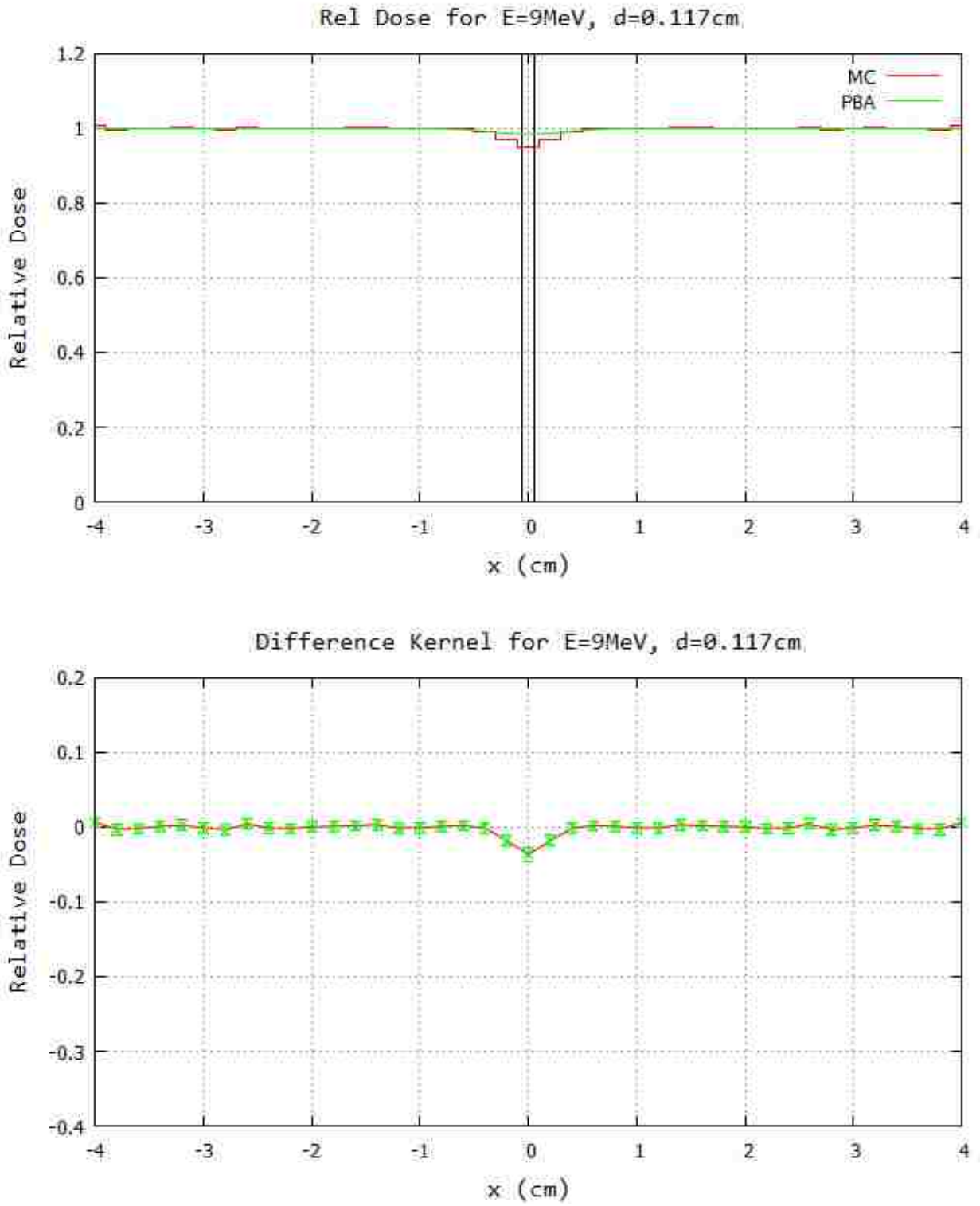


Figure A.1: Monte Carlo central axis block profile and kernel: monoenergetic 9 MeV beam with a central axis block of diameter d=0.117cm at depth z=0.5cm with air gap g=5.0cm. (top) Crossplane intensity profile (y=0) for MC and PBA. Upright block lines indicate the edges of the block. (bottom) MC-PBA difference kernel with error bars.

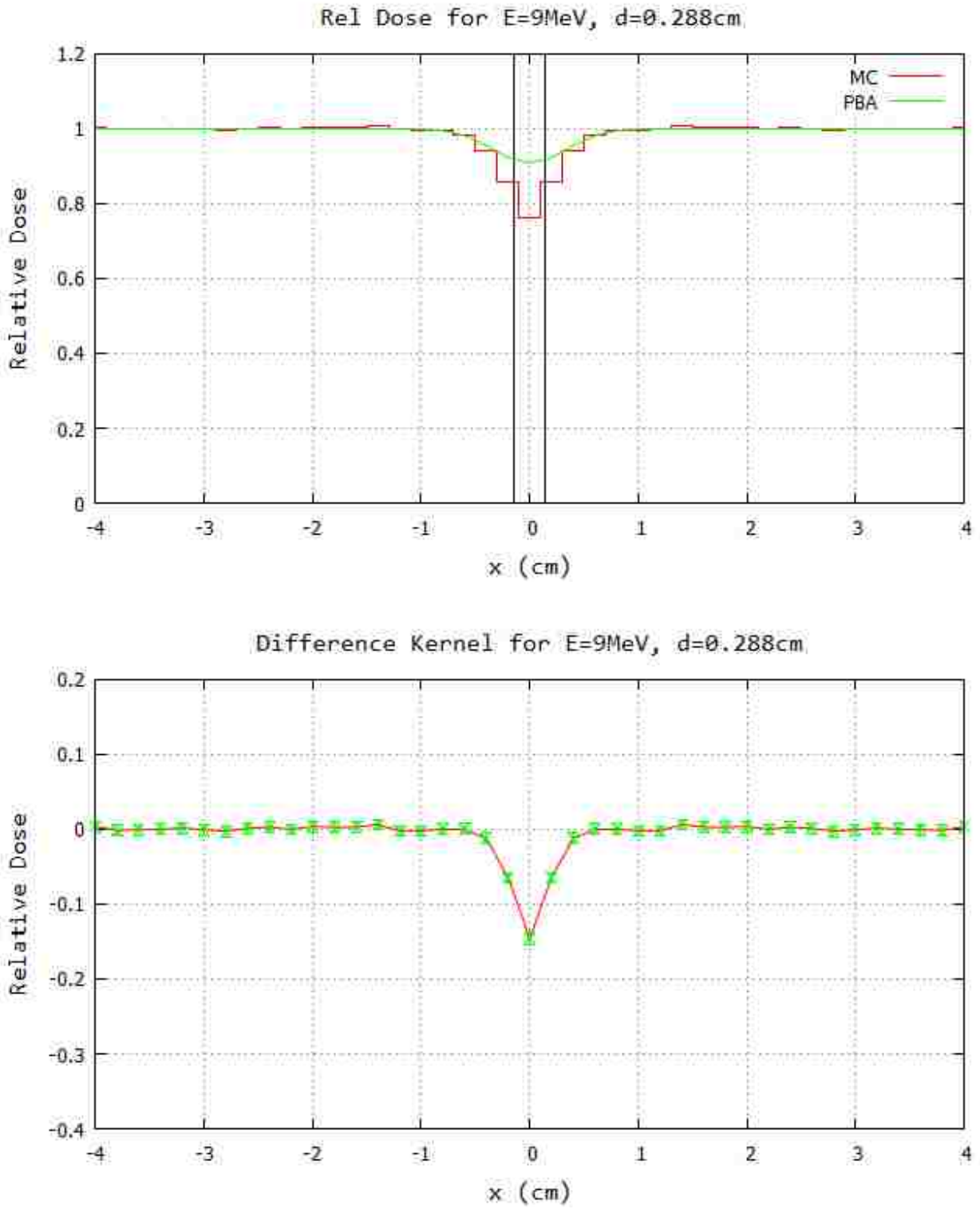


Figure A.2: Monte Carlo central axis block profile and kernel: monoenergetic 9 MeV beam with a central axis block of diameter d=0.288cm at depth z=0.5cm with air gap g=5.0cm. (top) Crossplane intensity profile (y=0) for MC and PBA. Upright block lines indicate the edges of the block. (bottom) MC-PBA difference kernel with error bars.

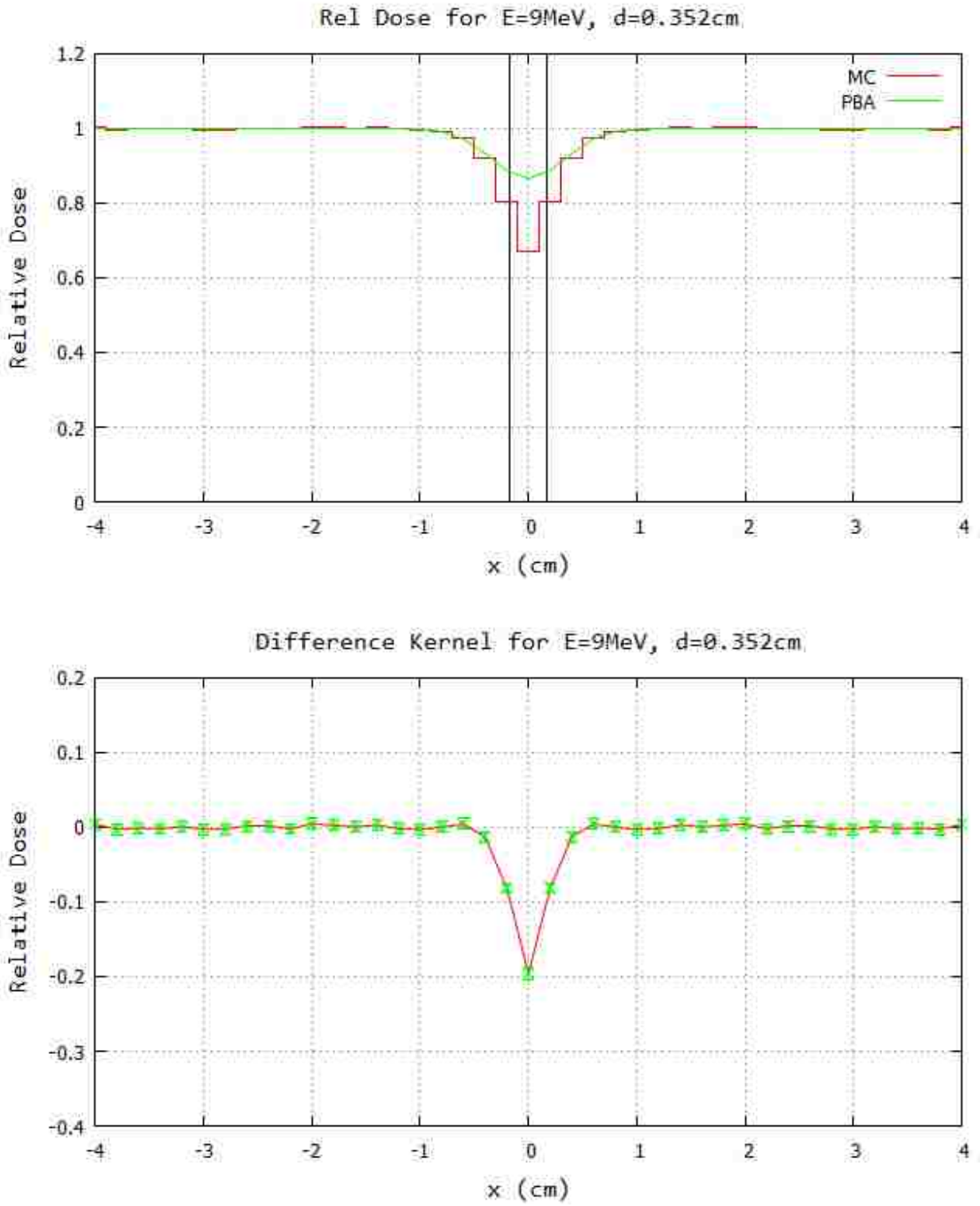


Figure A.3: Monte Carlo central axis block profile and kernel: monoenergetic 9 MeV beam with a central axis block of diameter d=0.352cm at depth z=0.5cm with air gap g=5.0cm. (top) Crossplane intensity profile (y=0) for MC and PBA. Upright block lines indicate the edges of the block. (bottom) MC-PBA difference kernel with error bars.

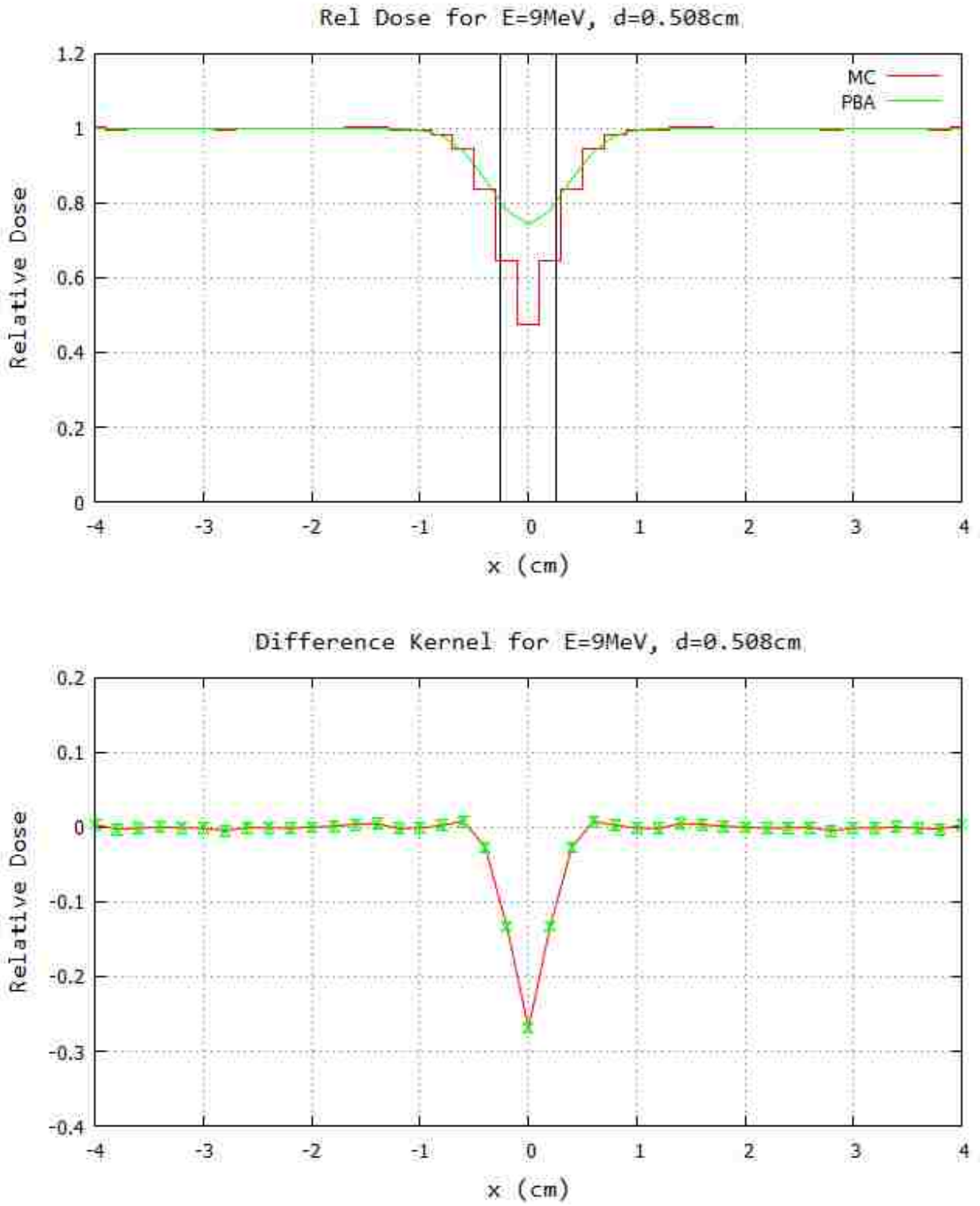


Figure A.4: Monte Carlo central axis block profile and kernel: monoenergetic 9 MeV beam with a central axis block of diameter d=0.508cm at depth z=0.5cm with air gap g=5.0cm. (top) Crossplane intensity profile (y=0) for MC and PBA. Upright block lines indicate the edges of the block. (bottom) MC-PBA difference kernel with error bars.

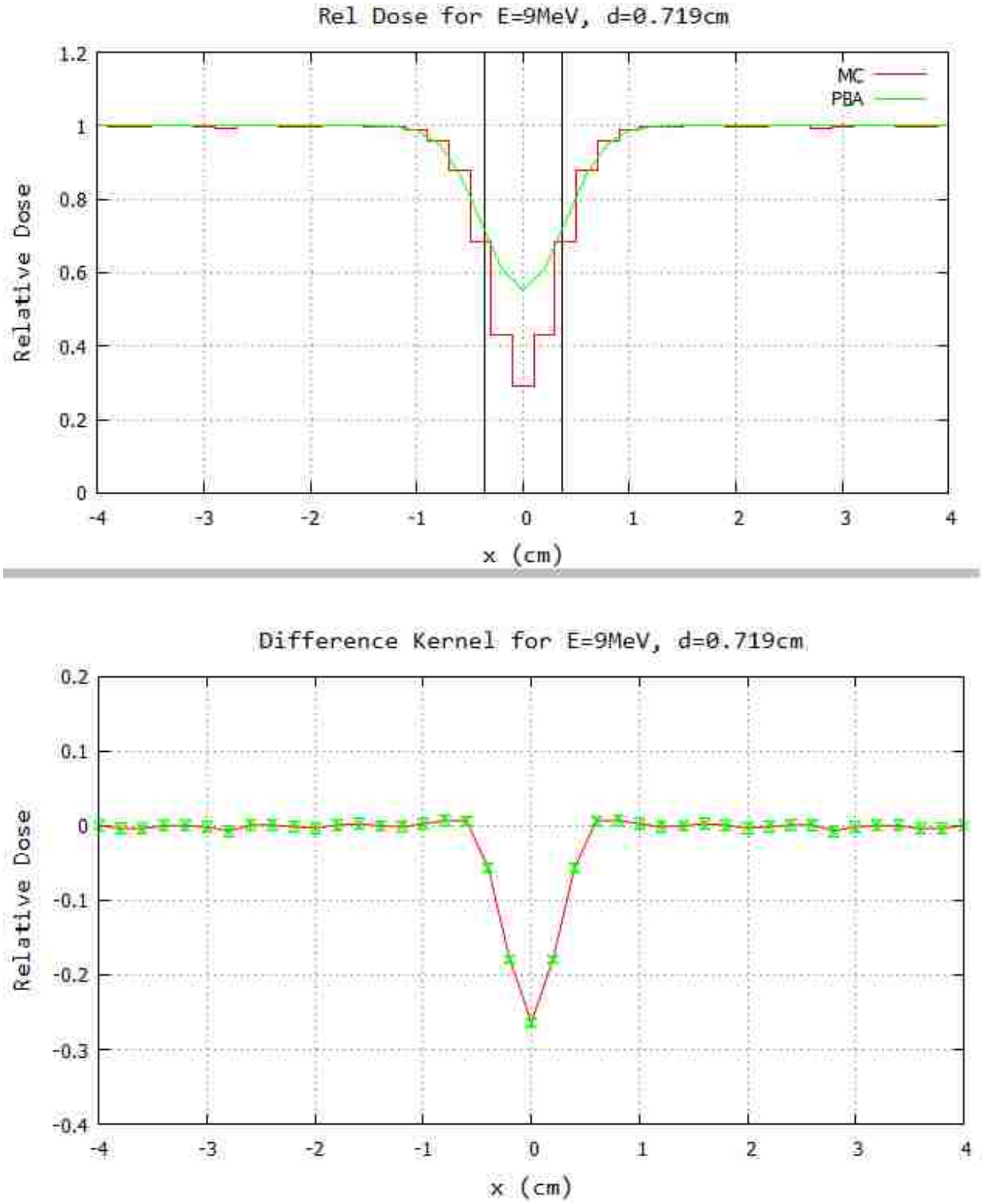


Figure A.5: Monte Carlo central axis block profile and kernel: monoenergetic 9 MeV beam with a central axis block of diameter d=0.719cm at depth z=0.5cm with air gap g=5.0cm. (top) Crossplane intensity profile (y=0) for MC and PBA. Upright block lines indicate the edges of the block. (bottom) MC-PBA difference kernel with error bars.

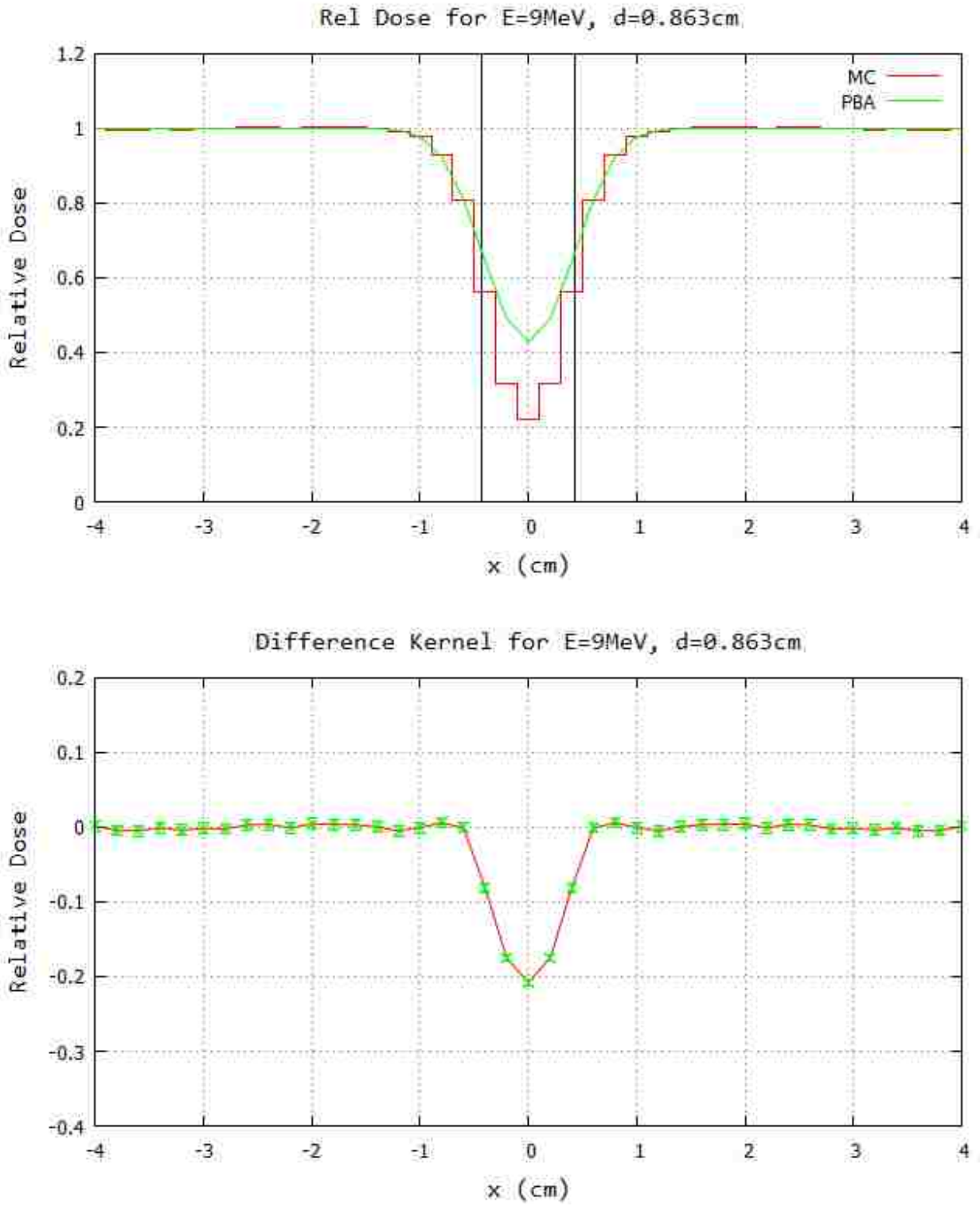


Figure A.6: Monte Carlo central axis block profile and kernel: monoenergetic 9 MeV beam with a central axis block of diameter d=0.863cm at depth z=0.5cm with air gap g=5.0cm. (top) Crossplane intensity profile (y=0) for MC and PBA. Upright block lines indicate the edges of the block. (bottom) MC-PBA difference kernel with error bars.

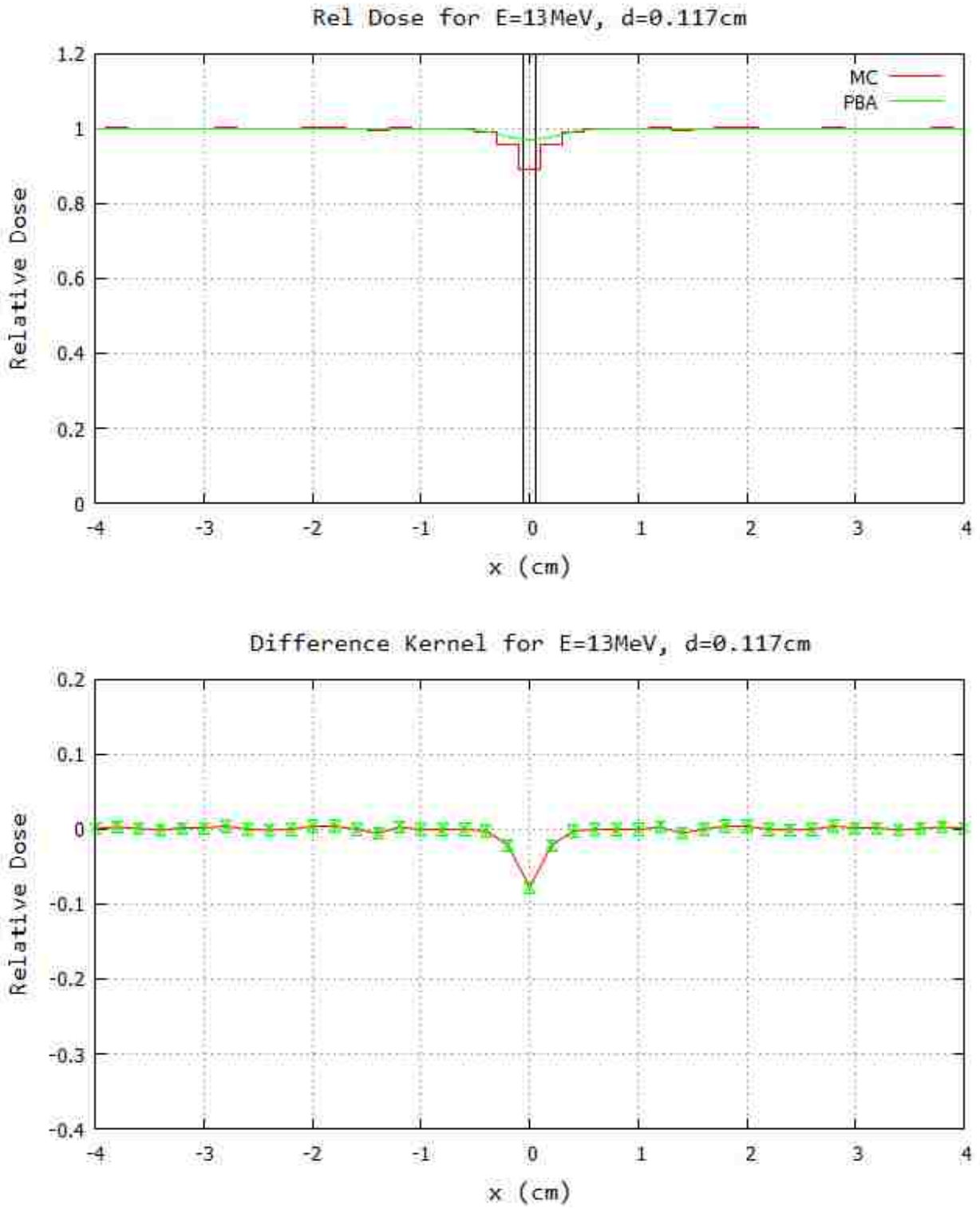


Figure A.7: Monte Carlo central axis block profile and kernel: monoenergetic 13 MeV beam with a central axis block of diameter d=0.117cm at depth z=0.5cm with air gap g=5.0cm. (top) Crossplane intensity profile (y=0) for MC and PBA. Upright block lines indicate the edges of the block. (bottom) MC-PBA difference kernel with error bars.

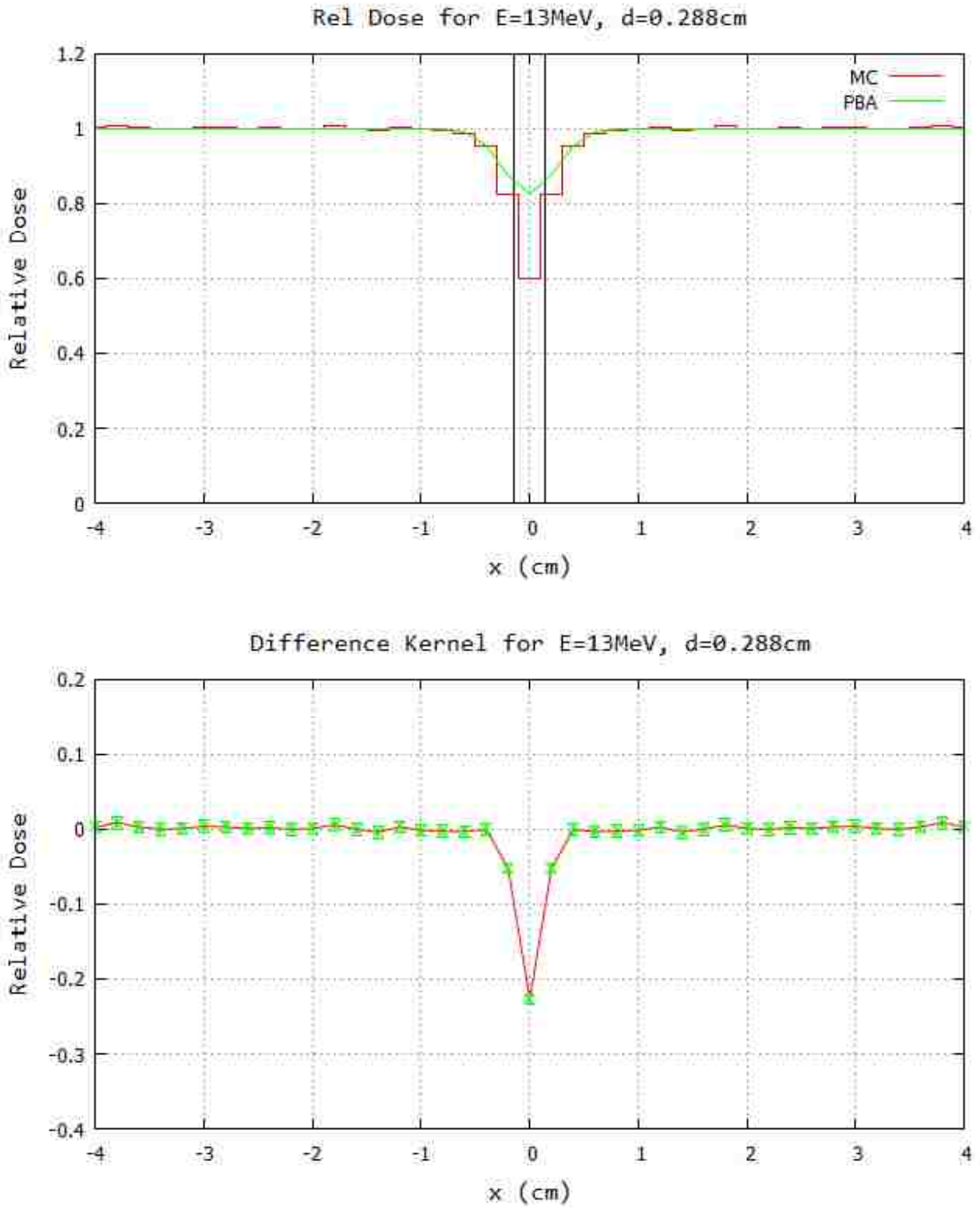


Figure A.8: Monte Carlo central axis block profile and kernel: monoenergetic 13 MeV beam with a central axis block of diameter d=0.288cm at depth z=0.5cm with air gap g=5.0cm. (top) Crossplane intensity profile (y=0) for MC and PBA. Upright block lines indicate the edges of the block. (bottom) MC-PBA difference kernel with error bars.

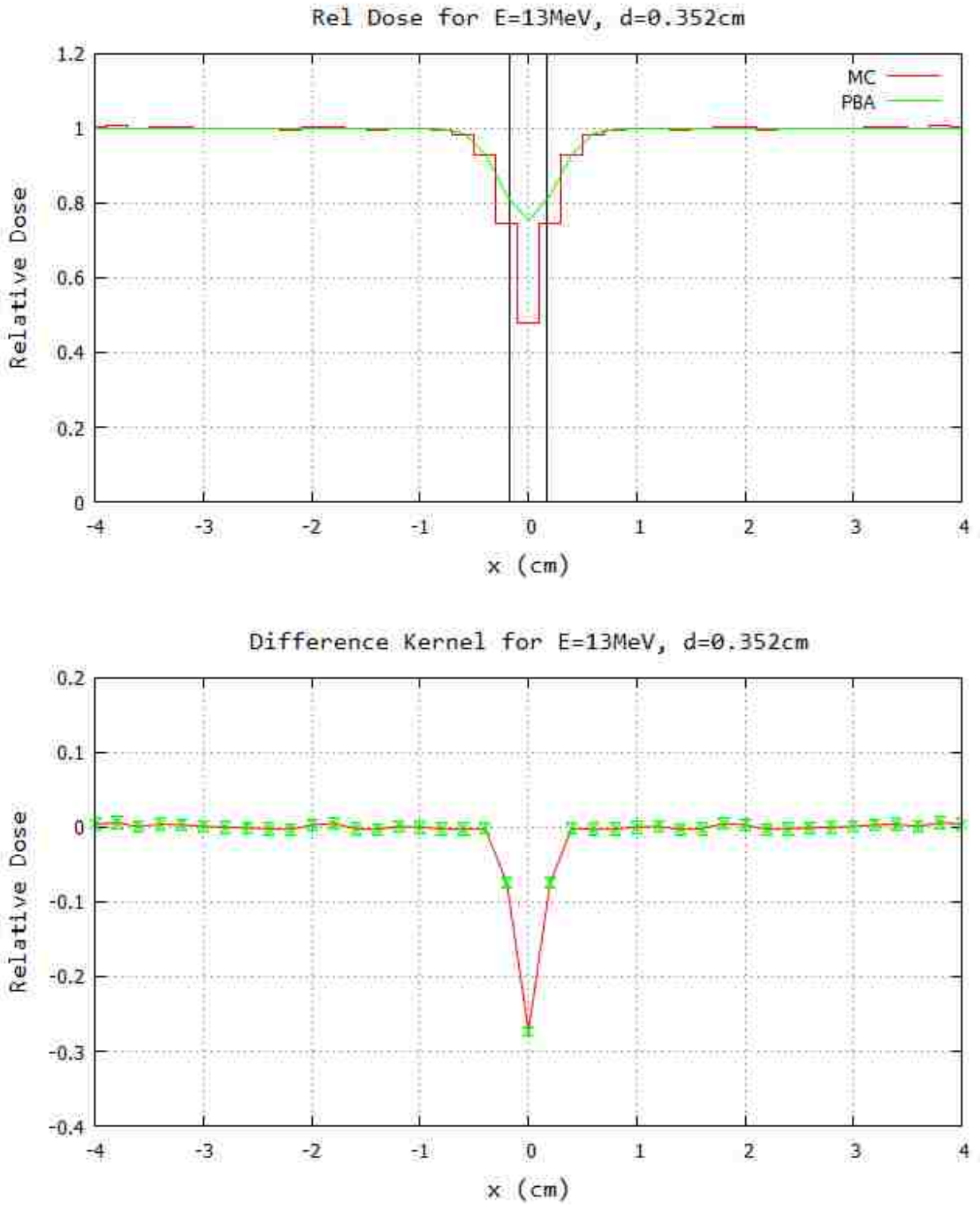


Figure A.9: Monte Carlo central axis block profile and kernel: monoenergetic 13 MeV beam with a central axis block of diameter d=0.352cm at depth z=0.5cm with air gap g=5.0cm. (top) Crossplane intensity profile (y=0) for MC and PBA. Upright block lines indicate the edges of the block. (bottom) MC-PBA difference kernel with error bars.

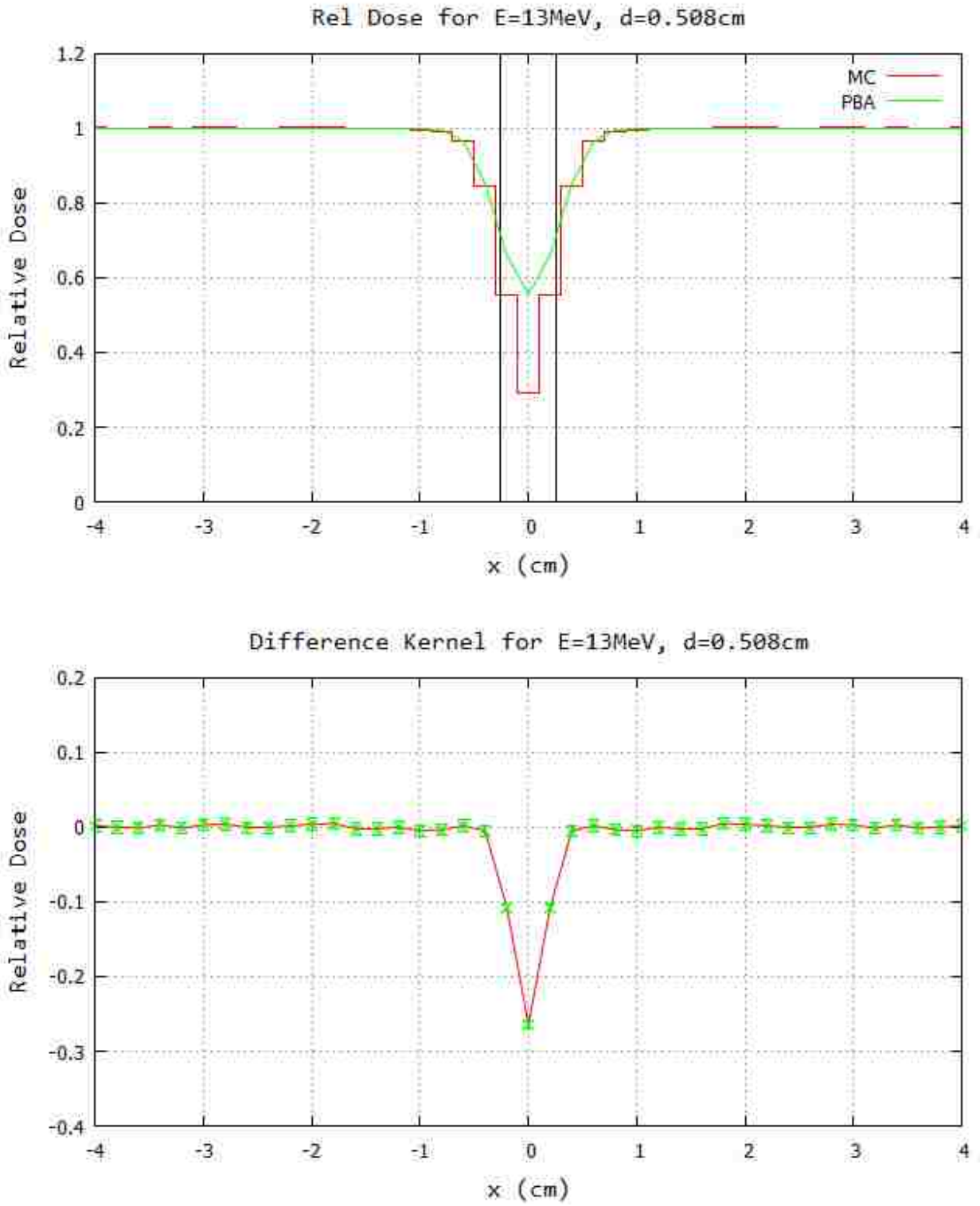


Figure A.10: Monte Carlo central axis block profile and kernel: monoenergetic 13 MeV beam with a central axis block of diameter d=0.508cm at depth z=0.5cm with air gap g=5.0cm. (top) Crossplane intensity profile (y=0) for MC and PBA. Upright block lines indicate the edges of the block. (bottom) MC-PBA difference kernel with error bars.

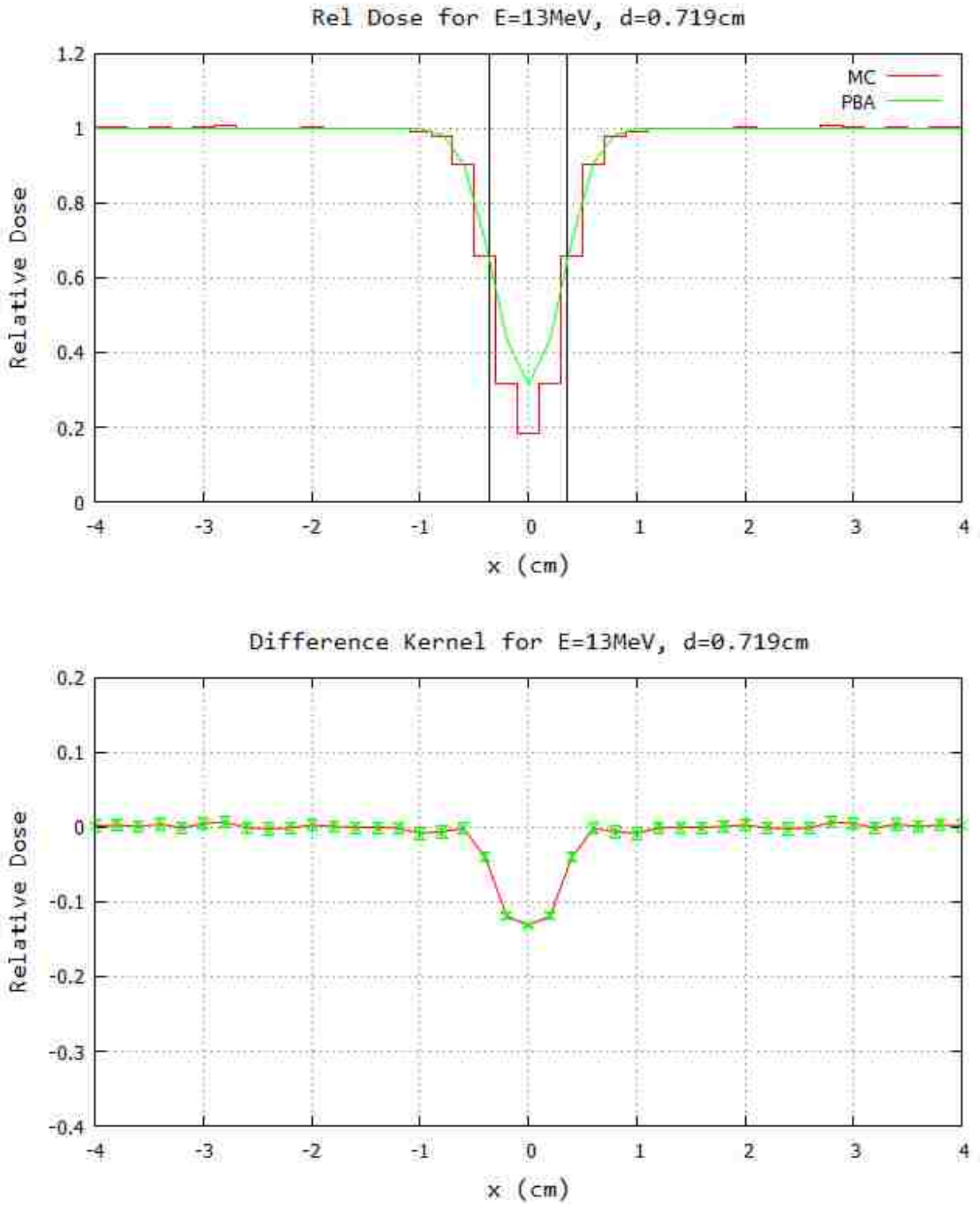


Figure A.11: Monte Carlo central axis block profile and kernel: monoenergetic 13 MeV beam with a central axis block of diameter d=0.719cm at depth z=0.5cm with air gap g=5.0cm. (top) Crossplane intensity profile (y=0) for MC and PBA. Upright block lines indicate the edges of the block. (bottom) MC-PBA difference kernel with error bars.

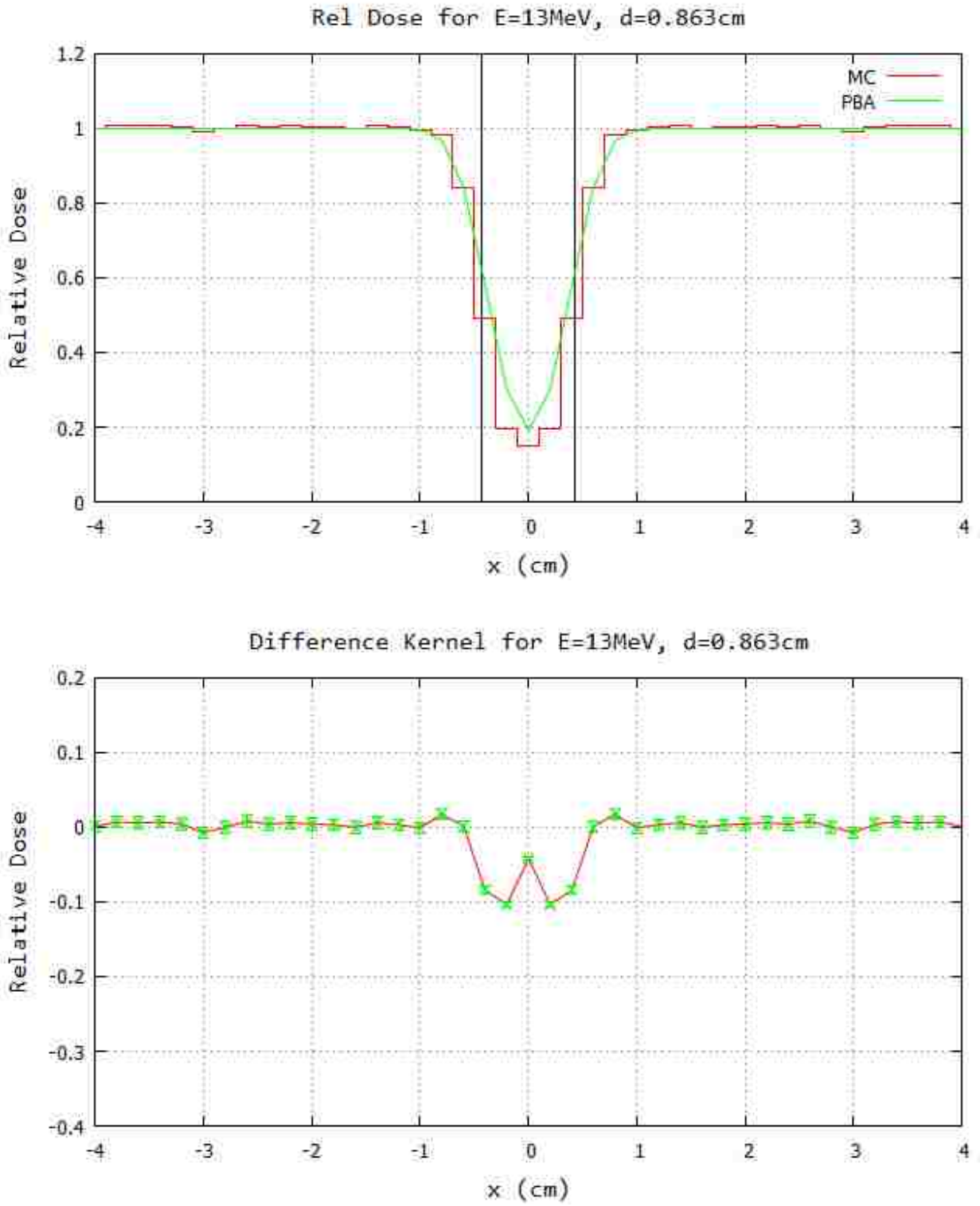


Figure A.12: Monte Carlo central axis block profile and kernel: monoenergetic 13 MeV beam with a central axis block of diameter d=0.863cm at depth z=0.5cm with air gap g=5.0cm. (top) Crossplane intensity profile (y=0) for MC and PBA. Upright block lines indicate the edges of the block. (bottom) MC-PBA difference kernel with error bars.

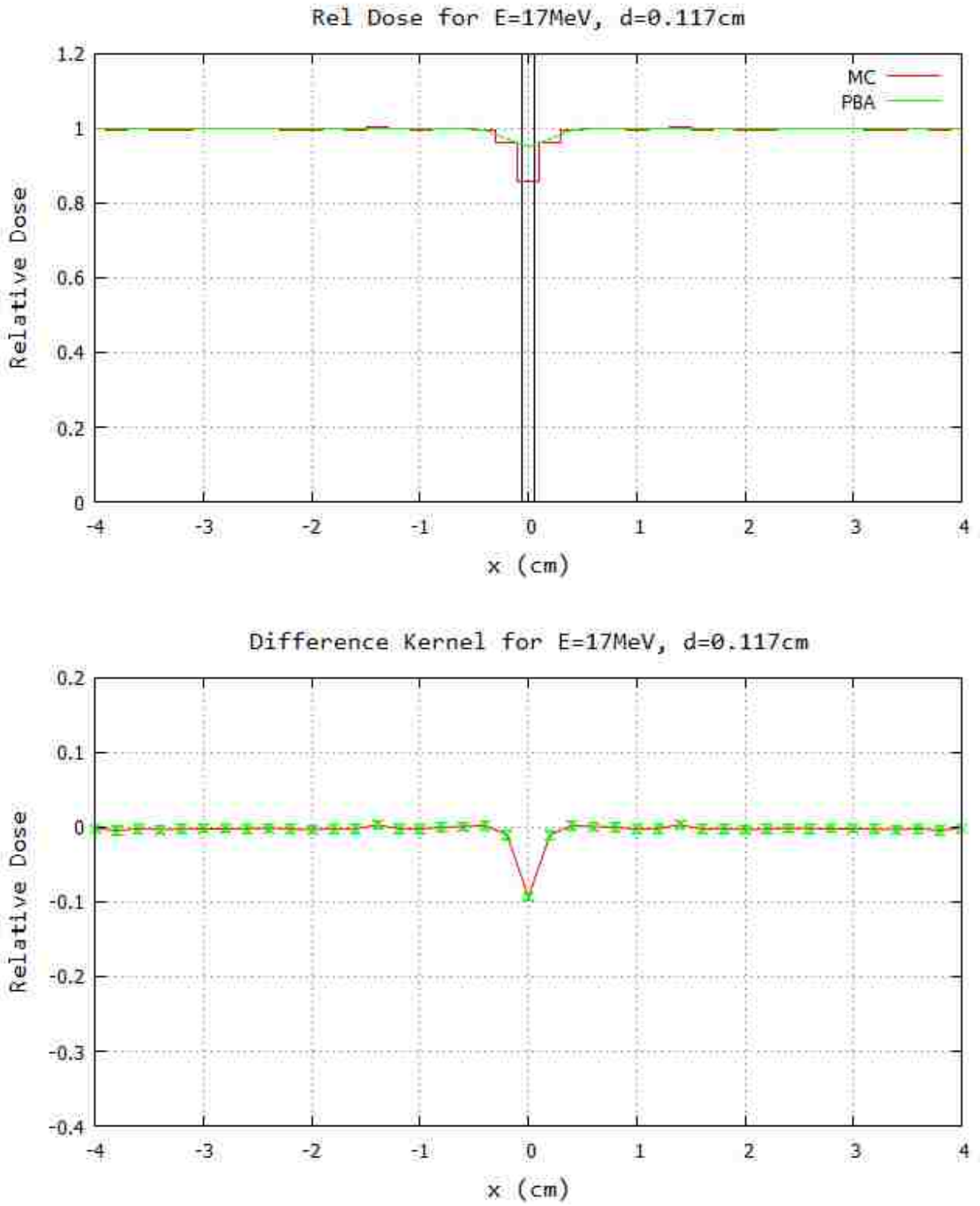


Figure A.13: Monte Carlo central axis block profile and kernel: monoenergetic 17 MeV beam with a central axis block of diameter d=0.117cm at depth z=0.5cm with air gap g=5.0cm. (top) Crossplane intensity profile (y=0) for MC and PBA. Upright block lines indicate the edges of the block. (bottom) MC-PBA difference kernel with error bars.

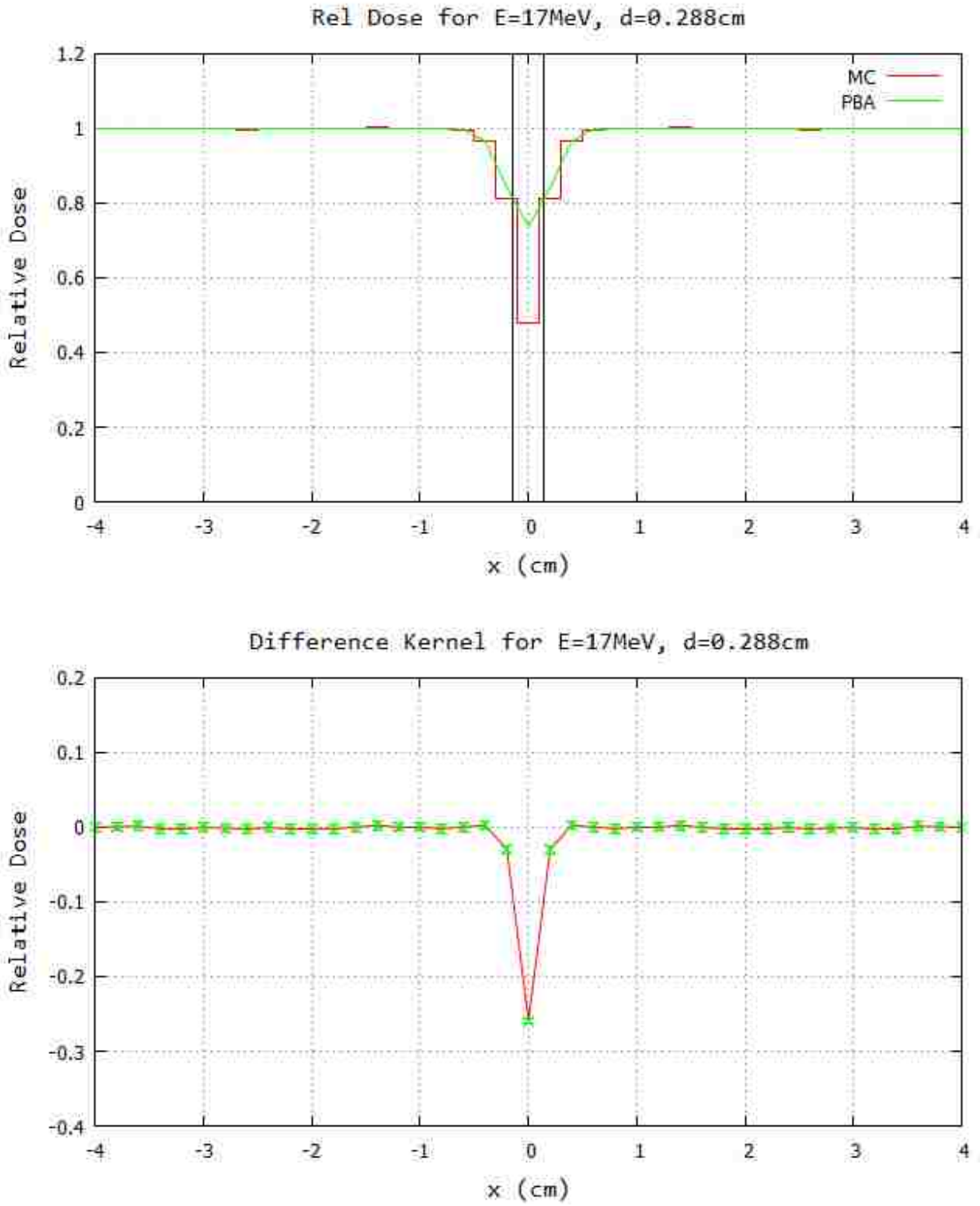


Figure A.14: Monte Carlo central axis block profile and kernel: monoenergetic 17 MeV beam with a central axis block of diameter d=0.288cm at depth z=0.5cm with air gap g=5.0cm. (top) Crossplane intensity profile (y=0) for MC and PBA. Upright block lines indicate the edges of the block. (bottom) MC-PBA difference kernel with error bars.

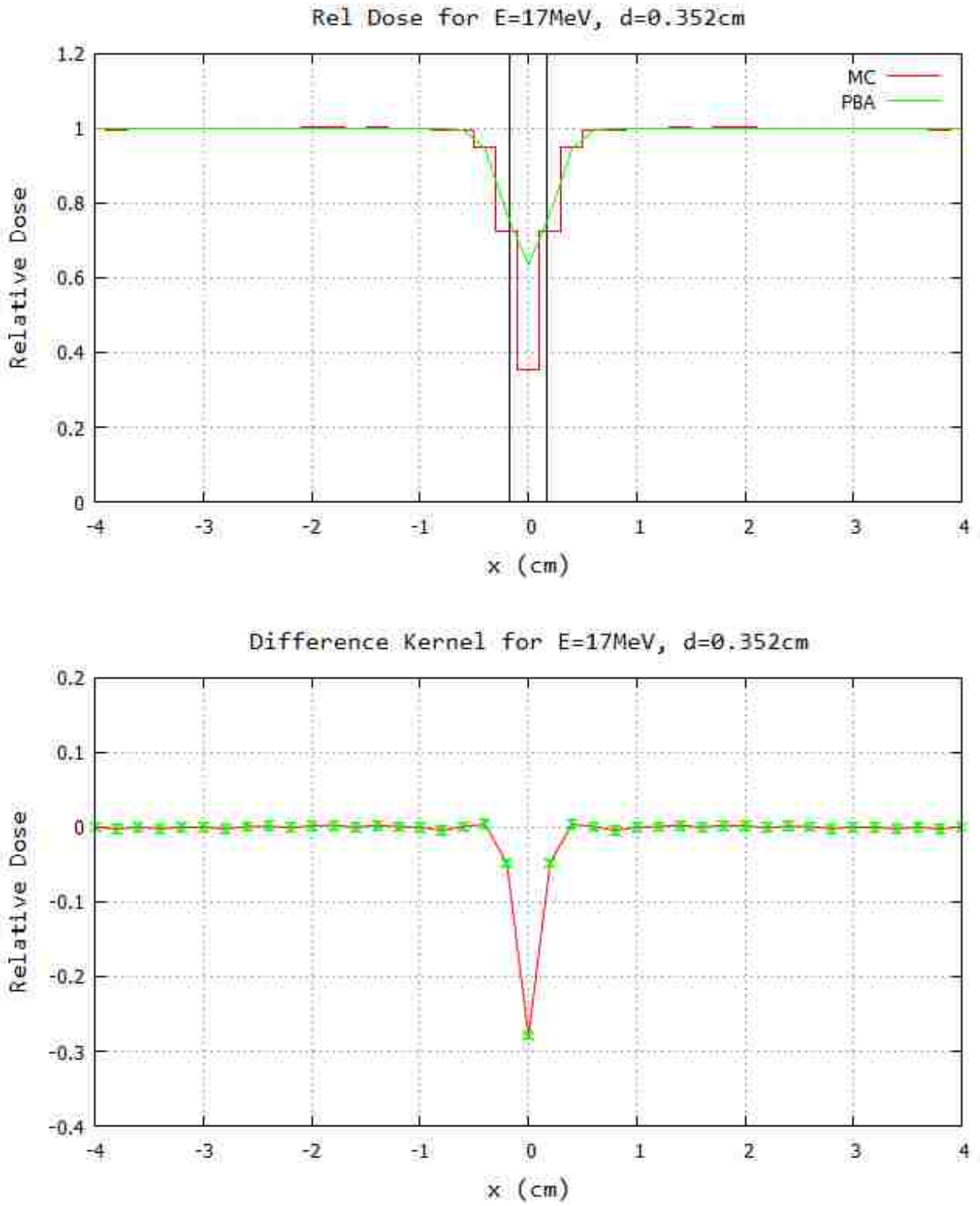


Figure A.15: Monte Carlo central axis block profile and kernel: monoenergetic 17 MeV beam with a central axis block of diameter d=0.352cm at depth z=0.5cm with air gap g=5.0cm. (top) Crossplane intensity profile (y=0) for MC and PBA. Upright block lines indicate the edges of the block. (bottom) MC-PBA difference kernel with error bars.

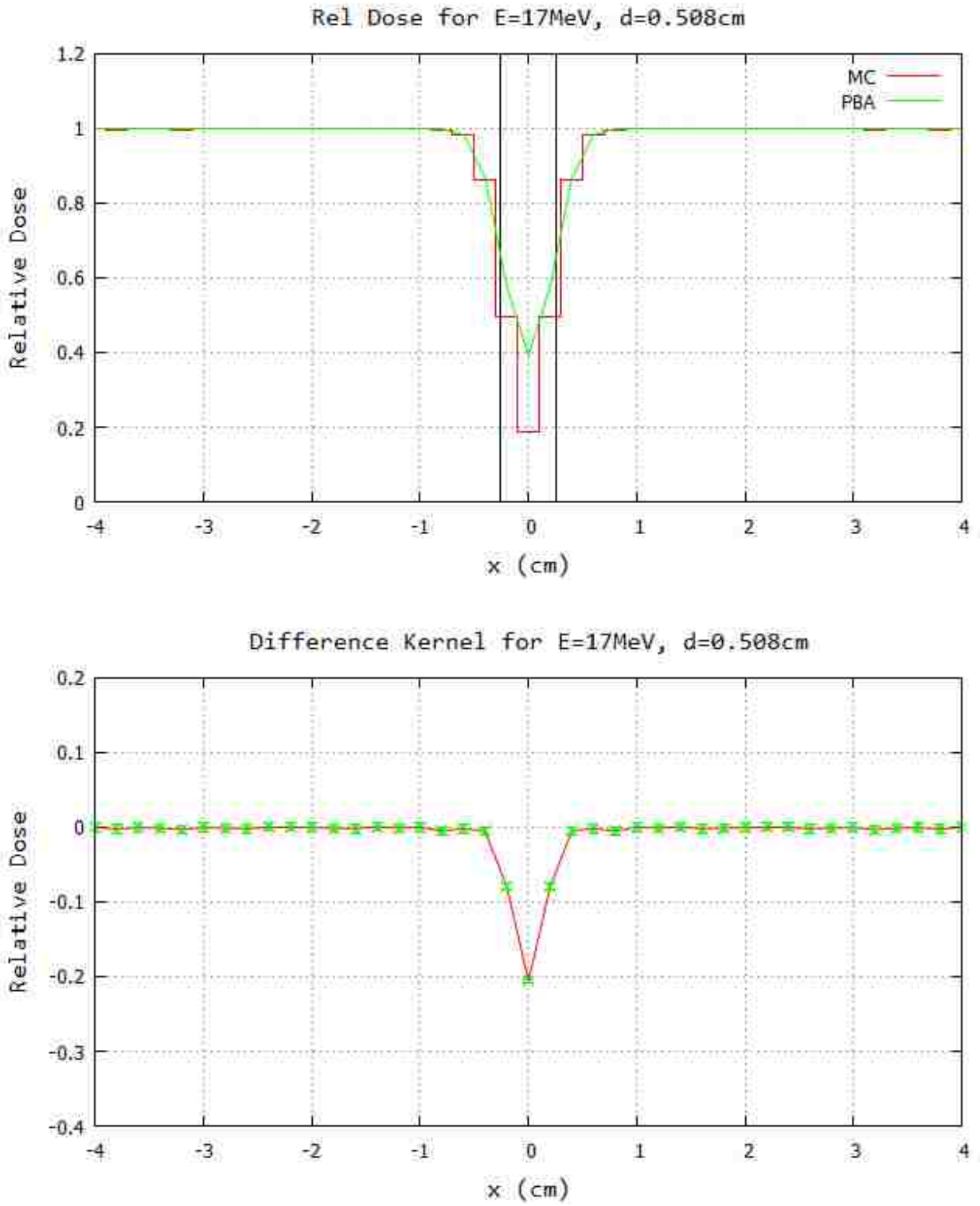


Figure A.16: Monte Carlo central axis block profile and kernel: monoenergetic 17 MeV beam with a central axis block of diameter d=0.508cm at depth z=0.5cm with air gap g=5.0cm. (top) Crossplane intensity profile (y=0) for MC and PBA. Upright block lines indicate the edges of the block. (bottom) MC-PBA difference kernel with error bars.

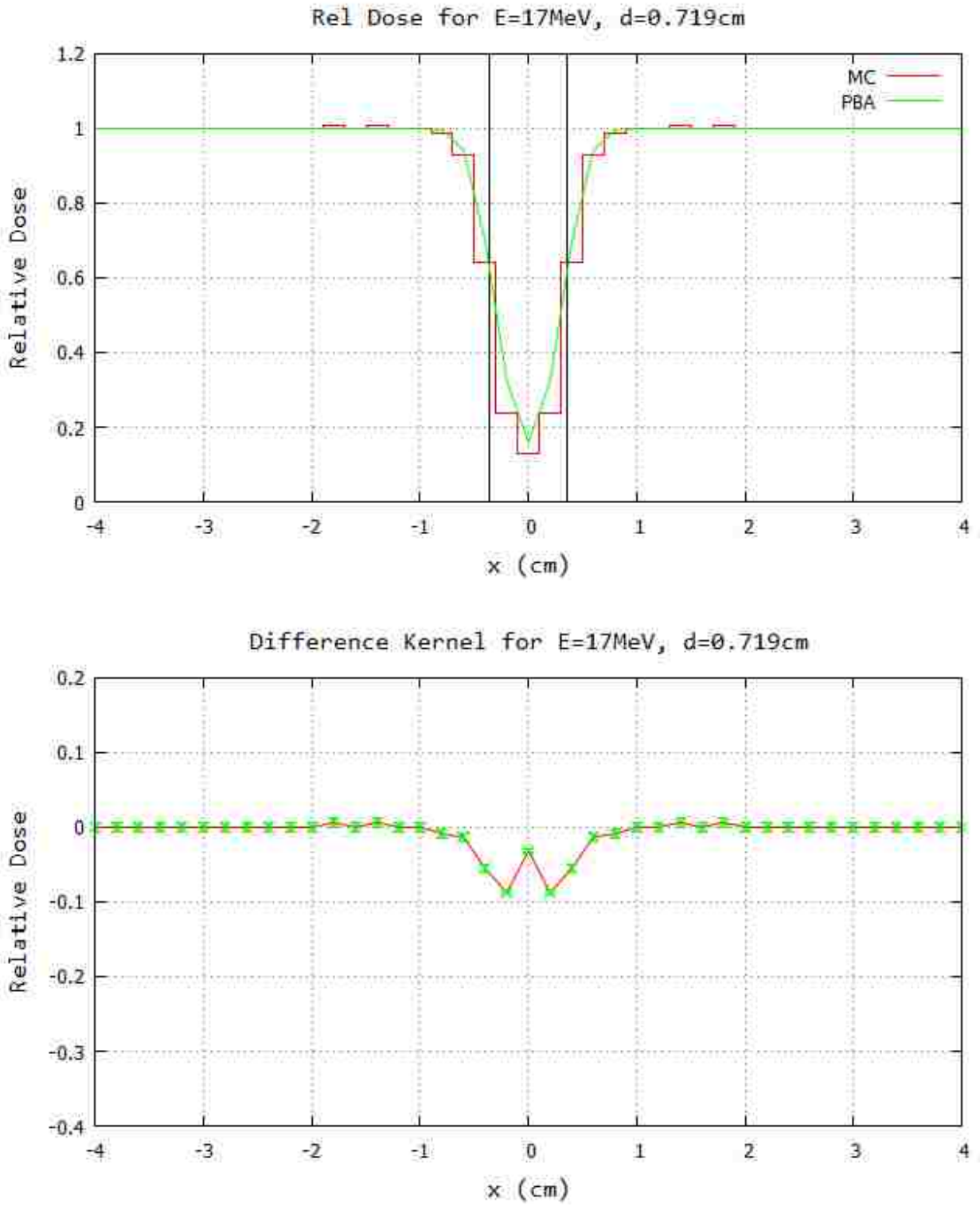


Figure A.17: Monte Carlo central axis block profile and kernel: monoenergetic 17 MeV beam with a central axis block of diameter d=0.719cm at depth z=0.5cm with air gap g=5.0cm. (top) Crossplane intensity profile (y=0) for MC and PBA. Upright block lines indicate the edges of the block. (bottom) MC-PBA difference kernel with error bars.

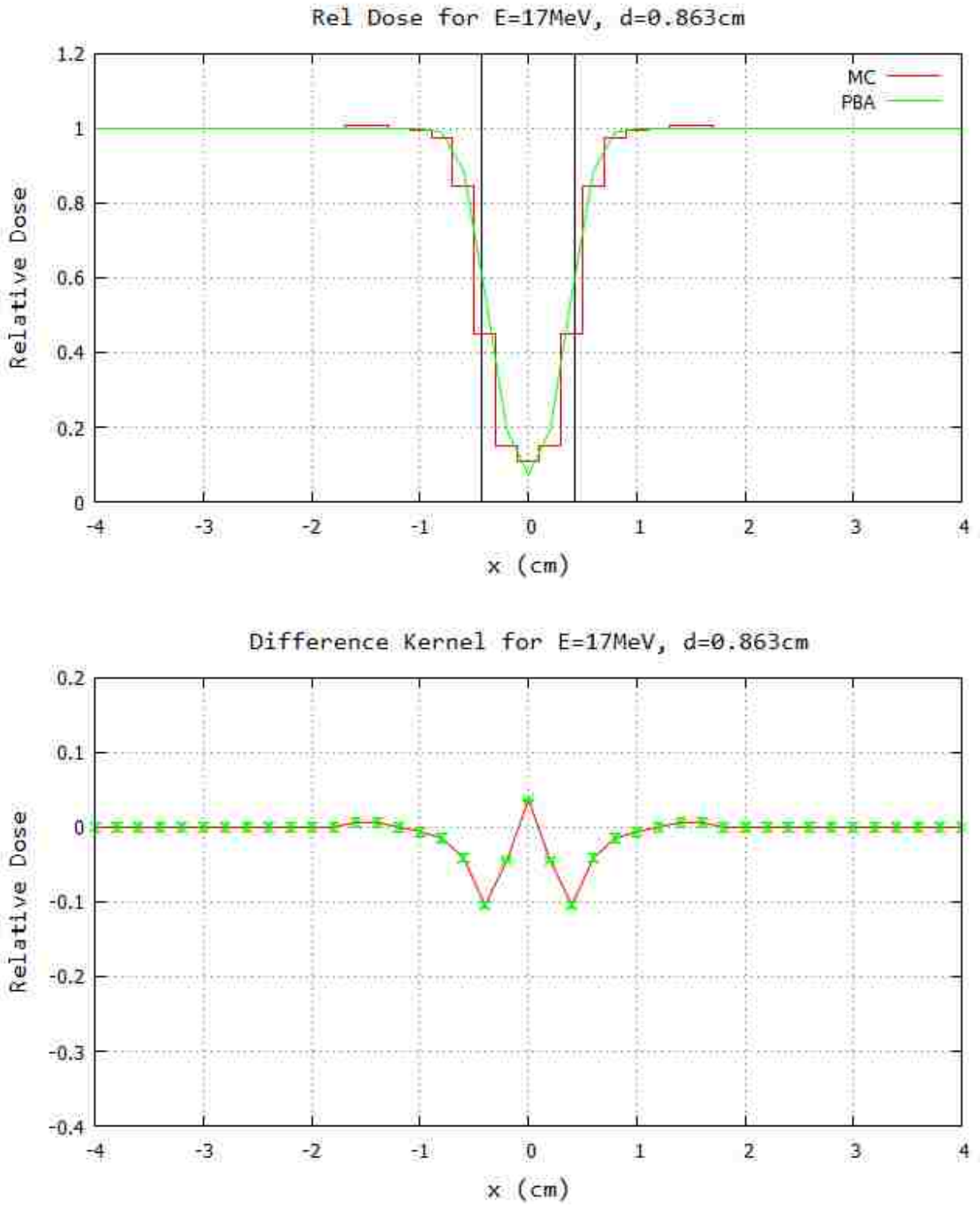


Figure A.18: Monte Carlo central axis block profile and kernel: monoenergetic 17 MeV beam with a central axis block of diameter d=0.863cm at depth z=0.5cm with air gap g=5.0cm. (top) Crossplane intensity profile (y=0) for MC and PBA. Upright block lines indicate the edges of the block. (bottom) MC-PBA difference kernel with error bars.

# APPENDIX B
# OFF-AXIS PROFILES UNDER ISLAND BLOCK ARRAYS CALCULATED WITH PBA

100 cm SSD

| Figure | E (MeV) | r (cm) | Depth (cm) |
|---|---|---|---|
| B.1 | 7 | 0.50 | 0.5, 2.0 |
| B.2 | 7 | 0.75 | 0.5, 2.0 |
| B.3 | 7 | 1.00 | 0.5, 2.0 |
| B.4 | 7 | 1.25 | 0.5, 2.0 |
| B.5 | 7 | 1.50 | 0.5, 2.0 |
| B.6 | 9 | 0.50 | 0.5, 2.0 |
| B.7 | 9 | 0.75 | 0.5, 2.0 |
| B.8 | 9 | 1.00 | 0.5, 2.0 |
| B.9 | 9 | 1.25 | 0.5, 2.0 |
| B.10 | 9 | 1.50 | 0.5, 2.0 |
| B.11 | 10 | 0.50 | 0.5, 2.0 |
| B.12 | 10 | 0.75 | 0.5, 2.0 |
| B.13 | 10 | 1.00 | 0.5, 2.0 |
| B.14 | 10 | 1.25 | 0.5, 2.0 |
| B.15 | 10 | 1.50 | 0.5, 2.0 |
| B.16 | 11 | 0.50 | 0.5, 2.0 |
| B.17 | 11 | 0.75 | 0.5, 2.0 |
| B.18 | 11 | 1.00 | 0.5, 2.0 |
| B.19 | 11 | 1.25 | 0.5, 2.0 |
| B.20 | 11 | 1.50 | 0.5, 2.0 |
| B.21 | 13 | 0.50 | 0.5, 2.0 |
| B.22 | 13 | 0.75 | 0.5, 2.0 |
| B.23 | 13 | 1.00 | 0.5, 2.0 |
| B.24 | 13 | 1.25 | 0.5, 2.0 |
| B.25 | 13 | 1.50 | 0.5, 2.0 |
| B.26 | 16 | 0.50 | 0.5, 2.0 |
| B.27 | 16 | 0.75 | 0.5, 2.0 |
| B.28 | 16 | 1.00 | 0.5, 2.0 |
| B.29 | 16 | 1.25 | 0.5, 2.0 |
| B.30 | 16 | 1.50 | 0.5, 2.0 |
| B.31 | 20 | 0.50 | 0.5, 2.0 |
| B.32 | 20 | 0.75 | 0.5, 2.0 |
| B.33 | 20 | 1.00 | 0.5, 2.0 |
| B.34 | 20 | 1.25 | 0.5, 2.0 |
| B.35 | 20 | 1.50 | 0.5, 2.0 |

103 cm SSD

| Figure | E (MeV) | r (cm) | Depth (cm) |
|---|---|---|---|
| B.36 | 7 | 0.50 | 0.5, 2.0 |
| B.37 | 7 | 0.75 | 0.5, 2.0 |
| B.38 | 7 | 1.00 | 0.5, 2.0 |
| B.39 | 7 | 1.25 | 0.5, 2.0 |
| B.40 | 7 | 1.50 | 0.5, 2.0 |
| B.41 | 9 | 0.50 | 0.5, 2.0 |
| B.42 | 9 | 0.75 | 0.5, 2.0 |
| B.43 | 9 | 1.00 | 0.5, 2.0 |
| B.44 | 9 | 1.25 | 0.5, 2.0 |
| B.45 | 9 | 1.50 | 0.5, 2.0 |
| B.46 | 10 | 0.50 | 0.5, 2.0 |
| B.47 | 10 | 0.75 | 0.5, 2.0 |
| B.48 | 10 | 1.00 | 0.5, 2.0 |
| B.49 | 10 | 1.25 | 0.5, 2.0 |
| B.50 | 10 | 1.50 | 0.5, 2.0 |
| B.51 | 11 | 0.50 | 0.5, 2.0 |
| B.52 | 11 | 0.75 | 0.5, 2.0 |
| B.53 | 11 | 1.00 | 0.5, 2.0 |
| B.54 | 11 | 1.25 | 0.5, 2.0 |
| B.55 | 11 | 1.50 | 0.5, 2.0 |
| B.56 | 13 | 0.50 | 0.5, 2.0 |
| B.57 | 13 | 0.75 | 0.5, 2.0 |
| B.58 | 13 | 1.00 | 0.5, 2.0 |
| B.59 | 13 | 1.25 | 0.5, 2.0 |
| B.60 | 13 | 1.50 | 0.5, 2.0 |
| B.61 | 16 | 0.50 | 0.5, 2.0 |
| B.62 | 16 | 0.75 | 0.5, 2.0 |
| B.63 | 16 | 1.00 | 0.5, 2.0 |
| B.64 | 16 | 1.25 | 0.5, 2.0 |
| B.65 | 16 | 1.50 | 0.5, 2.0 |
| B.66 | 20 | 0.50 | 0.5, 2.0 |
| B.67 | 20 | 0.75 | 0.5, 2.0 |
| B.68 | 20 | 1.00 | 0.5, 2.0 |
| B.69 | 20 | 1.25 | 0.5, 2.0 |
| B.70 | 20 | 1.50 | 0.5, 2.0 |

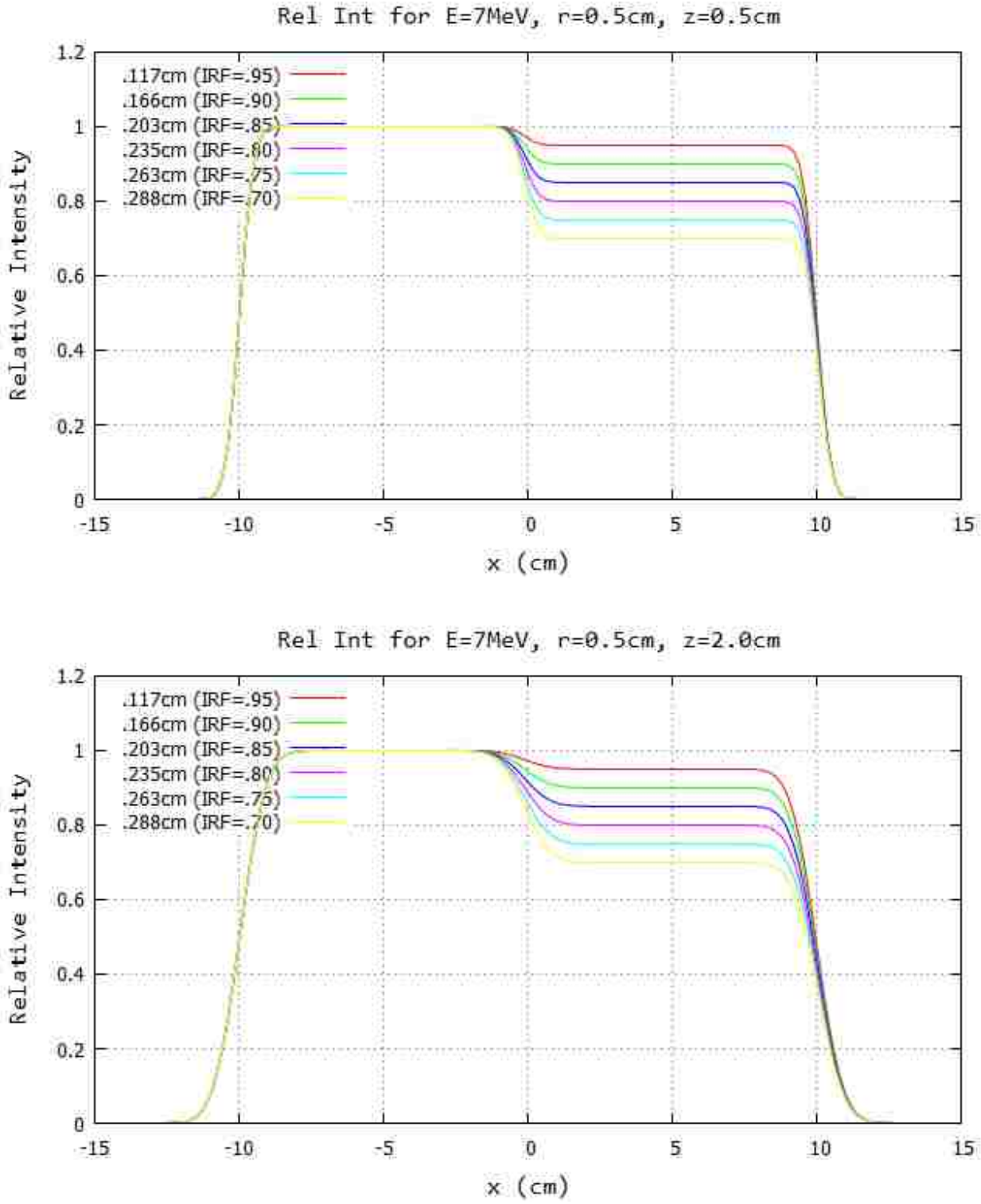


Figure B.1: Profile for 7 MeV and 100 cm SSD at y=0cm 20x20 half-blocked field. The computed island block diameter for 0.70, 0.75, 0.80, 0.85, 0.90, and 0.95 IRF values are listed in each plot's inserted key.

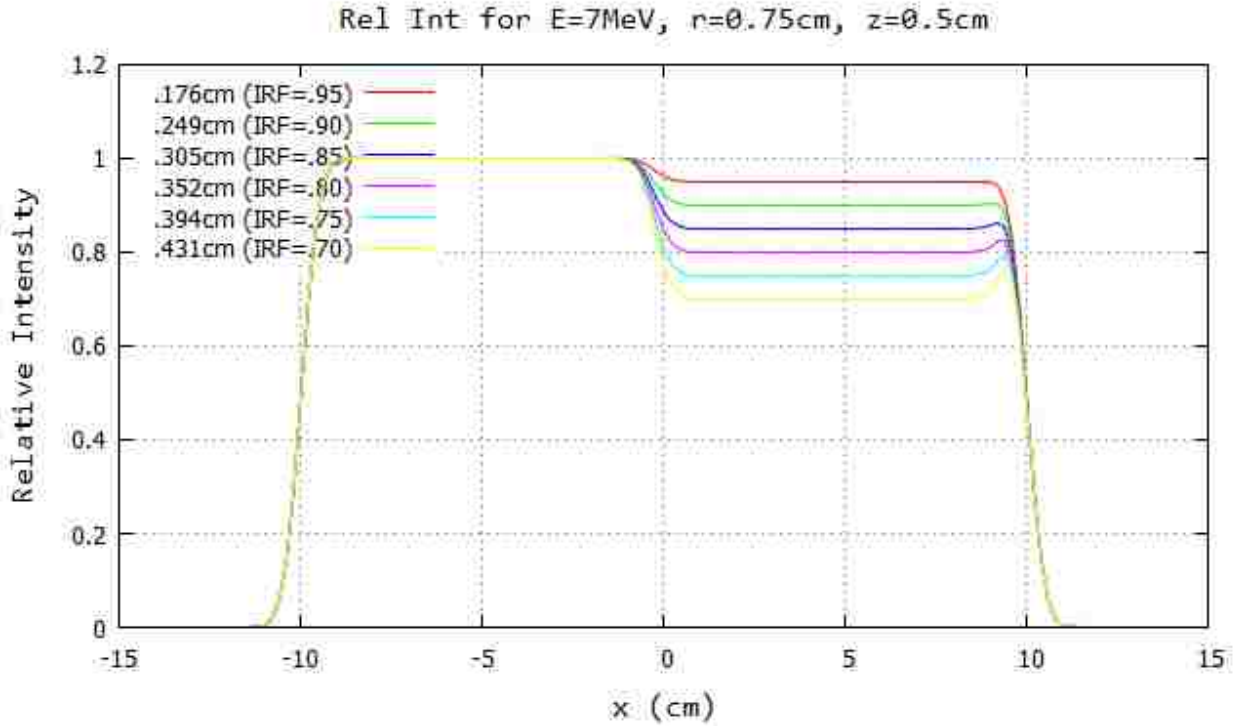


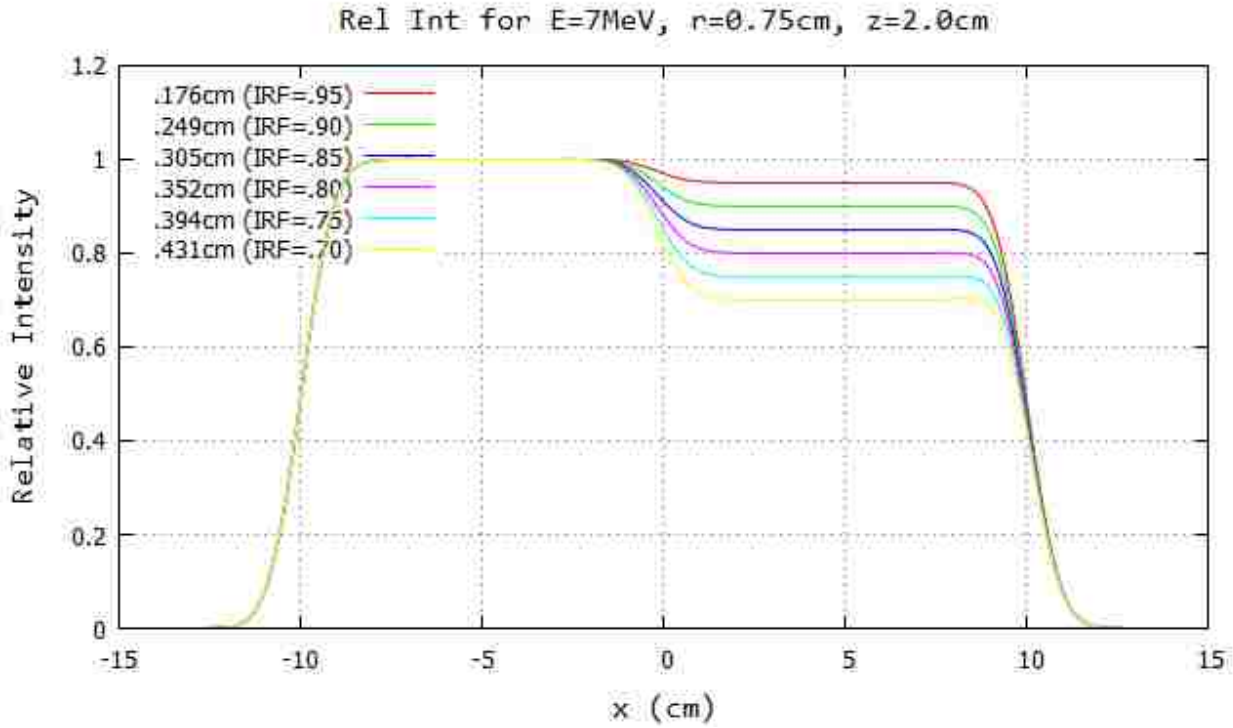


Figure B.2: Profile for 7 MeV and 100 cm SSD at y=0cm 20x20 half-blocked field. The computed island block diameter for 0.70, 0.75, 0.80, 0.85, 0.90, and 0.95 IRF values are listed in each plot's inserted key.

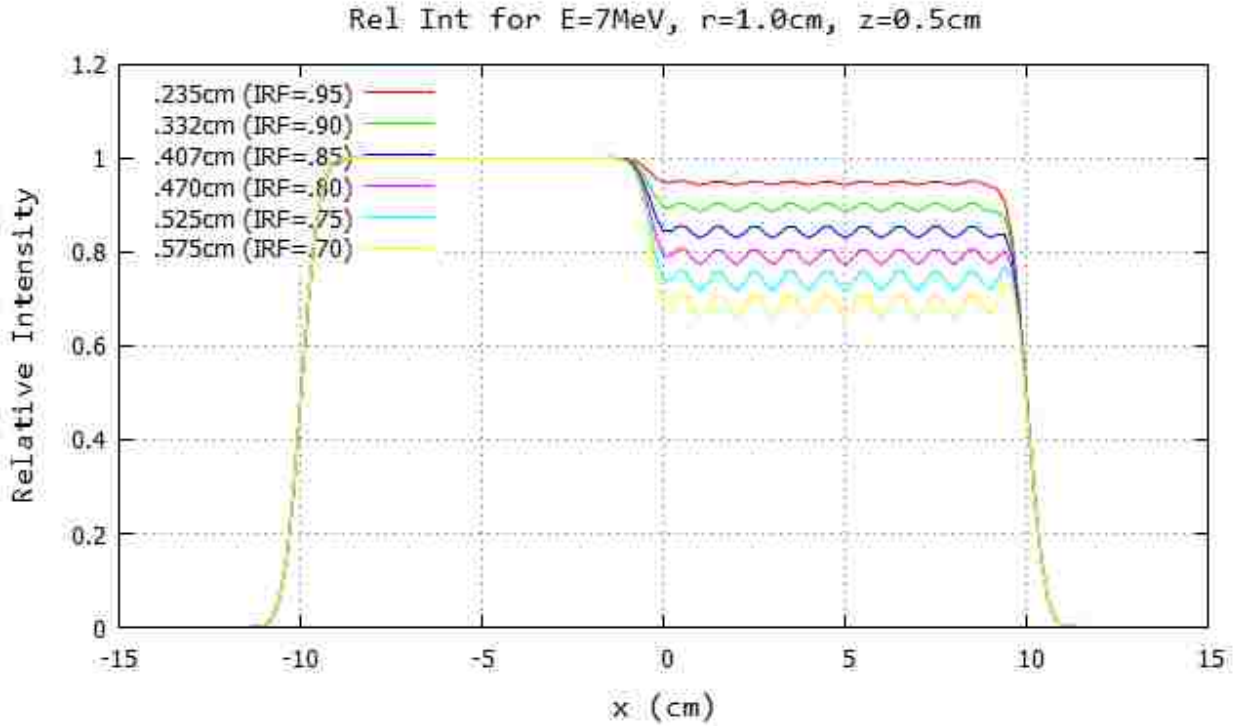


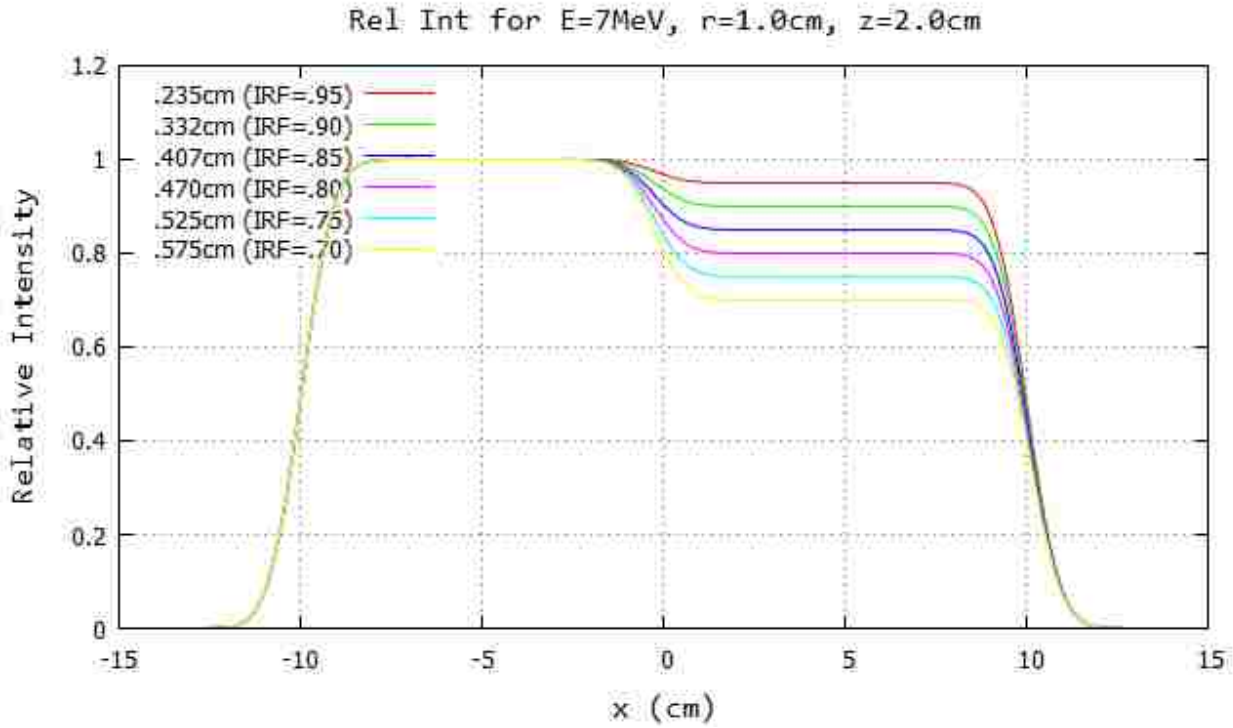


Figure B.3: Profile for 7 MeV and 100 cm SSD at y=0cm 20x20 half-blocked field. The computed island block diameter for 0.70, 0.75, 0.80, 0.85, 0.90, and 0.95 IRF values are listed in each plot's inserted key.

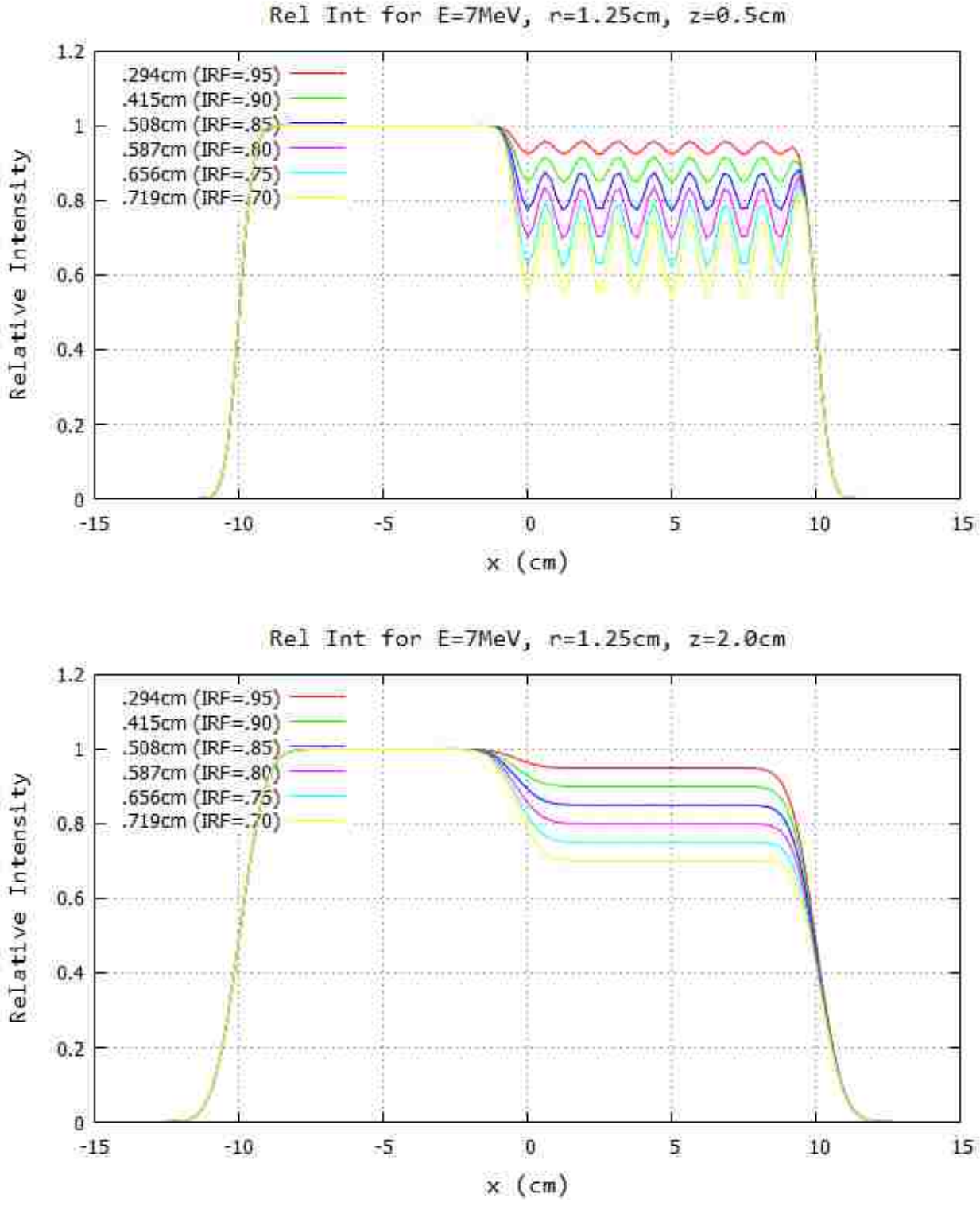


Figure B.4: Profile for 7 MeV and 100 cm SSD at y=0cm 20x20 half-blocked field. The computed island block diameter for 0.70, 0.75, 0.80, 0.85, 0.90, and 0.95 IRF values are listed in each plot's inserted key.

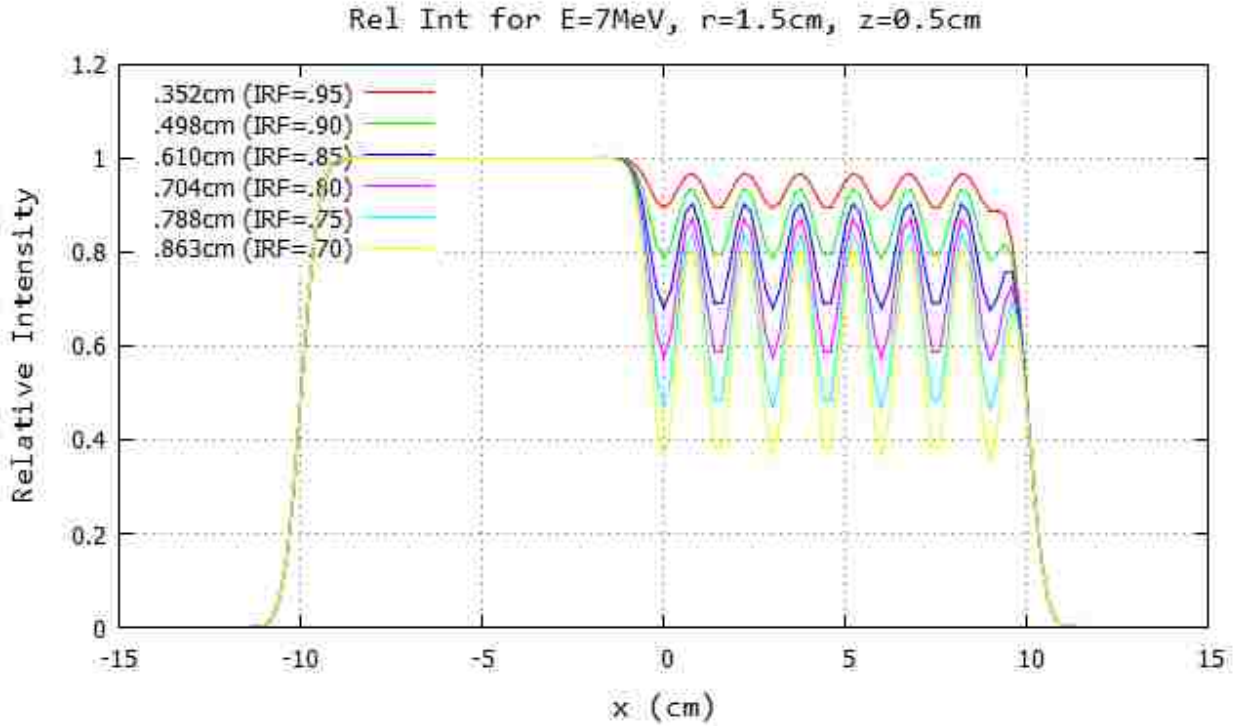


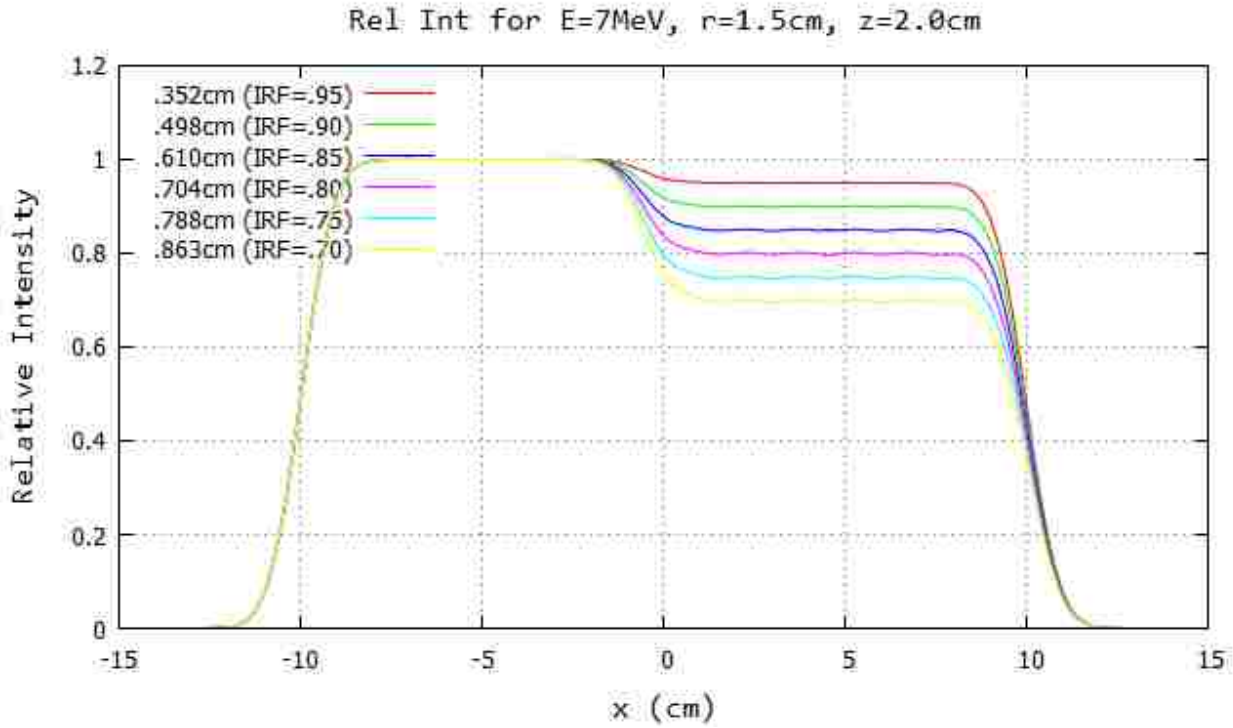


Figure B.5: Profile for 7 MeV and 100 cm SSD at y=0cm 20x20 half-blocked field. The computed island block diameter for 0.70, 0.75, 0.80, 0.85, 0.90, and 0.95 IRF values are listed in each plot's inserted key.

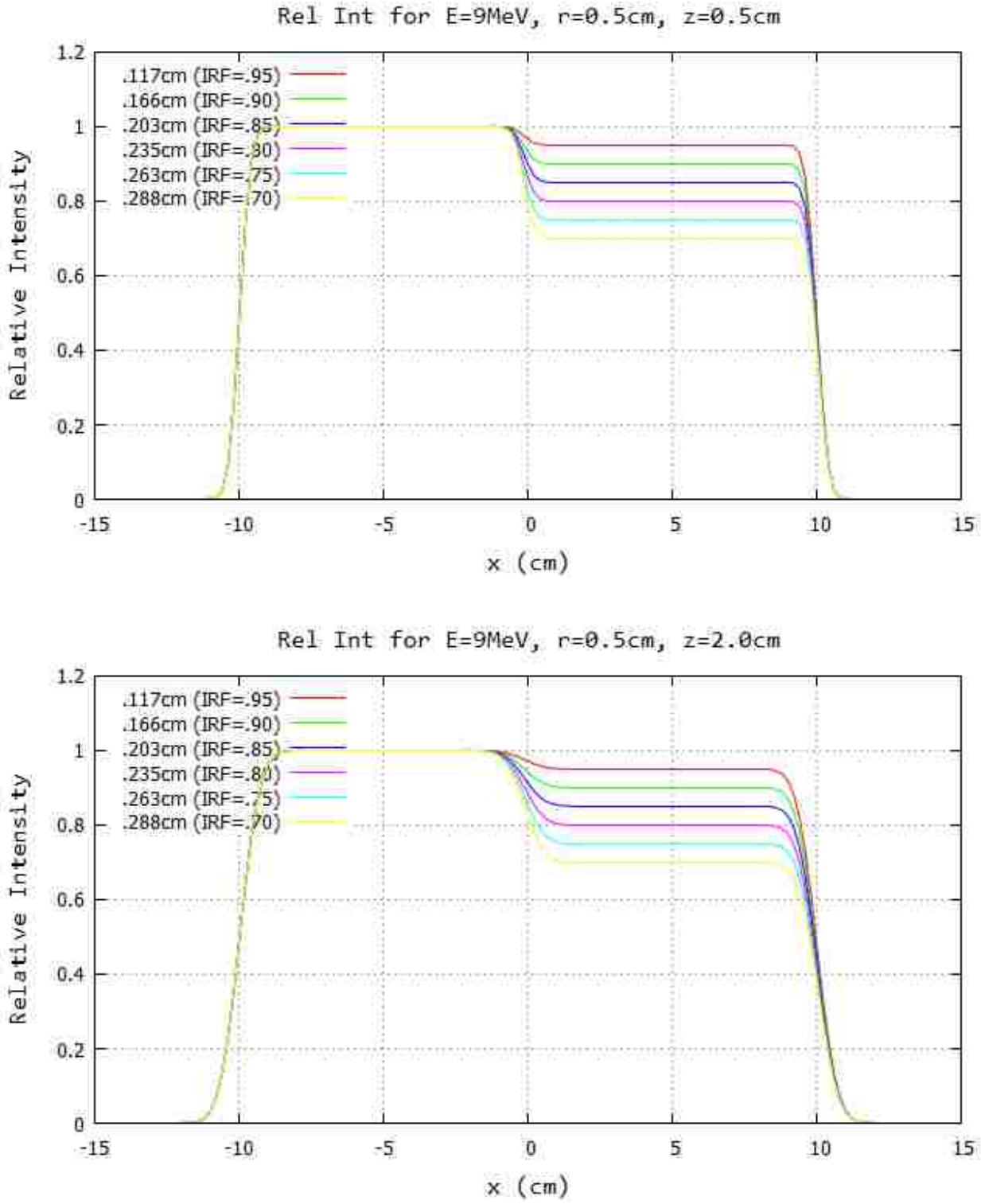


Figure B.6: Profile for 9 MeV and 100 cm SSD at y=0cm 20x20 half-blocked field. The computed island block diameter for 0.70, 0.75, 0.80, 0.85, 0.90, and 0.95 IRF values are listed in each plot's inserted key.

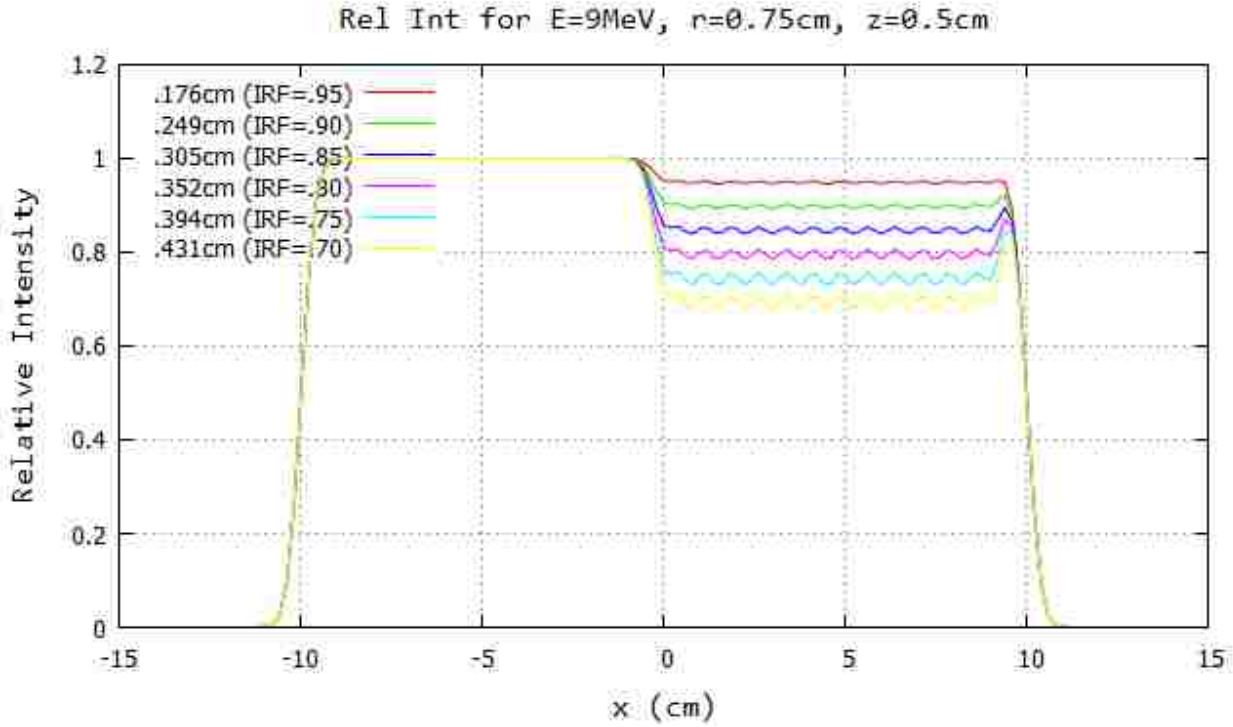


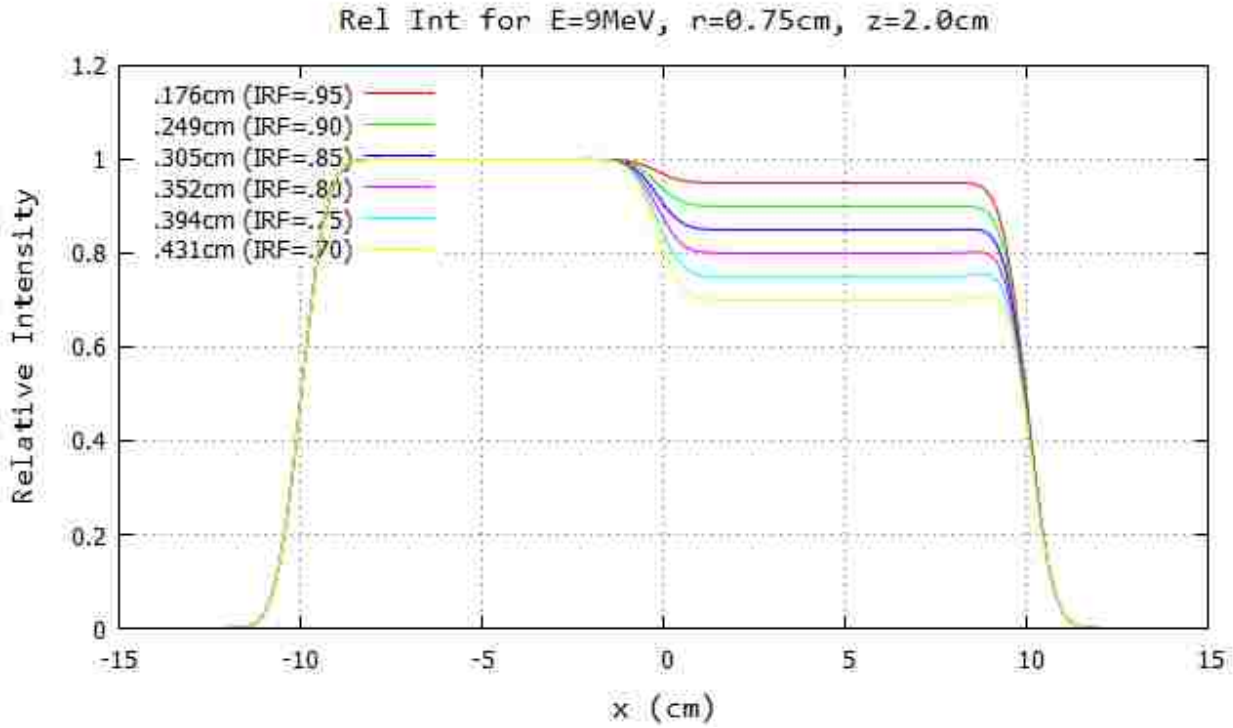


Figure B.7: Profile for 9 MeV and 100 cm SSD at y=0cm 20x20 half-blocked field. The computed island block diameter for 0.70, 0.75, 0.80, 0.85, 0.90, and 0.95 IRF values are listed in each plot's inserted key.

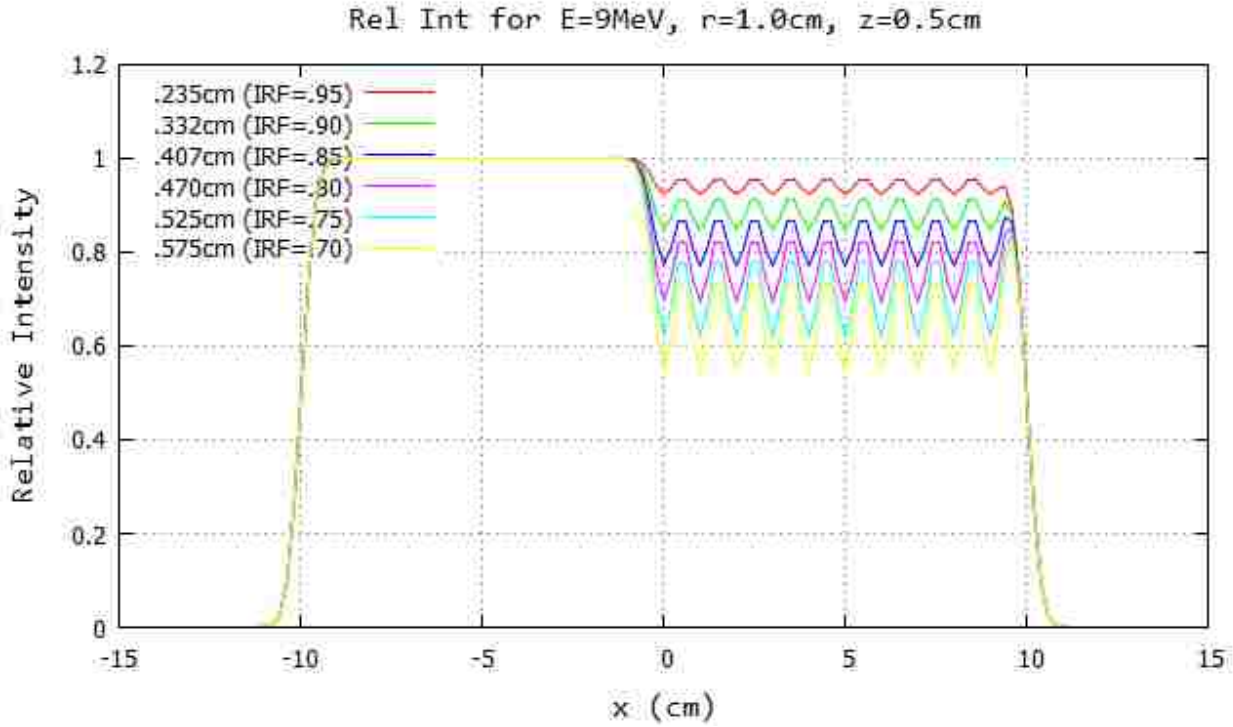


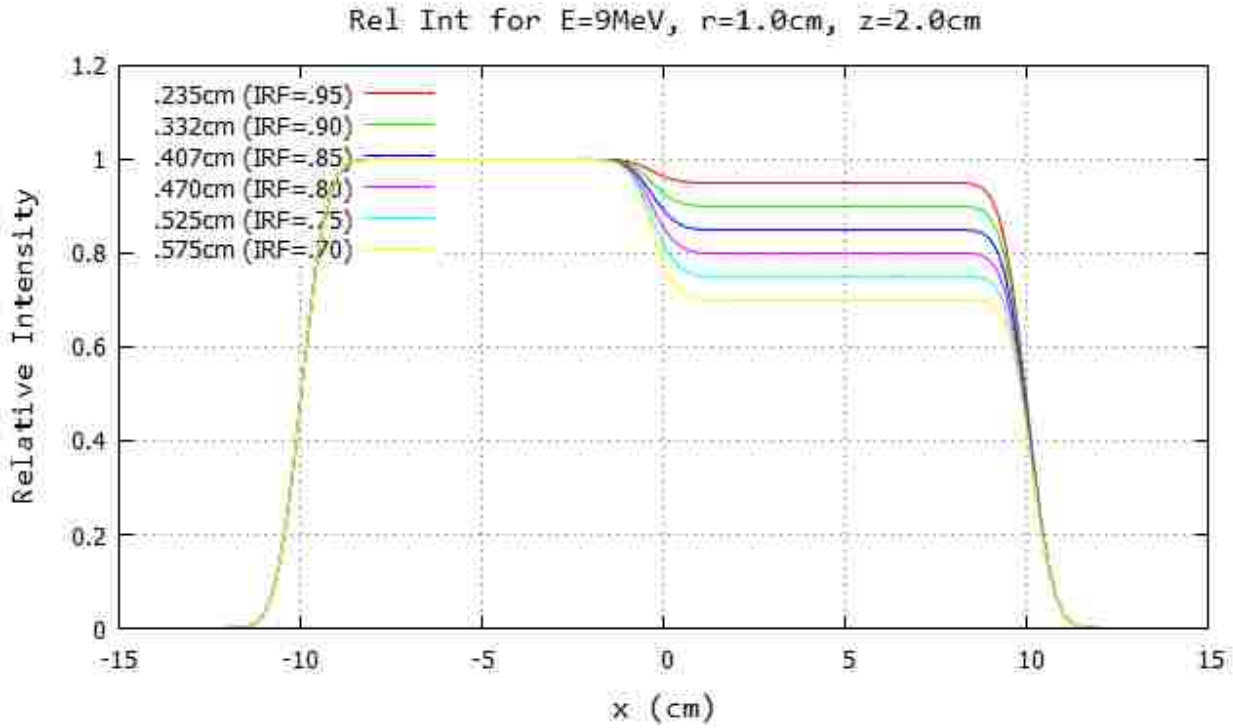


Figure B.8: Profile for 9 MeV and 100 cm SSD at y=0cm 20x20 half-blocked field. The computed island block diameter for 0.70, 0.75, 0.80, 0.85, 0.90, and 0.95 IRF values are listed in each plot's inserted key.

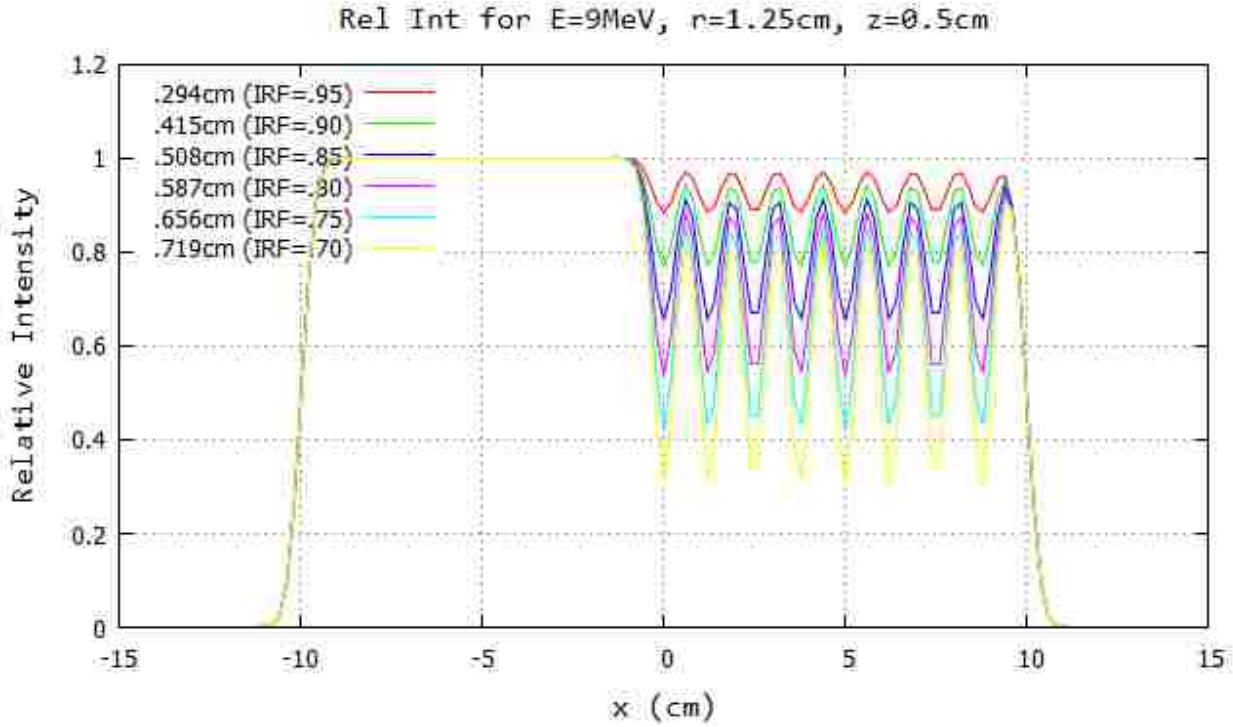


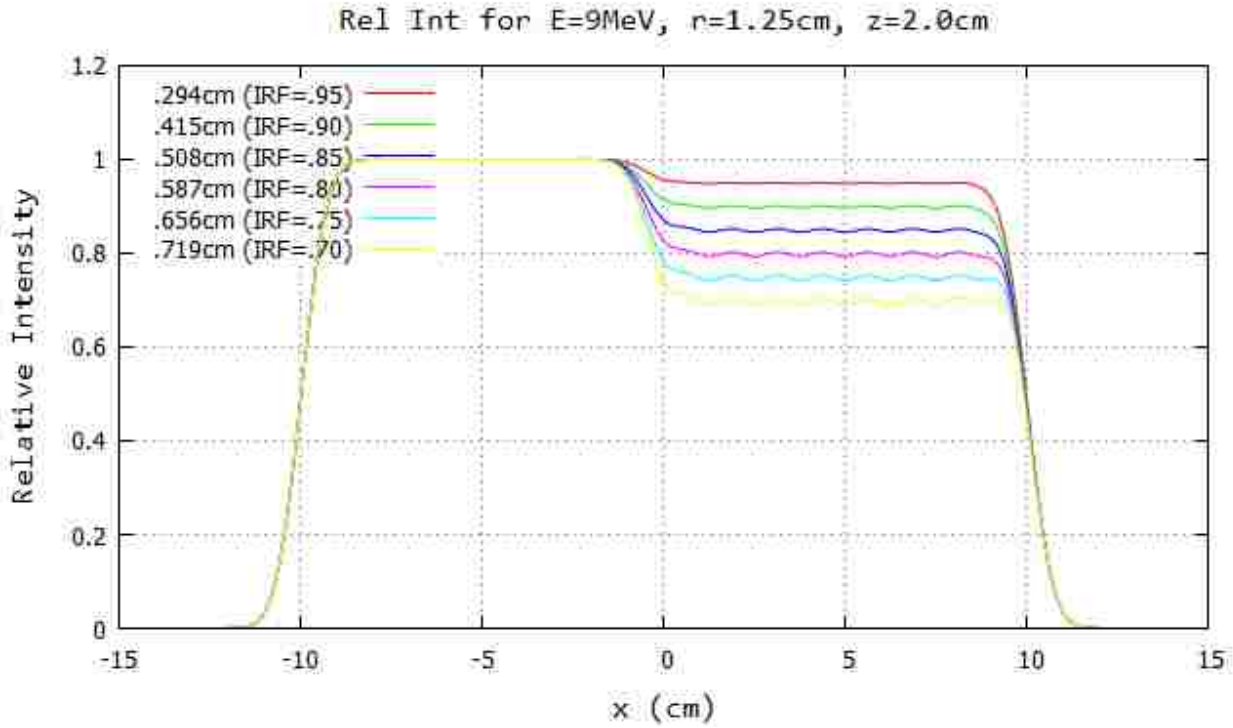


Figure B.9: Profile for 9 MeV and 100 cm SSD at y=0cm 20x20 half-blocked field. The computed island block diameter for 0.70, 0.75, 0.80, 0.85, 0.90, and 0.95 IRF values are listed in each plot's inserted key.

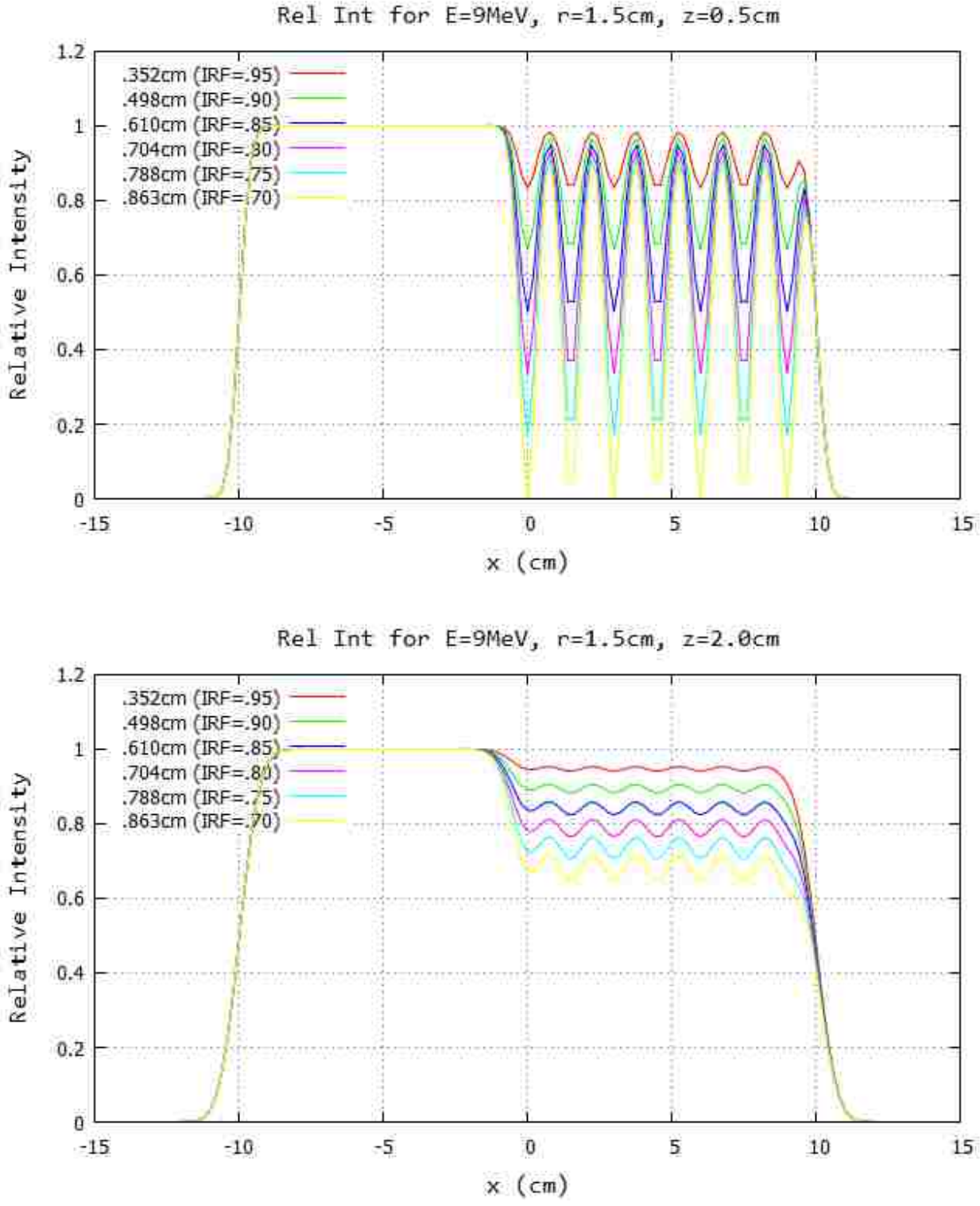


Figure B.10: Profile for 9 MeV and 100 cm SSD at y=0cm 20x20 half-blocked field. The computed island block diameter for 0.70, 0.75, 0.80, 0.85, 0.90, and 0.95 IRF values are listed in each plot's inserted key.

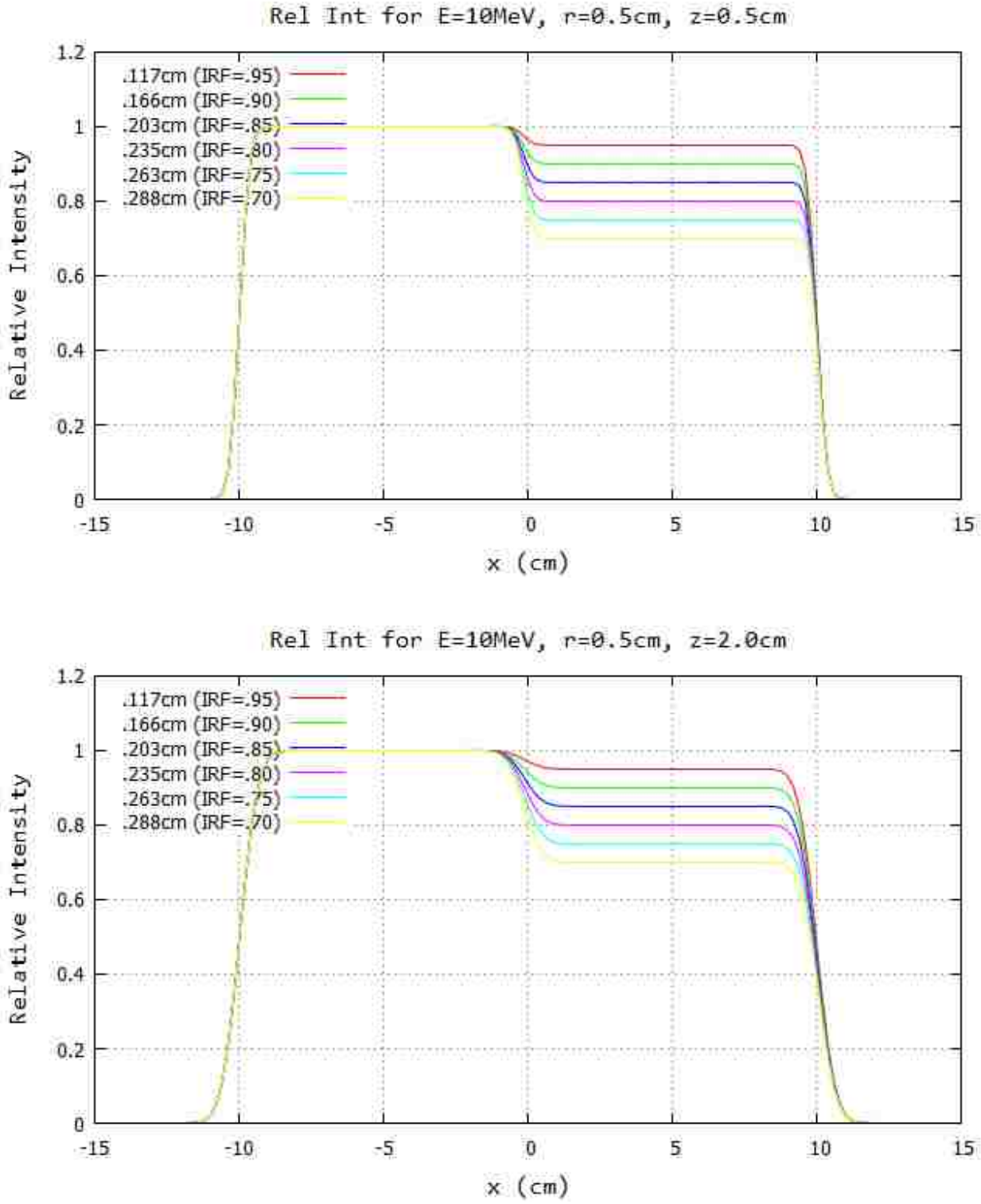


Figure B.11: Profile for 10 MeV and 100 cm SSD at y=0cm 20x20 half-blocked field. The computed island block diameter for 0.70, 0.75, 0.80, 0.85, 0.90, and 0.95 IRF values are listed in each plot's inserted key.

t

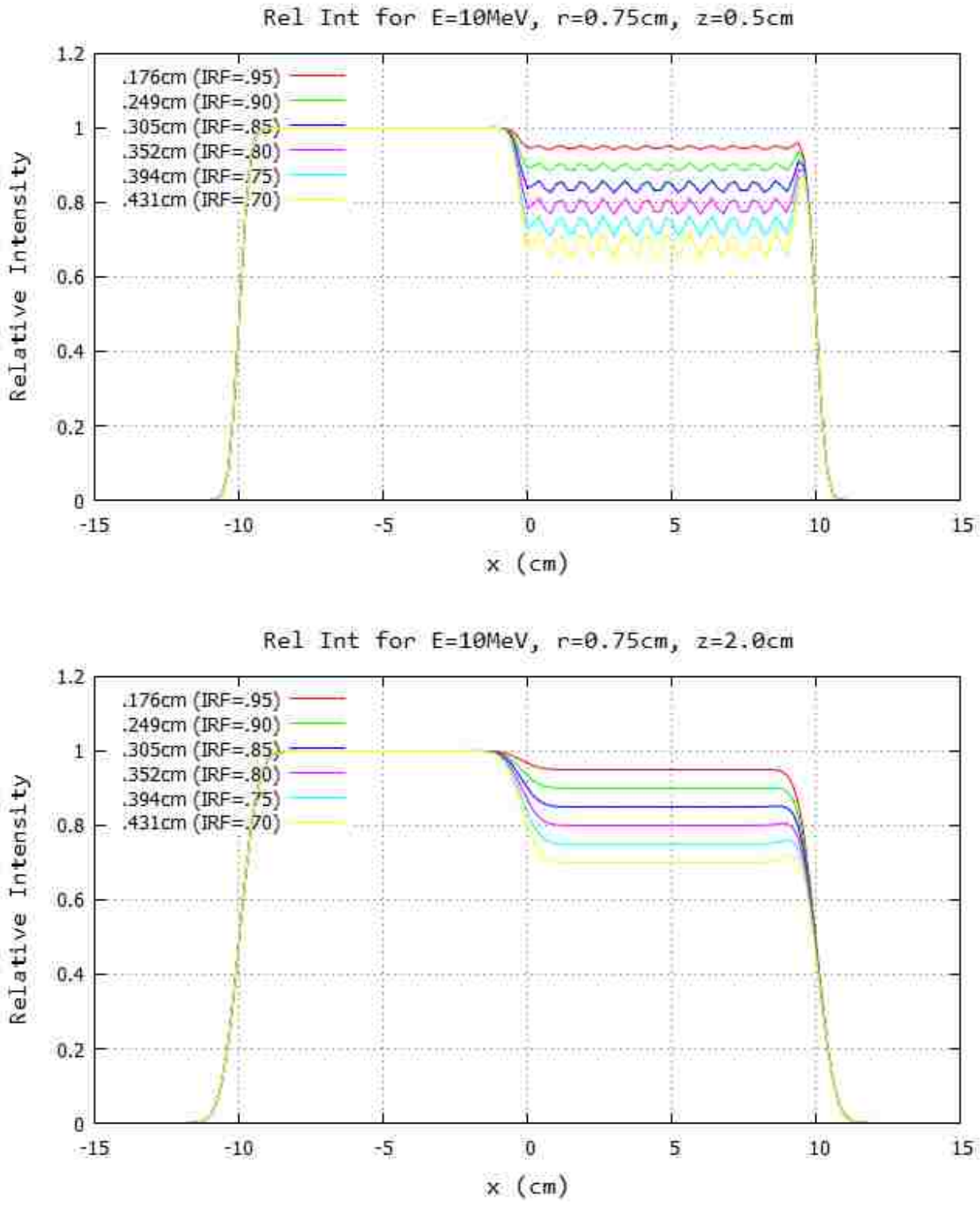


Figure B.12: Profile for 10 MeV and 100 cm SSD at y=0cm 20x20 half-blocked field. The computed island block diameter for 0.70, 0.75, 0.80, 0.85, 0.90, and 0.95 IRF values are listed in each plot's inserted key.

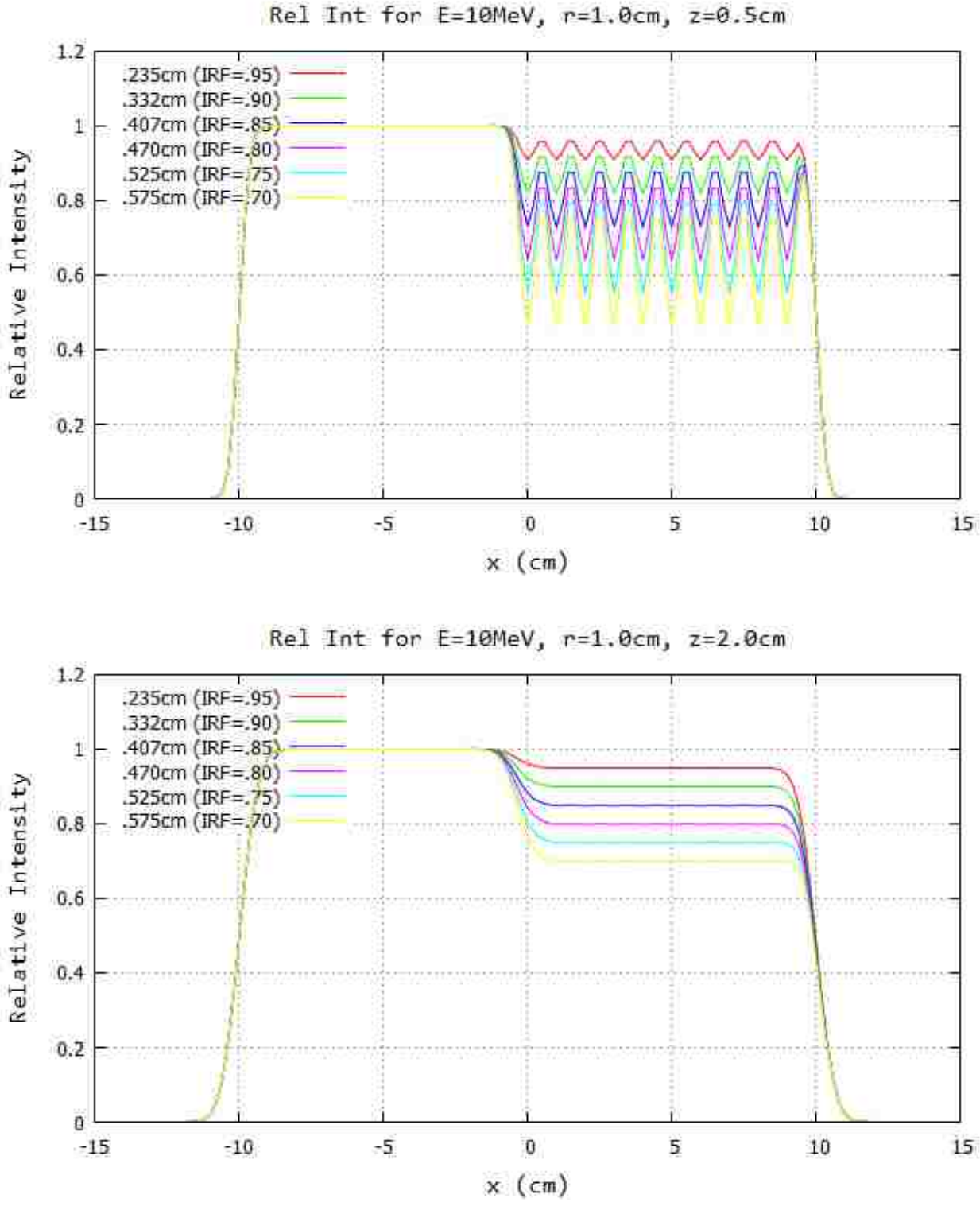


Figure B.13: Profile for 10 MeV and 100 cm SSD at y=0cm 20x20 half-blocked field. The computed island block diameter for 0.70, 0.75, 0.80, 0.85, 0.90, and 0.95 IRF values are listed in each plot's inserted key.

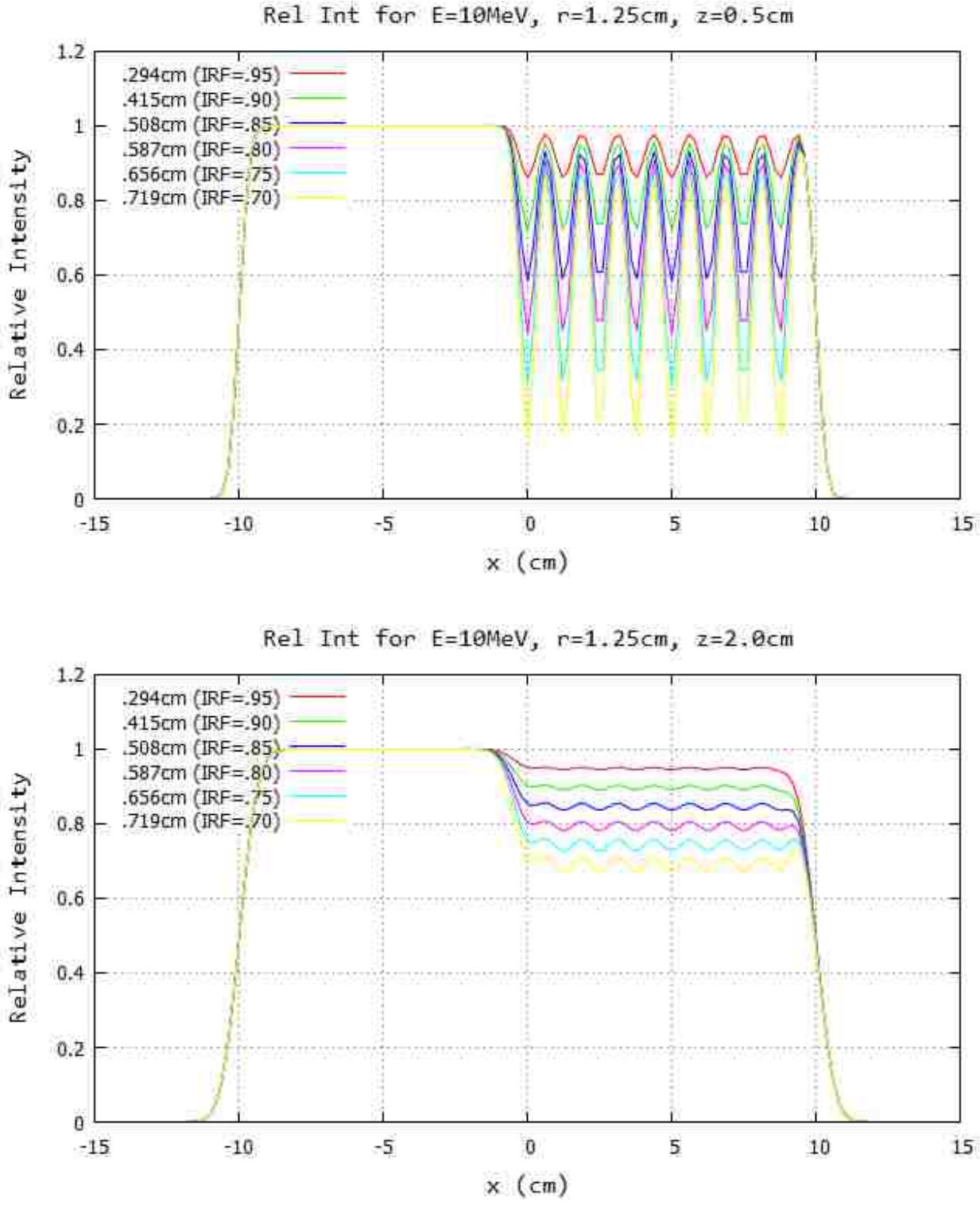


Figure B.14: Profile for 10 MeV and 100 cm SSD at y=0cm 20x20 half-blocked field. The computed island block diameter for 0.70, 0.75, 0.80, 0.85, 0.90, and 0.95 IRF values are listed in each plot's inserted key.

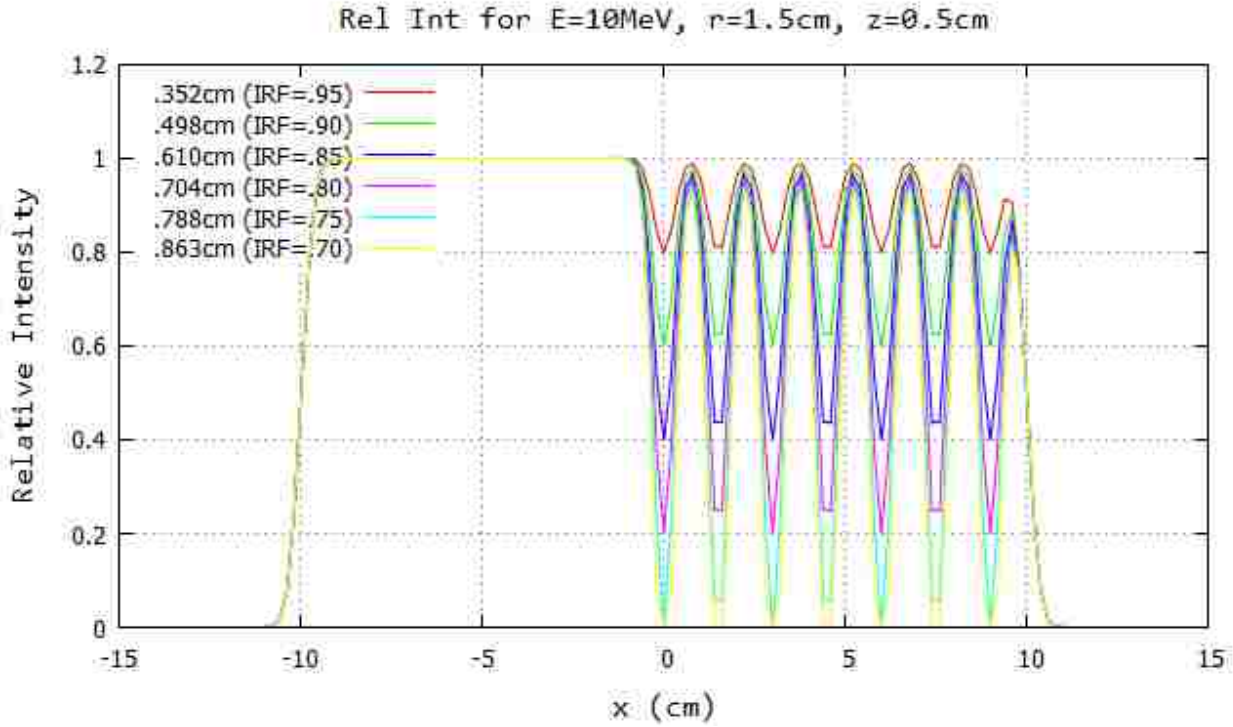


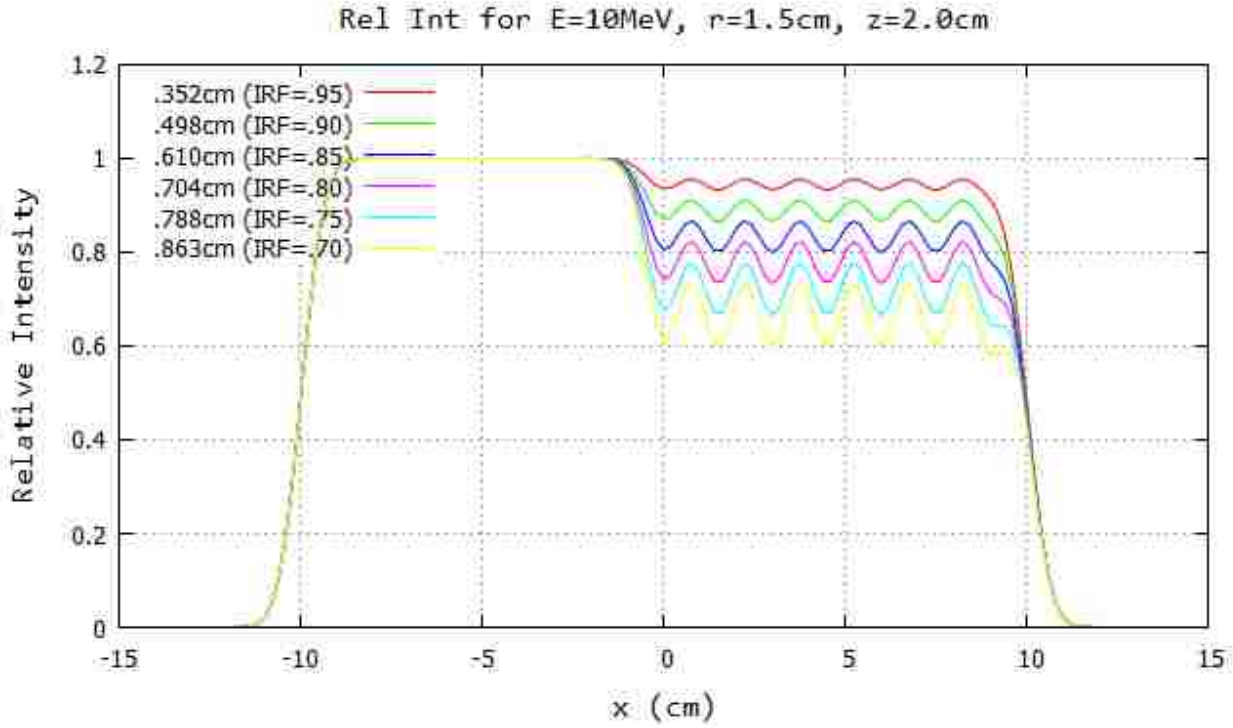


Figure B.15: Profile for 10 MeV and 100 cm SSD at y=0cm 20x20 half-blocked field. The computed island block diameter for 0.70, 0.75, 0.80, 0.85, 0.90, and 0.95 IRF values are listed in each plot's inserted key.

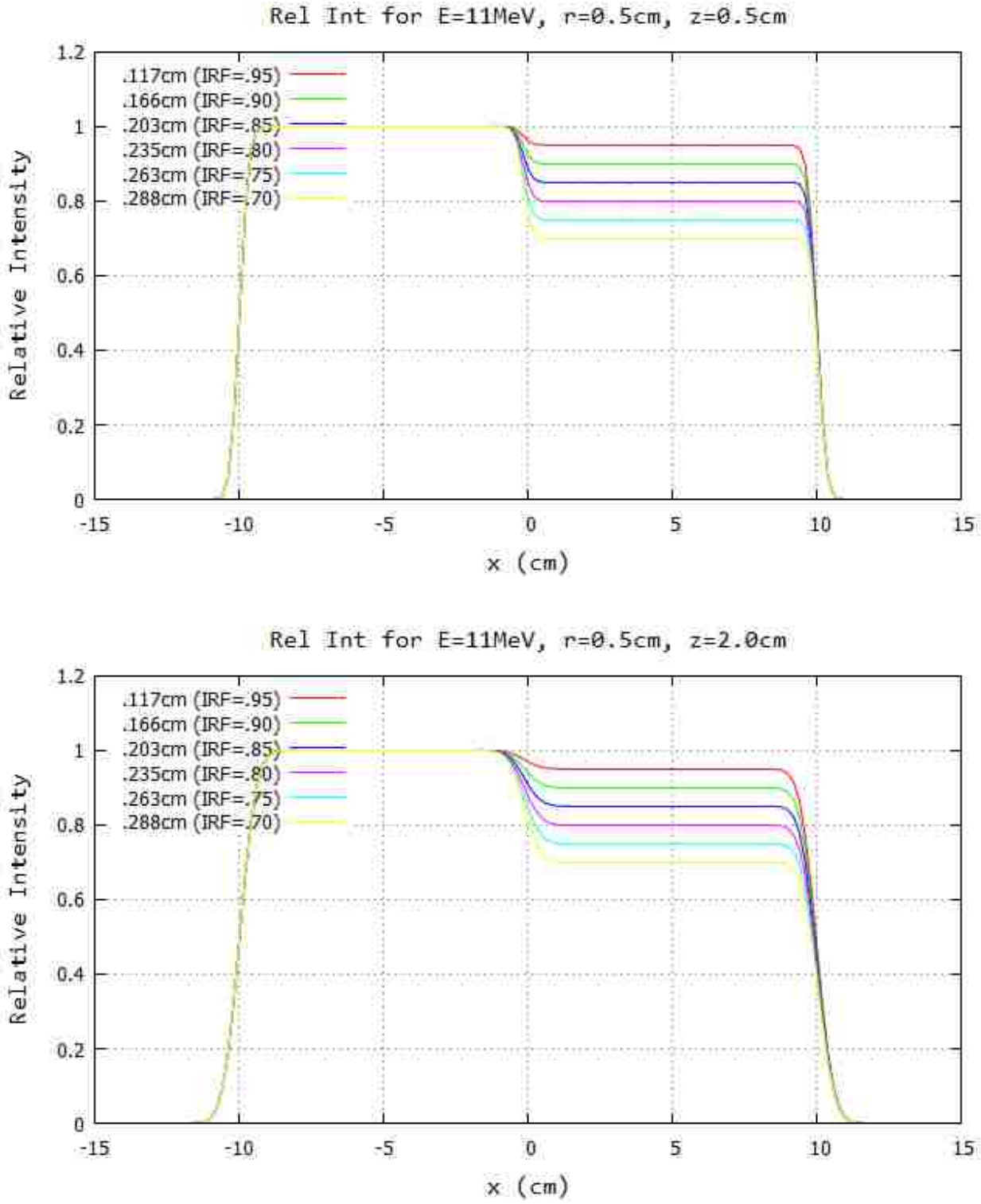


Figure B.16: Profile for 11 MeV and 100 cm SSD at y=0cm 20x20 half-blocked field. The computed island block diameter for 0.70, 0.75, 0.80, 0.85, 0.90, and 0.95 IRF values are listed in each plot's inserted key.

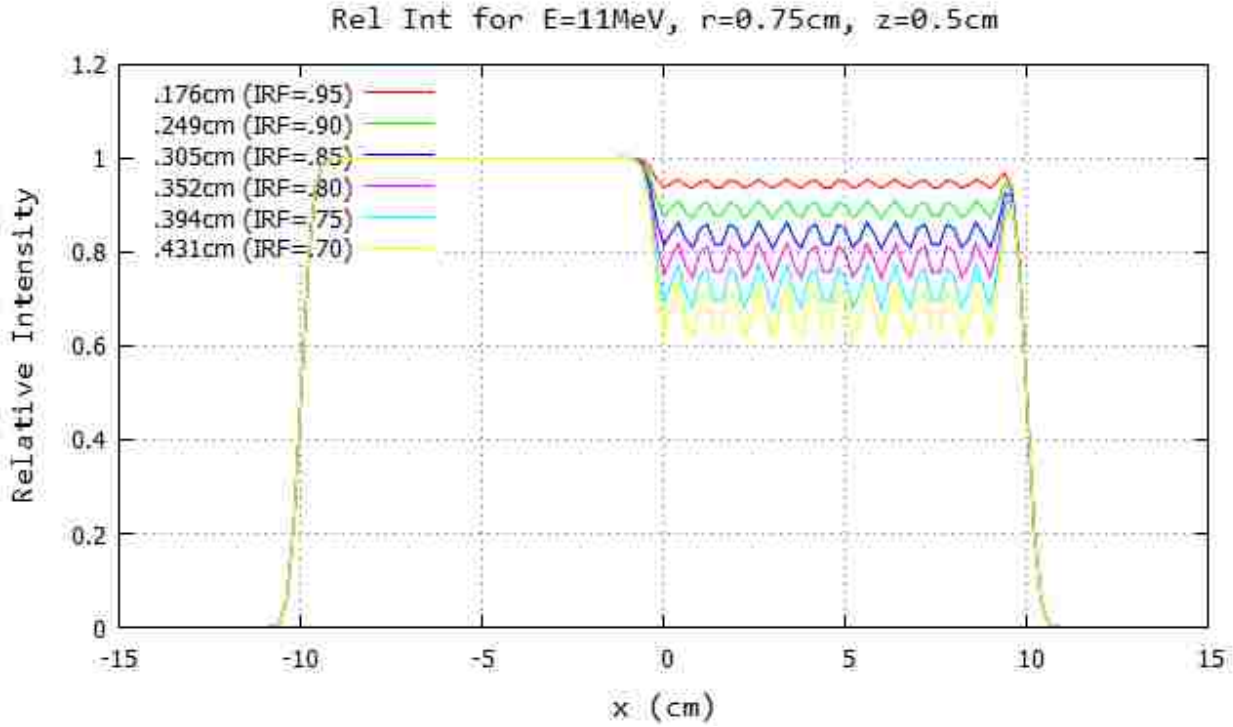


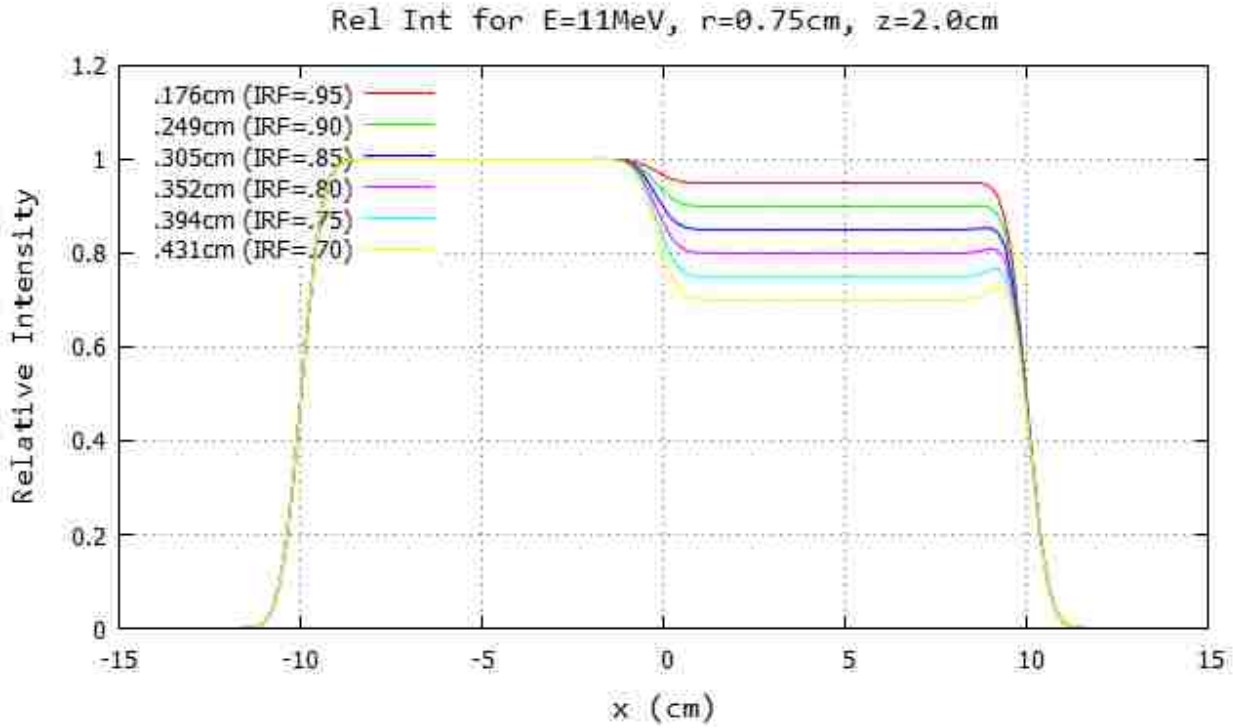


Figure B.17: Profile for 11 MeV and 100 cm SSD at y=0cm 20x20 half-blocked field. The computed island block diameter for 0.70, 0.75, 0.80, 0.85, 0.90, and 0.95 IRF values are listed in each plot's inserted key.

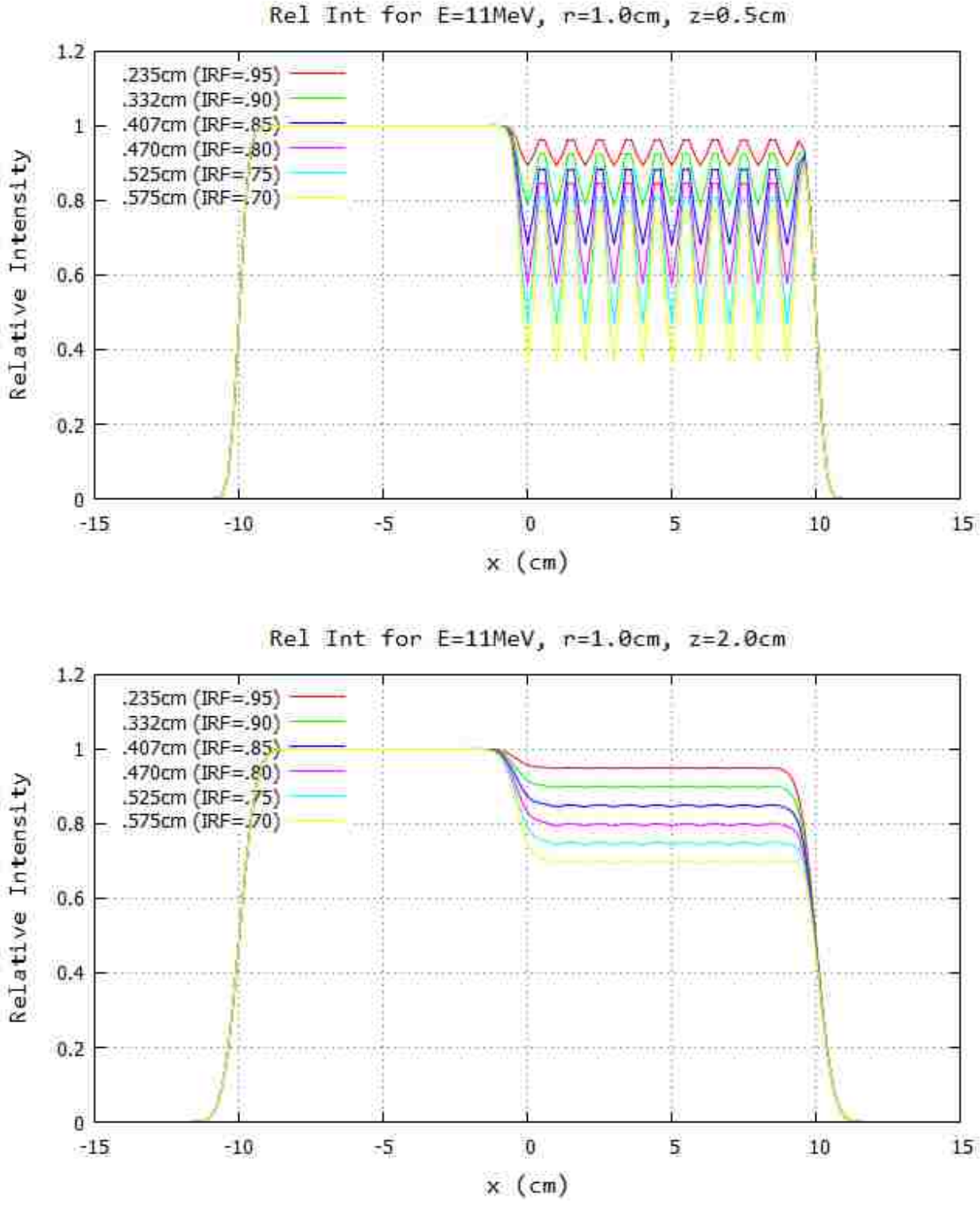


Figure B.18: Profile for 11 MeV and 100 cm SSD at y=0cm 20x20 half-blocked field. The computed island block diameter for 0.70, 0.75, 0.80, 0.85, 0.90, and 0.95 IRF values are listed in each plot's inserted key.

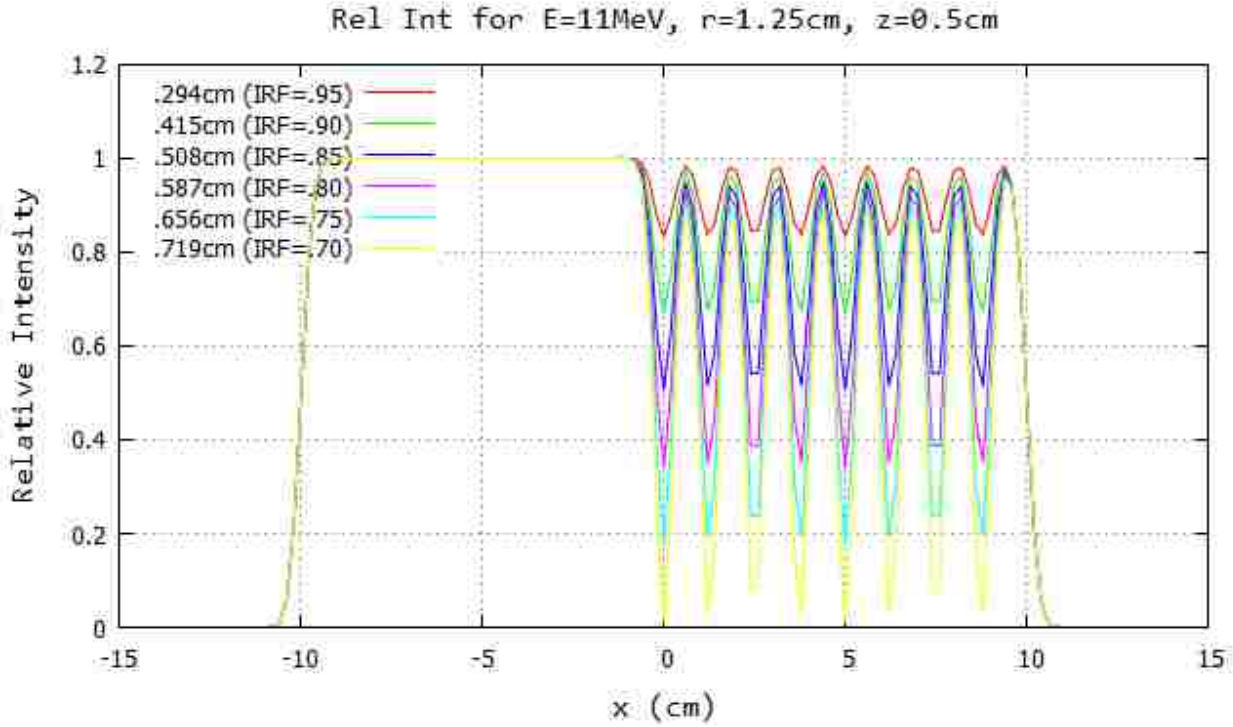


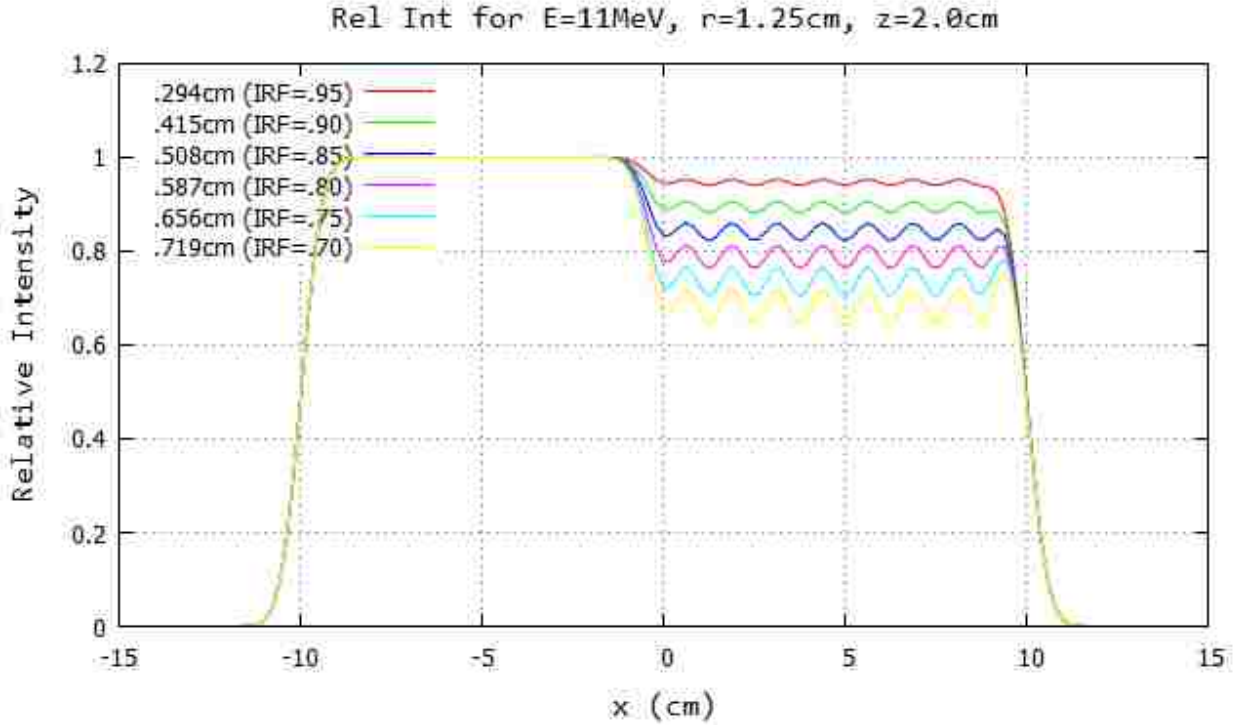


Figure B.19: Profile for 11 MeV and 100 cm SSD at y=0cm 20x20 half-blocked field. The computed island block diameter for 0.70, 0.75, 0.80, 0.85, 0.90, and 0.95 IRF values are listed in each plot's inserted key.

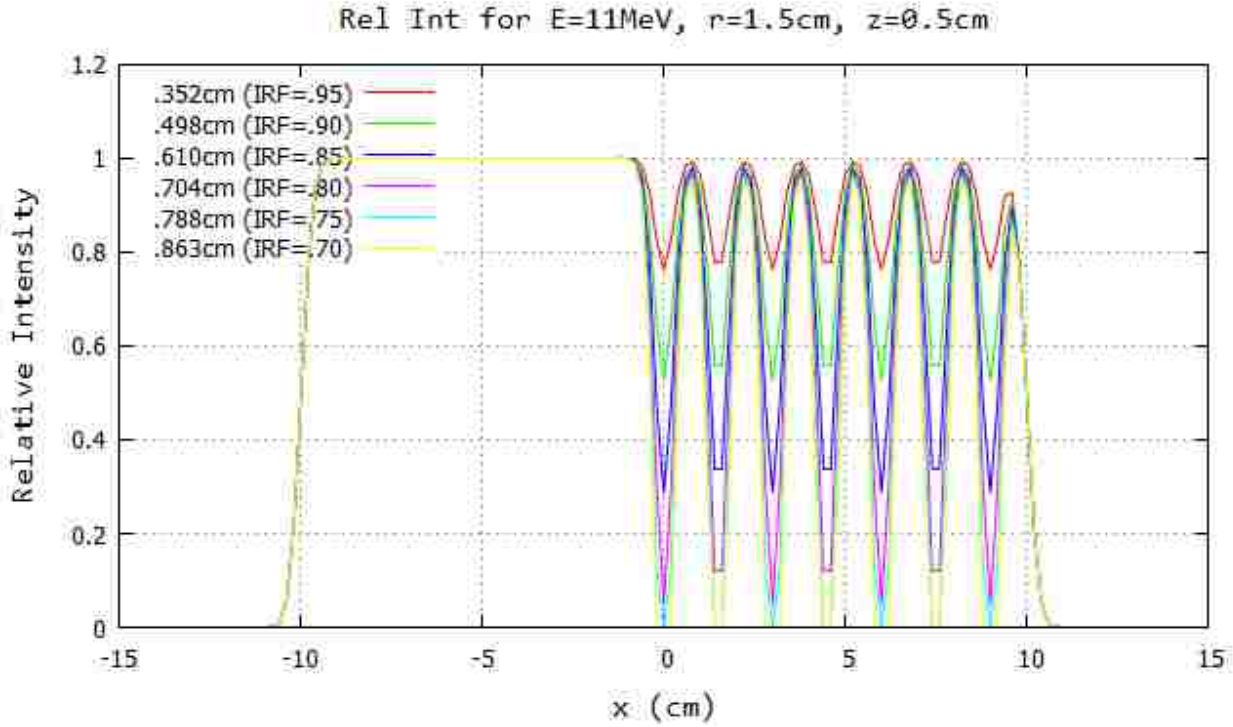


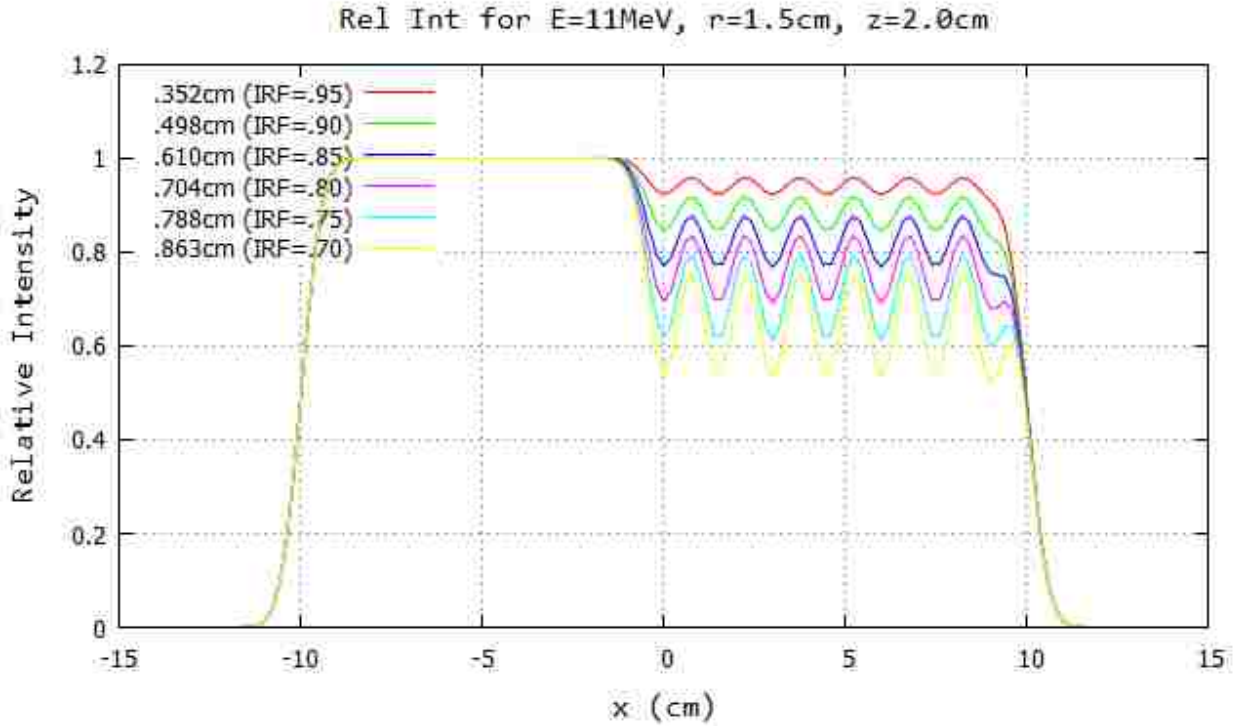


Figure B.20: Profile for 11 MeV and 100 cm SSD at y=0cm 20x20 half-blocked field. The computed island block diameter for 0.70, 0.75, 0.80, 0.85, 0.90, and 0.95 IRF values are listed in each plot's inserted key.

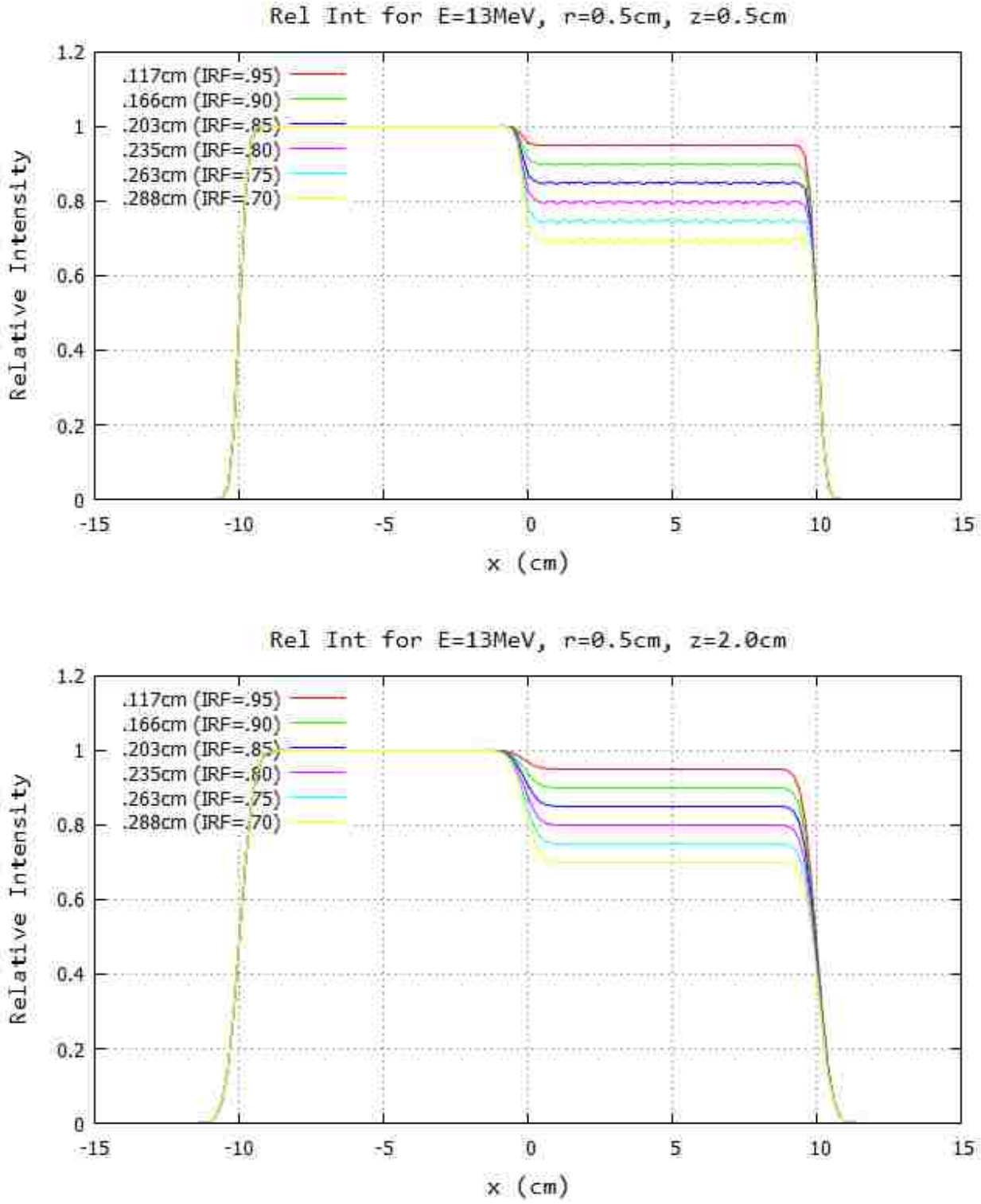


Figure B.21: Profile for 13 MeV and 100 cm SSD at y=0cm 20x20 half-blocked field. The computed island block diameter for 0.70, 0.75, 0.80, 0.85, 0.90, and 0.95 IRF values are listed in each plot's inserted key.

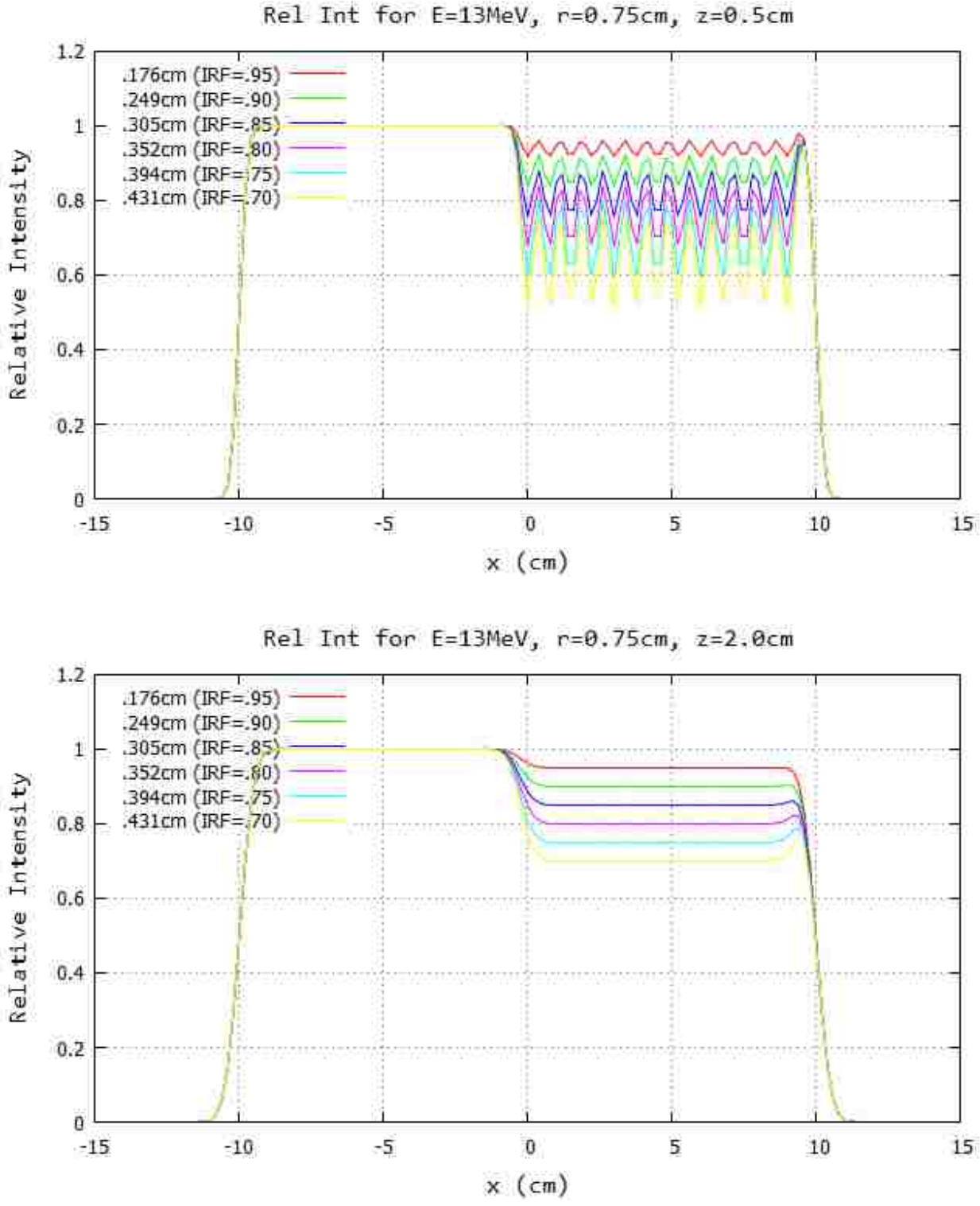


Figure B.22: Profile for 13 MeV and 100 cm SSD at y=0cm 20x20 half-blocked field. The computed island block diameter for 0.70, 0.75, 0.80, 0.85, 0.90, and 0.95 IRF values are listed in each plot's inserted key.

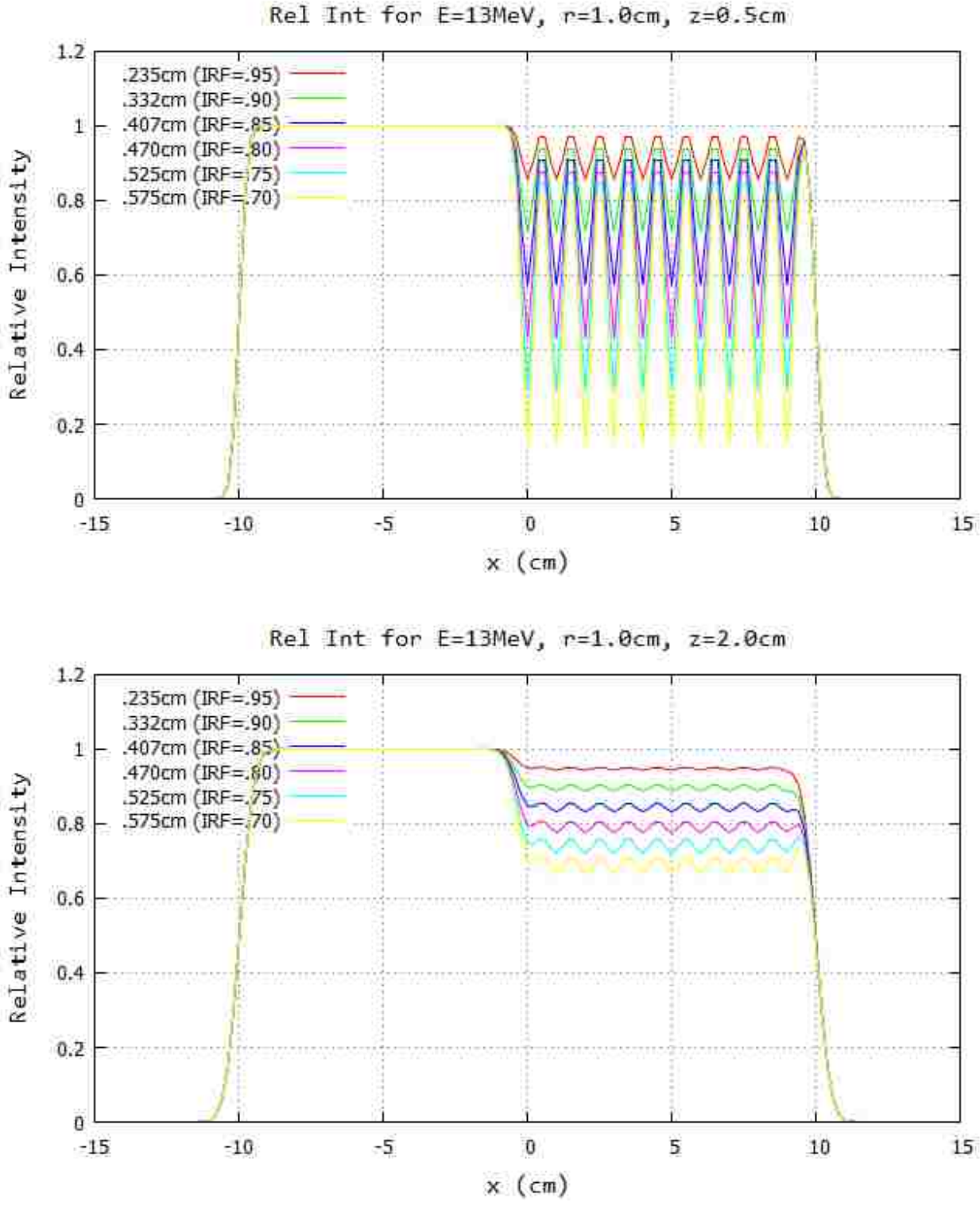


Figure B.23: Profile for 13 MeV and 100 cm SSD at y=0cm 20x20 half-blocked field. The computed island block diameter for 0.70, 0.75, 0.80, 0.85, 0.90, and 0.95 IRF values are listed in each plot's inserted key.

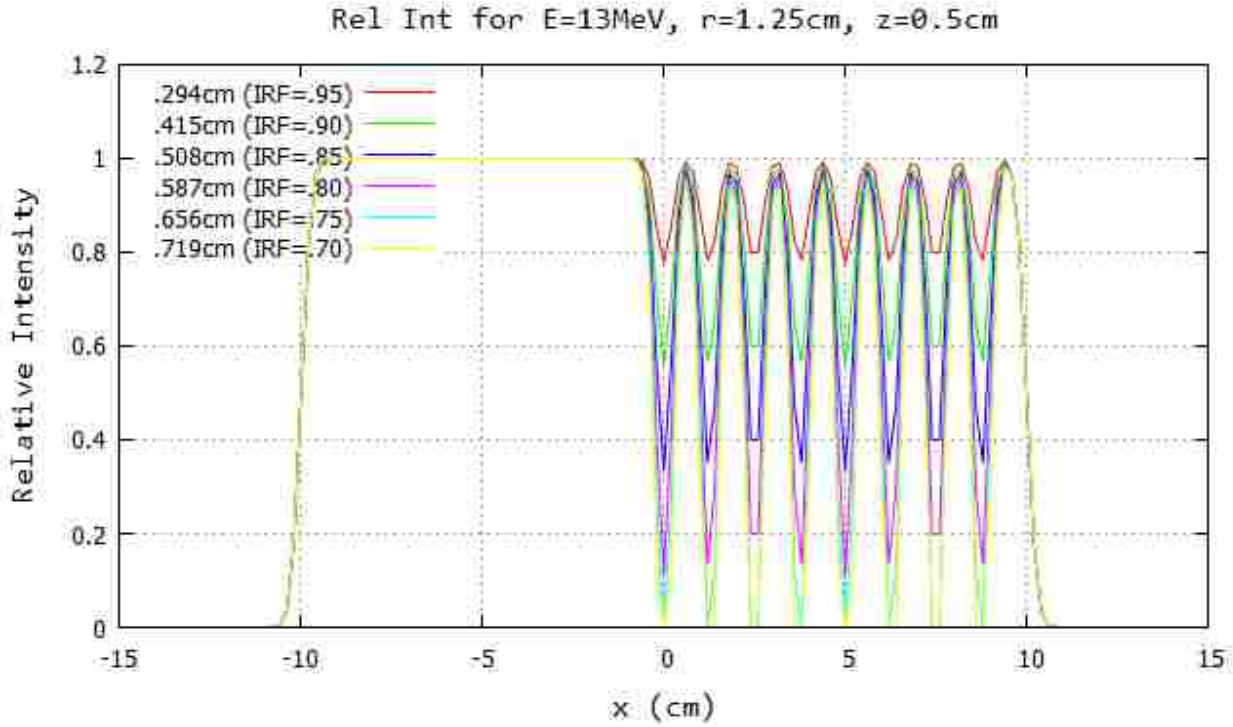


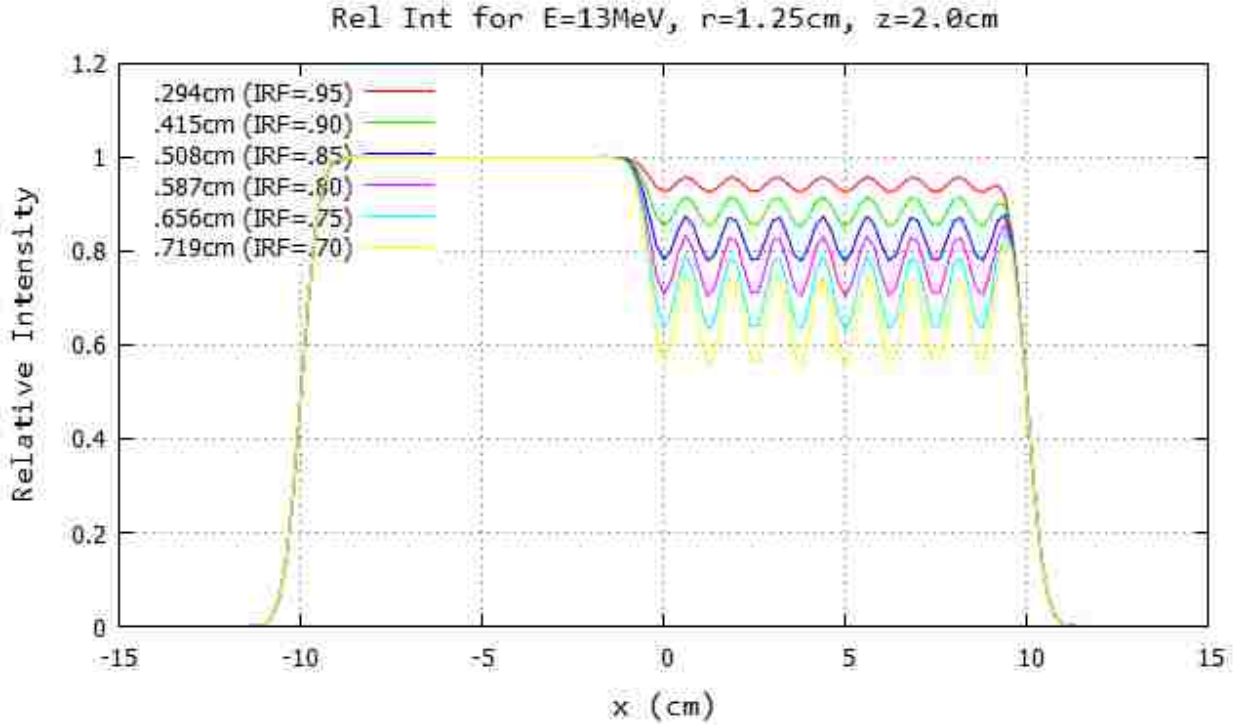


Figure B.24: Profile for 13 MeV and 100 cm SSD at y=0cm 20x20 half-blocked field. The computed island block diameter for 0.70, 0.75, 0.80, 0.85, 0.90, and 0.95 IRF values are listed in each plot's inserted key.

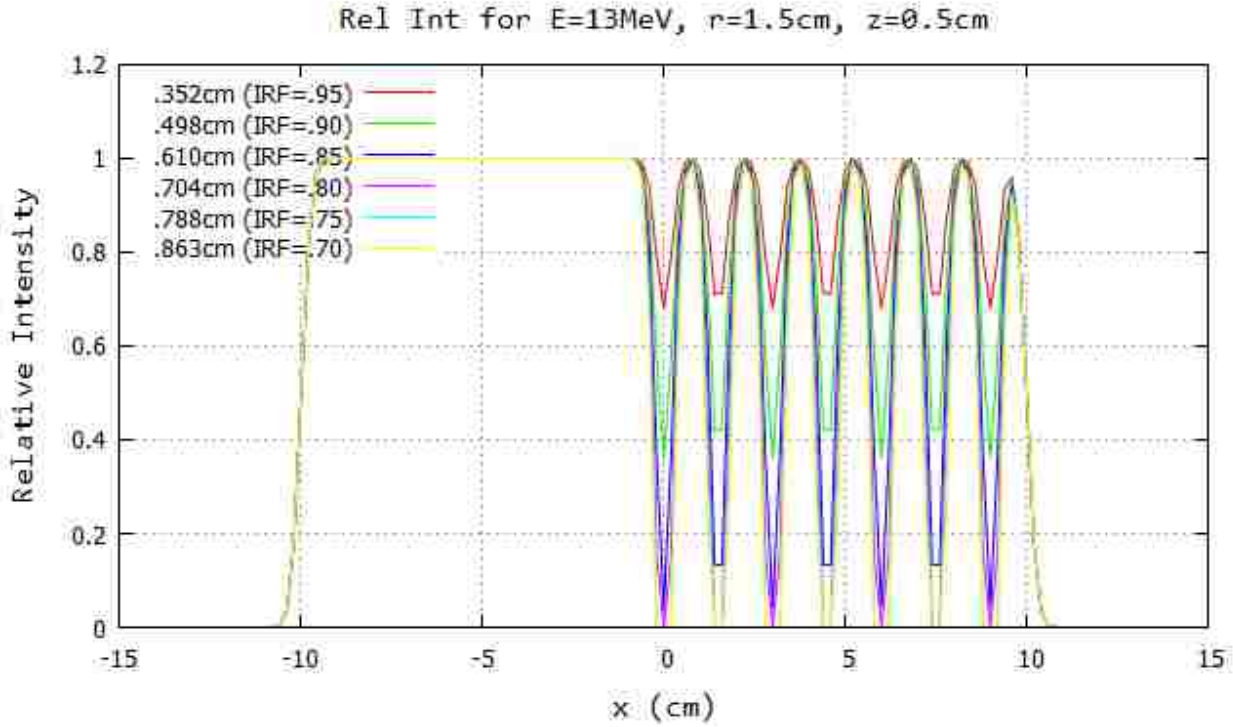


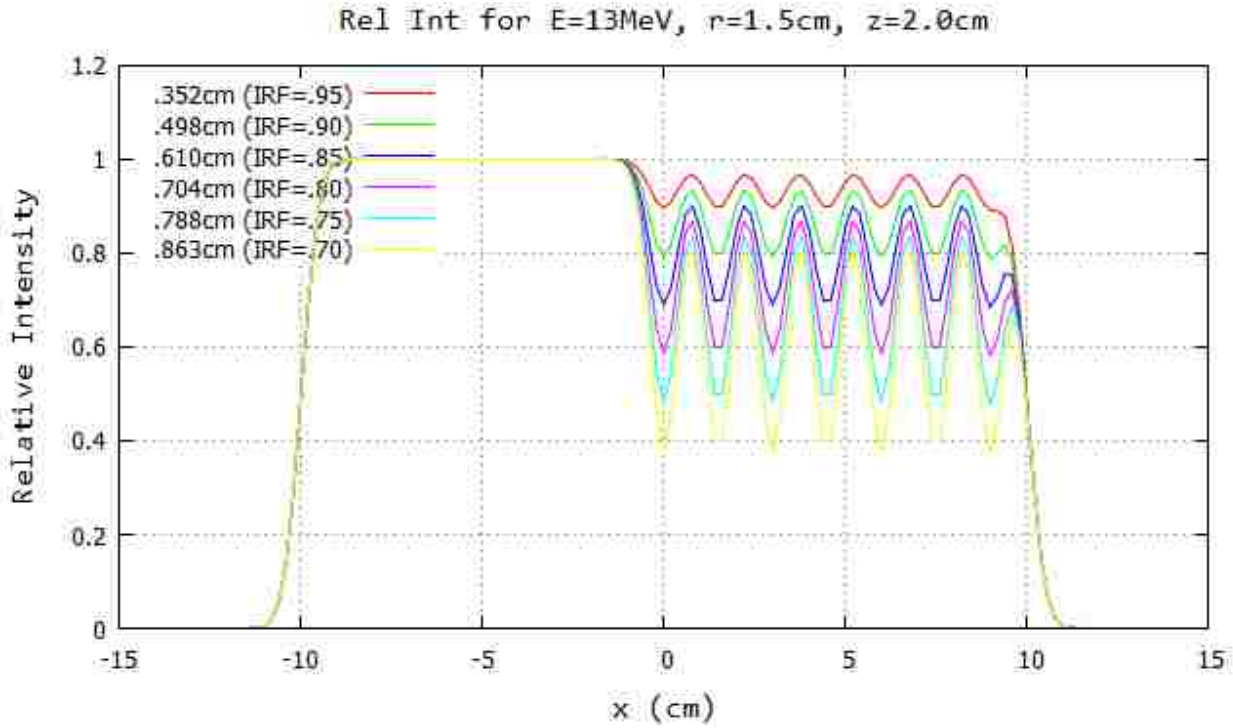


Figure B.25: Profile for 13 MeV and 100 cm SSD at y=0cm 20x20 half-blocked field. The computed island block diameter for 0.70, 0.75, 0.80, 0.85, 0.90, and 0.95 IRF values are listed in each plot's inserted key.

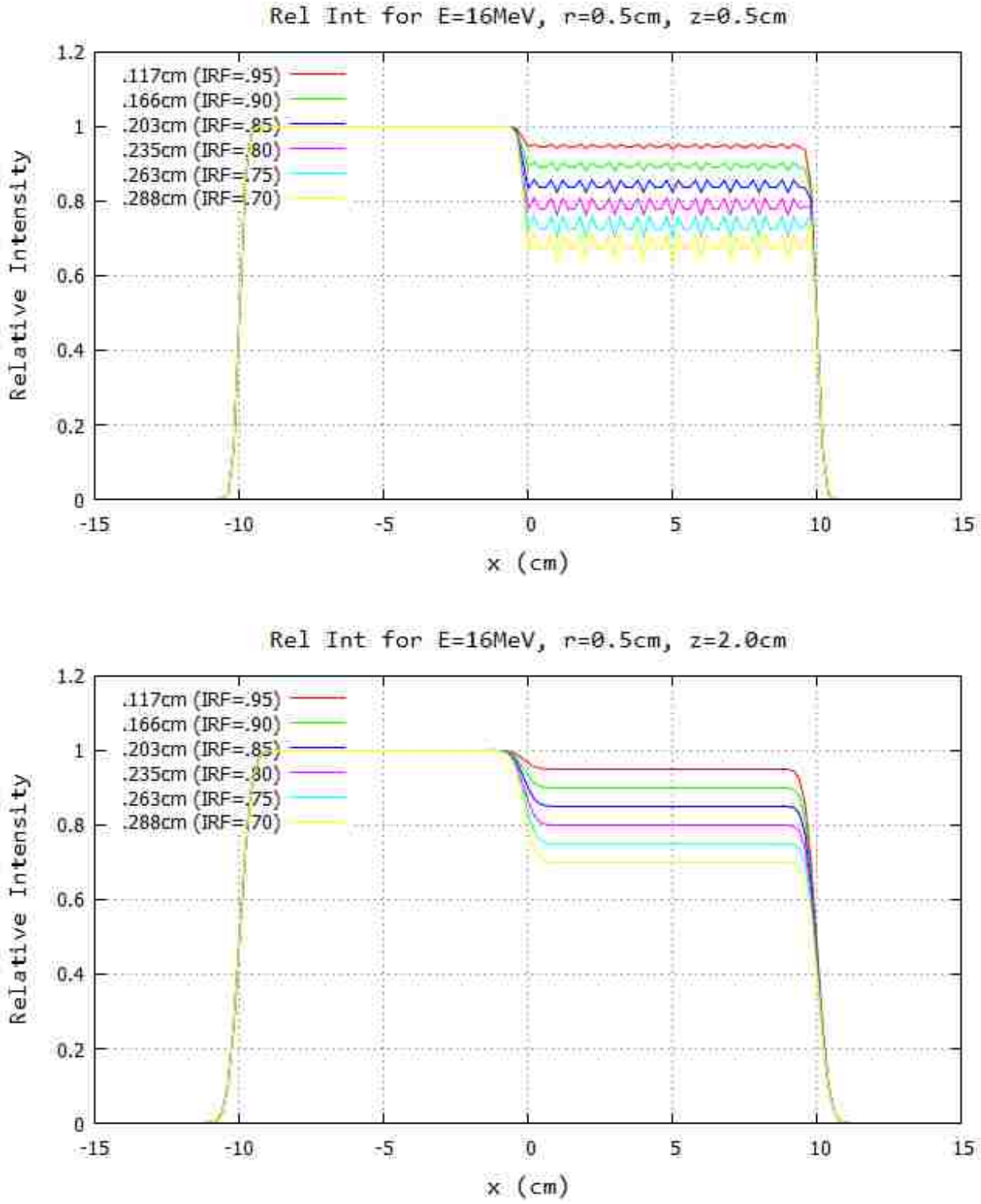


Figure B.26: Profile for 16 MeV and 100 cm SSD at y=0cm 20x20 half-blocked field. The computed island block diameter for 0.70, 0.75, 0.80, 0.85, 0.90, and 0.95 IRF values are listed in each plot's inserted key.

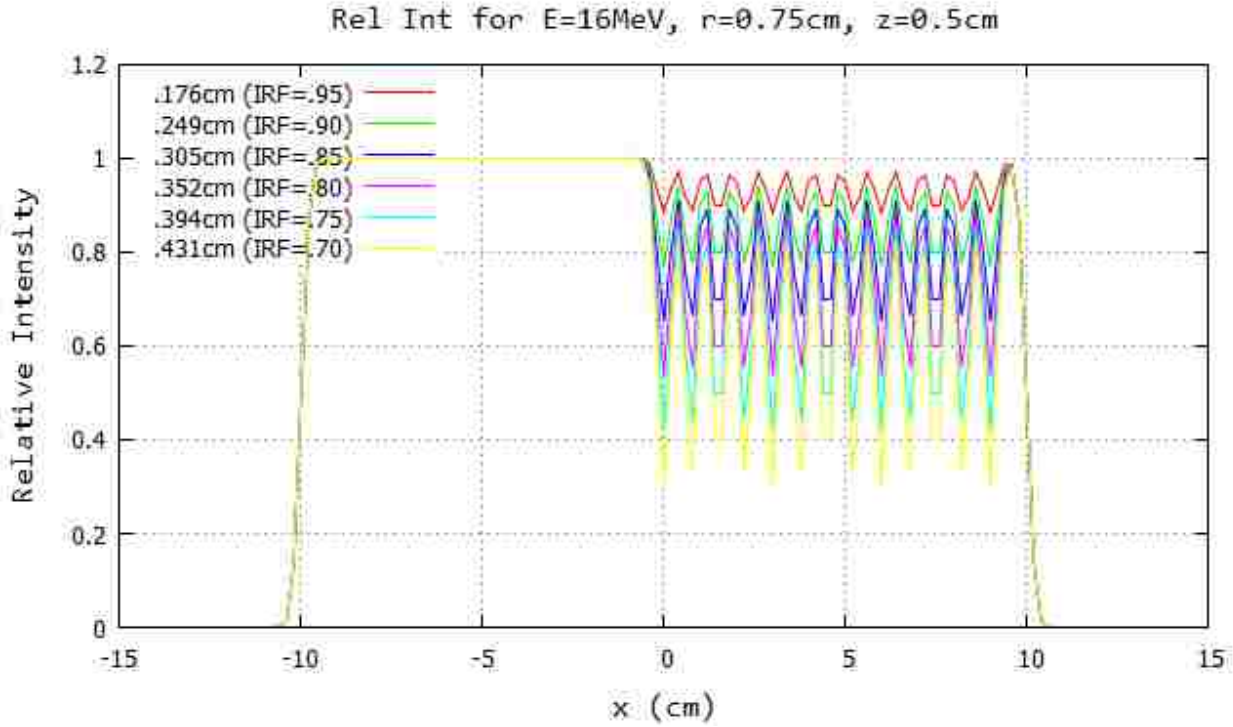


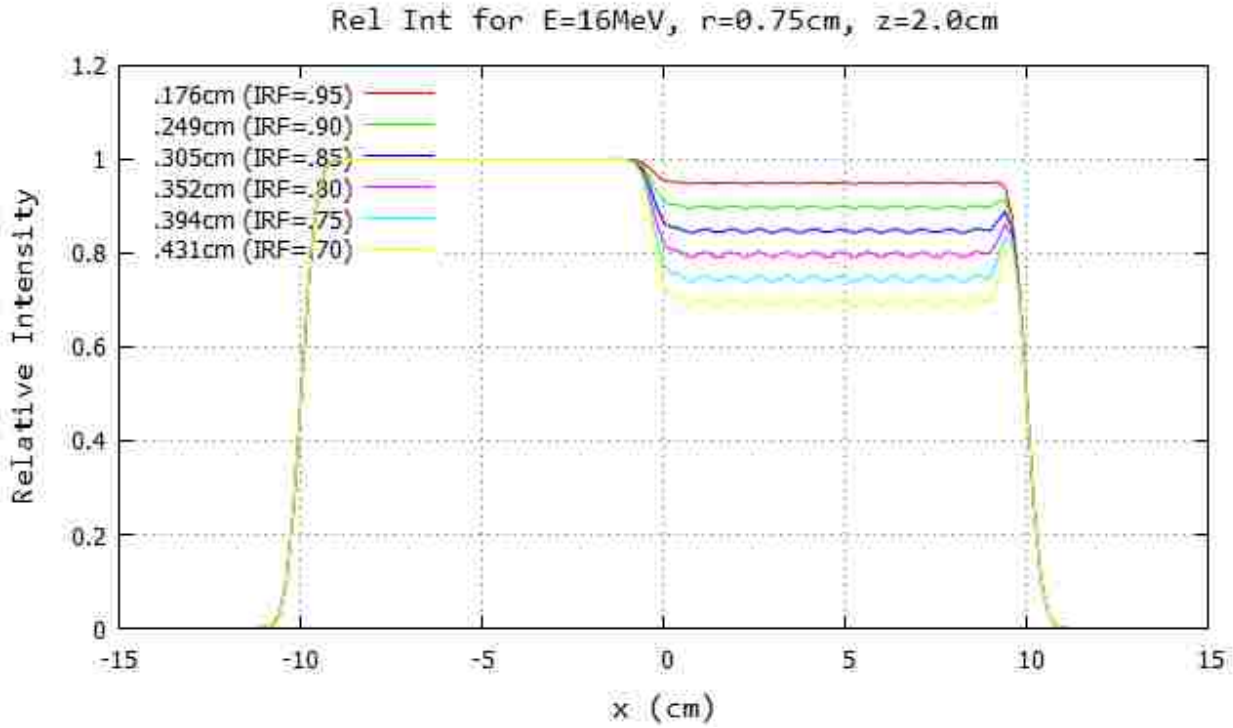


Figure B.27: Profile for 16 MeV and 100 cm SSD at y=0cm 20x20 half-blocked field. The computed island block diameter for 0.70, 0.75, 0.80, 0.85, 0.90, and 0.95 IRF values are listed in each plot's inserted key.

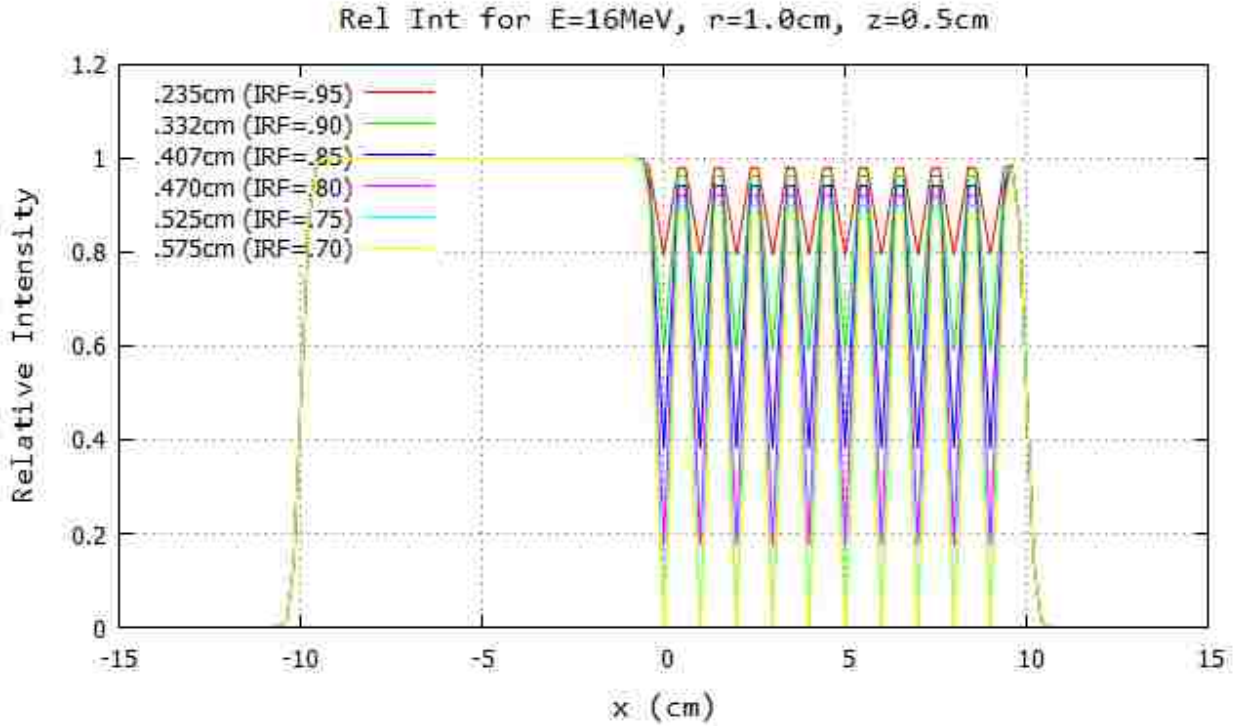


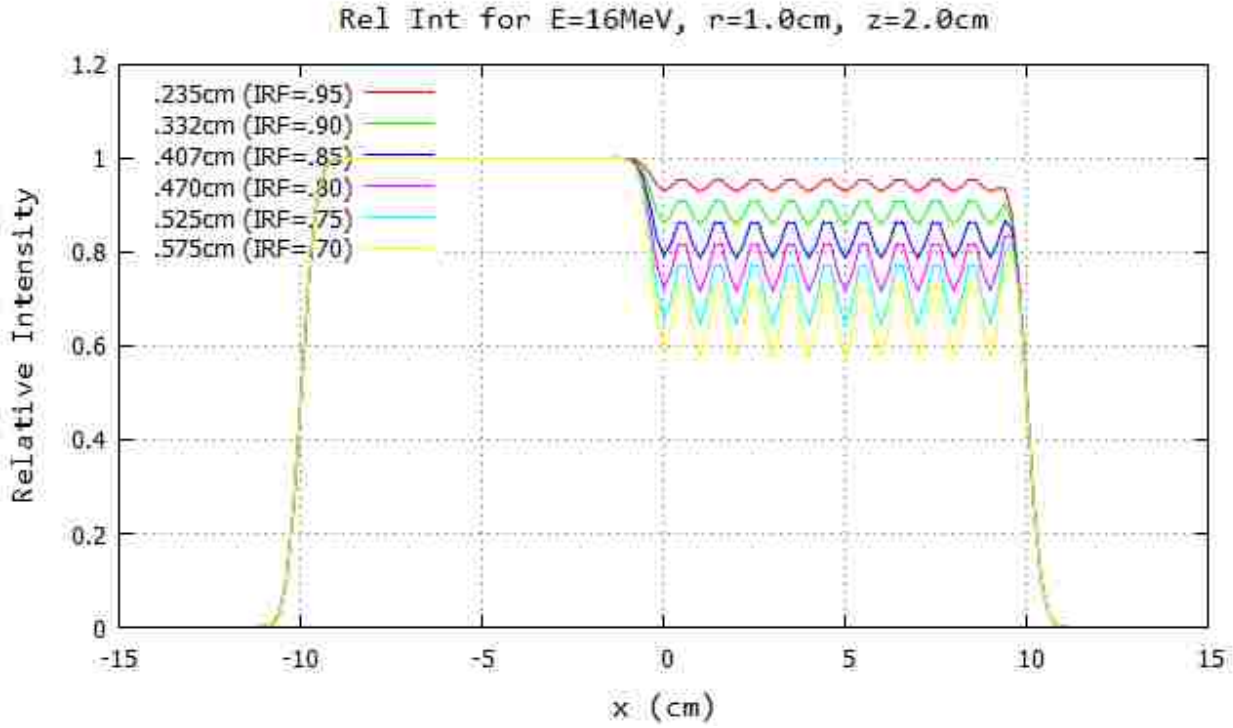


Figure B.28: Profile for 16 MeV and 100 cm SSD at y=0cm 20x20 half-blocked field. The computed island block diameter for 0.70, 0.75, 0.80, 0.85, 0.90, and 0.95 IRF values are listed in each plot's inserted key.

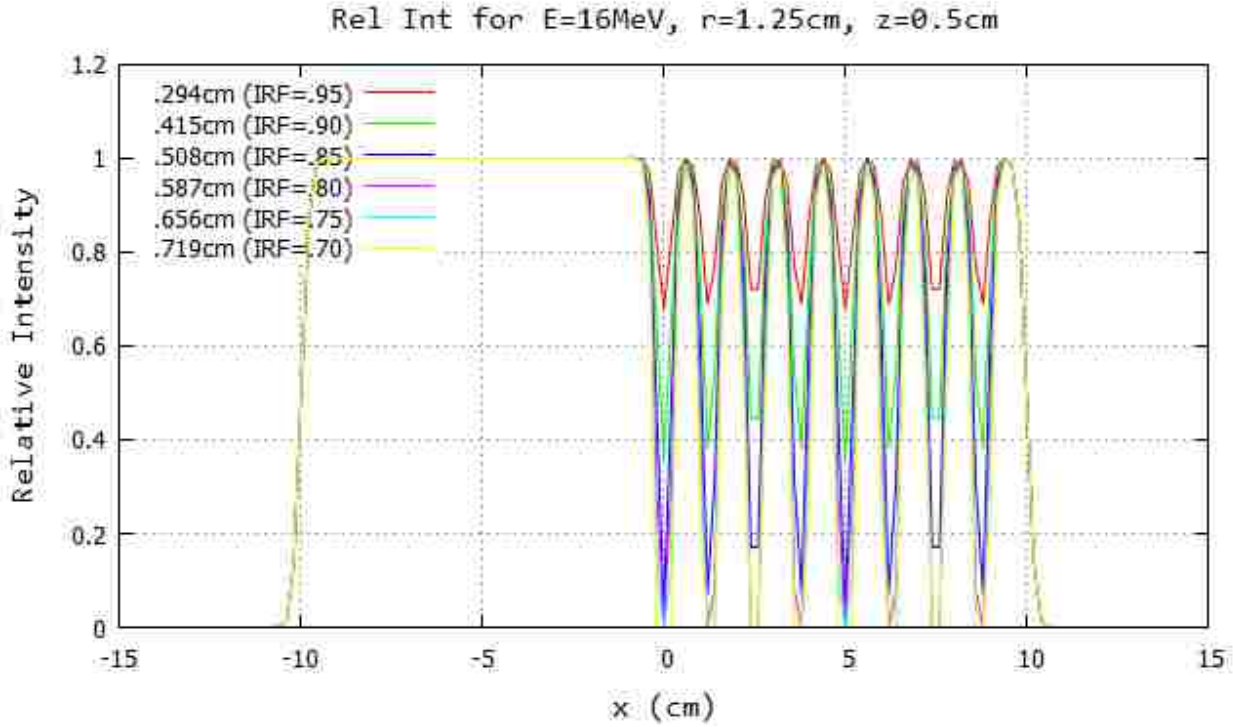


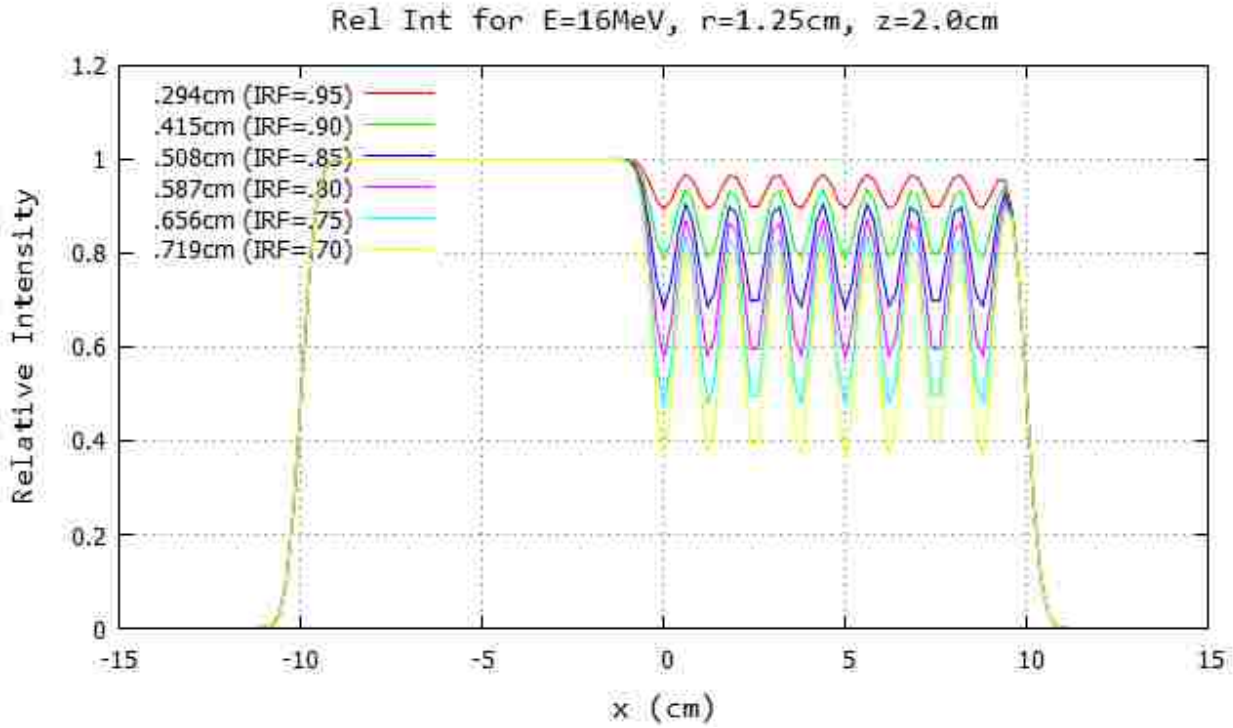


Figure B.29: Profile for 16 MeV and 100 cm SSD at y=0cm 20x20 half-blocked field. The computed island block diameter for 0.70, 0.75, 0.80, 0.85, 0.90, and 0.95 IRF values are listed in each plot's inserted key.

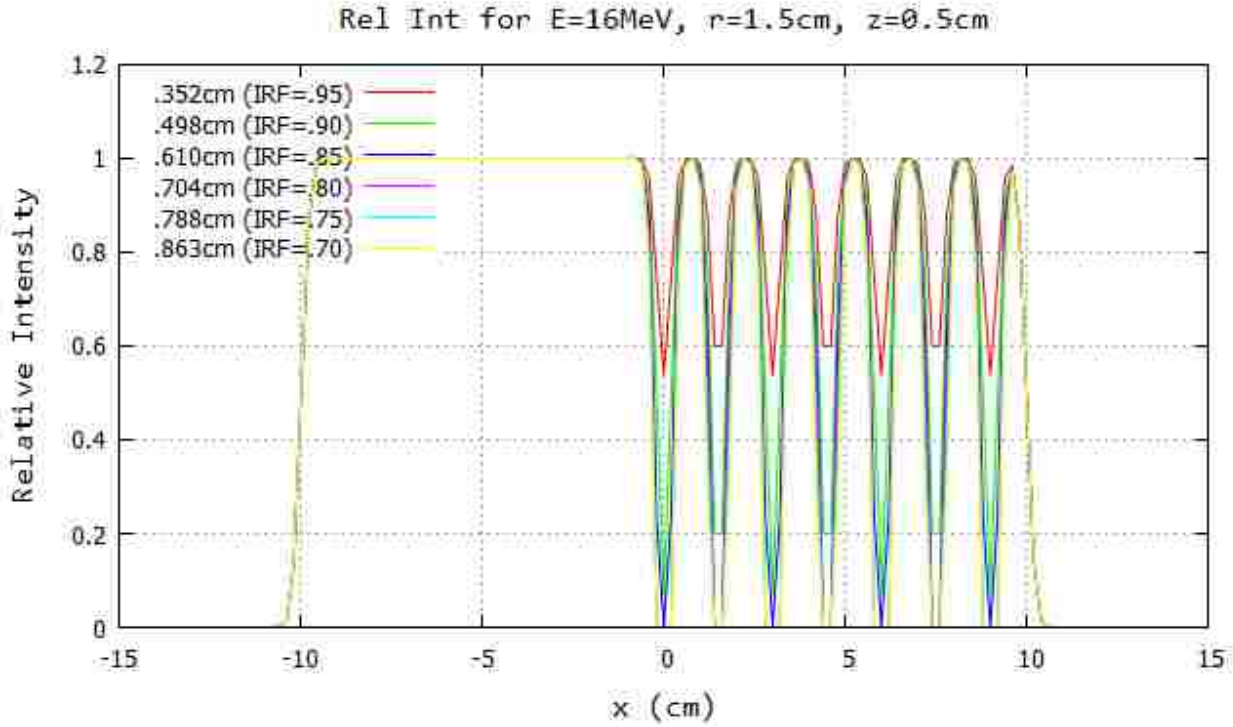


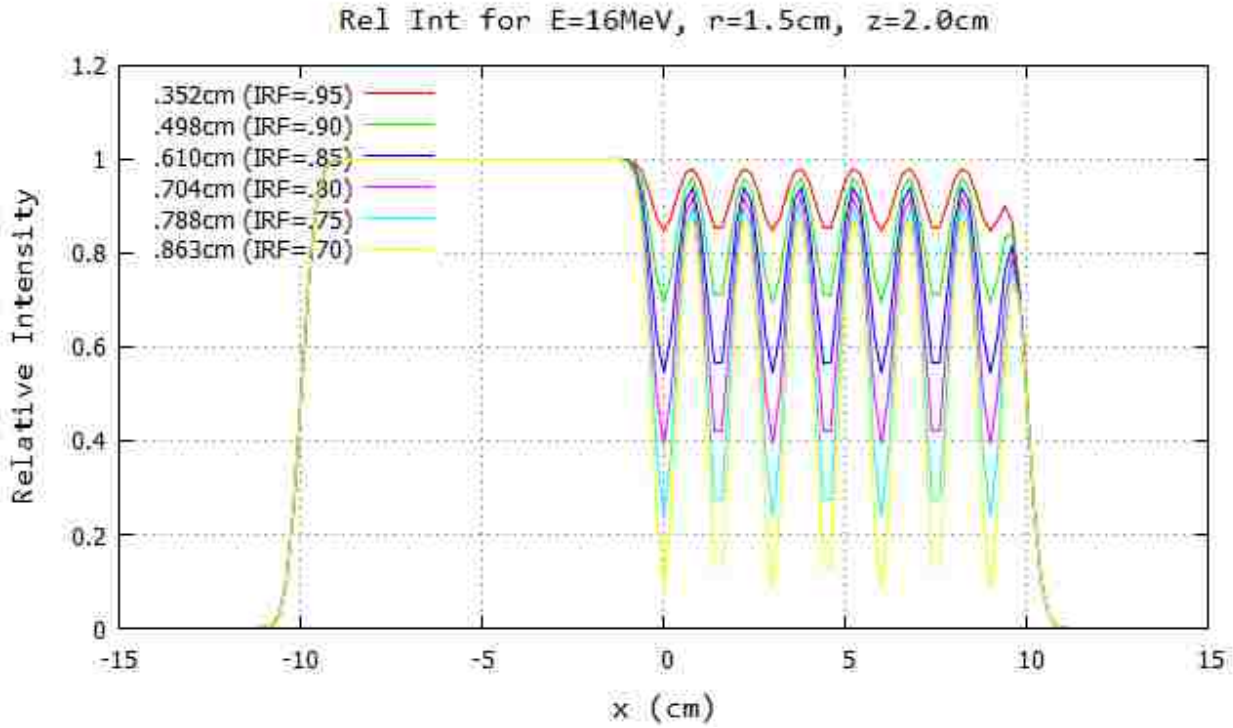


Figure B.30: Profile for 16 MeV and 100 cm SSD at y=0cm 20x20 half-blocked field. The computed island block diameter for 0.70, 0.75, 0.80, 0.85, 0.90, and 0.95 IRF values are listed in each plot's inserted key.

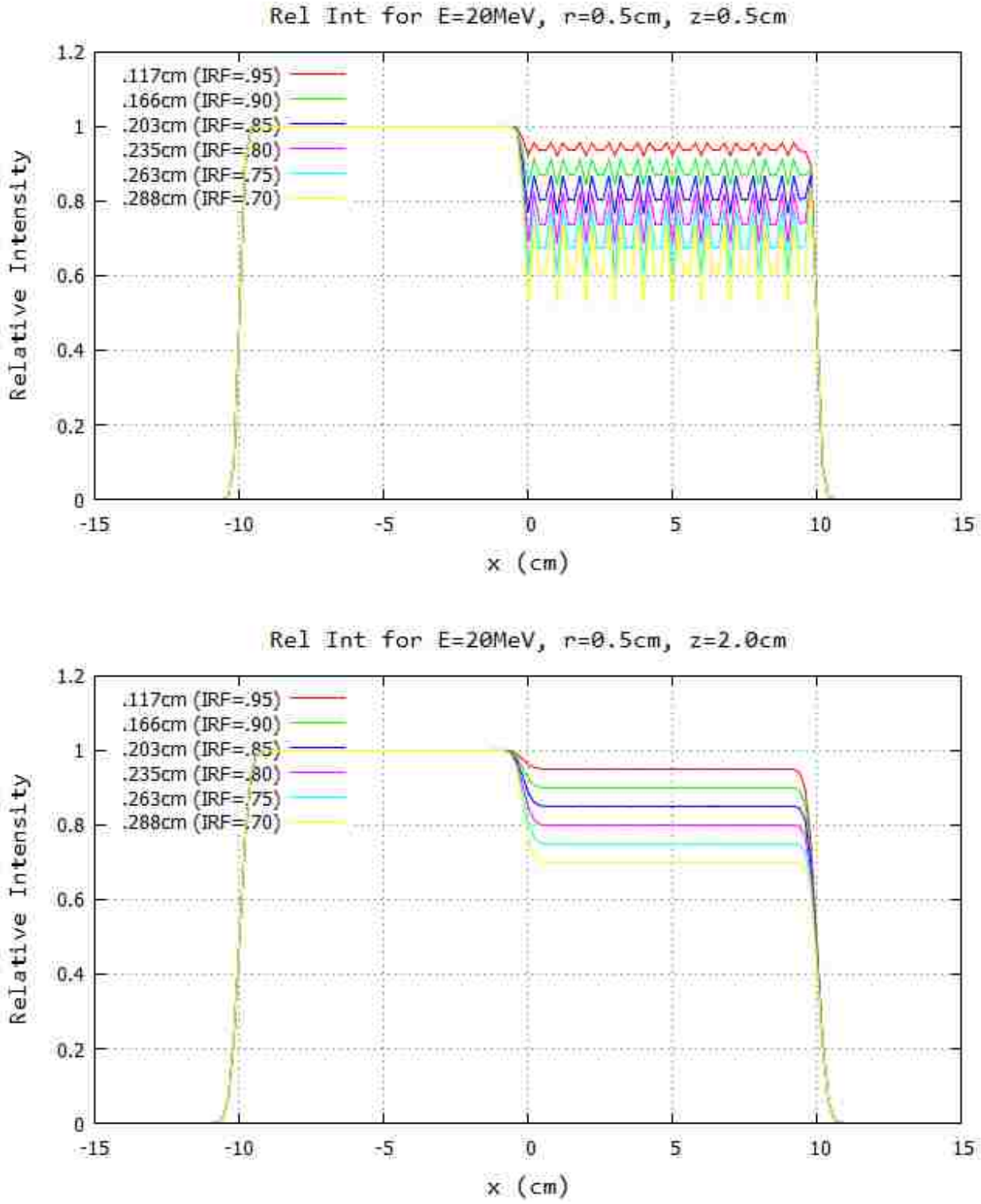


Figure B.31: Profile for 20 MeV and 100 cm SSD at y=0cm 20x20 half-blocked field. The computed island block diameter for 0.70, 0.75, 0.80, 0.85, 0.90, and 0.95 IRF values are listed in each plot's inserted key.

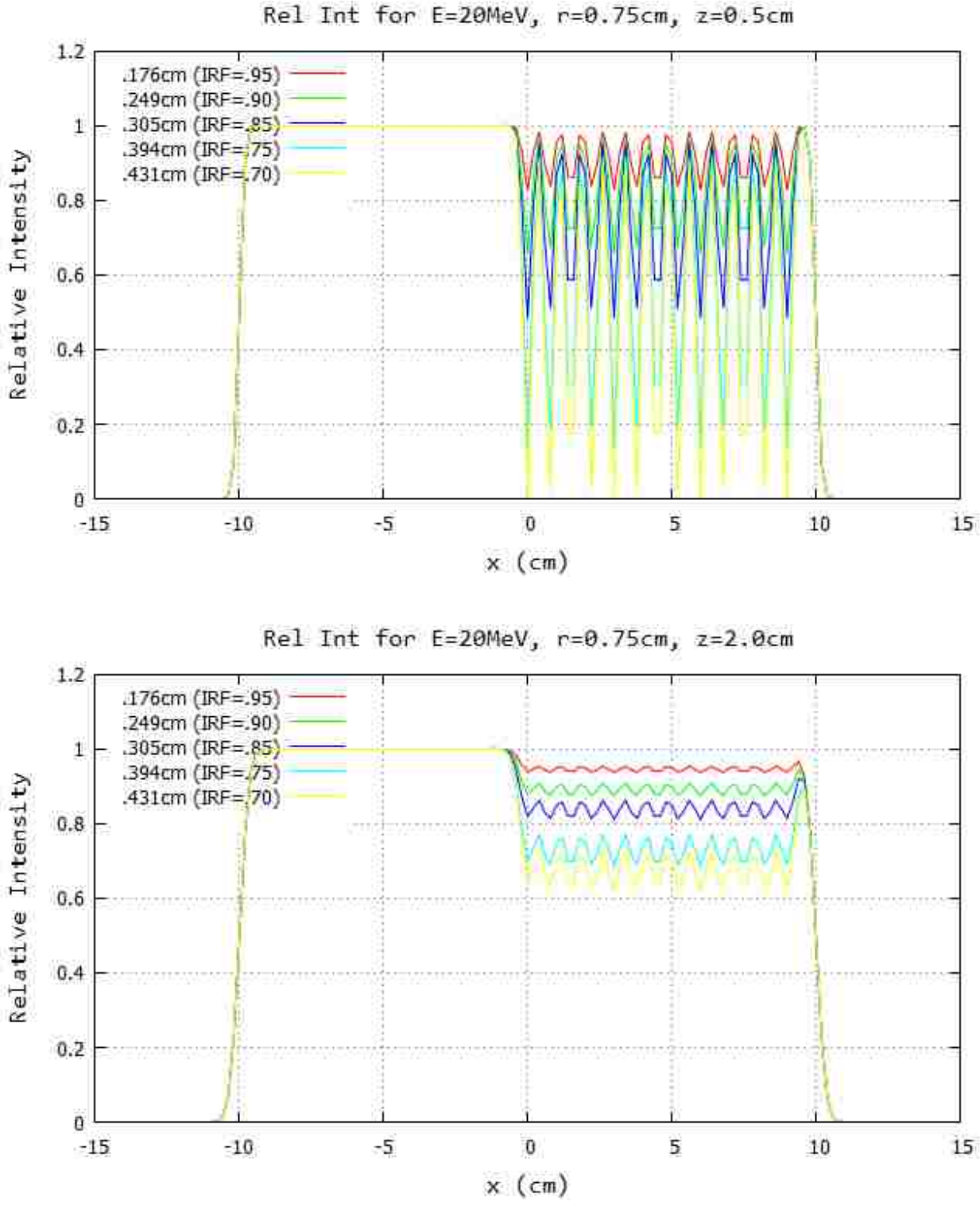


Figure B.32: Profile for 16 MeV and 100 cm SSD at y=0cm 20x20 half-blocked field. The computed island block diameter for 0.70, 0.75, 0.80, 0.85, 0.90, and 0.95 IRF values are listed in each plot's inserted key.

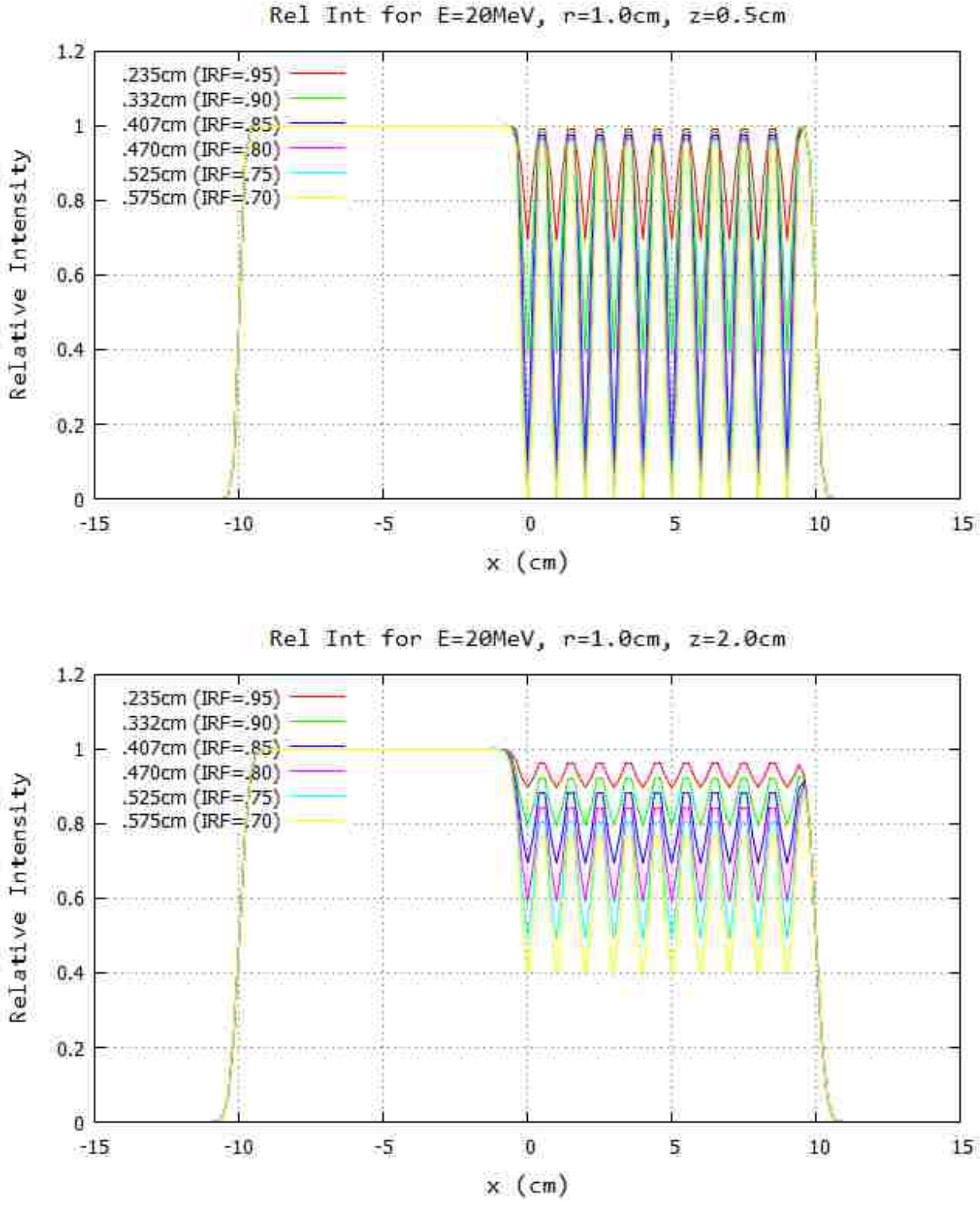


Figure B.33: Profile for 16 MeV and 100 cm SSD at y=0cm 20x20 half-blocked field. The computed island block diameter for 0.70, 0.75, 0.80, 0.85, 0.90, and 0.95 IRF values are listed in each plot's inserted key.

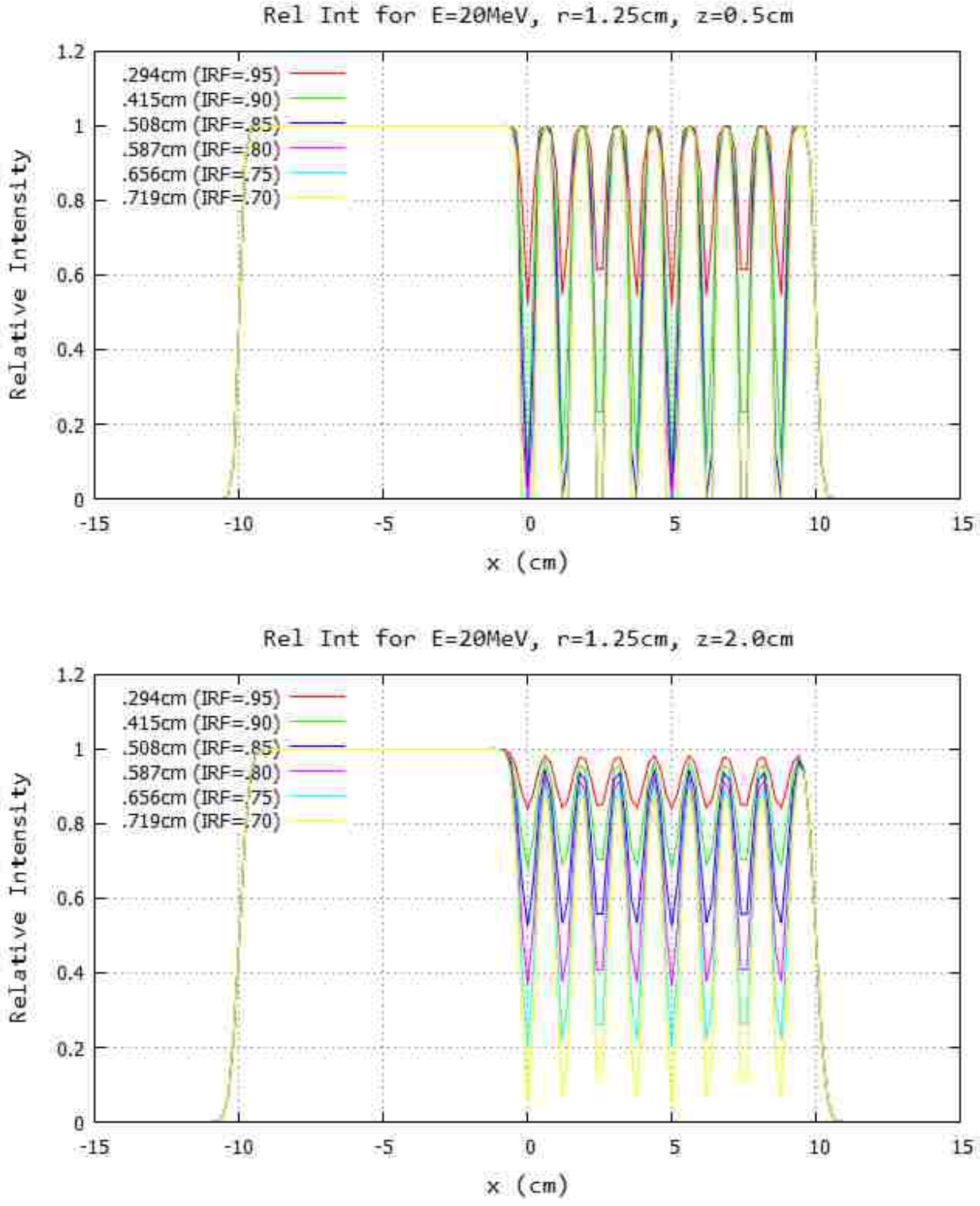


Figure B.34: Profile for 16 MeV and 100 cm SSD at y=0cm 20x20 half-blocked field. The computed island block diameter for 0.70, 0.75, 0.80, 0.85, 0.90, and 0.95 IRF values are listed in each plot's inserted key.

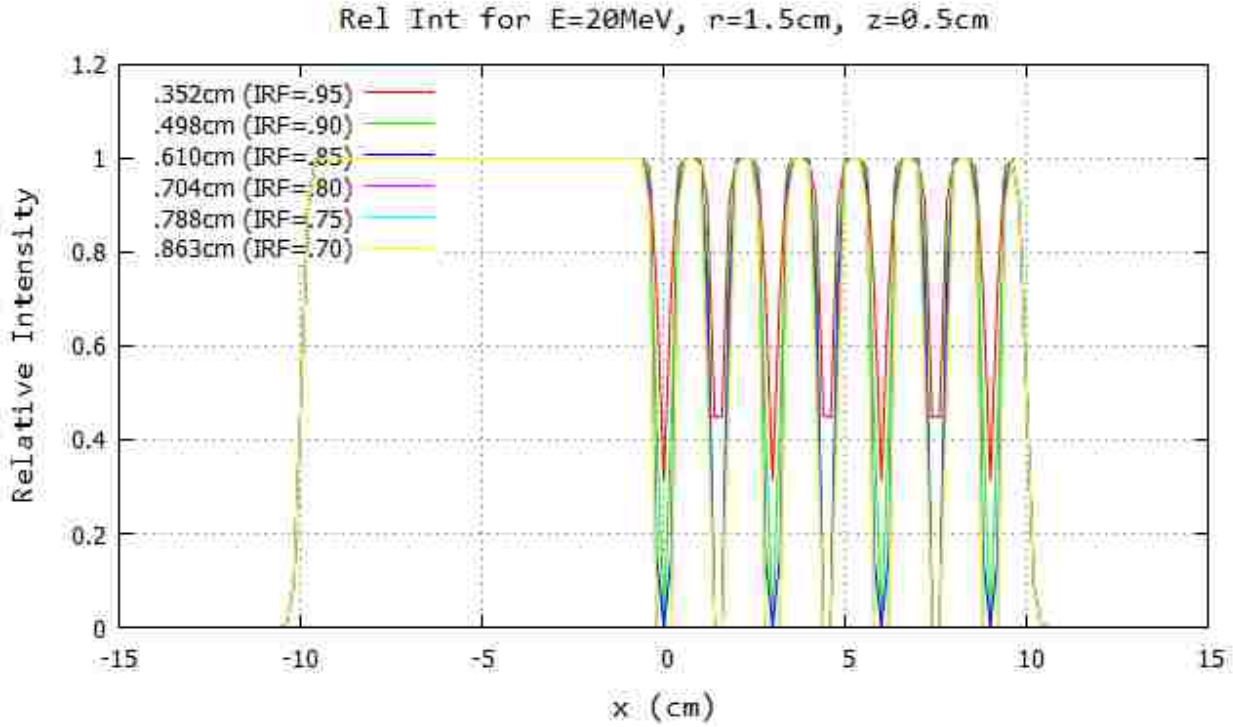


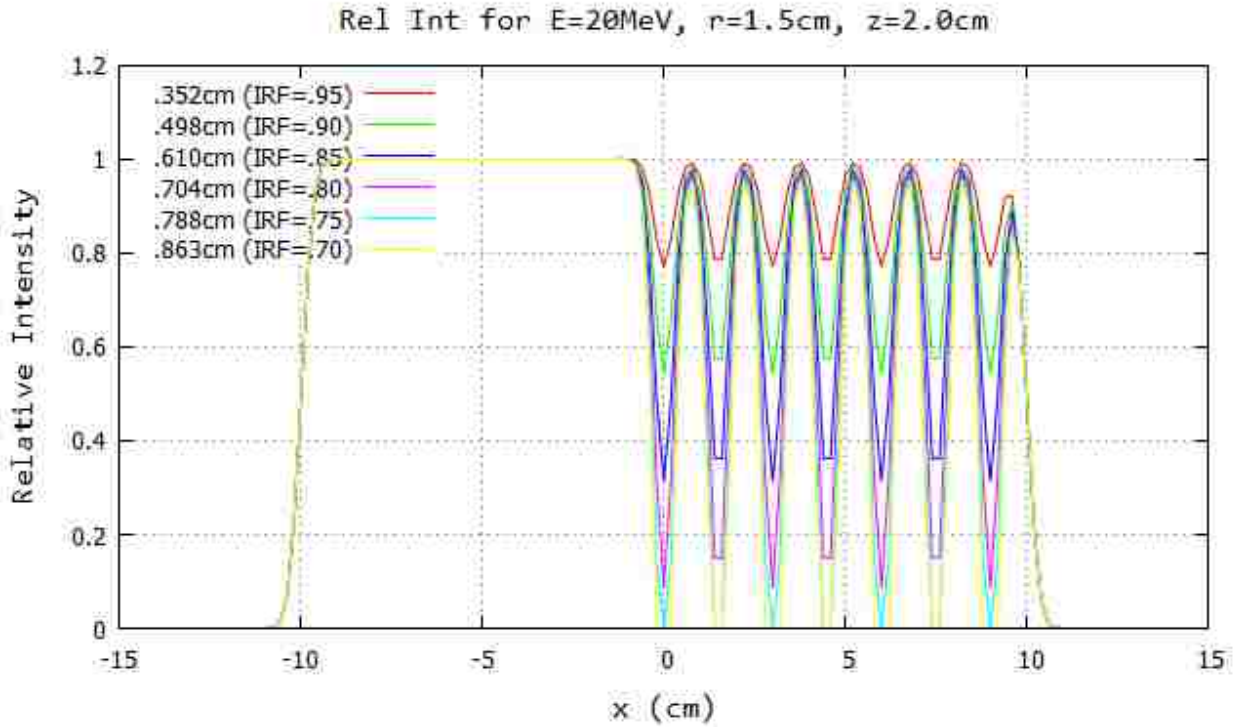


Figure B.35: Profile for 16 MeV and 100 cm SSD at y=0cm 20x20 half-blocked field. The computed island block diameter for 0.70, 0.75, 0.80, 0.85, 0.90, and 0.95 IRF values are listed in each plot's inserted key.

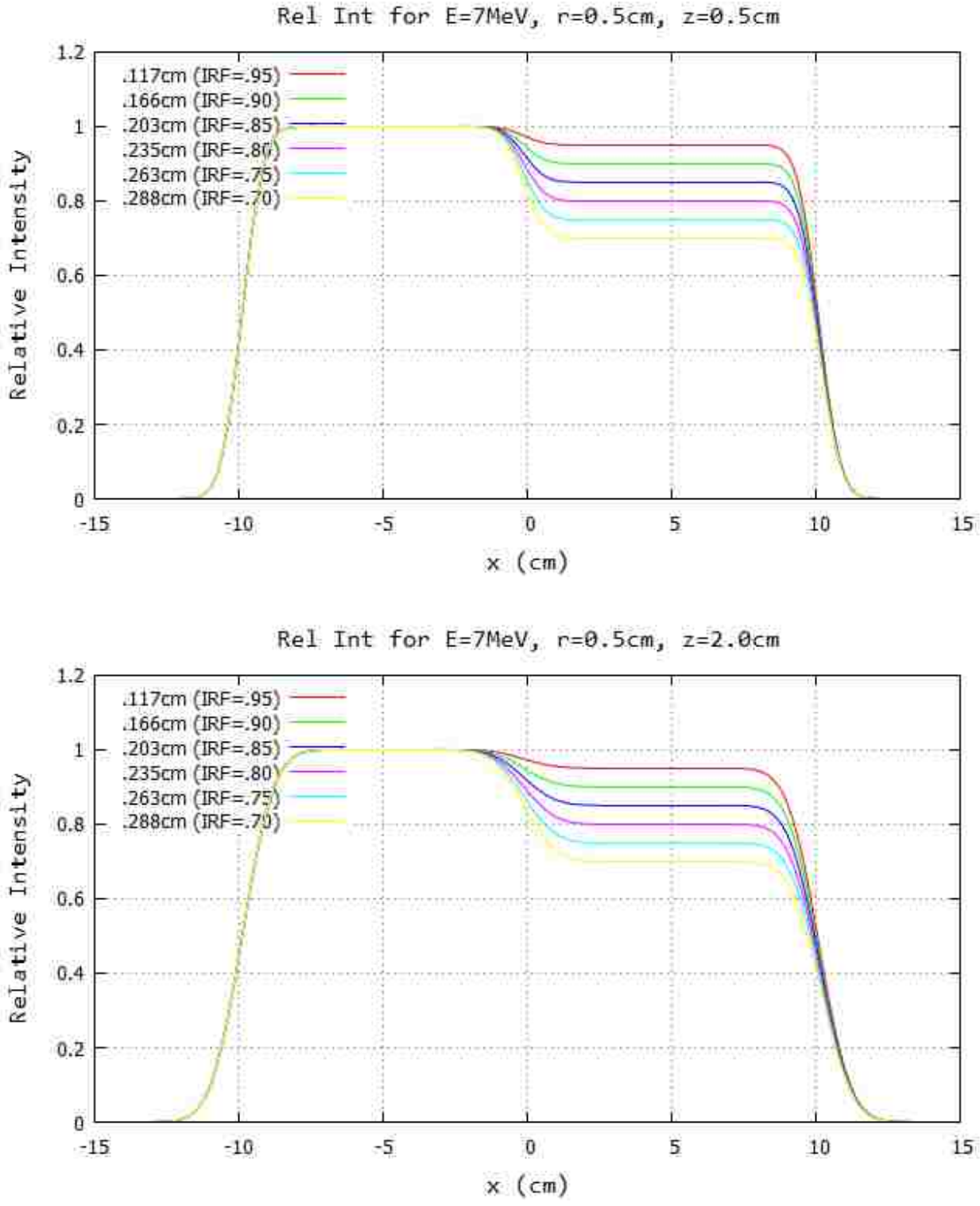


Figure B.36: Profile for 7 MeV and 103 cm SSD at y=0cm 20x20 half-blocked field. The computed island block diameter for 0.70, 0.75, 0.80, 0.85, 0.90, and 0.95 IRF values are listed in each plot's inserted key.

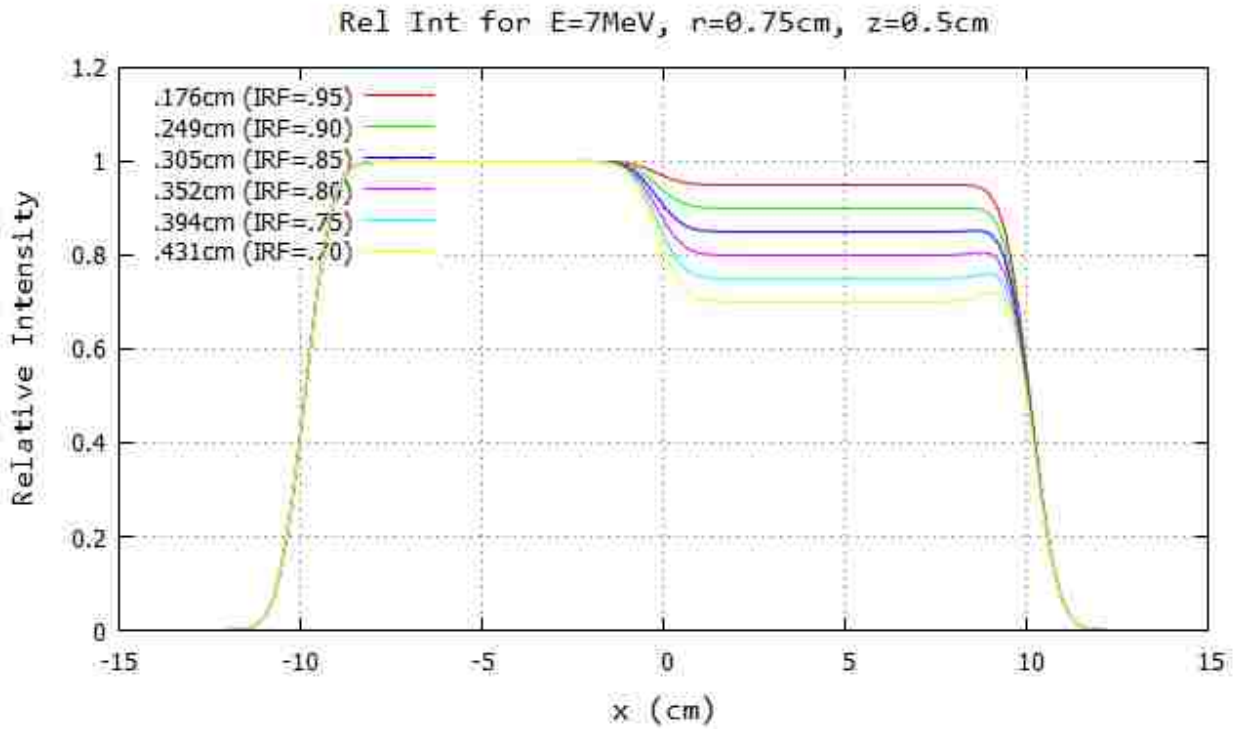


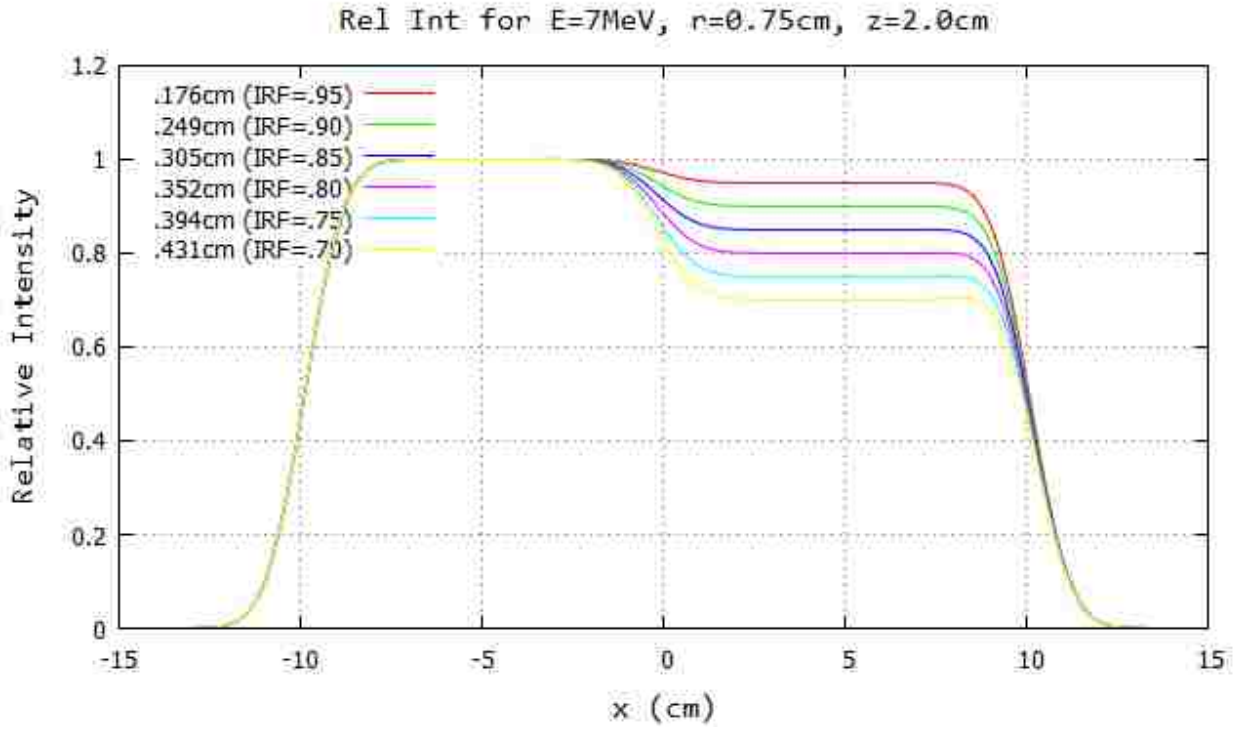


Figure B.37: Profile for 7 MeV and 103 cm SSD at y=0cm 20x20 half-blocked field. The computed island block diameter for 0.70, 0.75, 0.80, 0.85, 0.90, and 0.95 IRF values are listed in each plot's inserted key.

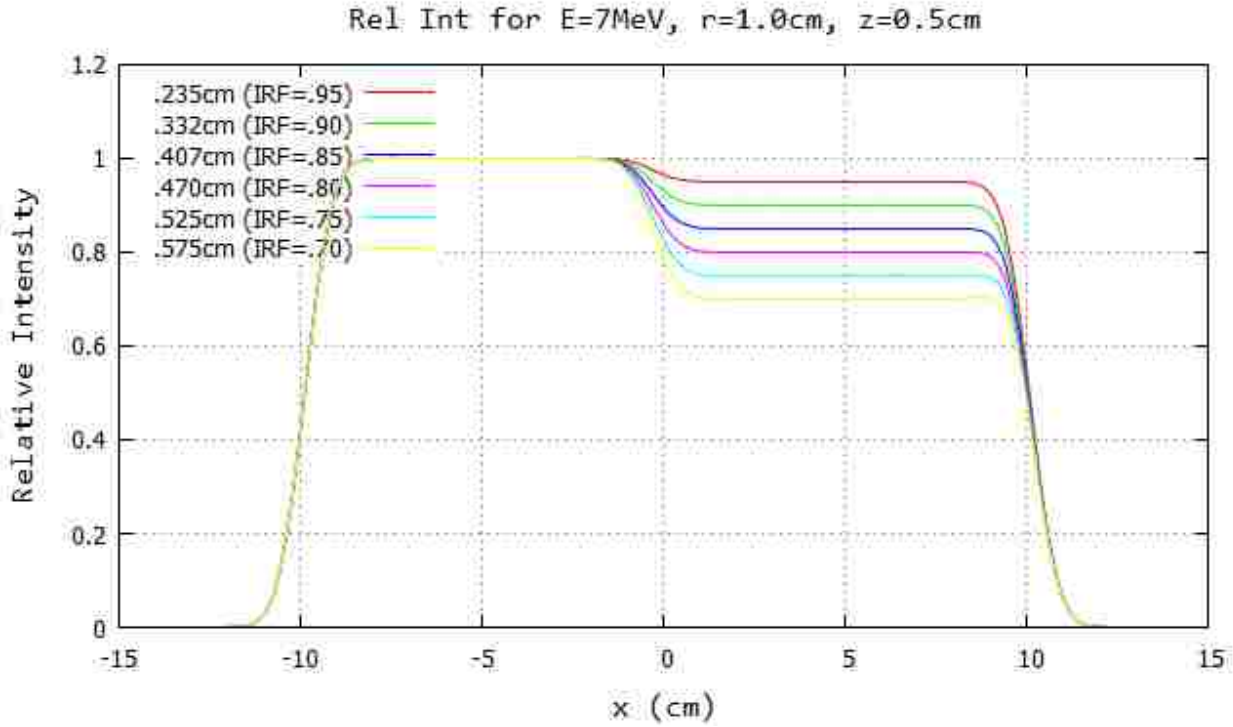


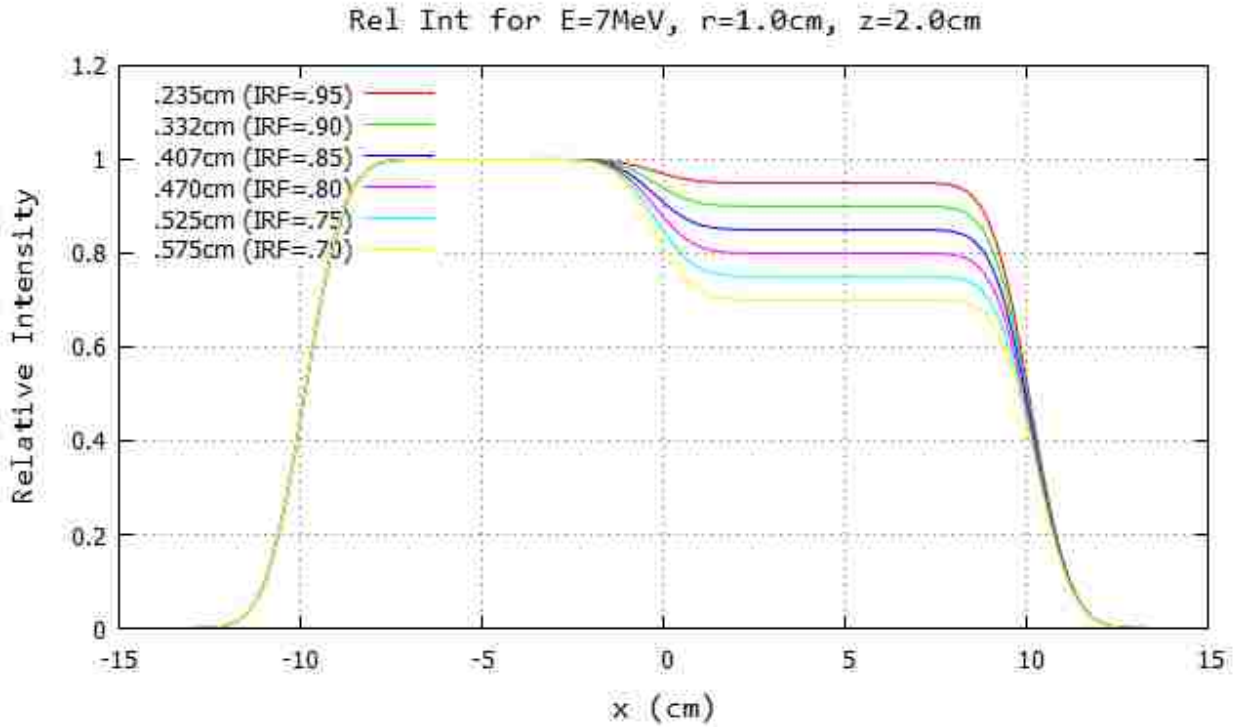


Figure B.38: Profile for 7 MeV and 103 cm SSD at y=0cm 20x20 half-blocked field. The computed island block diameter for 0.70, 0.75, 0.80, 0.85, 0.90, and 0.95 IRF values are listed in each plot's inserted key.

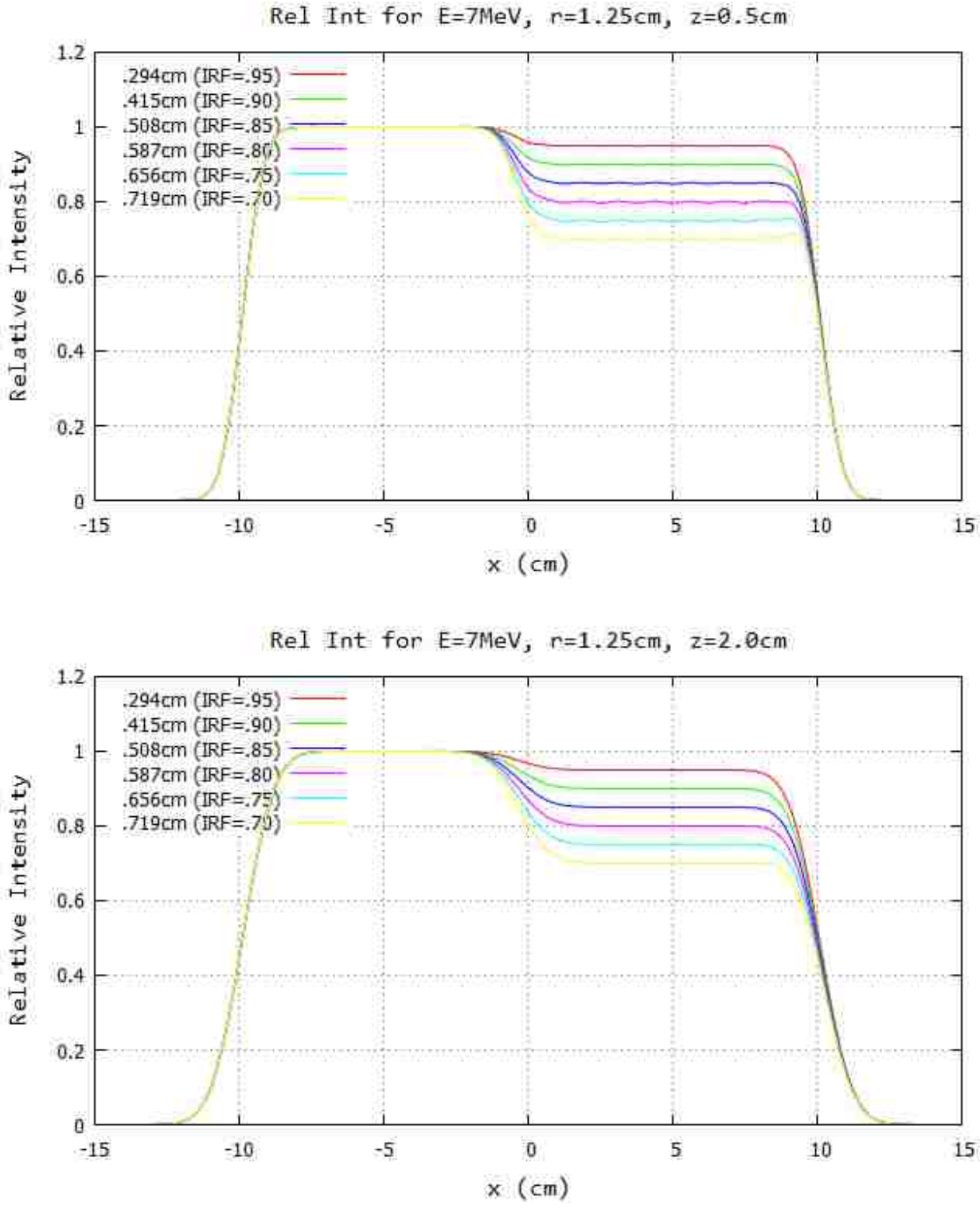


Figure B.39: Profile for 7 MeV and 103 cm SSD at y=0cm 20x20 half-blocked field.

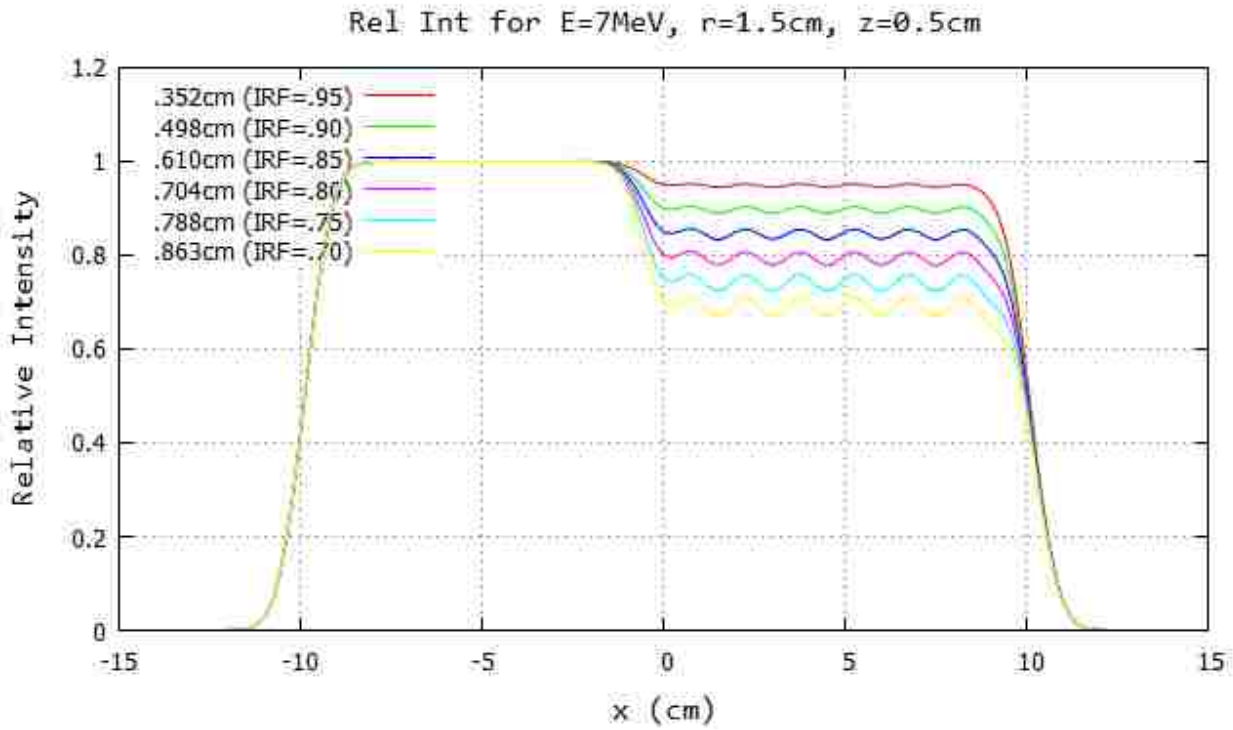


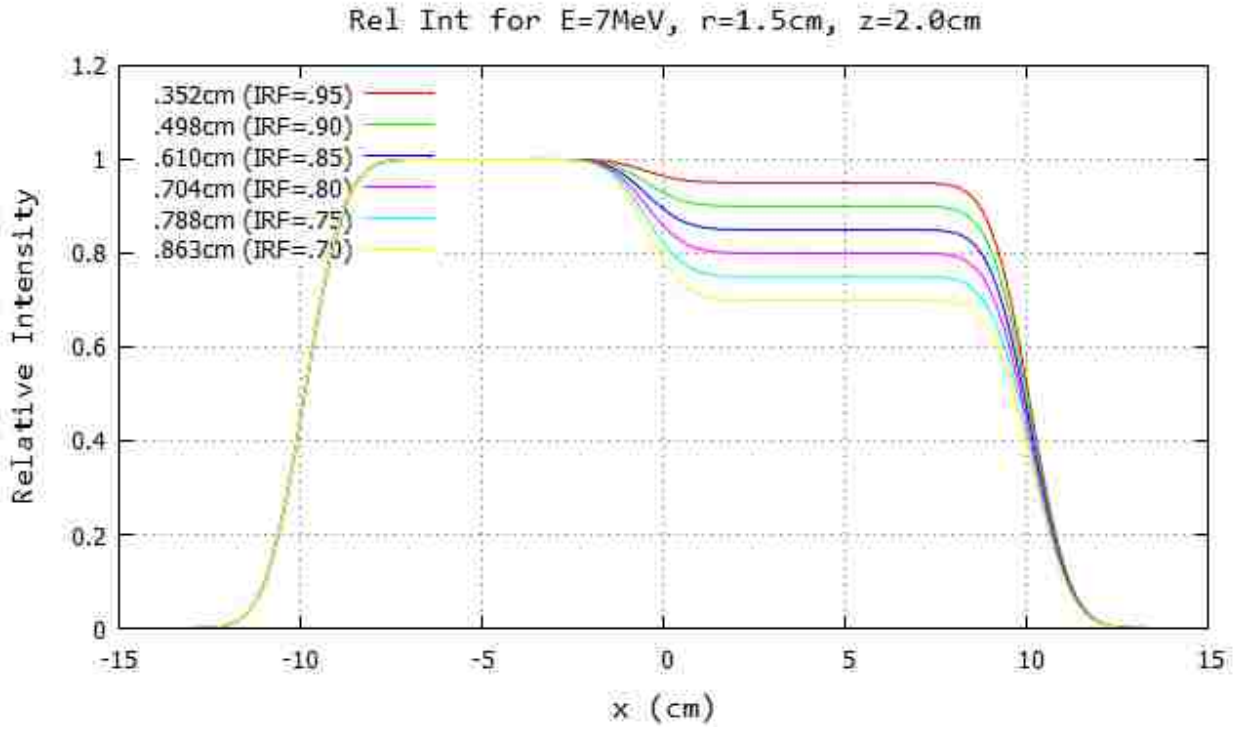


Figure B.40: Profile for 7 MeV and 103 cm SSD at y=0cm 20x20 half-blocked field. The computed island block diameter for 0.70, 0.75, 0.80, 0.85, 0.90, and 0.95 IRF values are listed in each plot's inserted key.

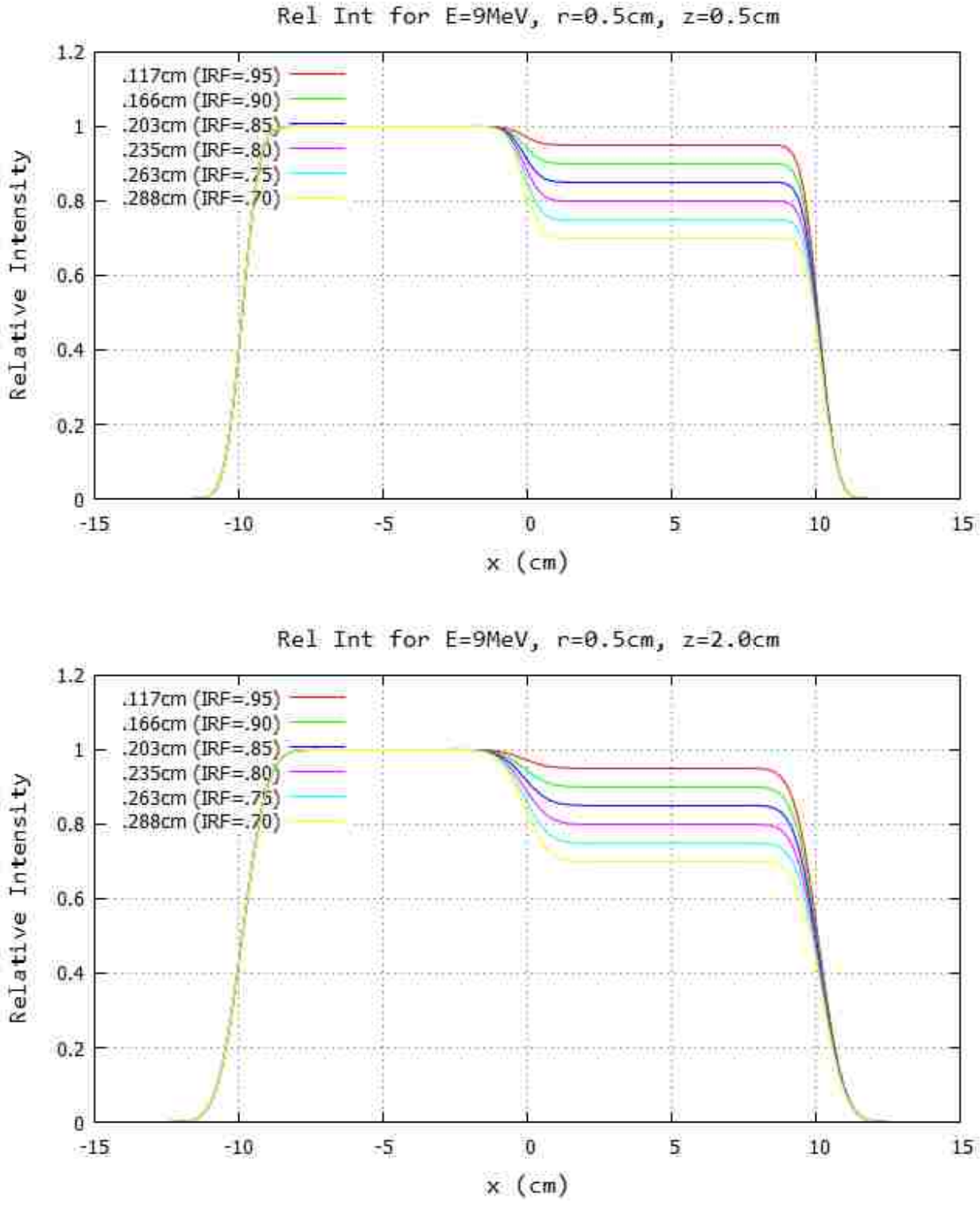


Figure B.41: Profile for 9 MeV and 103 cm SSD at y=0cm 20x20 half-blocked field. The computed island block diameter for 0.70, 0.75, 0.80, 0.85, 0.90, and 0.95 IRF values are listed in each plot's inserted key.

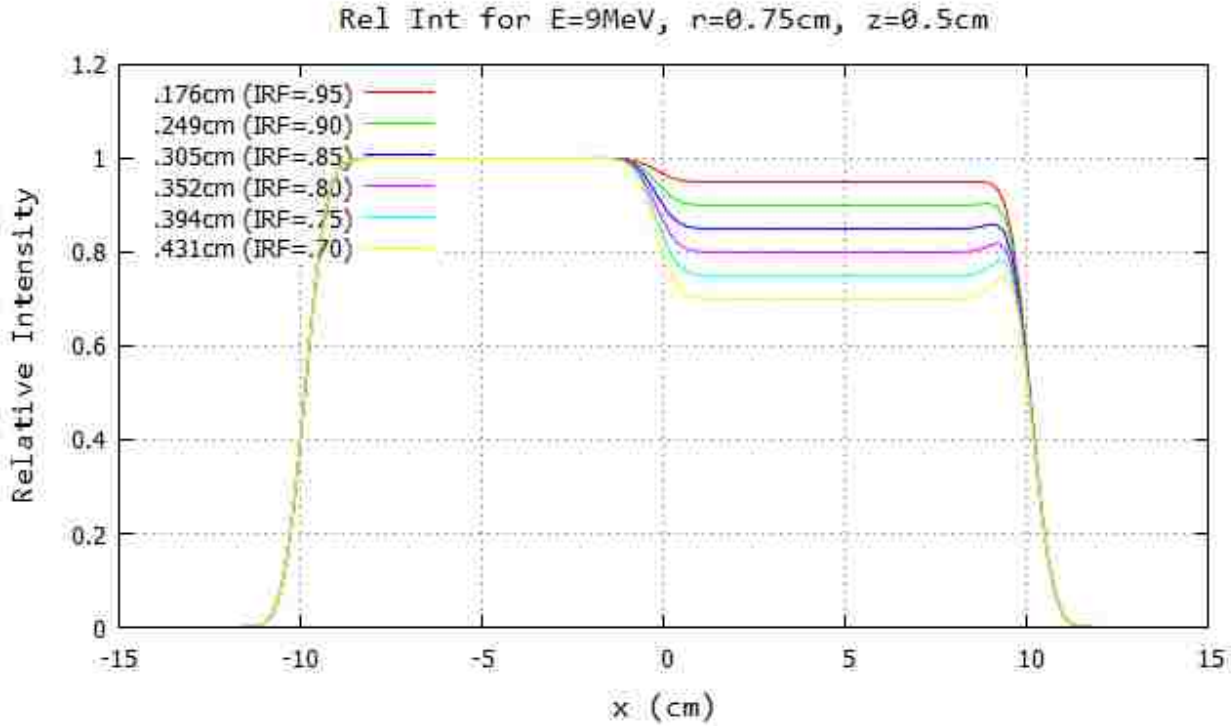


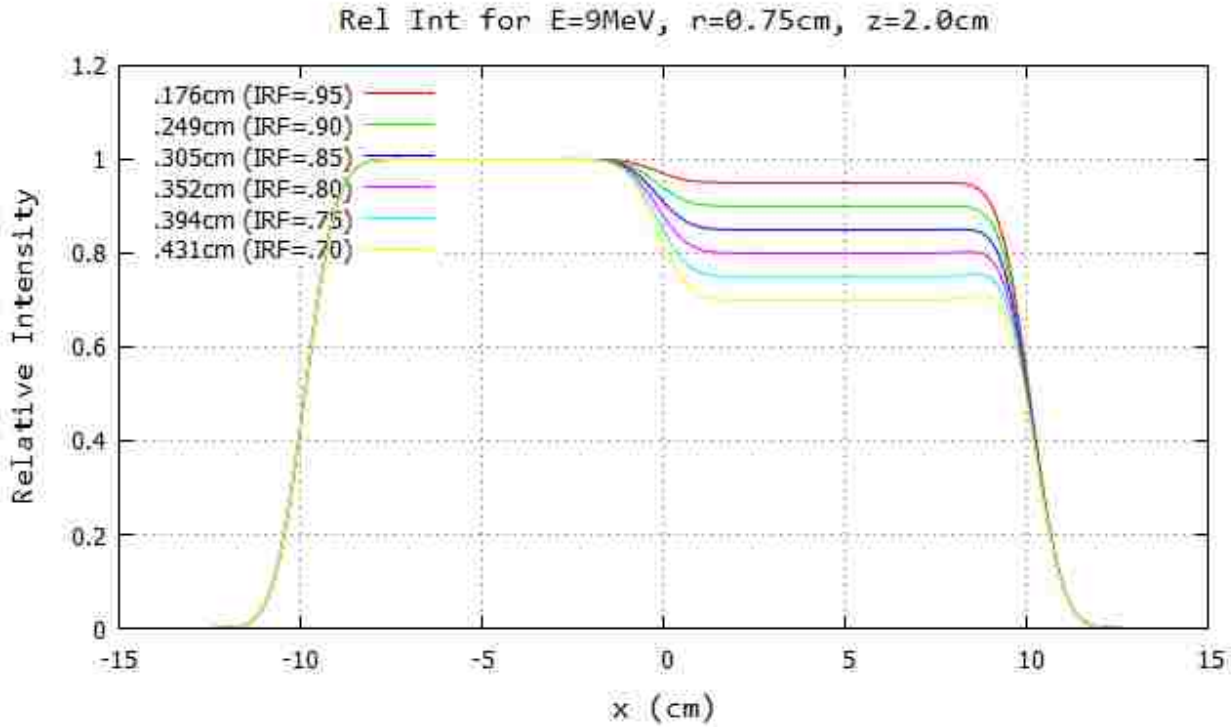


Figure B.42: Profile for 9 MeV and 103 cm SSD at y=0cm 20x20 half-blocked field. The computed island block diameter for 0.70, 0.75, 0.80, 0.85, 0.90, and 0.95 IRF values are listed in each plot's inserted key.

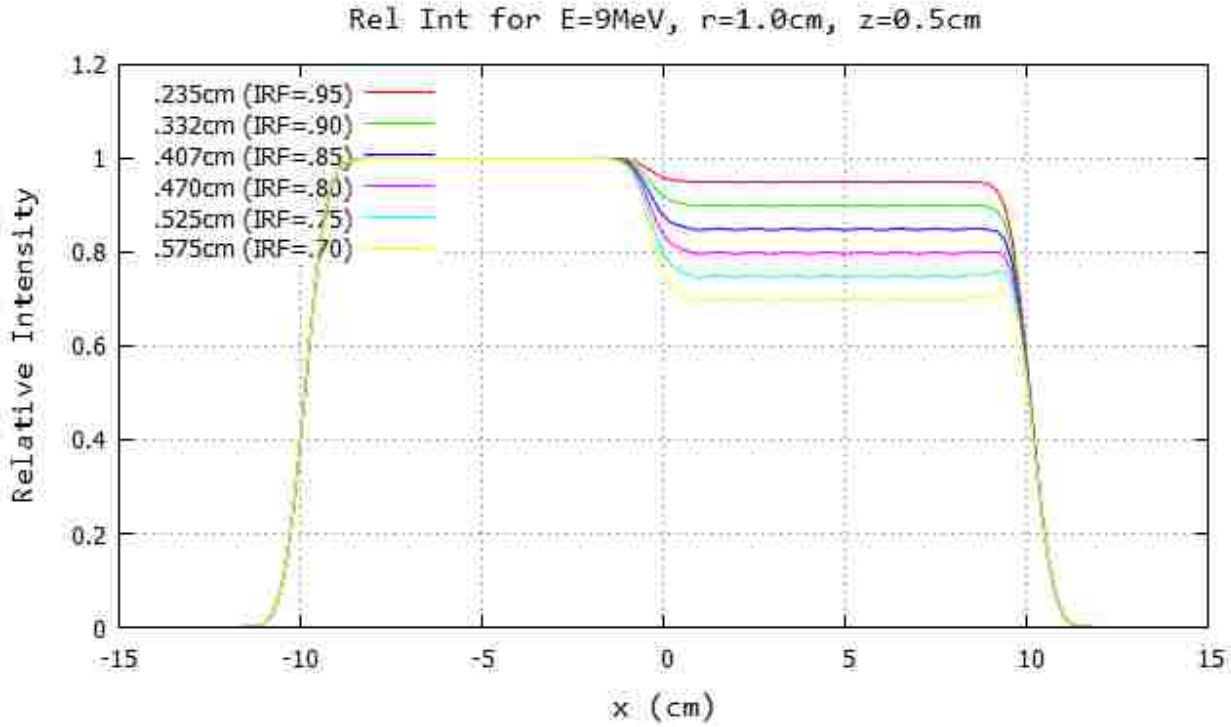


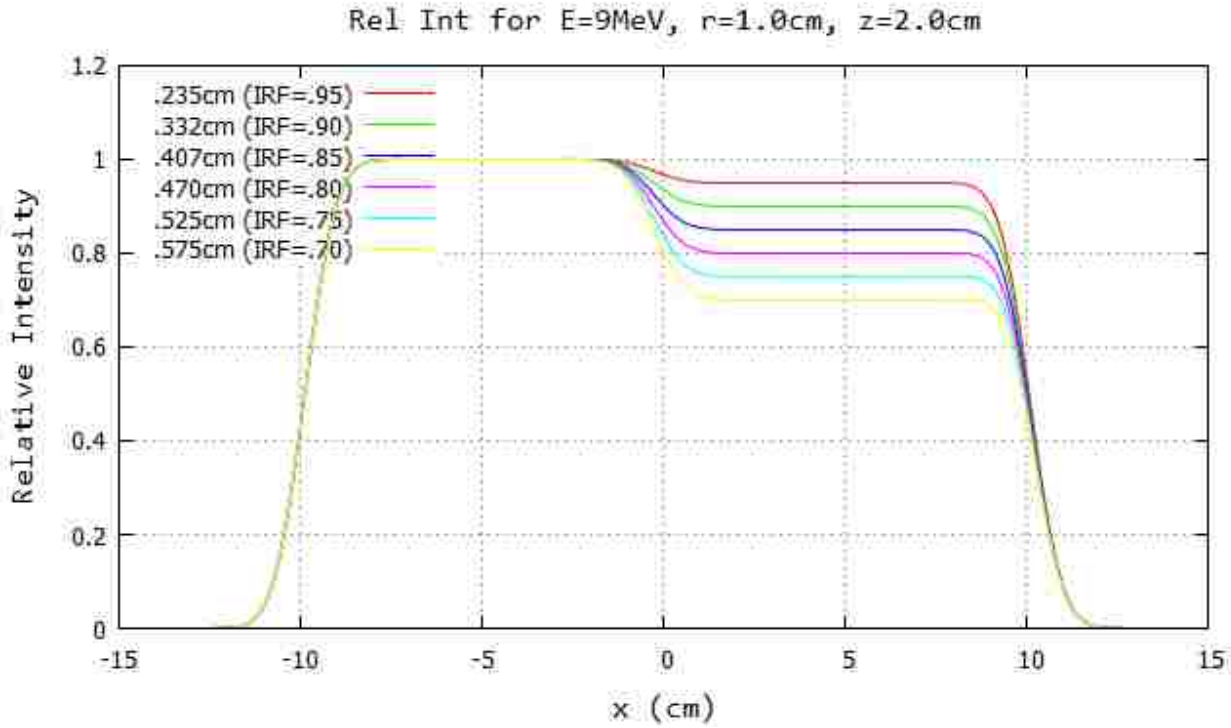


Figure B.43: Profile for 9 MeV and 103 cm SSD at y=0cm 20x20 half-blocked field. The computed island block diameter for 0.70, 0.75, 0.80, 0.85, 0.90, and 0.95 IRF values are listed in each plot's inserted key.

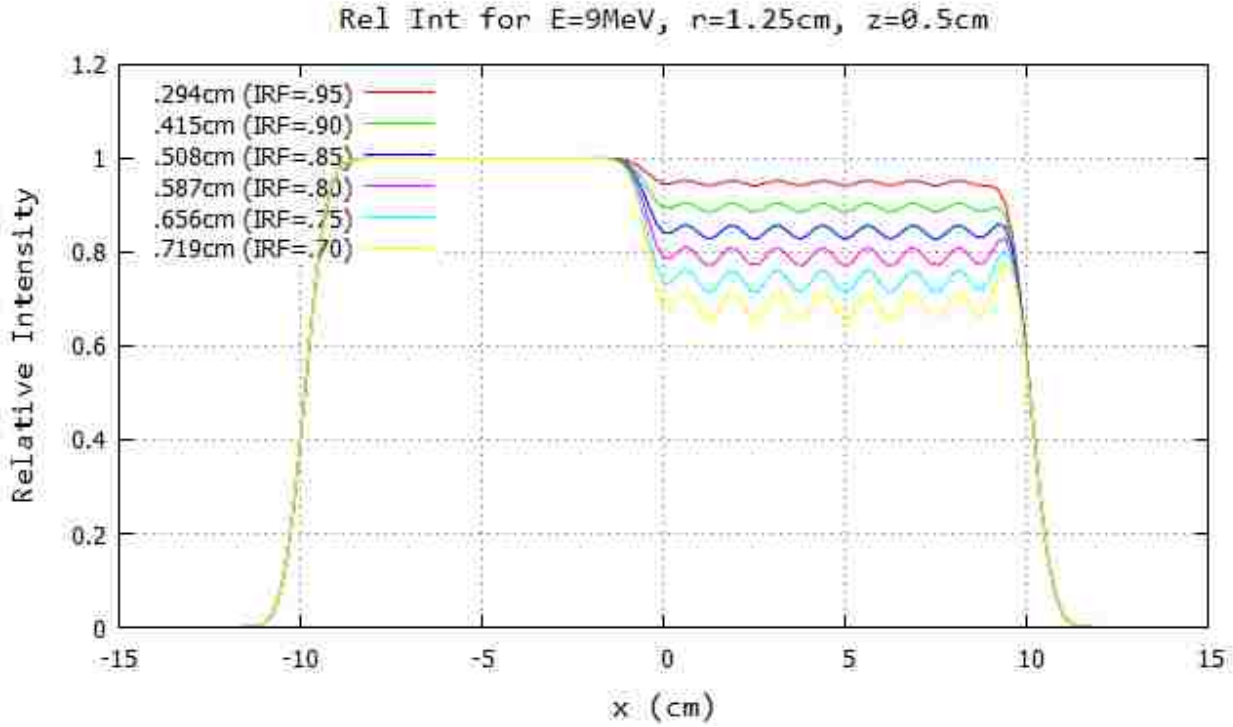


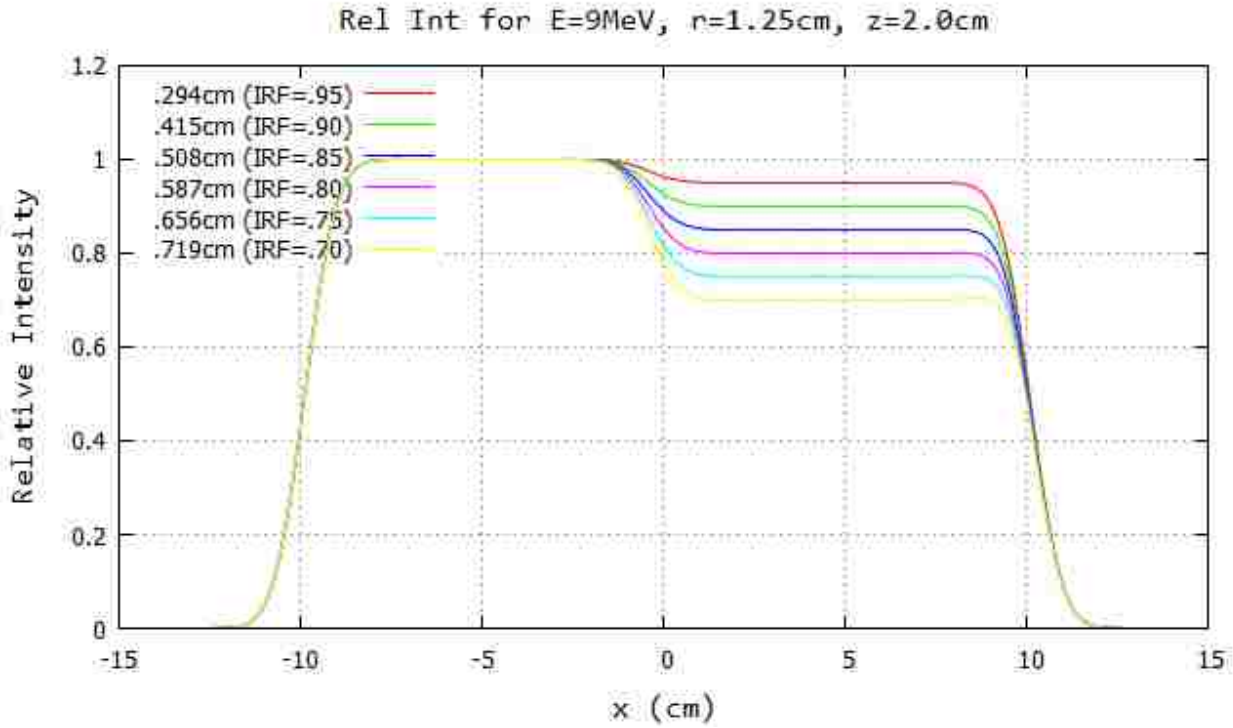


Figure B.44: Profile for 9 MeV and 103 cm SSD at y=0cm 20x20 half-blocked field. The computed island block diameter for 0.70, 0.75, 0.80, 0.85, 0.90, and 0.95 IRF values are listed in each plot's inserted key.

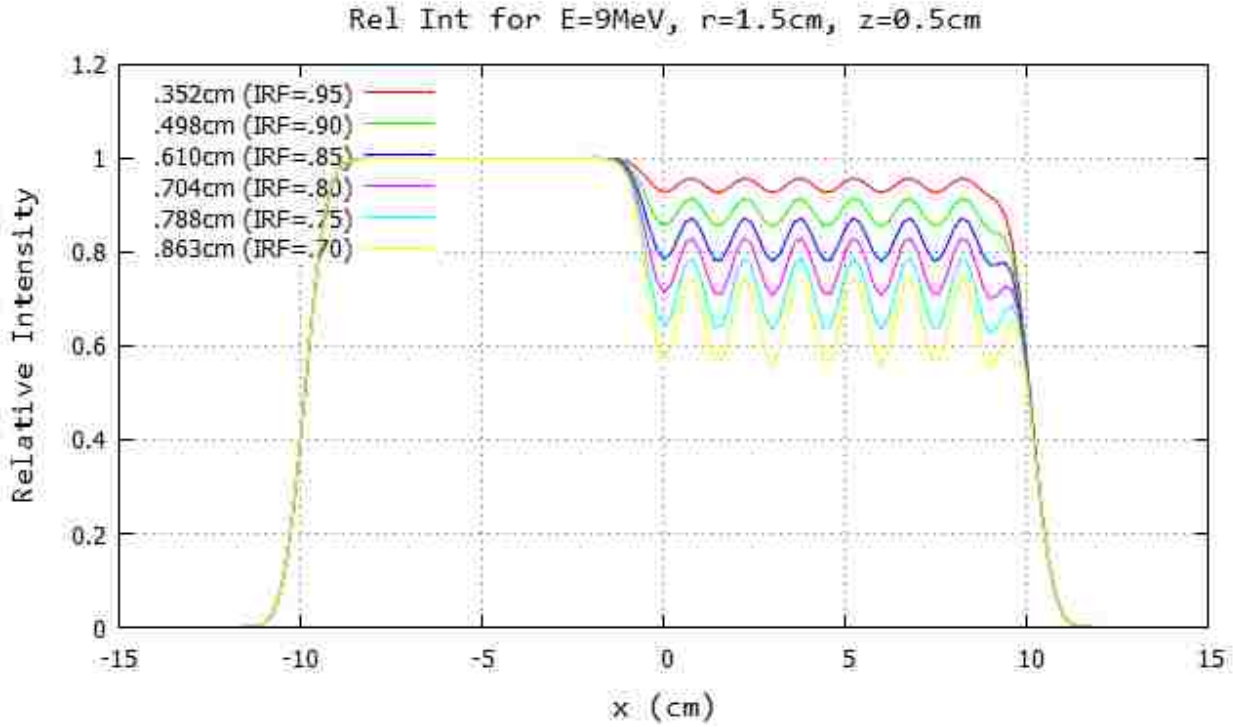


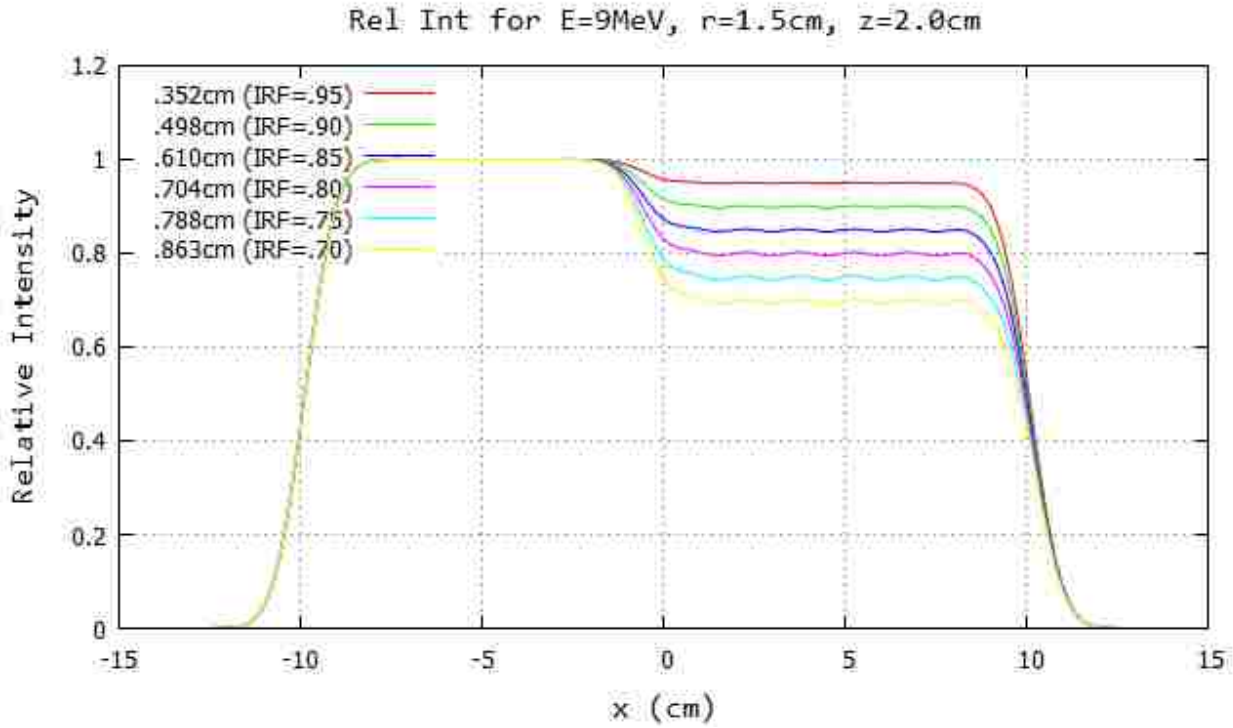


Figure B.45: Profile for 9 MeV and 103 cm SSD at y=0cm 20x20 half-blocked field. The computed island block diameter for 0.70, 0.75, 0.80, 0.85, 0.90, and 0.95 IRF values are listed in each plot's inserted key.

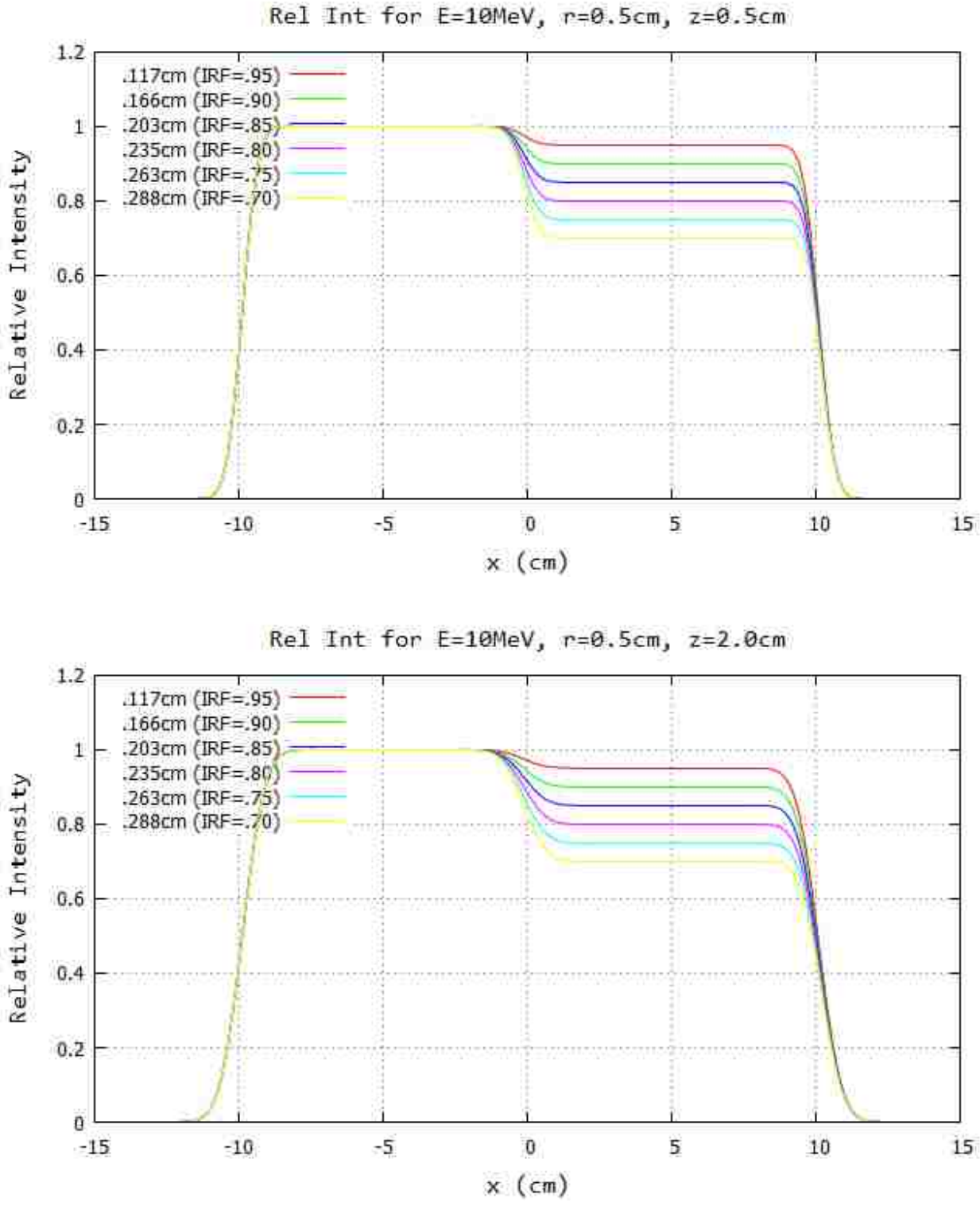


Figure B.46: Profile for 10 MeV and 103 cm SSD at y=0cm 20x20 half-blocked field. The computed island block diameter for 0.70, 0.75, 0.80, 0.85, 0.90, and 0.95 IRF values are listed in each plot's inserted key.

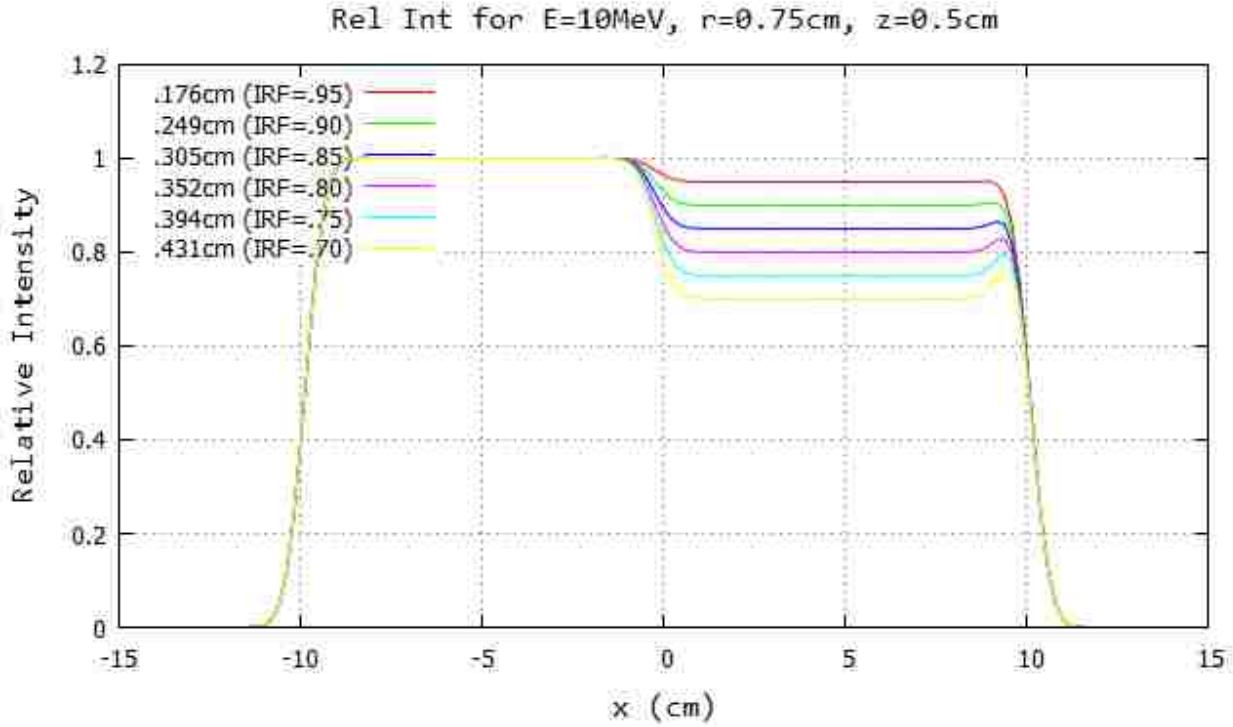


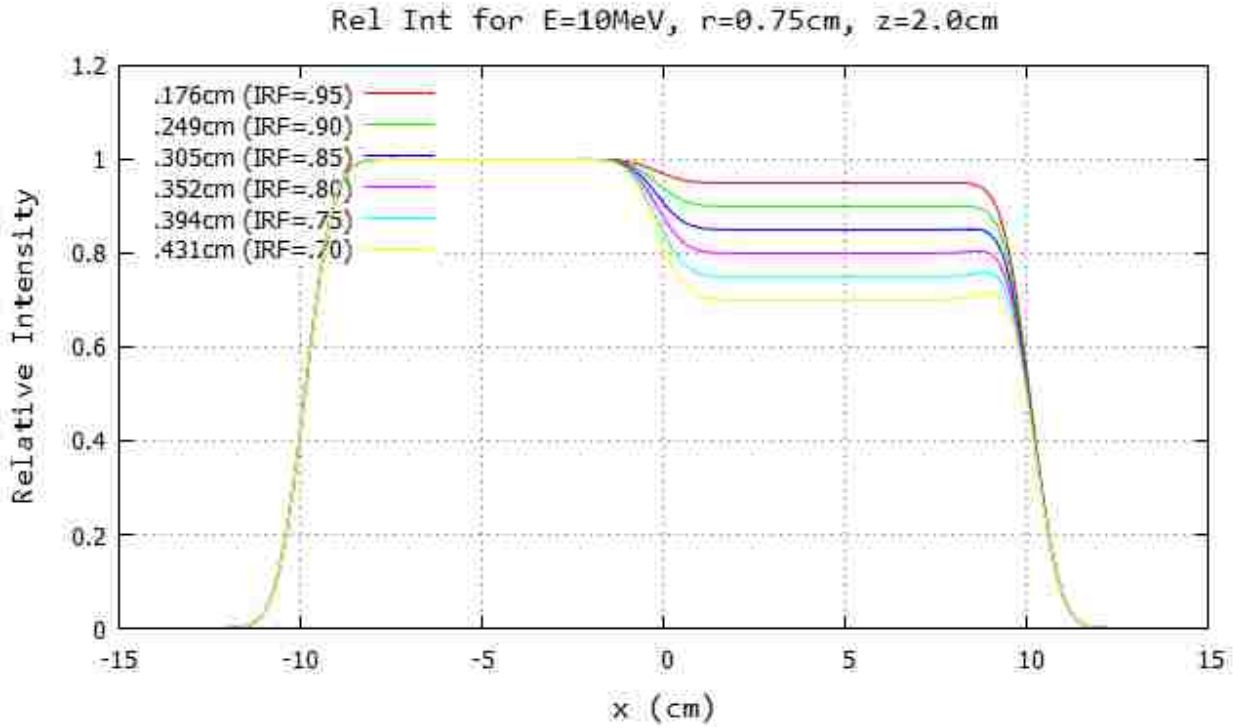


Figure B.47: Profile for 10 MeV and 103 cm SSD at y=0cm 20x20 half-blocked field. The computed island block diameter for 0.70, 0.75, 0.80, 0.85, 0.90, and 0.95 IRF values are listed in each plot's inserted key.

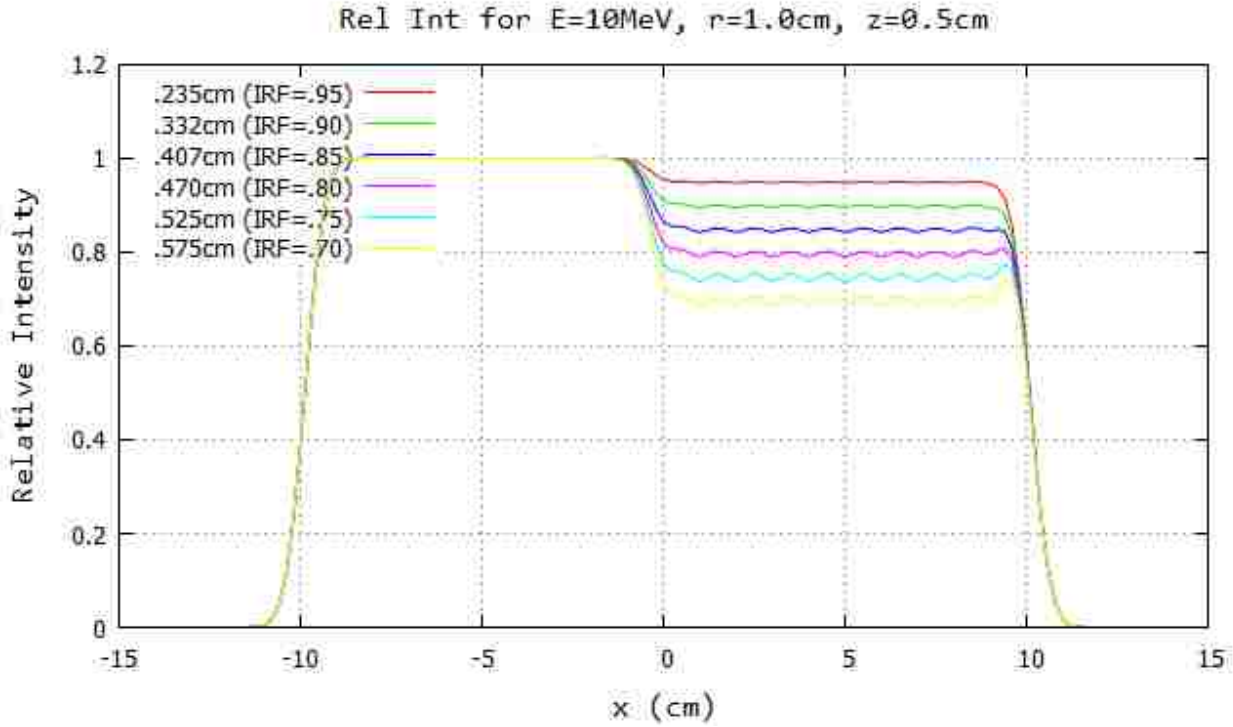


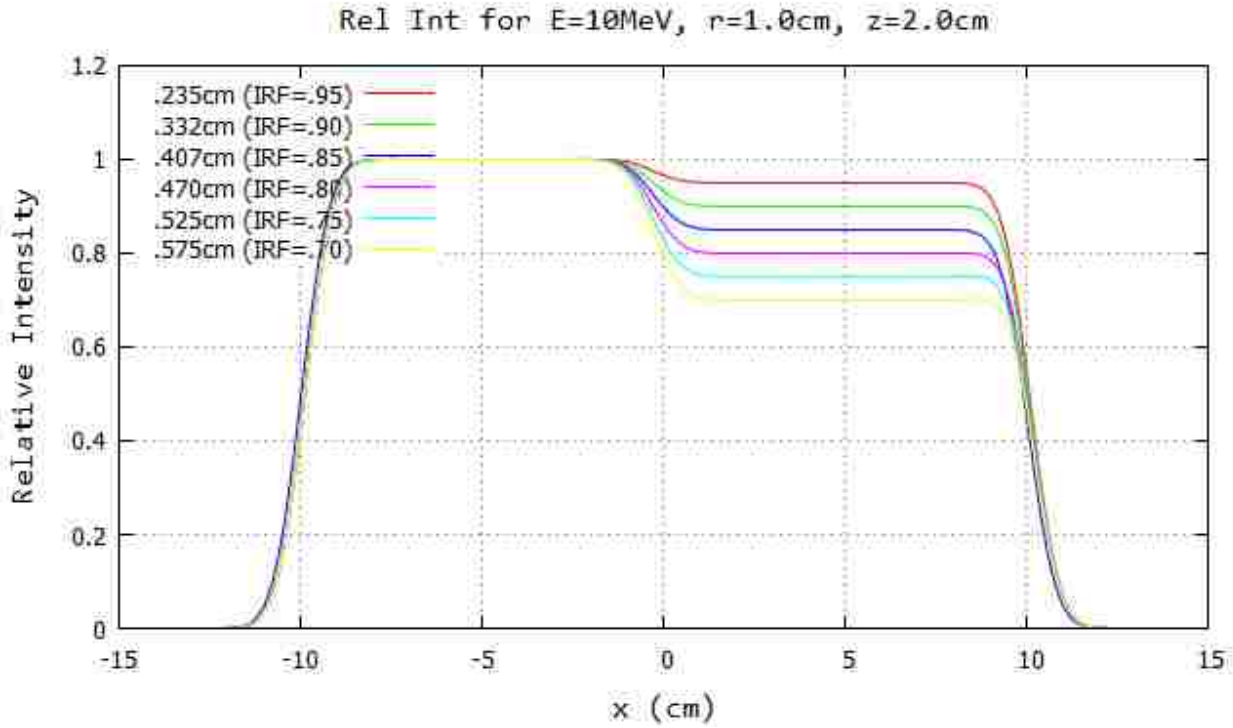


Figure B.48: Profile for 10 MeV and 103 cm SSD at y=0cm 20x20 half-blocked field. The computed island block diameter for 0.70, 0.75, 0.80, 0.85, 0.90, and 0.95 IRF values are listed in each plot's inserted key.

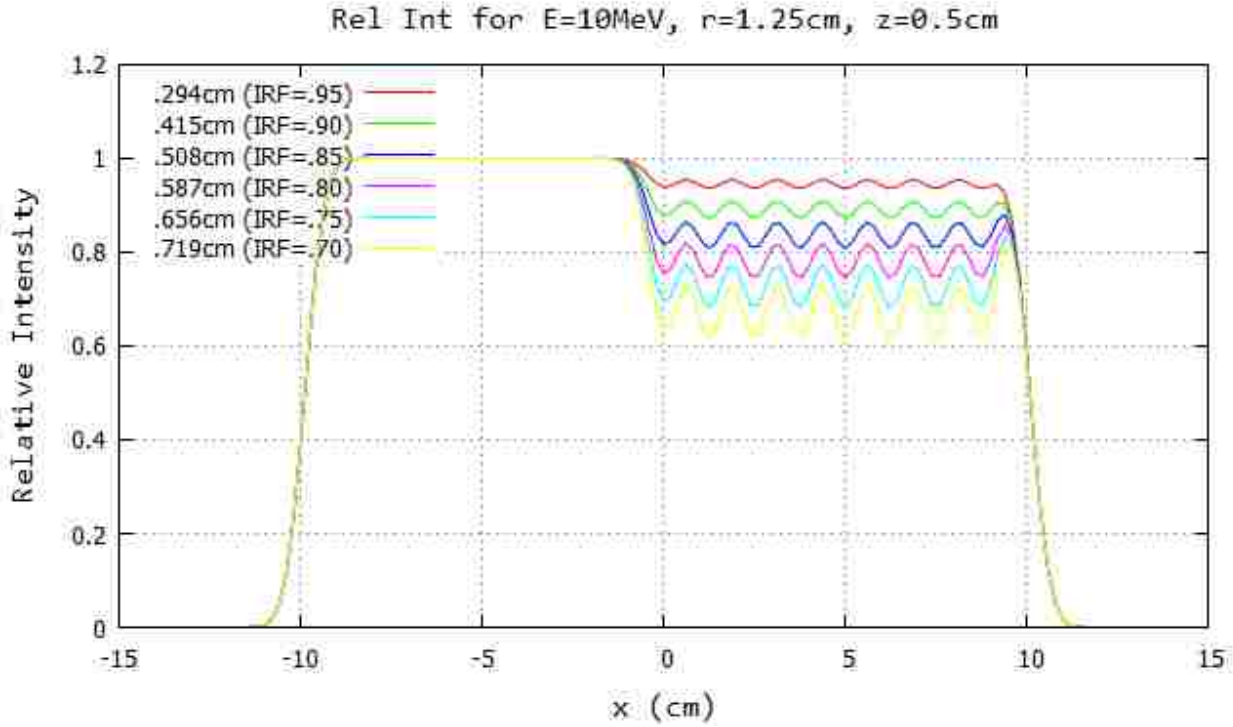


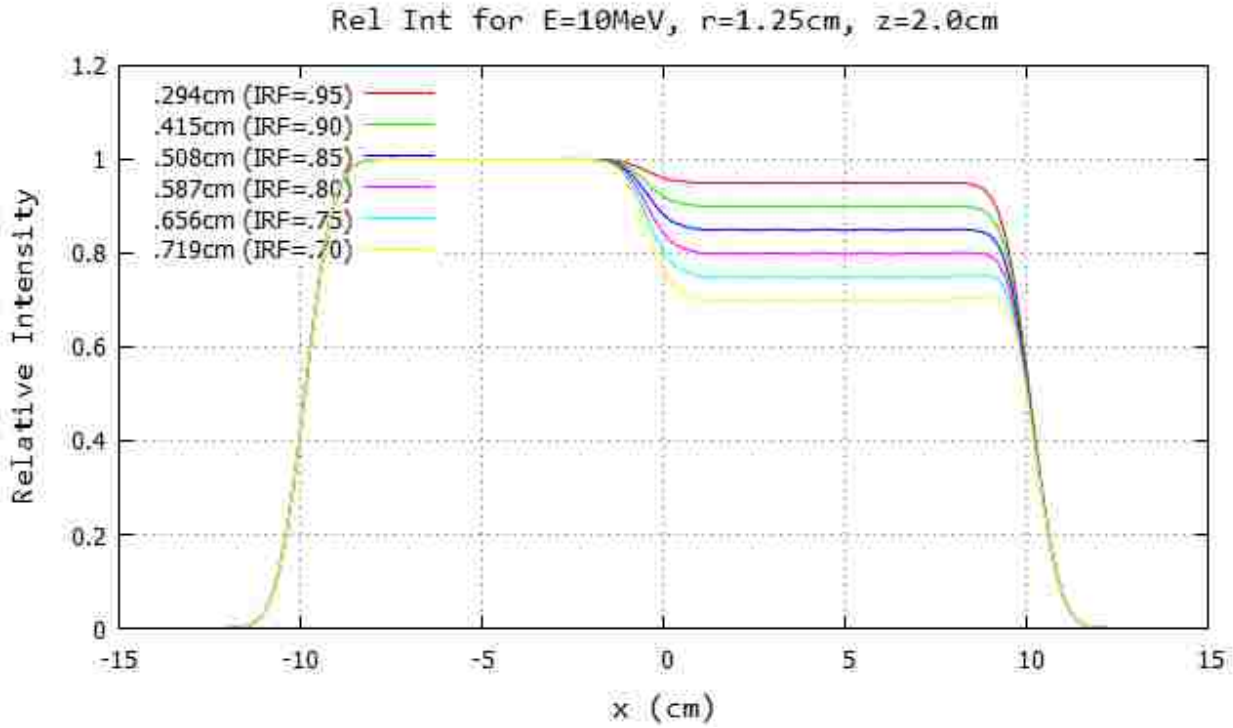


Figure B.49: Profile for 10 MeV and 103 cm SSD at y=0cm 20x20 half-blocked field. The computed island block diameter for 0.70, 0.75, 0.80, 0.85, 0.90, and 0.95 IRF values are listed in each plot's inserted key.

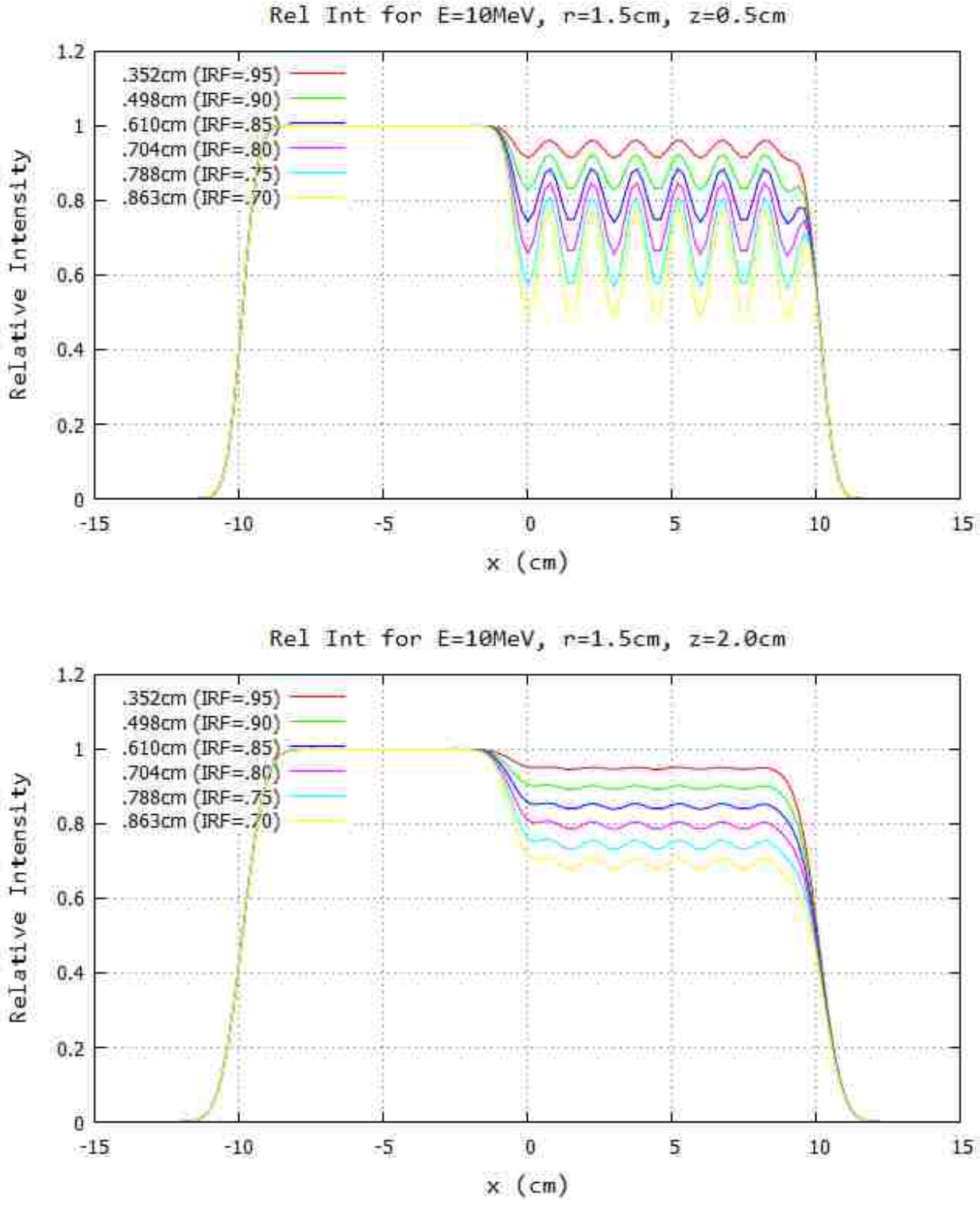


Figure B.50: Profile for 10 MeV and 103 cm SSD at y=0cm 20x20 half-blocked field. The computed island block diameter for 0.70, 0.75, 0.80, 0.85, 0.90, and 0.95 IRF values are listed in each plot's inserted key.

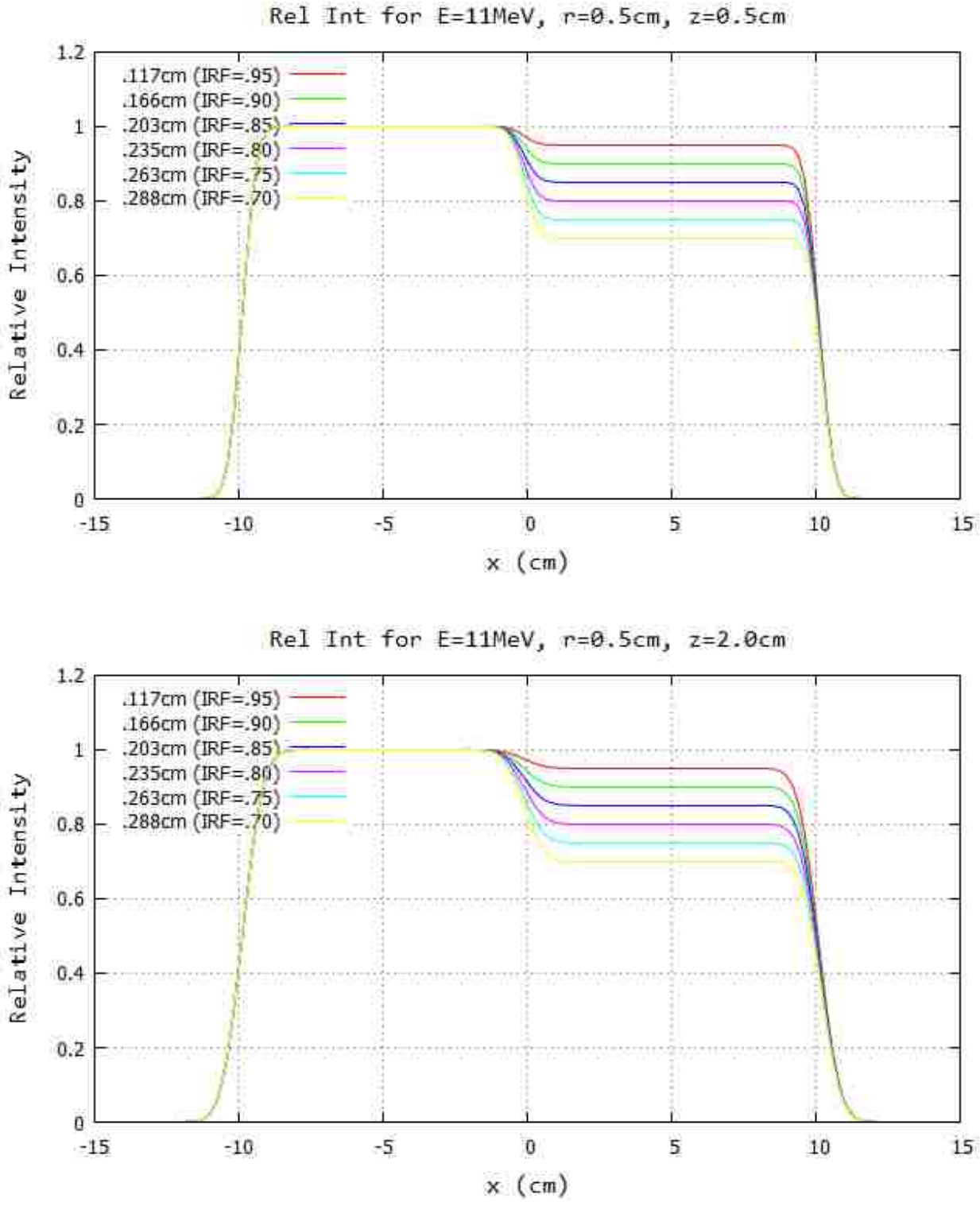


Figure B.51: Profile for 11 MeV and 103 cm SSD at y=0cm 20x20 half-blocked field. The computed island block diameter for 0.70, 0.75, 0.80, 0.85, 0.90, and 0.95 IRF values are listed in each plot's inserted key.

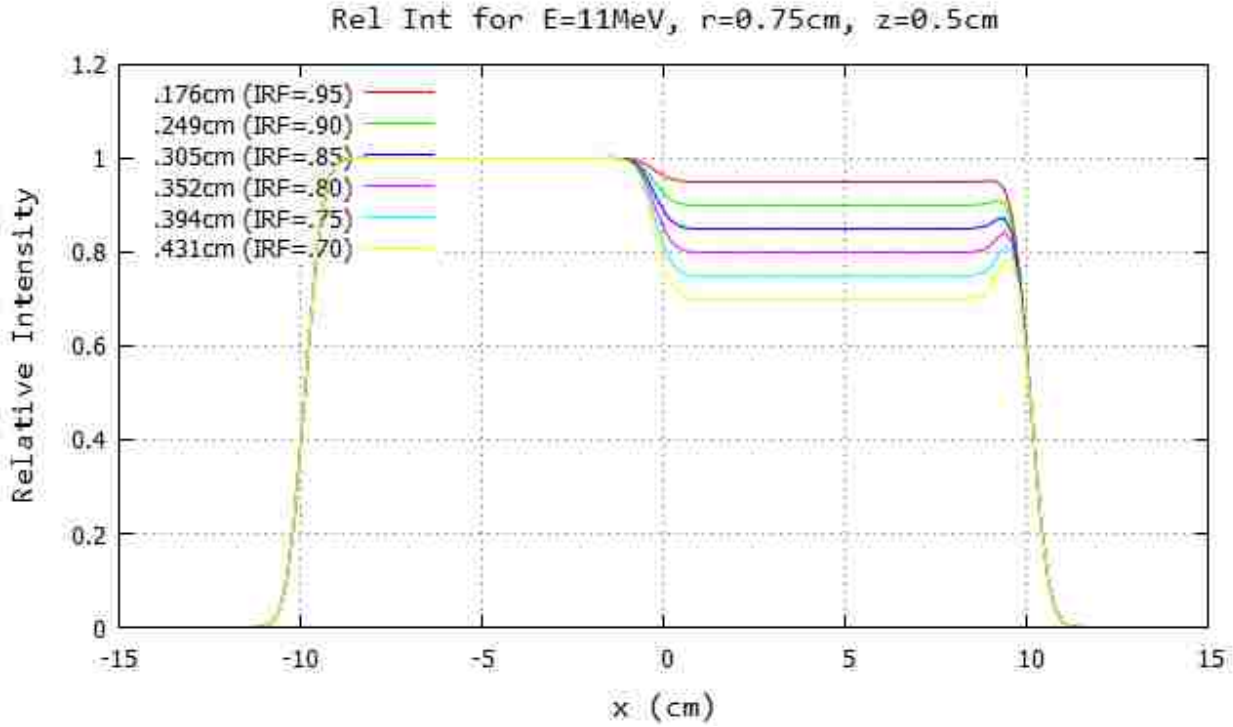


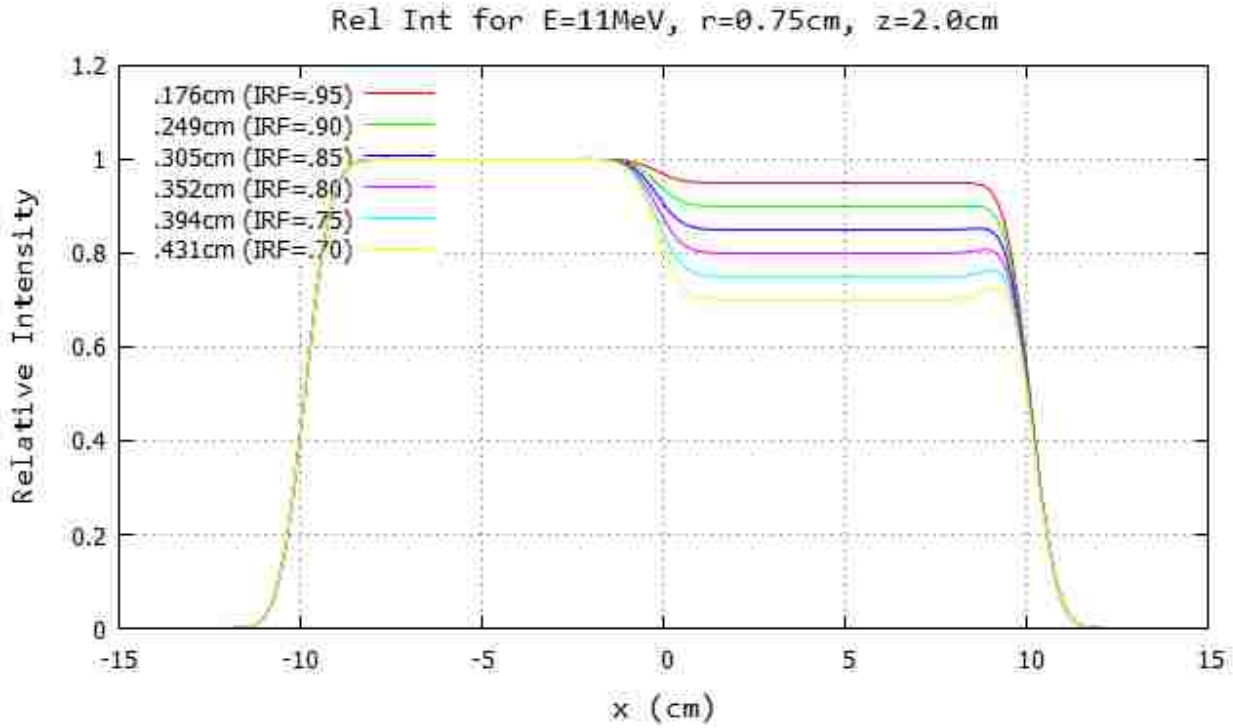


Figure B.52: Profile for 11 MeV and 103 cm SSD at y=0cm 20x20 half-blocked field. The computed island block diameter for 0.70, 0.75, 0.80, 0.85, 0.90, and 0.95 IRF values are listed in each plot's inserted key.

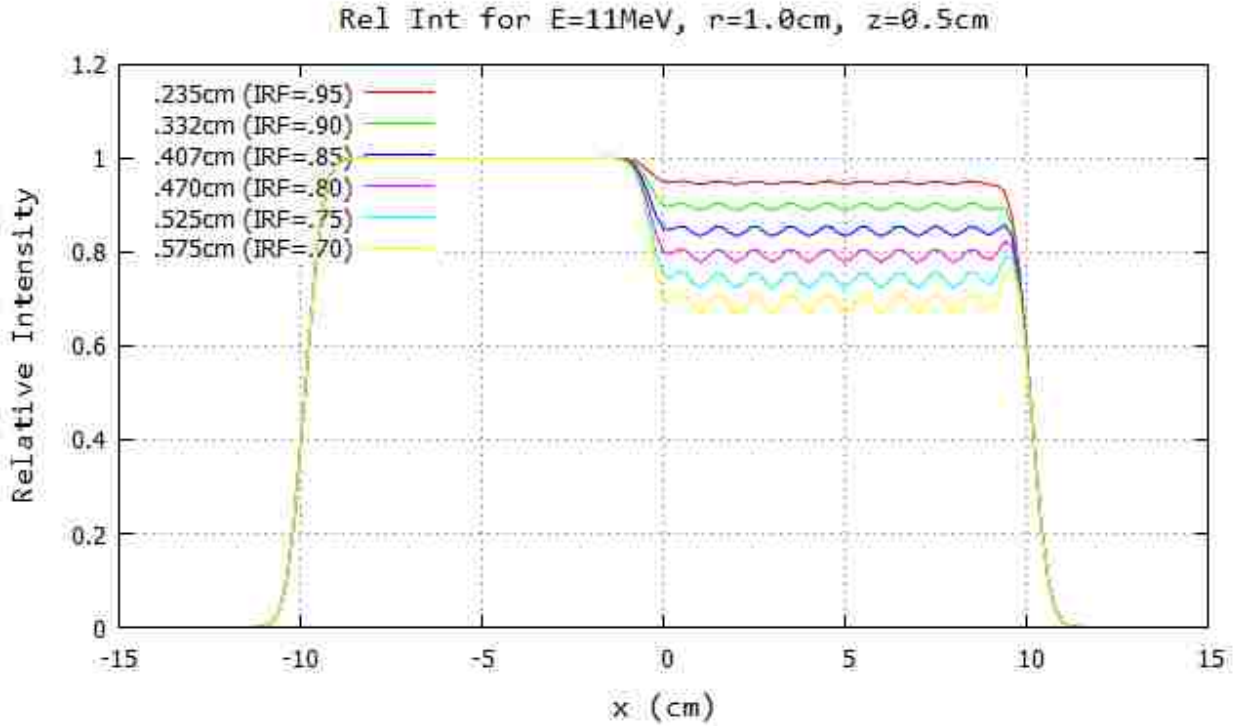


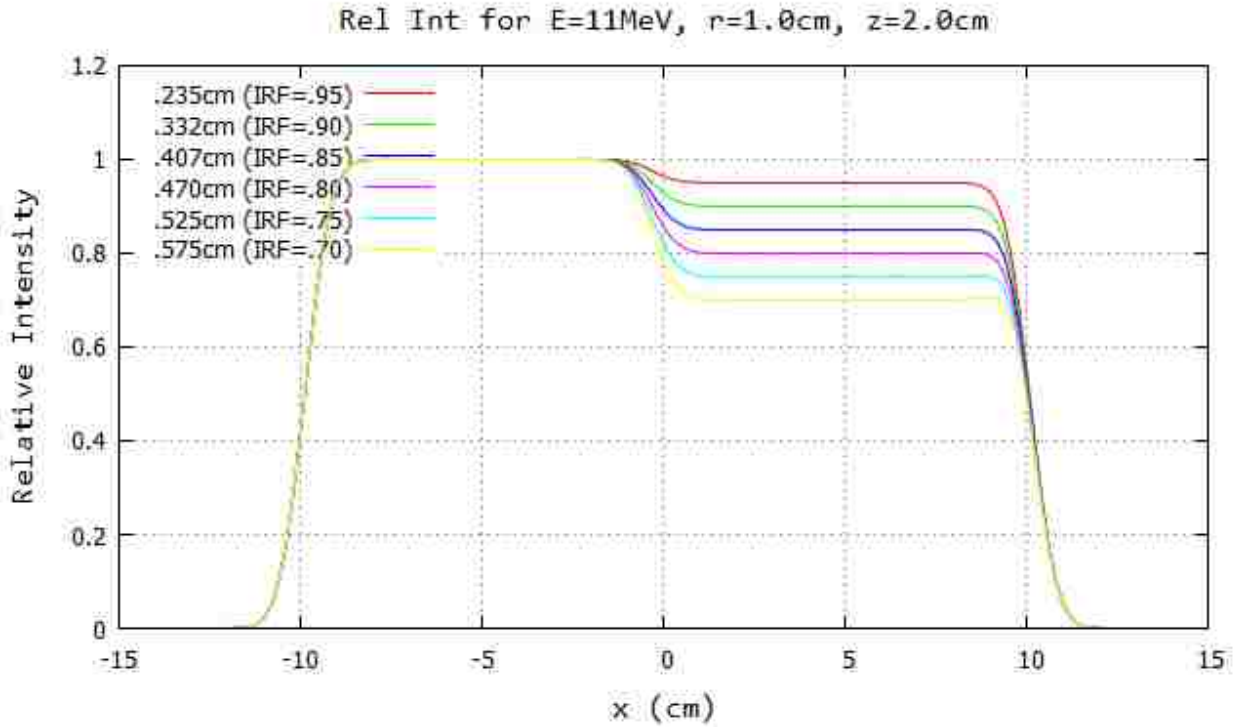


Figure B.53: Profile for 11 MeV and 103 cm SSD at y=0cm 20x20 half-blocked field. The computed island block diameter for 0.70, 0.75, 0.80, 0.85, 0.90, and 0.95 IRF values are listed in each plot's inserted key.

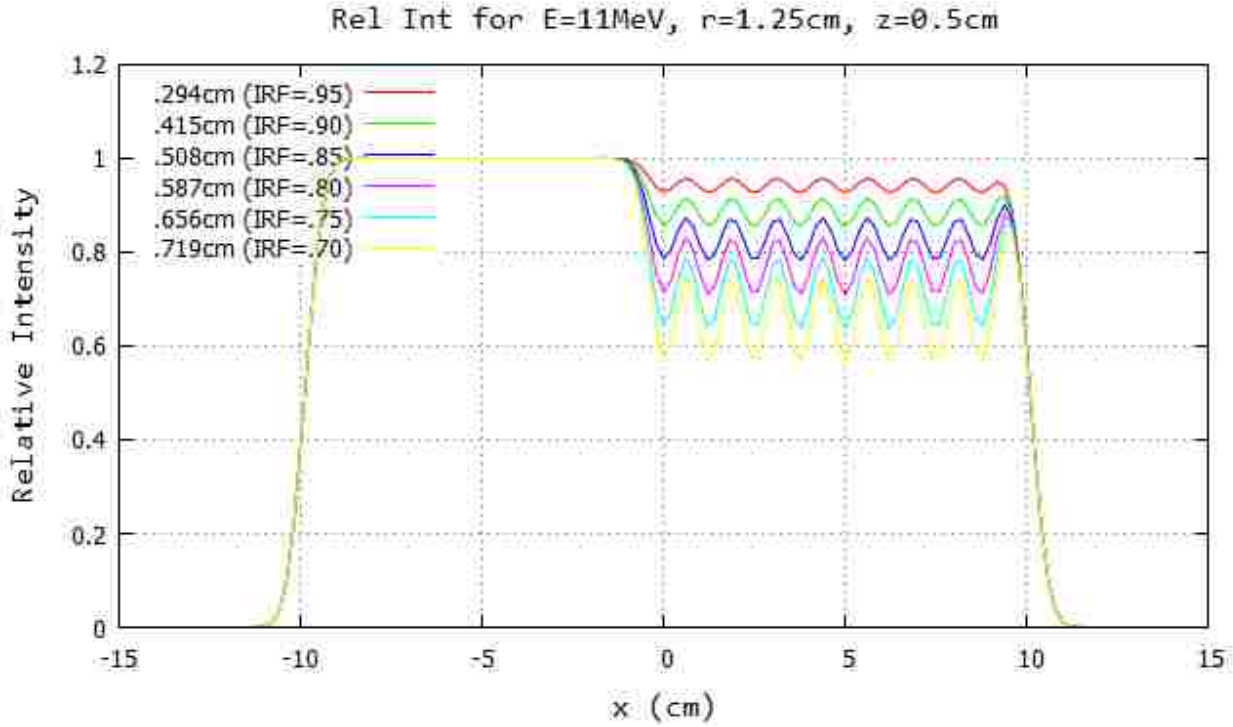


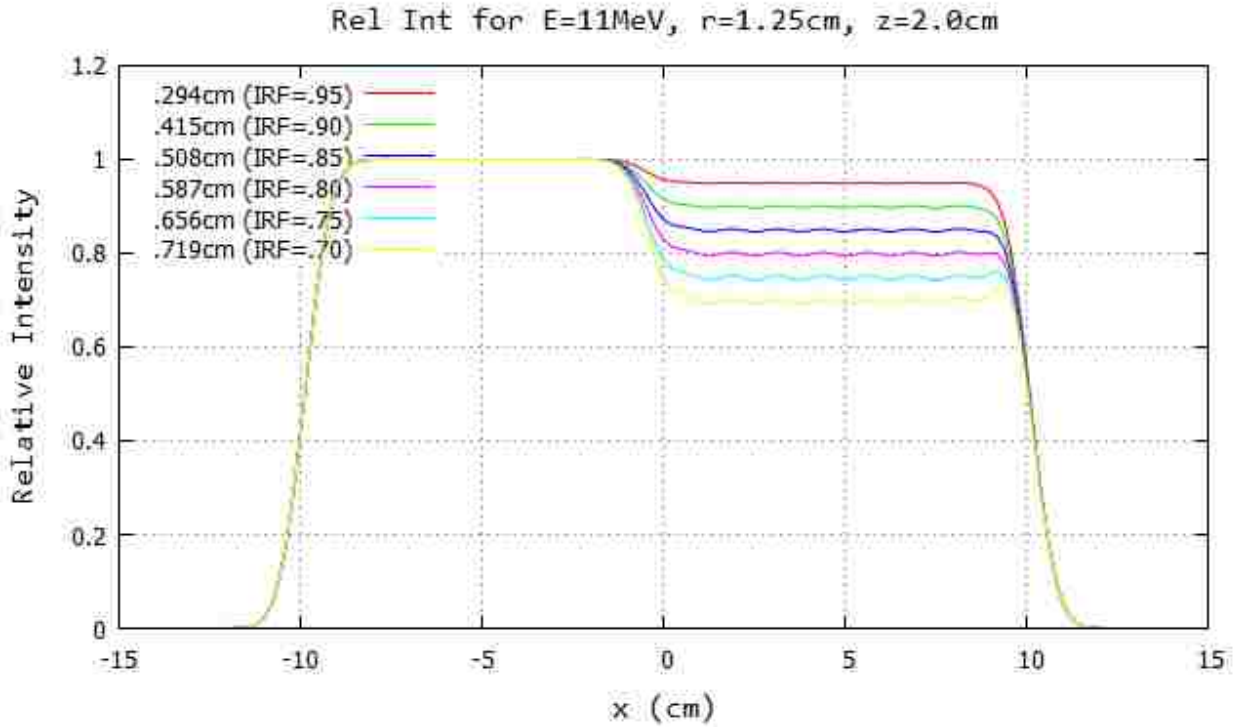


Figure B.54: Profile for 11 MeV and 103 cm SSD at y=0cm 20x20 half-blocked field. The computed island block diameter for 0.70, 0.75, 0.80, 0.85, 0.90, and 0.95 IRF values are listed in each plot's inserted key.

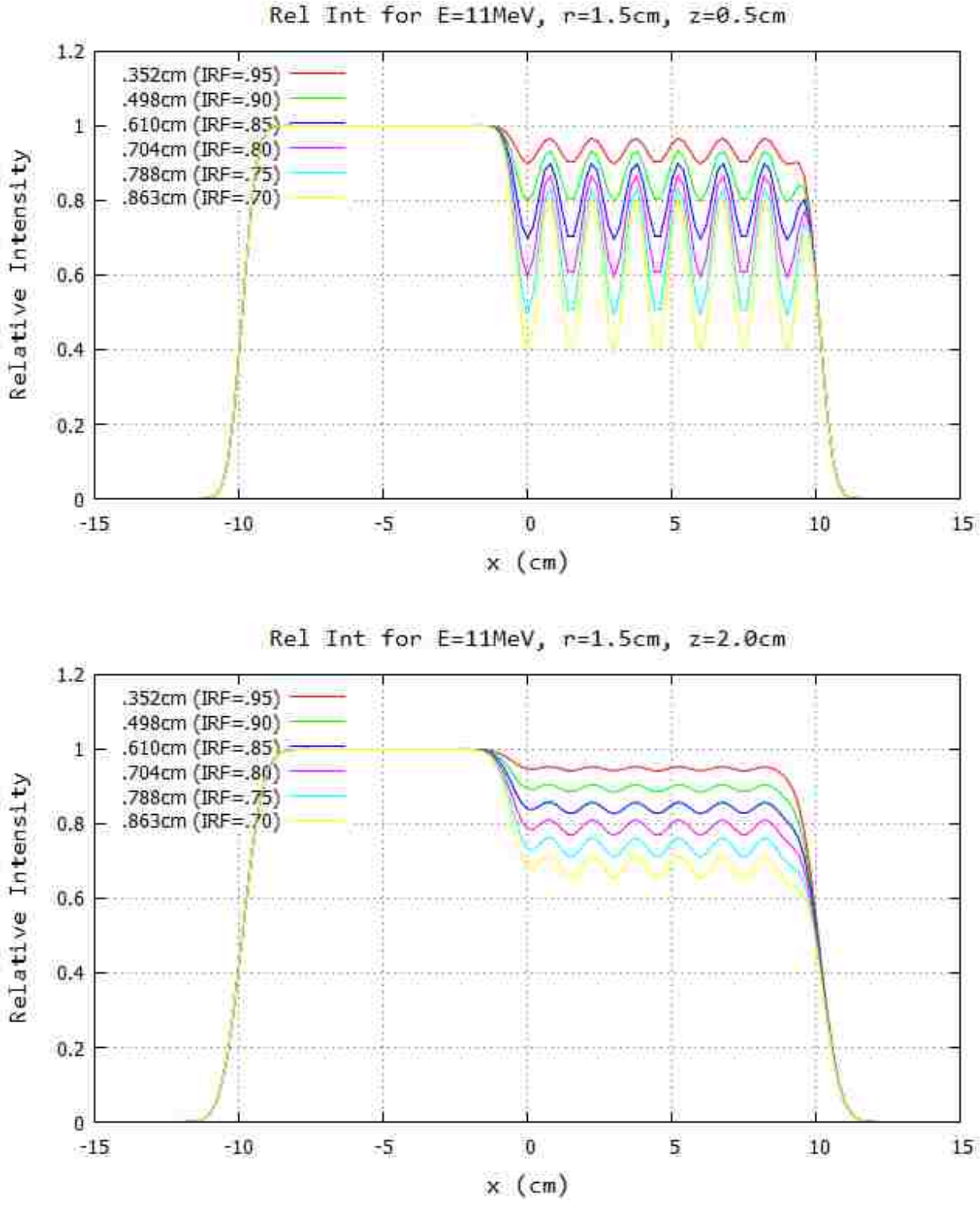


Figure B.55: Profile for 11 MeV and 103 cm SSD at y=0cm 20x20 half-blocked field. The computed island block diameter for 0.70, 0.75, 0.80, 0.85, 0.90, and 0.95 IRF values are listed in each plot's inserted key.

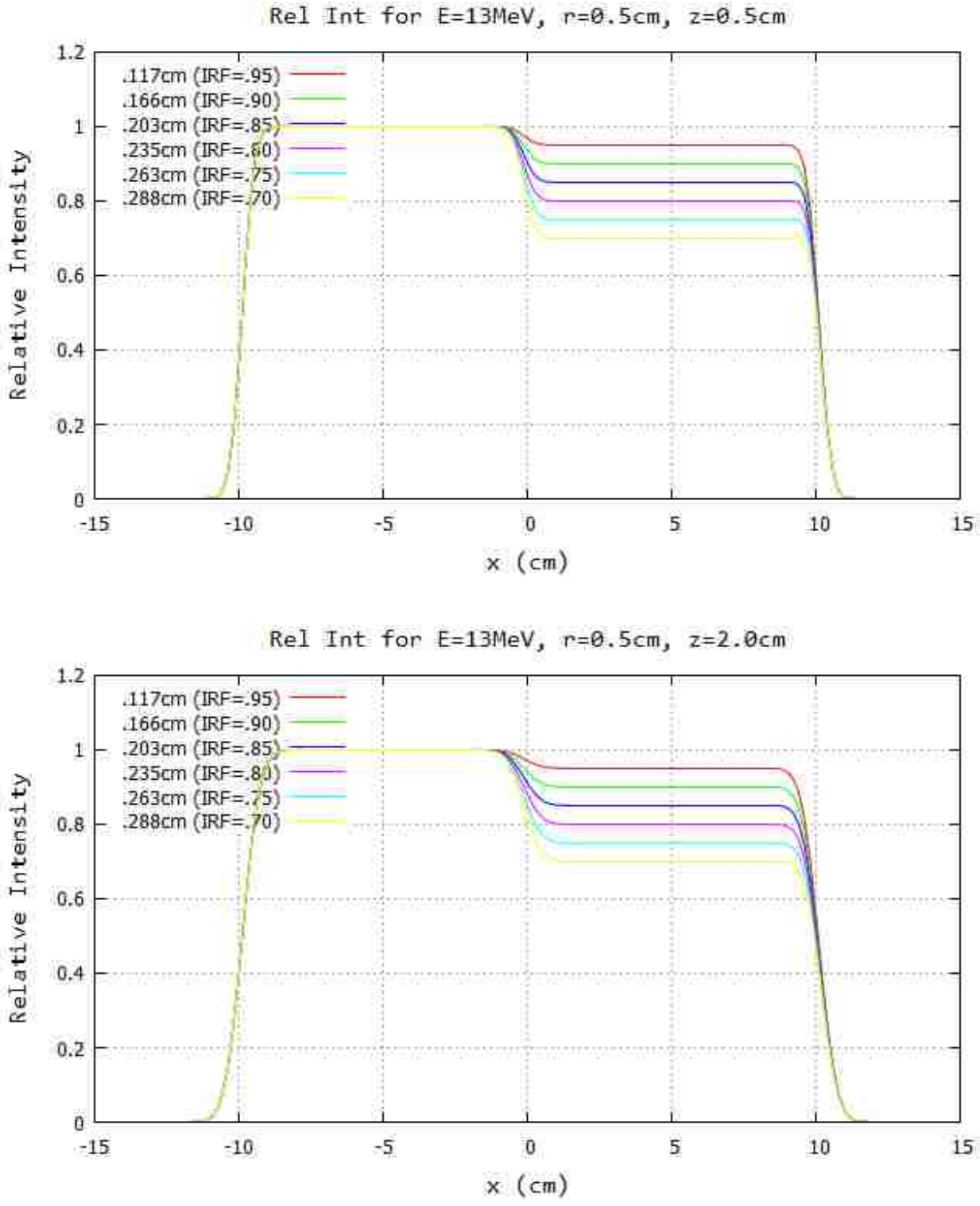


Figure B.56: Profile for 13 MeV and 103 cm SSD at y=0cm 20x20 half-blocked field. The computed island block diameter for 0.70, 0.75, 0.80, 0.85, 0.90, and 0.95 IRF values are listed in each plot's inserted key.

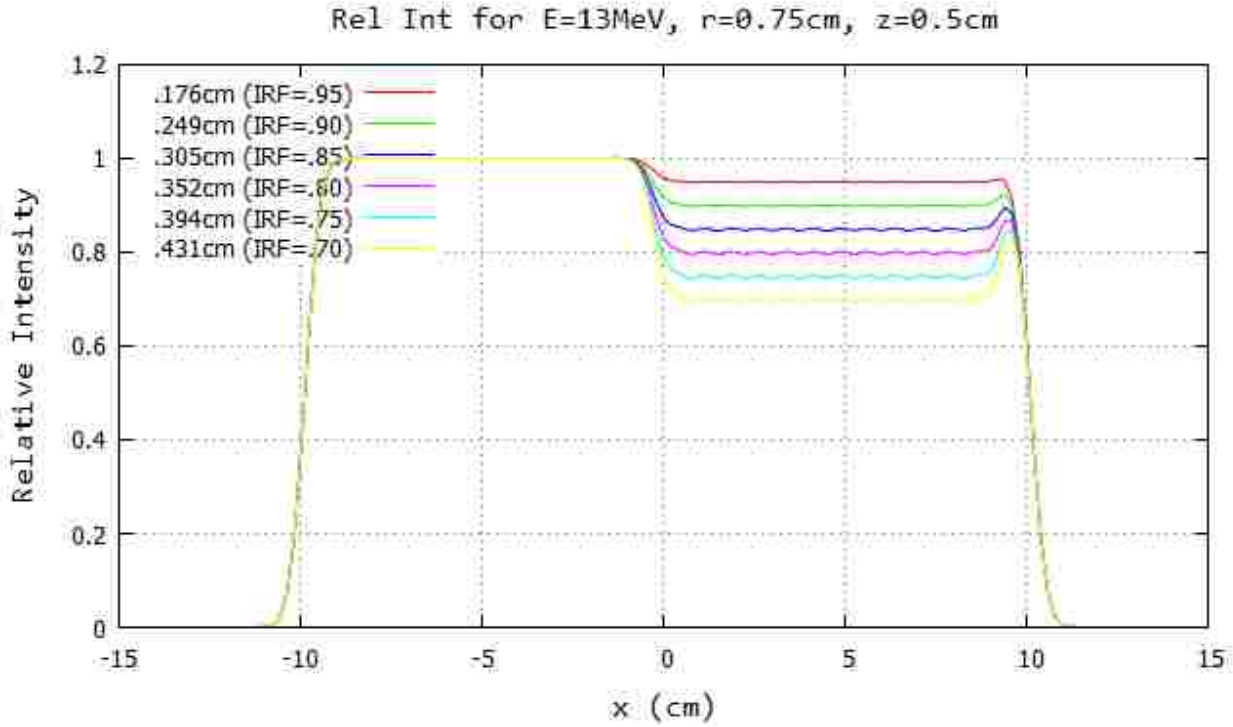


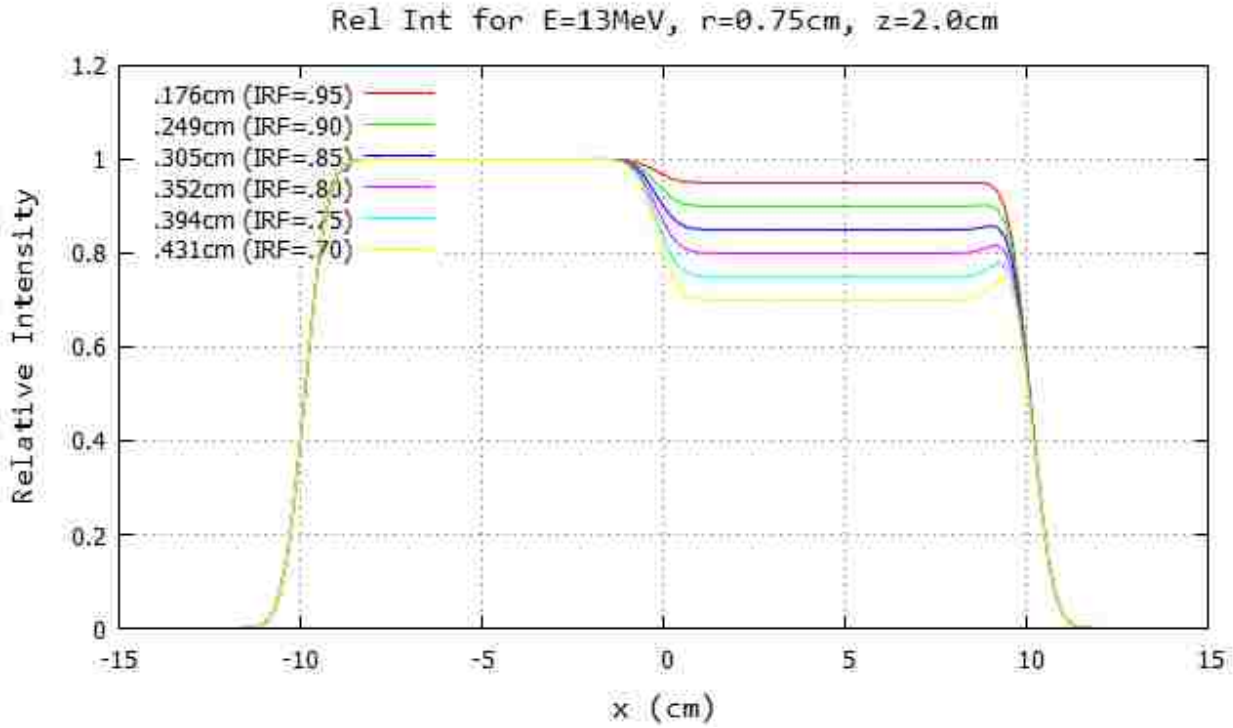


Figure B.57: Profile for 13 MeV and 103 cm SSD at y=0cm 20x20 half-blocked field. The computed island block diameter for 0.70, 0.75, 0.80, 0.85, 0.90, and 0.95 IRF values are listed in each plot's inserted key.

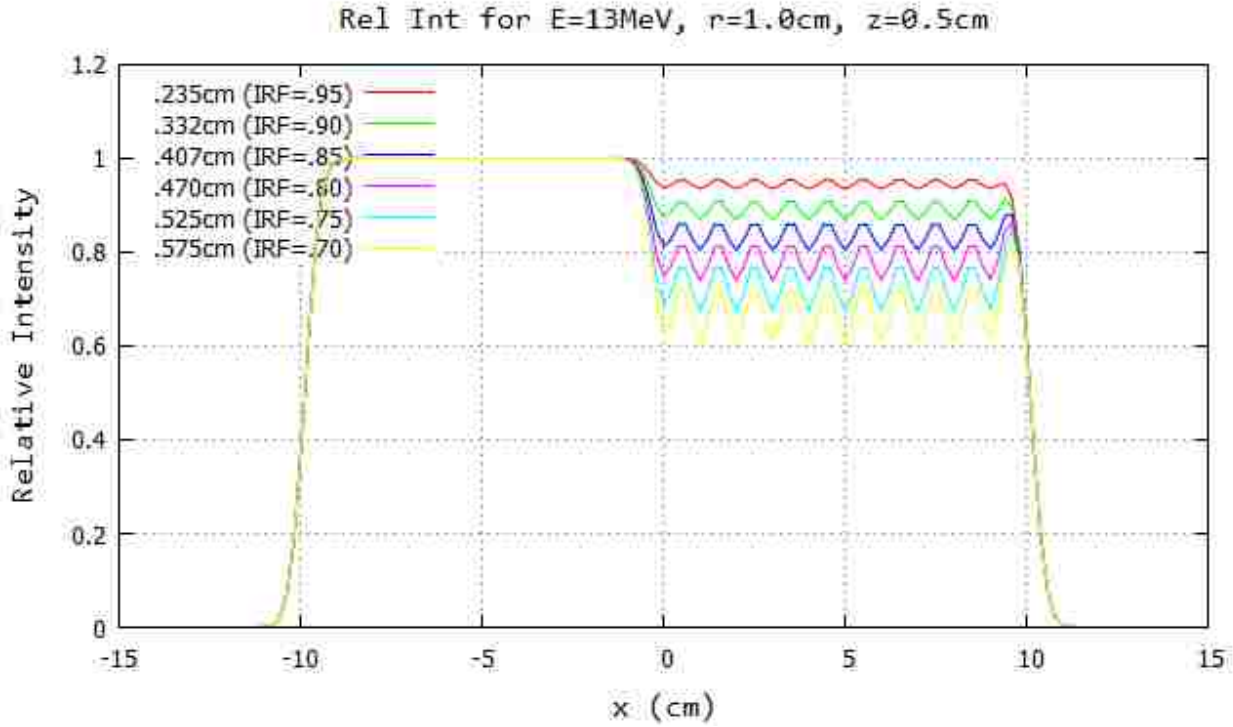


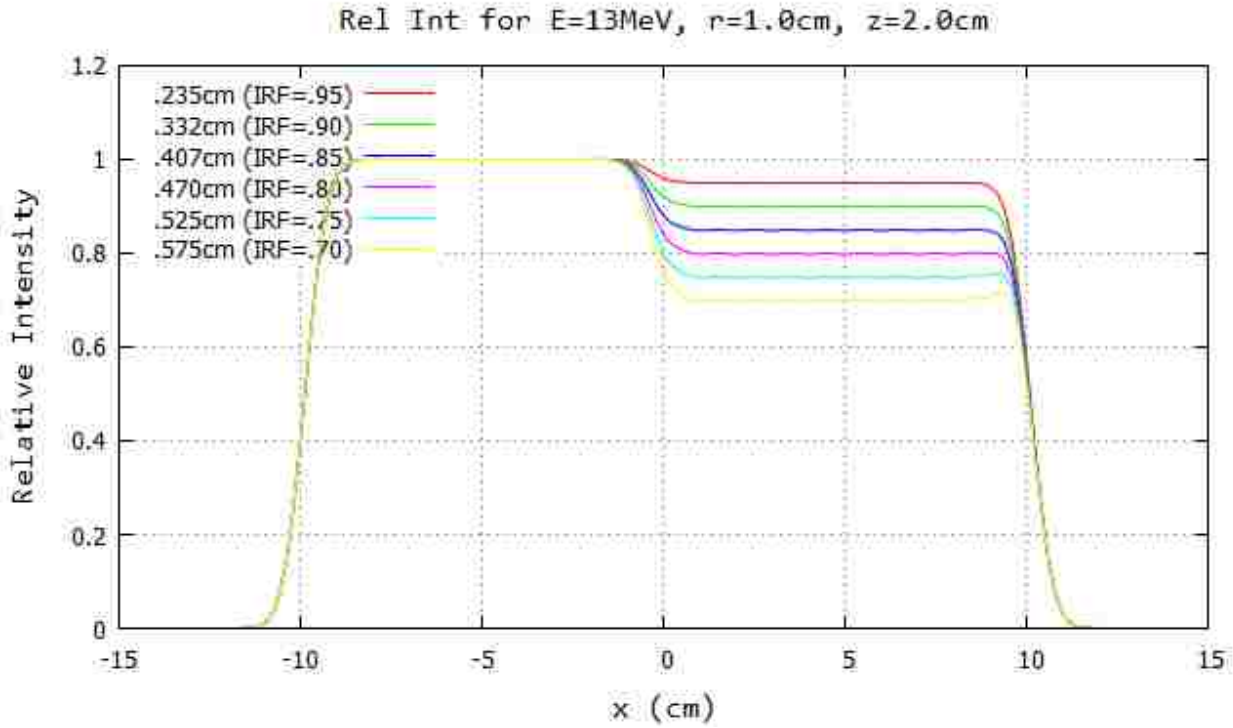


Figure B.58: Profile for 13 MeV and 103 cm SSD at y=0cm 20x20 half-blocked field. The computed island block diameter for 0.70, 0.75, 0.80, 0.85, 0.90, and 0.95 IRF values are listed in each plot's inserted key.

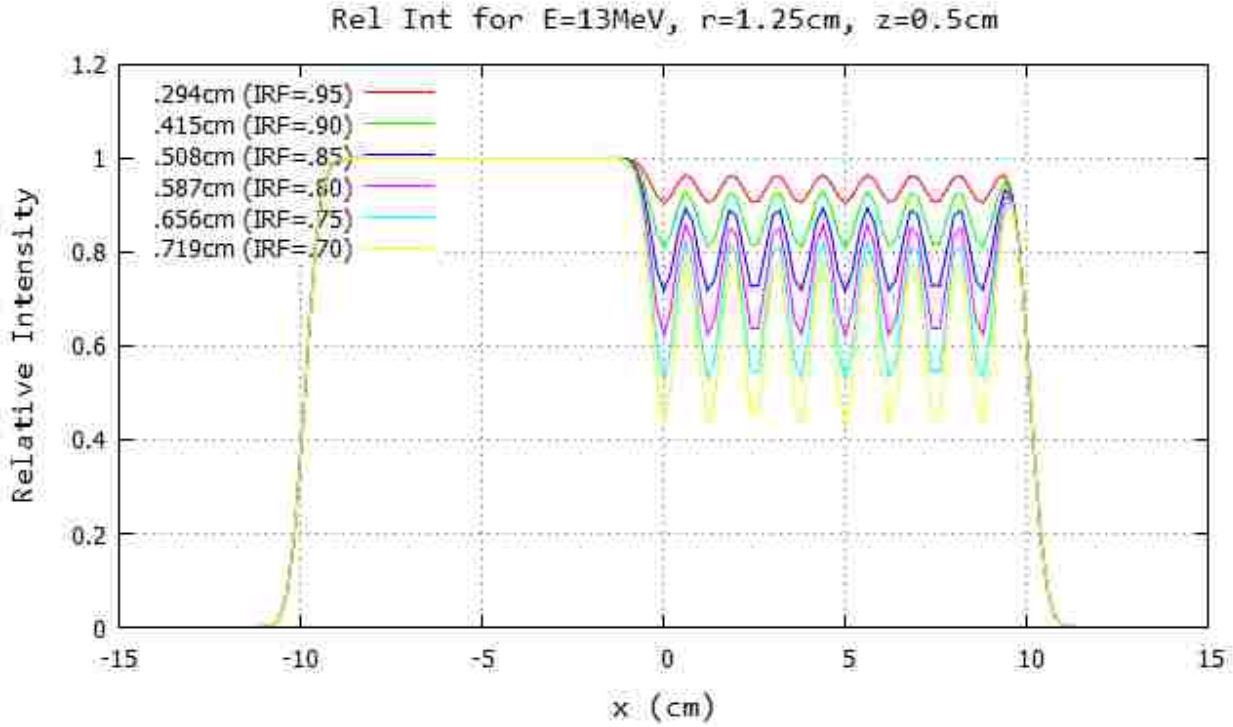


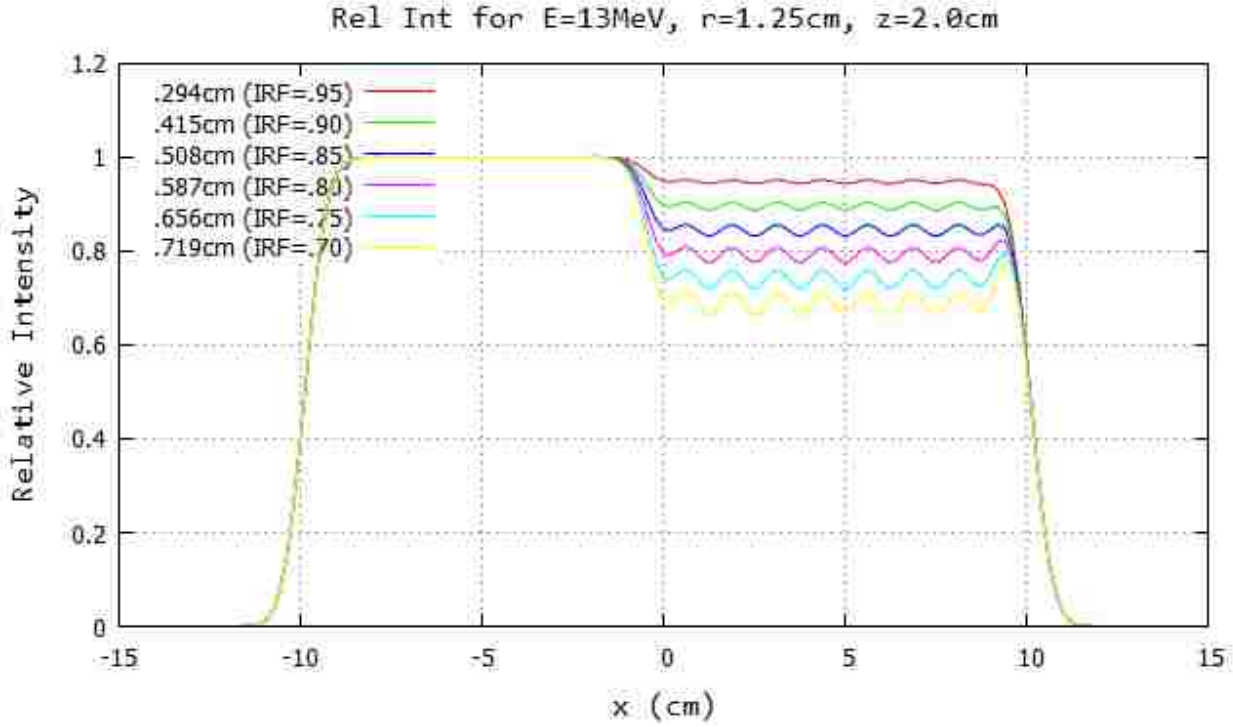


Figure B.59: Profile for 13 MeV and 103 cm SSD at y=0cm 20x20 half-blocked field. The computed island block diameter for 0.70, 0.75, 0.80, 0.85, 0.90, and 0.95 IRF values are listed in each plot's inserted key.

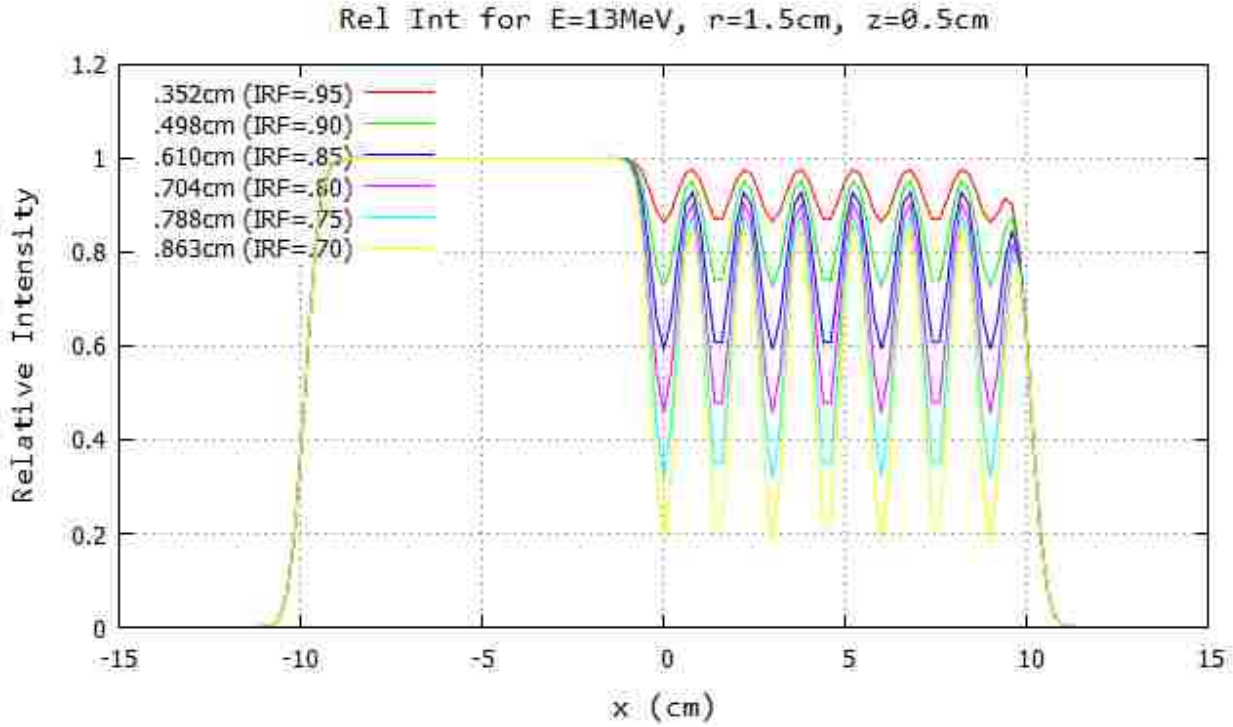


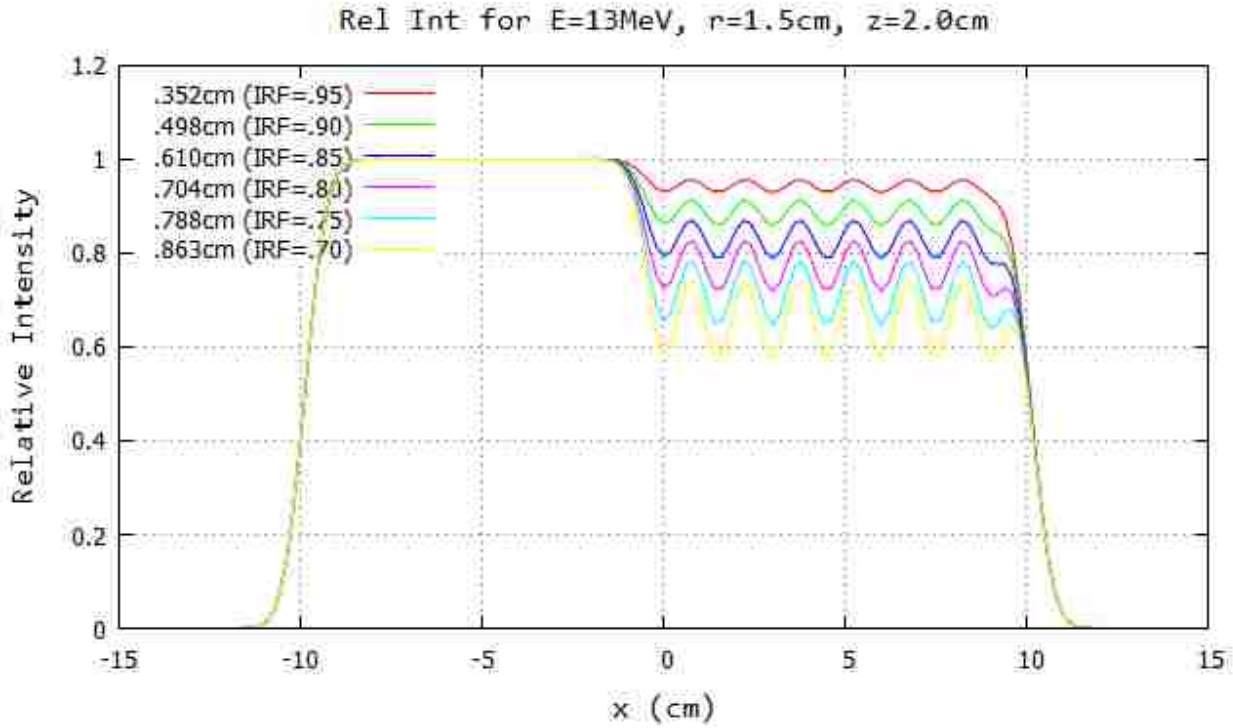


Figure B.60: Profile for 13 MeV and 103 cm SSD at y=0cm 20x20 half-blocked field. The computed island block diameter for 0.70, 0.75, 0.80, 0.85, 0.90, and 0.95 IRF values are listed in each plot's inserted key.

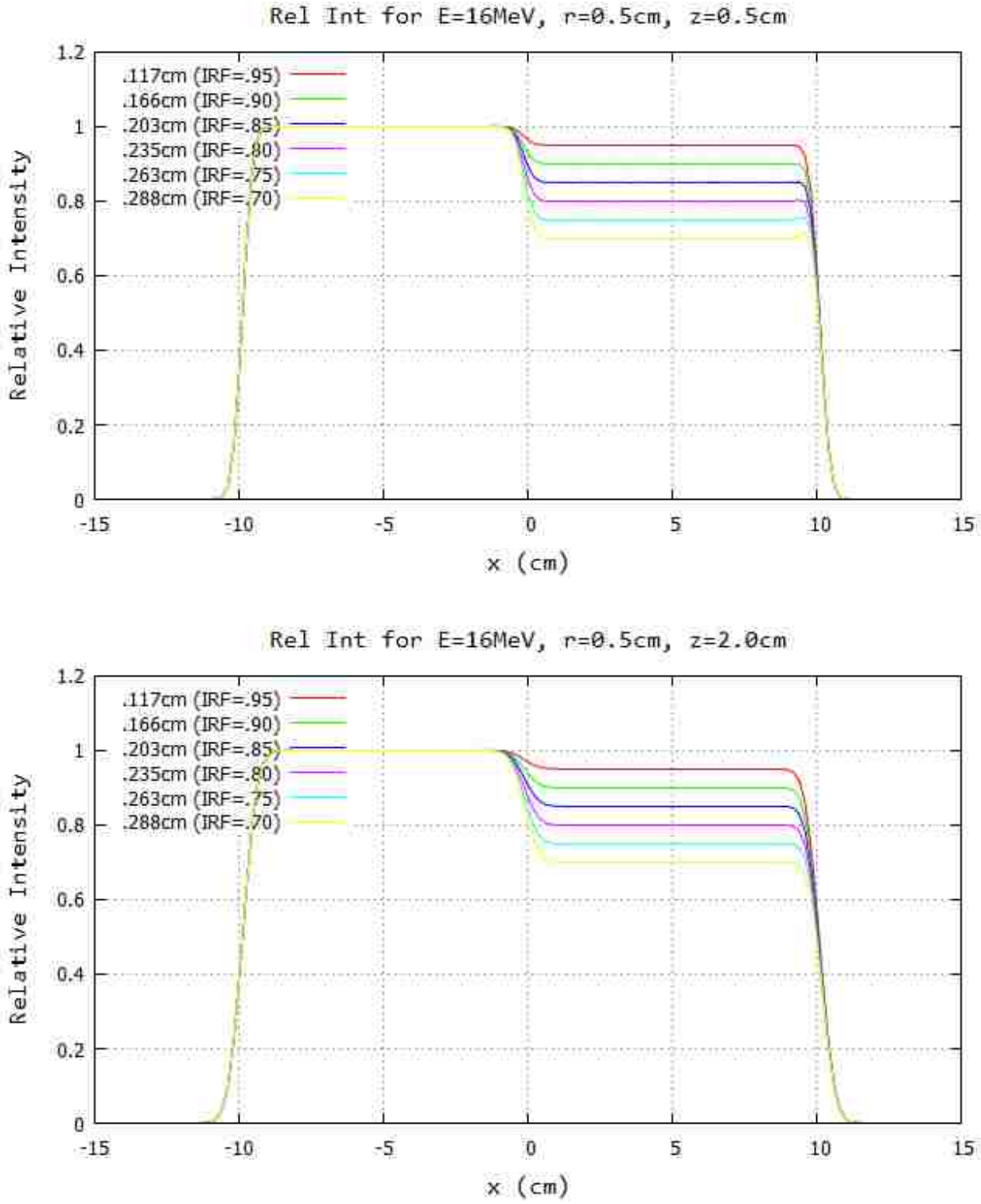


Figure B.61: Profile for 16 MeV and 103 cm SSD at y=0cm 20x20 half-blocked field. The computed island block diameter for 0.70, 0.75, 0.80, 0.85, 0.90, and 0.95 IRF values are listed in each plot's inserted key.

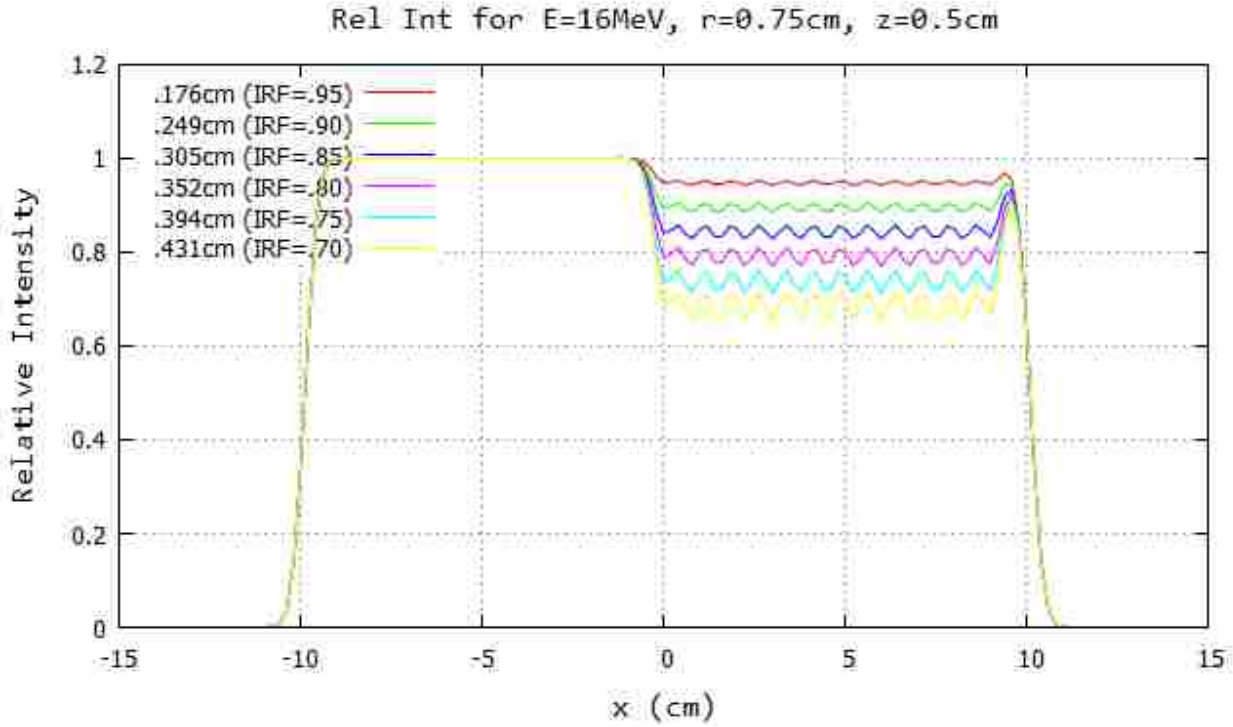


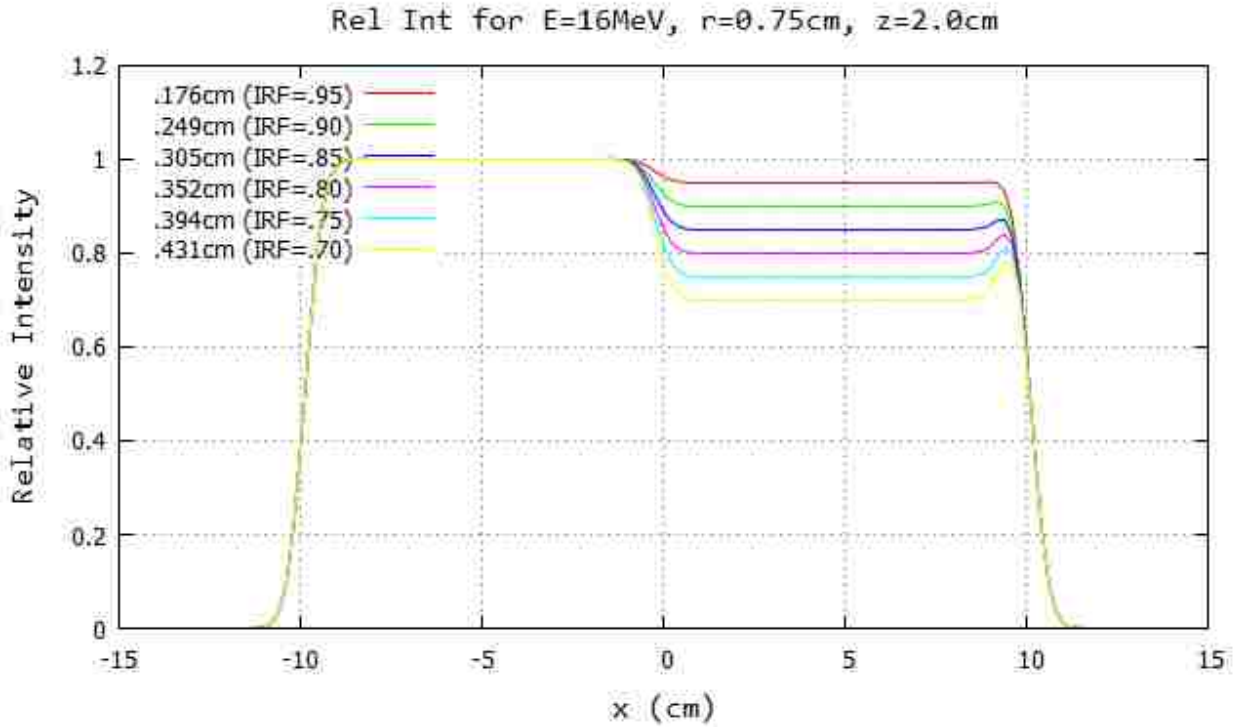


Figure B.62: Profile for 16 MeV and 103 cm SSD at y=0cm 20x20 half-blocked field. The computed island block diameter for 0.70, 0.75, 0.80, 0.85, 0.90, and 0.95 IRF values are listed in each plot's inserted key.

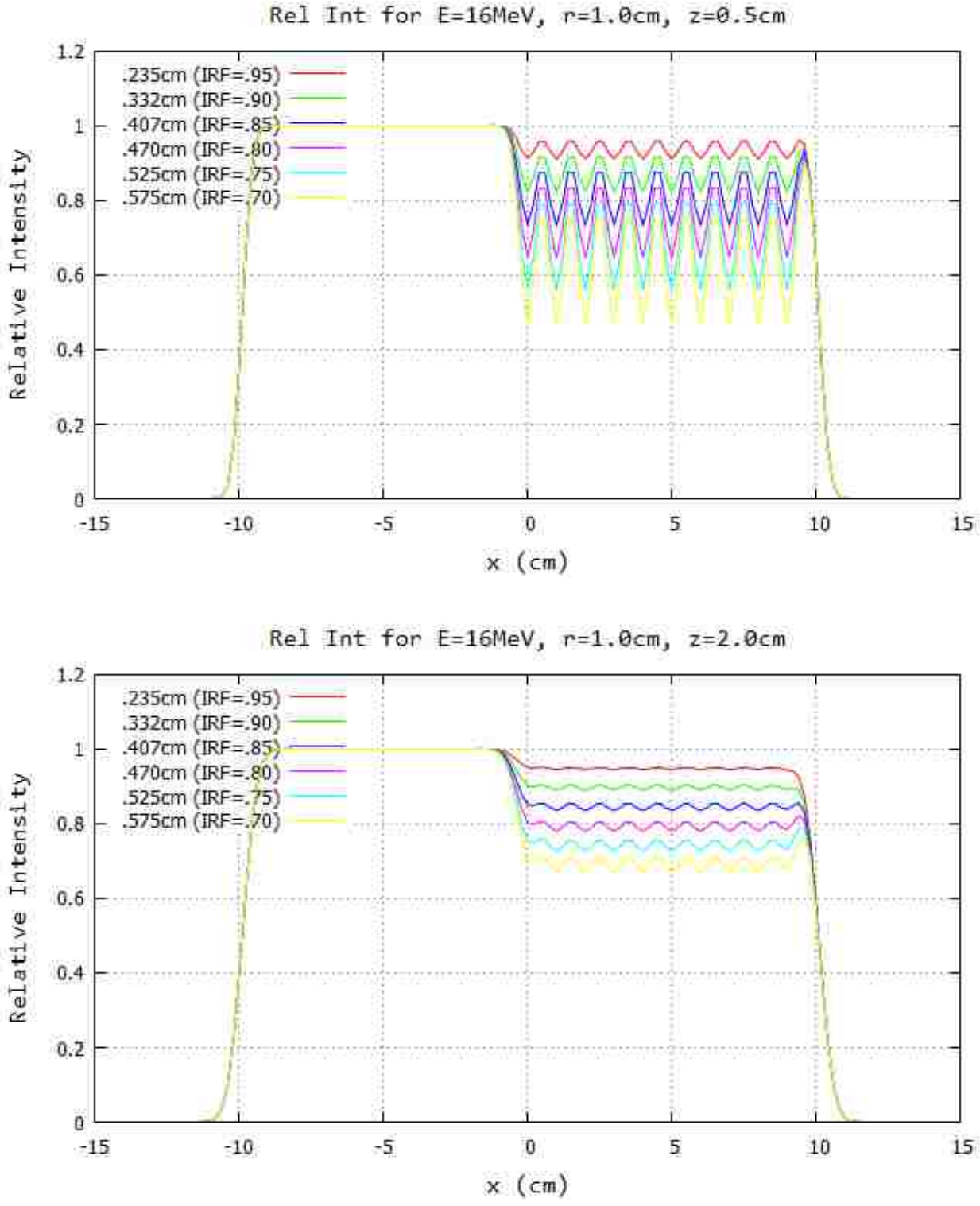


Figure B.63: Profile for 16 MeV and 103 cm SSD at y=0cm 20x20 half-blocked field. The computed island block diameter for 0.70, 0.75, 0.80, 0.85, 0.90, and 0.95 IRF values are listed in each plot's inserted key.

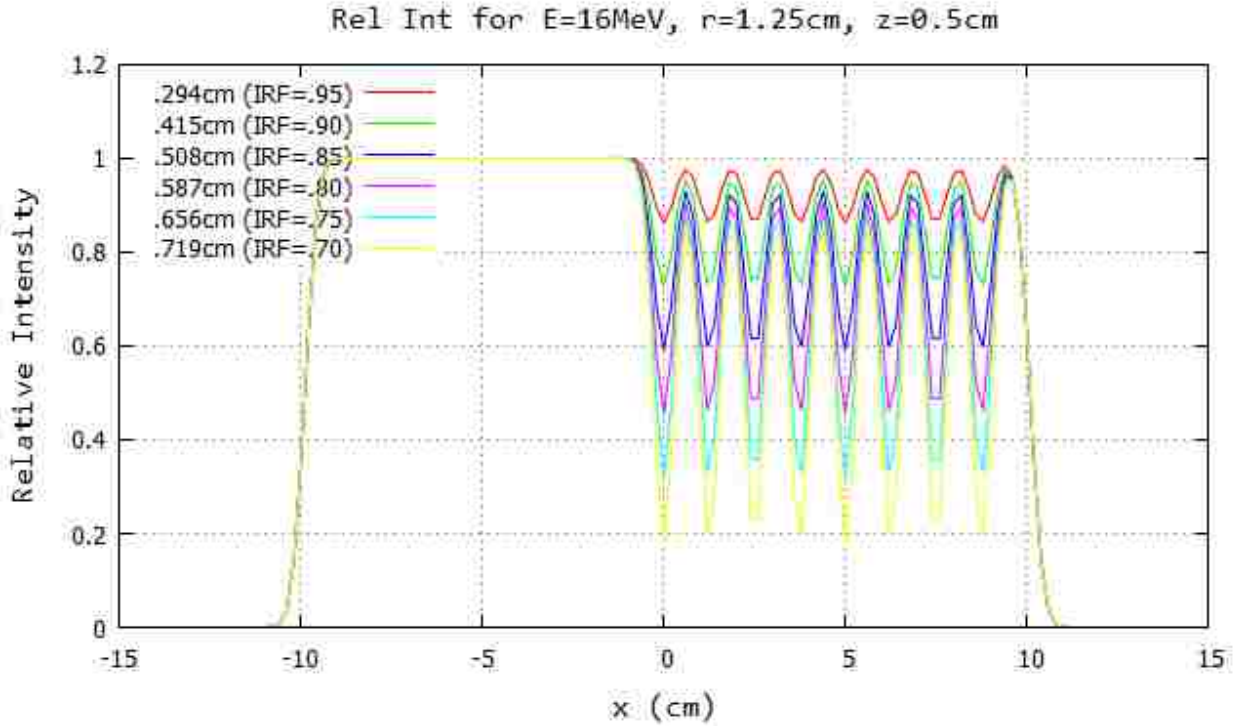


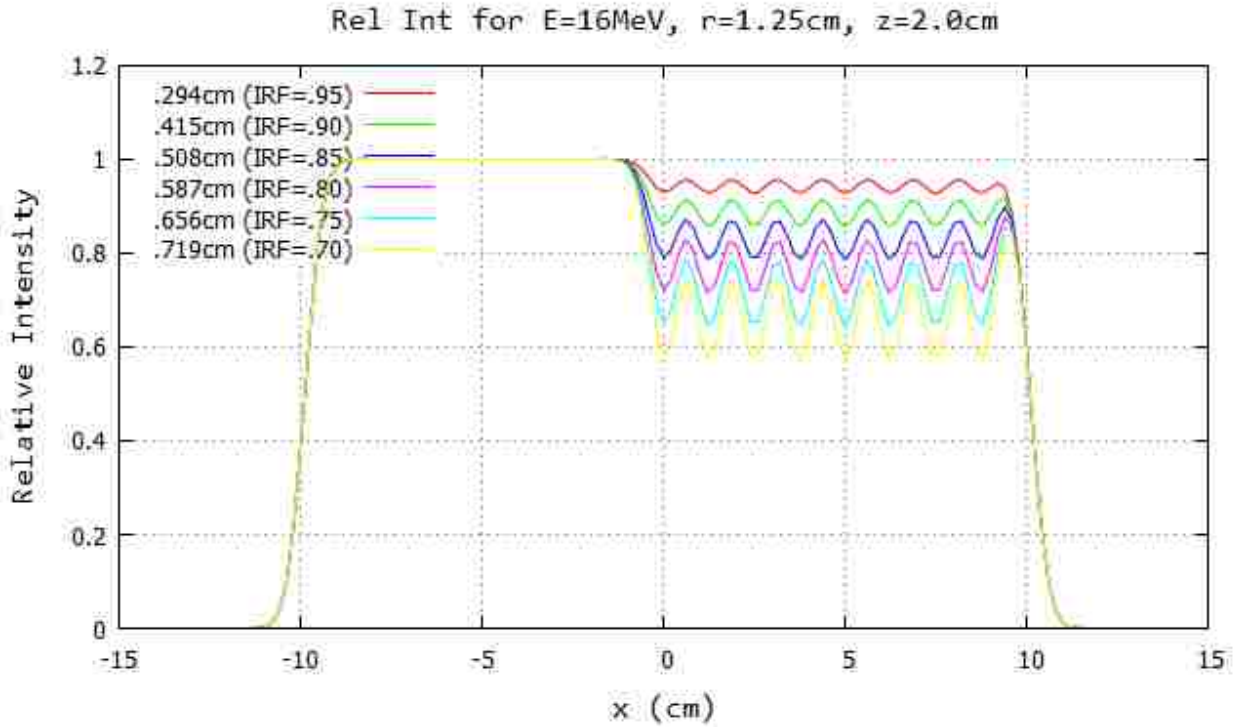


Figure B.64: Profile for 16 MeV and 103 cm SSD at y=0cm 20x20 half-blocked field. The computed island block diameter for 0.70, 0.75, 0.80, 0.85, 0.90, and 0.95 IRF values are listed in each plot's inserted key.

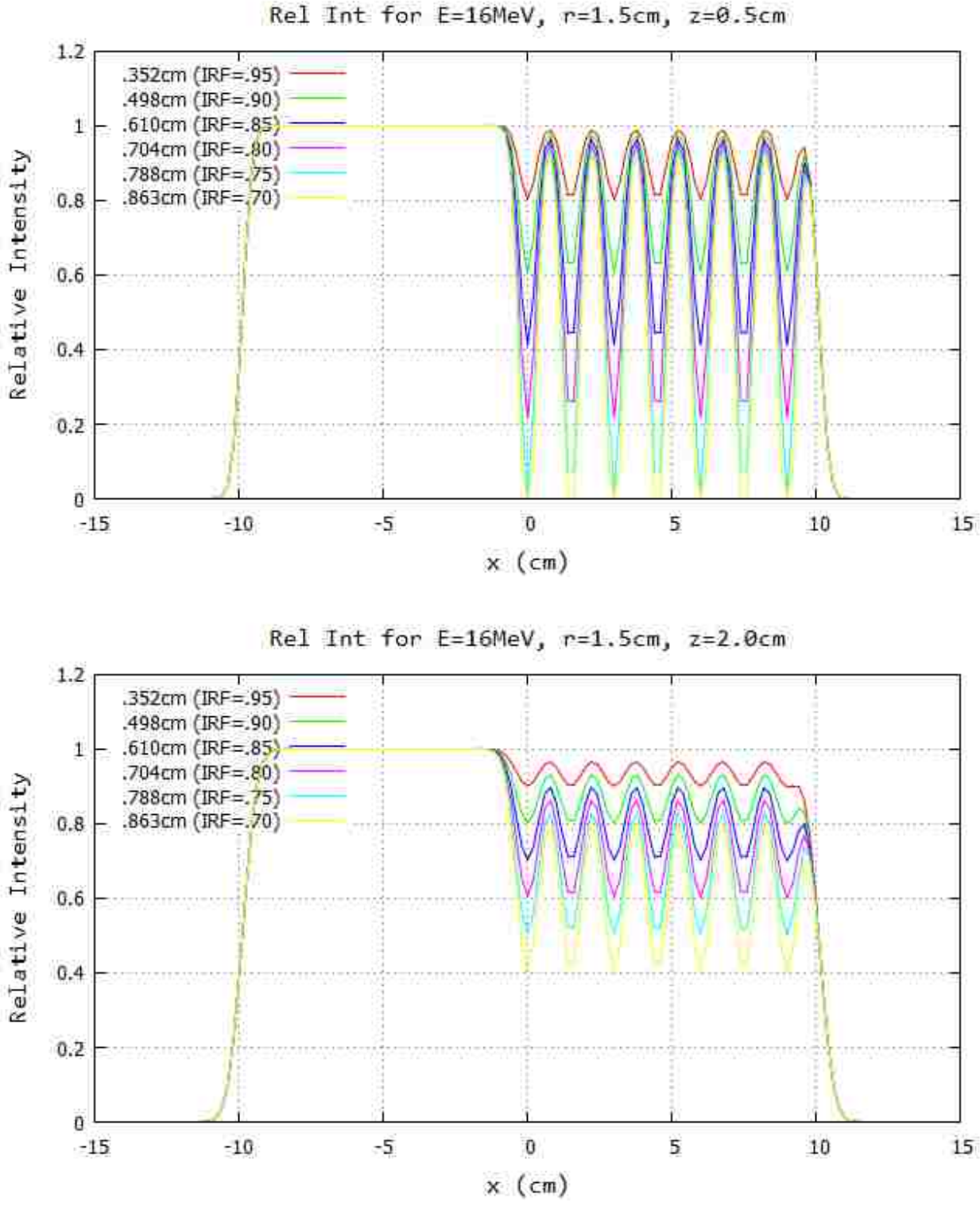


Figure B.65: Profile for 16 MeV and 103 cm SSD at y=0cm 20x20 half-blocked field. The computed island block diameter for 0.70, 0.75, 0.80, 0.85, 0.90, and 0.95 IRF values are listed in each plot's inserted key.

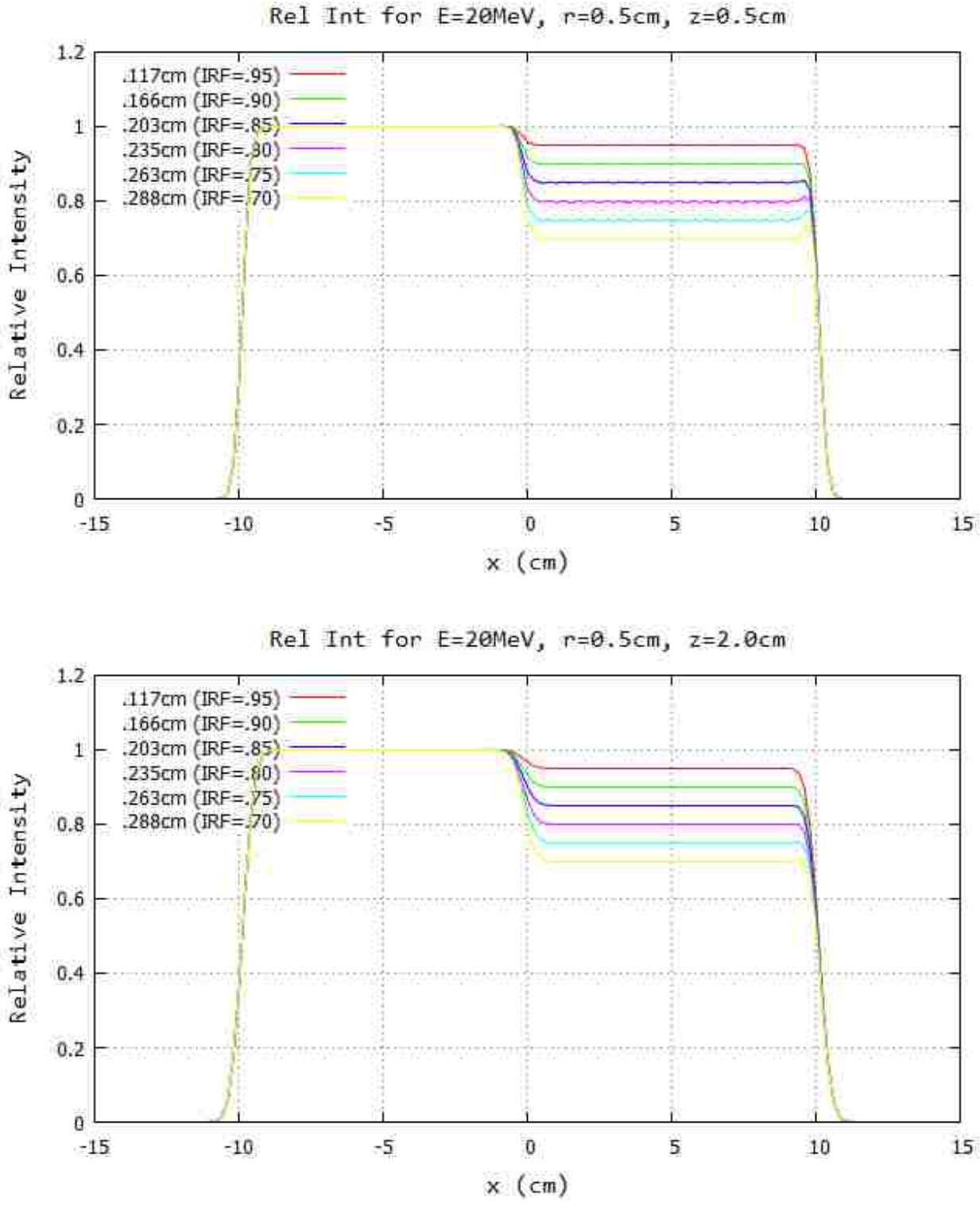


Figure B.66: Profile for 20 MeV and 103 cm SSD at y=0cm 20x20 half-blocked field. The computed island block diameter for 0.70, 0.75, 0.80, 0.85, 0.90, and 0.95 IRF values are listed in each plot's inserted key.

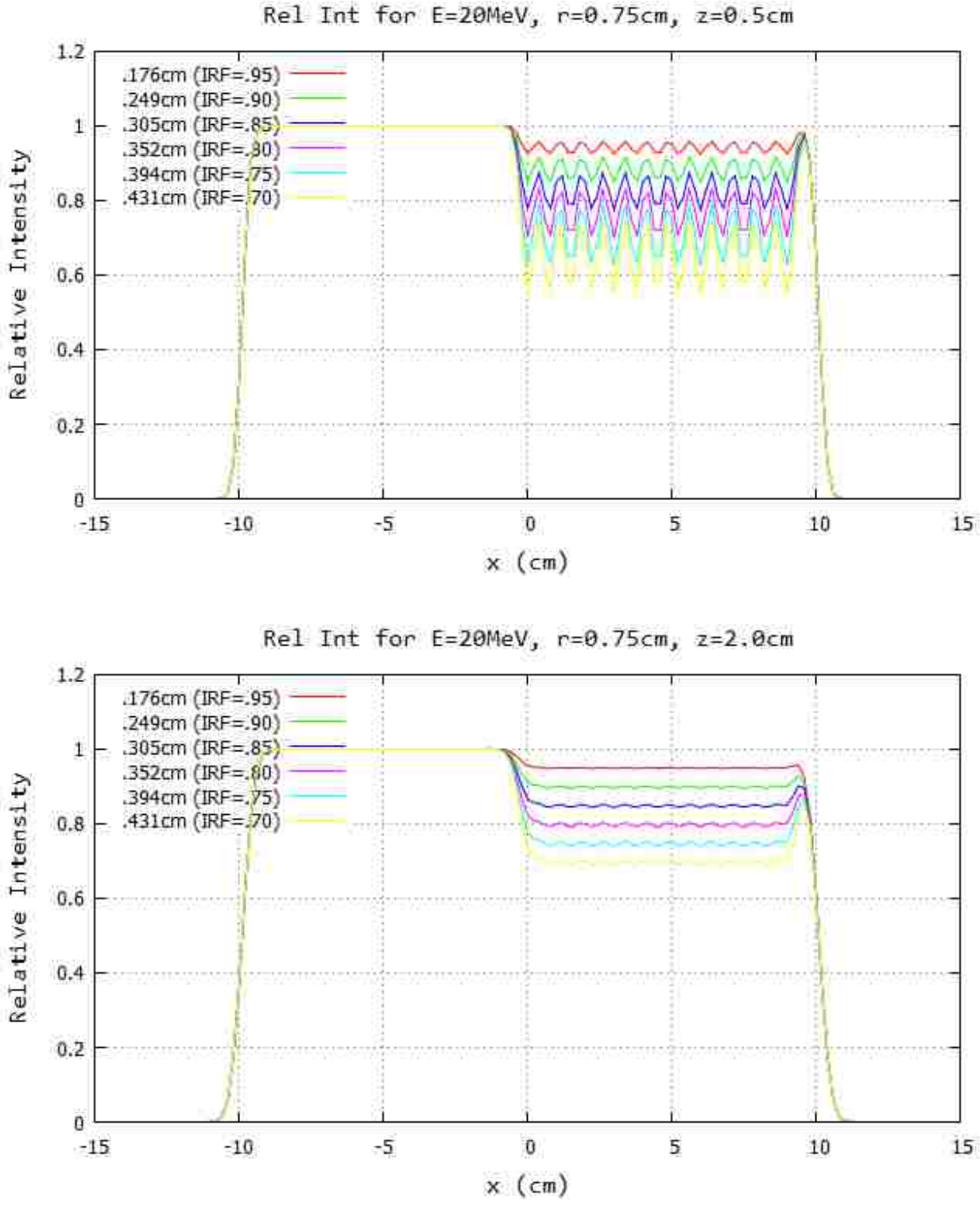


Figure B.67: Profile for 16 MeV and 103 cm SSD at y=0cm 20x20 half-blocked field. The computed island block diameter for 0.70, 0.75, 0.80, 0.85, 0.90, and 0.95 IRF values are listed in each plot's inserted key.

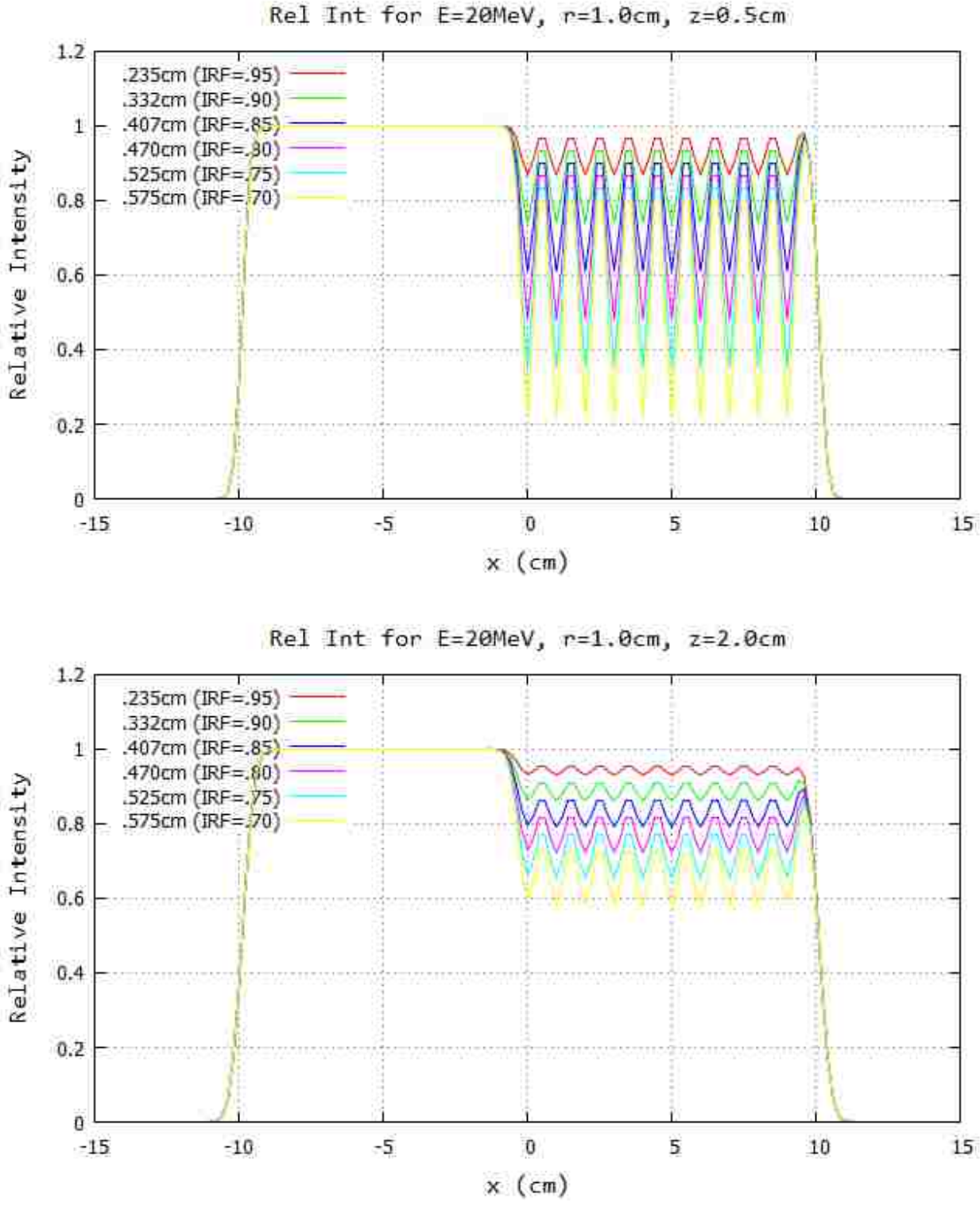


Figure B.68: Profile for 16 MeV and 103 cm SSD at y=0cm 20x20 half-blocked field. The computed island block diameter for 0.70, 0.75, 0.80, 0.85, 0.90, and 0.95 IRF values are listed in each plot's inserted key.

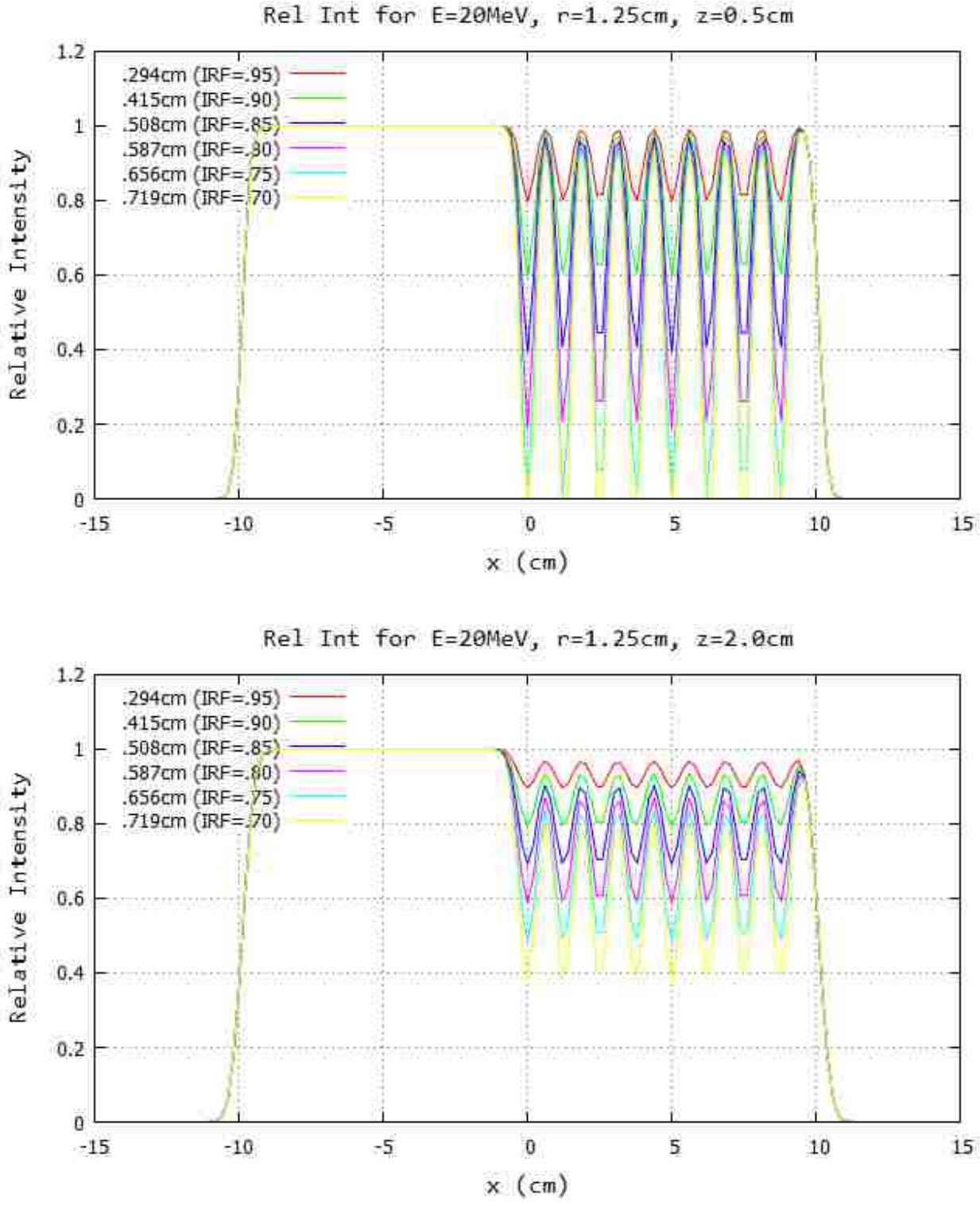


Figure B.69: Profile for 16 MeV and 103 cm SSD at y=0cm 20x20 half-blocked field. The computed island block diameter for 0.70, 0.75, 0.80, 0.85, 0.90, and 0.95 IRF values are listed in each plot's inserted key.

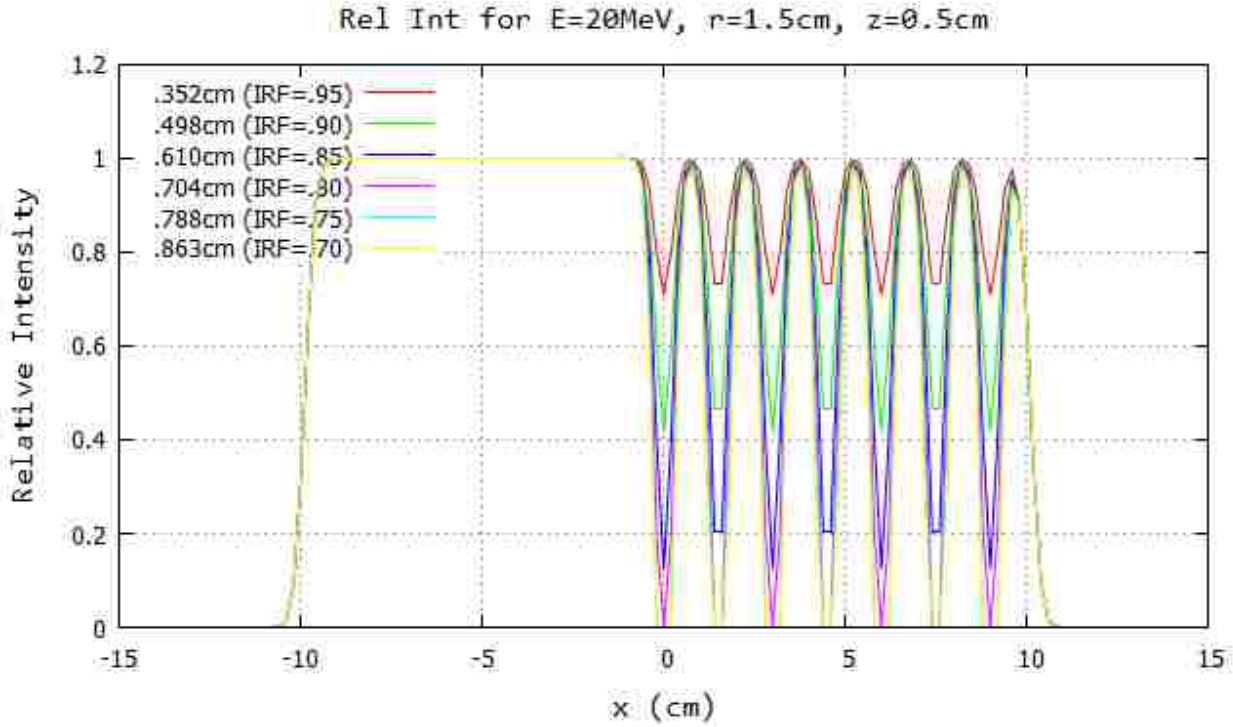


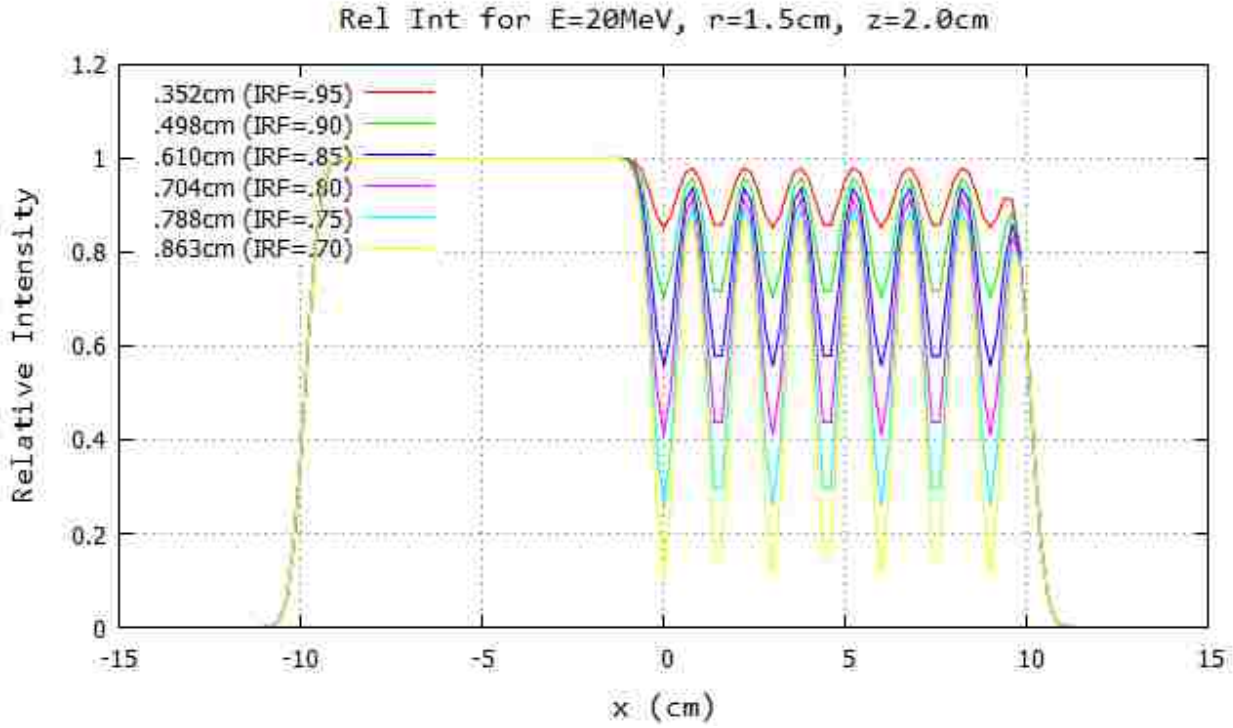


Figure B.70: Profile for 16 MeV and 103 cm SSD at y=0cm 20x20 half-blocked field. The computed island block diameter for 0.70, 0.75, 0.80, 0.85, 0.90, and 0.95 IRF values are listed in each plot's inserted key.

# APPENDIX C
# METRICS SUMMARIES FOR BLOCK PACKING GEOMETRIES CALCULATED WITH PBA

| Table | SSD (cm) | Energy (MeV) | z (cm) | r (cm) | IRF |
|---|---|---|---|---|---|
| C.1 | 100 | 7 | 0.5, 2.0 | 0.5, 0.75, 1.0, 1.25, 1.5 | 0.70, 0.75, 0.80, 0.85, 0.90, 0.95 |
| C.2 | 100 | 9 | 0.5, 2.0 | 0.5, 0.75, 1.0, 1.25, 1.5 | 0.70, 0.75, 0.80, 0.85, 0.90, 0.95 |
| C.3 | 100 | 10 | 0.5, 2.0 | 0.5, 0.75, 1.0, 1.25, 1.5 | 0.70, 0.75, 0.80, 0.85, 0.90, 0.95 |
| C.4 | 100 | 11 | 0.5, 2.0 | 0.5, 0.75, 1.0, 1.25, 1.5 | 0.70, 0.75, 0.80, 0.85, 0.90, 0.95 |
| C.5 | 100 | 13 | 0.5, 2.0 | 0.5, 0.75, 1.0, 1.25, 1.5 | 0.70, 0.75, 0.80, 0.85, 0.90, 0.95 |
| C.6 | 100 | 16 | 0.5, 2.0 | 0.5, 0.75, 1.0, 1.25, 1.5 | 0.70, 0.75, 0.80, 0.85, 0.90, 0.95 |
| C.7 | 100 | 20 | 0.5, 2.0 | 0.5, 0.75, 1.0, 1.25, 1.5 | 0.70, 0.75, 0.80, 0.85, 0.90, 0.95 |
| C.8 | 103 | 7 | 0.5, 2.0 | 0.5, 0.75, 1.0, 1.25, 1.5 | 0.70, 0.75, 0.80, 0.85, 0.90, 0.95 |
| C.9 | 103 | 9 | 0.5, 2.0 | 0.5, 0.75, 1.0, 1.25, 1.5 | 0.70, 0.75, 0.80, 0.85, 0.90, 0.95 |
| C.10 | 103 | 10 | 0.5, 2.0 | 0.5, 0.75, 1.0, 1.25, 1.5 | 0.70, 0.75, 0.80, 0.85, 0.90, 0.95 |
| C.11 | 103 | 11 | 0.5, 2.0 | 0.5, 0.75, 1.0, 1.25, 1.5 | 0.70, 0.75, 0.80, 0.85, 0.90, 0.95 |
| C.12 | 103 | 13 | 0.5, 2.0 | 0.5, 0.75, 1.0, 1.25, 1.5 | 0.70, 0.75, 0.80, 0.85, 0.90, 0.95 |
| C.13 | 103 | 16 | 0.5, 2.0 | 0.5, 0.75, 1.0, 1.25, 1.5 | 0.70, 0.75, 0.80, 0.85, 0.90, 0.95 |
| C.14 | 103 | 20 | 0.5, 2.0 | 0.5, 0.75, 1.0, 1.25, 1.5 | 0.70, 0.75, 0.80, 0.85, 0.90, 0.95 |

Table C.1: Metrics summary for 7 MeV at 100 cm SSD at y=0cm 20x20 half-blocked field for z=0.5cm (left) and z=2.0cm (right).

| r (cm) | IRF | d (cm) | $d_T$ | $\sigma_{d_T}$ | $I_{avg}$ | $\Delta I_R$ | $d_T$ | $\sigma_{d_T}$ | $I_{avg}$ | $\Delta I_R$ |
|---|---|---|---|---|---|---|---|---|---|---|
| | 0.95 | 0.117 | 0.60 | 0.00 | 0.950 | 0.000 | 1.21 | 0.04 | 0.950 | 0.000 |
| | 0.90 | 0.166 | 1.00 | 0.00 | 0.900 | 0.000 | 1.88 | 0.03 | 0.900 | 0.000 |
| 0.50 cm | 0.85 | 0.203 | 1.20 | 0.00 | 0.851 | 0.000 | 2.27 | 0.03 | 0.851 | 0.000 |
| | 0.80 | 0.235 | 1.39 | 0.00 | 0.800 | 0.000 | 2.31 | 0.03 | 0.800 | 0.000 |
| | 0.75 | 0.263 | 1.40 | 0.00 | 0.749 | 0.000 | 2.48 | 0.03 | 0.749 | 0.000 |
| | 0.70 | 0.288 | 1.40 | 0.00 | 0.699 | 0.000 | 2.68 | 0.03 | 0.699 | 0.000 |
| r (cm) | IRF | d (cm) | $d_T$ | $\sigma_{d_T}$ | $I_{avg}$ | $\Delta I_R$ | $d_T$ | $\sigma_{d_T}$ | $I_{avg}$ | $\Delta I_R$ |
| | 0.95 | 0.176 | 0.63 | 0.01 | 0.950 | 0.000 | 1.21 | 0.04 | 0.950 | 0.000 |
| | 0.90 | 0.249 | 0.97 | 0.01 | 0.900 | 0.001 | 1.88 | 0.03 | 0.900 | 0.000 |
| 0.75 cm | 0.85 | 0.305 | 1.17 | 0.01 | 0.850 | 0.001 | 2.10 | 0.03 | 0.850 | 0.000 |
| | 0.80 | 0.352 | 1.20 | 0.00 | 0.800 | 0.002 | 2.47 | 0.03 | 0.800 | 0.000 |
| | 0.75 | 0.394 | 1.27 | 0.01 | 0.750 | 0.002 | 2.49 | 0.03 | 0.750 | 0.000 |
| | 0.70 | 0.431 | 1.40 | 0.00 | 0.701 | 0.003 | 2.67 | 0.03 | 0.701 | 0.000 |
| r (cm) | IRF | d (cm) | $d_T$ | $\sigma_{d_T}$ | $I_{avg}$ | $\Delta I_R$ | $d_T$ | $\sigma_{d_T}$ | $I_{avg}$ | $\Delta I_R$ |
| | 0.95 | 0.235 | 0.55 | 0.01 | 0.950 | 0.010 | 1.20 | 0.04 | 0.950 | 0.000 |
| | 0.90 | 0.332 | 1.20 | 0.04 | 0.900 | 0.019 | 1.87 | 0.03 | 0.900 | 0.000 |
| 1.00 cm | 0.85 | 0.407 | 1.42 | 0.02 | 0.850 | 0.029 | 2.19 | 0.03 | 0.850 | 0.000 |
| | 0.80 | 0.470 | 2.02 | 0.06 | 0.800 | 0.039 | 2.34 | 0.03 | 0.800 | 0.000 |
| | 0.75 | 0.525 | 2.13 | 0.06 | 0.750 | 0.048 | 2.49 | 0.03 | 0.750 | 0.000 |
| | 0.70 | 0.575 | 2.16 | 0.06 | 0.700 | 0.058 | 2.67 | 0.02 | 0.700 | 0.000 |
| r (cm) | IRF | d (cm) | $d_T$ | $\sigma_{d_T}$ | $I_{avg}$ | $\Delta I_R$ | $d_T$ | $\sigma_{d_T}$ | $I_{avg}$ | $\Delta I_R$ |
| | 0.95 | 0.294 | 1.71 | 0.07 | 0.950 | 0.039 | 1.16 | 0.04 | 0.950 | 0.000 |
| | 0.90 | 0.415 | 2.04 | 0.07 | 0.900 | 0.077 | 1.85 | 0.02 | 0.900 | 0.000 |
| 1.25 cm | 0.85 | 0.508 | 1.95 | 0.06 | 0.850 | 0.116 | 2.15 | 0.03 | 0.850 | 0.000 |
| | 0.80 | 0.587 | 1.98 | 0.06 | 0.800 | 0.154 | 2.30 | 0.02 | 0.800 | 0.000 |
| | 0.75 | 0.656 | 1.99 | 0.06 | 0.751 | 0.193 | 2.49 | 0.02 | 0.750 | 0.001 |
| | 0.70 | 0.719 | 1.97 | 0.06 | 0.700 | 0.232 | 2.61 | 0.02 | 0.700 | 0.001 |
| r (cm) | IRF | d (cm) | $d_T$ | $\sigma_{d_T}$ | $I_{avg}$ | $\Delta I_R$ | $d_T$ | $\sigma_{d_T}$ | $I_{avg}$ | $\Delta I_R$ |
| | 0.95 | 0.352 | 1.86 | 0.08 | 0.951 | 0.082 | 1.11 | 0.04 | 0.950 | 0.001 |
| | 0.90 | 0.498 | 2.11 | 0.07 | 0.901 | 0.163 | 1.82 | 0.03 | 0.900 | 0.003 |
| 1.50 cm | 0.85 | 0.610 | 2.36 | 0.06 | 0.852 | 0.245 | 2.05 | 0.03 | 0.850 | 0.004 |
| | 0.80 | 0.704 | 2.38 | 0.06 | 0.803 | 0.326 | 2.34 | 0.03 | 0.800 | 0.005 |
| | 0.75 | 0.788 | 2.41 | 0.05 | 0.753 | 0.409 | 2.41 | 0.03 | 0.750 | 0.006 |
| | 0.70 | 0.863 | 2.19 | 0.05 | 0.703 | 0.491 | 2.56 | 0.03 | 0.700 | 0.008 |

Table C.2: Metrics summary for 9 MeV at 100 cm SSD at y=0cm 20x20 half-blocked field for z=0.5cm (left) and z=2.0cm (right).

| r (cm) | IRF | d (cm) | $d_T$ | $\sigma_{d_T}$ | $I_{avg}$ | $\Delta I_R$ | $d_T$ | $\sigma_{d_T}$ | $I_{avg}$ | $\Delta I_R$ |
|---|---|---|---|---|---|---|---|---|---|---|
| | 0.95 | 0.117 | 0.60 | 0.00 | 0.950 | 0.000 | 1.05 | 0.03 | 0.950 | 0.000 |
| | 0.90 | 0.166 | 0.80 | 0.00 | 0.900 | 0.000 | 1.47 | 0.03 | 0.900 | 0.000 |
| 0.50 cm | 0.85 | 0.203 | 1.00 | 0.00 | 0.851 | 0.000 | 1.85 | 0.03 | 0.851 | 0.000 |
| | 0.80 | 0.235 | 1.00 | 0.00 | 0.800 | 0.000 | 1.87 | 0.03 | 0.800 | 0.000 |
| | 0.75 | 0.263 | 1.00 | 0.00 | 0.749 | 0.000 | 1.88 | 0.03 | 0.749 | 0.000 |
| | 0.70 | 0.288 | 1.11 | 0.01 | 0.699 | 0.000 | 2.06 | 0.03 | 0.699 | 0.000 |
| r (cm) | IRF | d (cm) | $d_T$ | $\sigma_{d_T}$ | $I_{avg}$ | $\Delta I_R$ | $d_T$ | $\sigma_{d_T}$ | $I_{avg}$ | $\Delta I_R$ |
| | 0.95 | 0.176 | 0.48 | 0.01 | 0.950 | 0.006 | 0.87 | 0.03 | 0.950 | 0.000 |
| | 0.90 | 0.249 | 0.69 | 0.01 | 0.900 | 0.011 | 1.49 | 0.03 | 0.900 | 0.000 |
| 0.75 cm | 0.85 | 0.305 | 1.11 | 0.03 | 0.850 | 0.017 | 1.67 | 0.03 | 0.850 | 0.000 |
| | 0.80 | 0.352 | 1.23 | 0.02 | 0.800 | 0.023 | 1.87 | 0.03 | 0.800 | 0.000 |
| | 0.75 | 0.394 | 1.60 | 0.08 | 0.750 | 0.029 | 2.06 | 0.03 | 0.750 | 0.000 |
| | 0.70 | 0.431 | 2.04 | 0.09 | 0.701 | 0.034 | 2.06 | 0.03 | 0.701 | 0.000 |
| r (cm) | IRF | d (cm) | $d_T$ | $\sigma_{d_T}$ | $I_{avg}$ | $\Delta I_R$ | $d_T$ | $\sigma_{d_T}$ | $I_{avg}$ | $\Delta I_R$ |
| | 0.95 | 0.235 | 1.28 | 0.06 | 0.950 | 0.039 | 0.96 | 0.03 | 0.950 | 0.000 |
| | 0.90 | 0.332 | 1.26 | 0.08 | 0.900 | 0.077 | 1.40 | 0.02 | 0.900 | 0.000 |
| 1.00 cm | 0.85 | 0.407 | 1.45 | 0.07 | 0.850 | 0.116 | 1.75 | 0.03 | 0.850 | 0.000 |
| | 0.80 | 0.470 | 1.49 | 0.07 | 0.800 | 0.155 | 1.80 | 0.03 | 0.800 | 0.001 |
| | 0.75 | 0.525 | 1.63 | 0.07 | 0.751 | 0.193 | 1.95 | 0.03 | 0.750 | 0.001 |
| | 0.70 | 0.575 | 1.63 | 0.07 | 0.701 | 0.232 | 2.02 | 0.03 | 0.700 | 0.001 |
| r (cm) | IRF | d (cm) | $d_T$ | $\sigma_{d_T}$ | $I_{avg}$ | $\Delta I_R$ | $d_T$ | $\sigma_{d_T}$ | $I_{avg}$ | $\Delta I_R$ |
| | 0.95 | 0.294 | 1.33 | 0.07 | 0.950 | 0.095 | 0.87 | 0.03 | 0.950 | 0.003 |
| | 0.90 | 0.415 | 1.45 | 0.09 | 0.900 | 0.189 | 1.35 | 0.03 | 0.900 | 0.005 |
| 1.25 cm | 0.85 | 0.508 | 1.38 | 0.08 | 0.851 | 0.283 | 1.63 | 0.03 | 0.850 | 0.008 |
| | 0.80 | 0.587 | 1.49 | 0.08 | 0.801 | 0.378 | 1.75 | 0.03 | 0.800 | 0.011 |
| | 0.75 | 0.656 | 1.58 | 0.08 | 0.751 | 0.472 | 1.89 | 0.03 | 0.750 | 0.014 |
| | 0.70 | 0.719 | 1.61 | 0.08 | 0.701 | 0.567 | 2.00 | 0.03 | 0.700 | 0.016 |
| r (cm) | IRF | d (cm) | $d_T$ | $\sigma_{d_T}$ | $I_{avg}$ | $\Delta I_R$ | $d_T$ | $\sigma_{d_T}$ | $I_{avg}$ | $\Delta I_R$ |
| | 0.95 | 0.352 | 1.08 | 0.10 | 0.951 | 0.157 | 0.81 | 0.04 | 0.950 | 0.013 |
| | 0.90 | 0.498 | 1.28 | 0.06 | 0.902 | 0.314 | 1.78 | 0.04 | 0.900 | 0.026 |
| 1.50 cm | 0.85 | 0.610 | 1.25 | 0.07 | 0.853 | 0.471 | 2.72 | 0.08 | 0.850 | 0.039 |
| | 0.80 | 0.704 | 1.23 | 0.08 | 0.805 | 0.627 | 2.76 | 0.11 | 0.801 | 0.052 |
| | 0.75 | 0.788 | 1.32 | 0.07 | 0.756 | 0.785 | 2.73 | 0.10 | 0.750 | 0.065 |
| | 0.70 | 0.863 | 1.29 | 0.07 | 0.707 | 0.942 | 3.22 | 0.08 | 0.700 | 0.078 |

Table C.3: Metrics summary for 10 MeV at 100 cm SSD at y=0cm 20x20 half-blocked field for z=0.5cm (left) and z=2.0cm (right).

| r (cm) | IRF | d (cm) | $d_T$ | $\sigma_{d_T}$ | $I_{avg}$ | $\Delta I_R$ | $d_T$ | $\sigma_{d_T}$ | $I_{avg}$ | $\Delta I_R$ |
|---|---|---|---|---|---|---|---|---|---|---|
| | 0.95 | 0.117 | 0.55 | 0.01 | 0.950 | 0.000 | 1.03 | 0.03 | 0.950 | 0.000 |
| | 0.90 | 0.166 | 0.68 | 0.01 | 0.900 | 0.000 | 1.44 | 0.03 | 0.900 | 0.000 |
| 0.50 cm | 0.85 | 0.203 | 0.92 | 0.01 | 0.851 | 0.000 | 1.44 | 0.02 | 0.851 | 0.000 |
| | 0.80 | 0.235 | 1.00 | 0.00 | 0.800 | 0.001 | 1.64 | 0.02 | 0.800 | 0.000 |
| | 0.75 | 0.263 | 1.00 | 0.00 | 0.749 | 0.001 | 1.83 | 0.02 | 0.749 | 0.000 |
| | 0.70 | 0.288 | 1.00 | 0.00 | 0.699 | 0.001 | 1.84 | 0.02 | 0.699 | 0.000 |
| r (cm) | IRF | d (cm) | $d_T$ | $\sigma_{d_T}$ | $I_{avg}$ | $\Delta I_R$ | $d_T$ | $\sigma_{d_T}$ | $I_{avg}$ | $\Delta I_R$ |
| | 0.95 | 0.176 | 0.44 | 0.01 | 0.950 | 0.012 | 0.84 | 0.02 | 0.950 | 0.000 |
| | 0.90 | 0.249 | 0.73 | 0.02 | 0.900 | 0.024 | 1.24 | 0.02 | 0.900 | 0.000 |
| 0.75 cm | 0.85 | 0.305 | 1.72 | 0.09 | 0.850 | 0.036 | 1.63 | 0.02 | 0.850 | 0.000 |
| | 0.80 | 0.352 | 2.12 | 0.08 | 0.800 | 0.048 | 1.64 | 0.02 | 0.800 | 0.000 |
| | 0.75 | 0.394 | 2.41 | 0.06 | 0.750 | 0.060 | 1.65 | 0.03 | 0.750 | 0.000 |
| | 0.70 | 0.431 | 2.45 | 0.09 | 0.701 | 0.072 | 1.91 | 0.02 | 0.701 | 0.000 |
| r (cm) | IRF | d (cm) | $d_T$ | $\sigma_{d_T}$ | $I_{avg}$ | $\Delta I_R$ | $d_T$ | $\sigma_{d_T}$ | $I_{avg}$ | $\Delta I_R$ |
| | 0.95 | 0.235 | 1.15 | 0.06 | 0.950 | 0.059 | 0.84 | 0.02 | 0.950 | 0.001 |
| | 0.90 | 0.332 | 1.16 | 0.07 | 0.900 | 0.118 | 1.28 | 0.03 | 0.900 | 0.001 |
| 1.00 cm | 0.85 | 0.407 | 1.28 | 0.07 | 0.850 | 0.177 | 1.49 | 0.03 | 0.850 | 0.002 |
| | 0.80 | 0.470 | 1.43 | 0.07 | 0.801 | 0.236 | 1.64 | 0.02 | 0.800 | 0.003 |
| | 0.75 | 0.525 | 1.50 | 0.07 | 0.751 | 0.295 | 1.73 | 0.03 | 0.750 | 0.003 |
| | 0.70 | 0.575 | 1.54 | 0.06 | 0.701 | 0.353 | 1.76 | 0.02 | 0.700 | 0.004 |
| r (cm) | IRF | d (cm) | $d_T$ | $\sigma_{d_T}$ | $I_{avg}$ | $\Delta I_R$ | $d_T$ | $\sigma_{d_T}$ | $I_{avg}$ | $\Delta I_R$ |
| | 0.95 | 0.294 | 1.19 | 0.08 | 0.950 | 0.125 | 0.74 | 0.03 | 0.950 | 0.007 |
| | 0.90 | 0.415 | 1.31 | 0.08 | 0.901 | 0.250 | 1.18 | 0.03 | 0.900 | 0.014 |
| 1.25 cm | 0.85 | 0.508 | 1.40 | 0.08 | 0.851 | 0.374 | 1.57 | 0.04 | 0.850 | 0.021 |
| | 0.80 | 0.587 | 1.52 | 0.08 | 0.801 | 0.500 | 1.91 | 0.05 | 0.800 | 0.028 |
| | 0.75 | 0.656 | 1.53 | 0.08 | 0.752 | 0.624 | 2.51 | 0.07 | 0.750 | 0.035 |
| | 0.70 | 0.719 | 1.53 | 0.08 | 0.702 | 0.750 | 2.56 | 0.05 | 0.700 | 0.042 |
| r (cm) | IRF | d (cm) | $d_T$ | $\sigma_{d_T}$ | $I_{avg}$ | $\Delta I_R$ | $d_T$ | $\sigma_{d_T}$ | $I_{avg}$ | $\Delta I_R$ |
| | 0.95 | 0.352 | 0.67 | 0.07 | 0.952 | 0.195 | 1.30 | 0.06 | 0.950 | 0.025 |
| | 0.90 | 0.498 | 0.69 | 0.05 | 0.903 | 0.391 | 2.60 | 0.06 | 0.900 | 0.050 |
| 1.50 cm | 0.85 | 0.610 | 0.77 | 0.04 | 0.854 | 0.587 | 2.70 | 0.10 | 0.851 | 0.075 |
| | 0.80 | 0.704 | 0.94 | 0.06 | 0.806 | 0.781 | 2.79 | 0.10 | 0.801 | 0.099 |
| | 0.75 | 0.788 | 0.91 | 0.06 | 0.757 | 0.974 | 2.81 | 0.09 | 0.751 | 0.125 |
| | 0.70 | 0.863 | 1.02 | 0.07 | 0.713 | 0.969 | 3.01 | 0.08 | 0.701 | 0.150 |

Table C.4: Metrics summary for 11 MeV at 100 cm SSD at y=0cm 20x20 half-blocked field for z=0.5cm (left) and z=2.0cm (right).

| r (cm) | IRF | d (cm) | $d_T$ | $\sigma_{d_T}$ | $I_{avg}$ | $\Delta I_R$ | $d_T$ | $\sigma_{d_T}$ | $I_{avg}$ | $\Delta I_R$ |
|---|---|---|---|---|---|---|---|---|---|---|
| | 0.95 | 0.117 | 0.55 | 0.01 | 0.950 | 0.000 | 1.03 | 0.03 | 0.950 | 0.000 |
| | 0.90 | 0.166 | 0.68 | 0.01 | 0.900 | 0.000 | 1.44 | 0.03 | 0.900 | 0.000 |
| 0.50 cm | 0.85 | 0.203 | 0.92 | 0.01 | 0.851 | 0.000 | 1.44 | 0.02 | 0.851 | 0.000 |
| | 0.80 | 0.235 | 1.00 | 0.00 | 0.800 | 0.001 | 1.64 | 0.02 | 0.800 | 0.000 |
| | 0.75 | 0.263 | 1.00 | 0.00 | 0.749 | 0.001 | 1.83 | 0.02 | 0.749 | 0.000 |
| | 0.70 | 0.288 | 1.00 | 0.00 | 0.699 | 0.001 | 1.84 | 0.02 | 0.699 | 0.000 |
| r (cm) | IRF | d (cm) | $d_T$ | $\sigma_{d_T}$ | $I_{avg}$ | $\Delta I_R$ | $d_T$ | $\sigma_{d_T}$ | $I_{avg}$ | $\Delta I_R$ |
| | 0.95 | 0.176 | 0.74 | 0.04 | 0.950 | 0.021 | 0.84 | 0.03 | 0.950 | 0.000 |
| | 0.90 | 0.249 | 1.71 | 0.08 | 0.900 | 0.042 | 1.24 | 0.03 | 0.900 | 0.000 |
| 0.75 cm | 0.85 | 0.305 | 1.96 | 0.10 | 0.850 | 0.063 | 1.32 | 0.03 | 0.850 | 0.000 |
| | 0.80 | 0.352 | 2.07 | 0.10 | 0.800 | 0.085 | 1.60 | 0.03 | 0.800 | 0.000 |
| | 0.75 | 0.394 | 1.95 | 0.08 | 0.750 | 0.106 | 1.64 | 0.02 | 0.750 | 0.000 |
| | 0.70 | 0.431 | 1.99 | 0.08 | 0.701 | 0.127 | 1.64 | 0.02 | 0.701 | 0.000 |
| r (cm) | IRF | d (cm) | $d_T$ | $\sigma_{d_T}$ | $I_{avg}$ | $\Delta I_R$ | $d_T$ | $\sigma_{d_T}$ | $I_{avg}$ | $\Delta I_R$ |
| | 0.95 | 0.235 | 0.96 | 0.05 | 0.950 | 0.081 | 0.77 | 0.03 | 0.950 | 0.002 |
| | 0.90 | 0.332 | 0.95 | 0.05 | 0.901 | 0.162 | 1.14 | 0.03 | 0.900 | 0.004 |
| 1.00 cm | 0.85 | 0.407 | 1.11 | 0.06 | 0.851 | 0.244 | 1.30 | 0.03 | 0.850 | 0.006 |
| | 0.80 | 0.470 | 1.29 | 0.07 | 0.801 | 0.326 | 1.43 | 0.03 | 0.800 | 0.008 |
| | 0.75 | 0.525 | 1.30 | 0.07 | 0.752 | 0.406 | 1.59 | 0.03 | 0.750 | 0.010 |
| | 0.70 | 0.575 | 1.41 | 0.06 | 0.702 | 0.487 | 1.68 | 0.03 | 0.700 | 0.012 |
| r (cm) | IRF | d (cm) | $d_T$ | $\sigma_{d_T}$ | $I_{avg}$ | $\Delta I_R$ | $d_T$ | $\sigma_{d_T}$ | $I_{avg}$ | $\Delta I_R$ |
| | 0.95 | 0.294 | 0.73 | 0.05 | 0.950 | 0.157 | 0.66 | 0.03 | 0.950 | 0.014 |
| | 0.90 | 0.415 | 1.26 | 0.09 | 0.901 | 0.312 | 1.64 | 0.03 | 0.900 | 0.028 |
| 1.25 cm | 0.85 | 0.508 | 1.38 | 0.08 | 0.851 | 0.467 | 2.18 | 0.07 | 0.850 | 0.042 |
| | 0.80 | 0.587 | 1.45 | 0.08 | 0.801 | 0.624 | 2.43 | 0.07 | 0.800 | 0.056 |
| | 0.75 | 0.656 | 1.48 | 0.08 | 0.752 | 0.779 | 2.31 | 0.08 | 0.750 | 0.070 |
| | 0.70 | 0.719 | 1.49 | 0.07 | 0.702 | 0.936 | 2.33 | 0.07 | 0.700 | 0.084 |
| r (cm) | IRF | d (cm) | $d_T$ | $\sigma_{d_T}$ | $I_{avg}$ | $\Delta I_R$ | $d_T$ | $\sigma_{d_T}$ | $I_{avg}$ | $\Delta I_R$ |
| | 0.95 | 0.352 | 0.30 | 0.03 | 0.952 | 0.235 | 2.32 | 0.09 | 0.950 | 0.040 |
| | 0.90 | 0.498 | 1.04 | 0.05 | 0.904 | 0.470 | 2.2 | 0.1 | 0.901 | 0.081 |
| 1.50 cm | 0.85 | 0.610 | 0.95 | 0.06 | 0.855 | 0.706 | 2.4 | 0.1 | 0.851 | 0.121 |
| | 0.80 | 0.704 | 1.06 | 0.07 | 0.807 | 0.940 | 2.4 | 0.1 | 0.801 | 0.161 |
| | 0.75 | 0.788 | 1.11 | 0.07 | 0.762 | 0.980 | 2.5 | 0.1 | 0.751 | 0.202 |
| | 0.70 | 0.863 | 1.18 | 0.07 | 0.724 | 0.984 | 2.6 | 0.1 | 0.702 | 0.242 |

Table C.5: Metrics summary for 13 MeV at 100 cm SSD at y=0cm 20x20 half-blocked field for z=0.5cm (left) and z=2.0cm (right).

| r (cm) | IRF | d (cm) | $d_T$ | $\sigma_{d_T}$ | $I_{avg}$ | $\Delta I_R$ | $d_T$ | $\sigma_{d_T}$ | $I_{avg}$ | $\Delta I_R$ |
|---|---|---|---|---|---|---|---|---|---|---|
| | 0.95 | 0.117 | 0.55 | 0.01 | 0.950 | 0.000 | 1.03 | 0.03 | 0.950 | 0.000 |
| | 0.90 | 0.166 | 0.68 | 0.01 | 0.900 | 0.000 | 1.44 | 0.03 | 0.900 | 0.000 |
| 0.50 cm | 0.85 | 0.203 | 0.92 | 0.01 | 0.851 | 0.000 | 1.44 | 0.02 | 0.851 | 0.000 |
| | 0.80 | 0.235 | 1.00 | 0.00 | 0.800 | 0.001 | 1.64 | 0.02 | 0.800 | 0.000 |
| | 0.75 | 0.263 | 1.00 | 0.00 | 0.749 | 0.001 | 1.83 | 0.02 | 0.749 | 0.000 |
| | 0.70 | 0.288 | 1.00 | 0.00 | 0.699 | 0.001 | 1.84 | 0.02 | 0.699 | 0.000 |
| r (cm) | IRF | d (cm) | $d_T$ | $\sigma_{d_T}$ | $I_{avg}$ | $\Delta I_R$ | $d_T$ | $\sigma_{d_T}$ | $I_{avg}$ | $\Delta I_R$ |
| | 0.95 | 0.176 | 0.74 | 0.04 | 0.950 | 0.021 | 0.84 | 0.03 | 0.950 | 0.000 |
| | 0.90 | 0.249 | 1.71 | 0.08 | 0.900 | 0.042 | 1.24 | 0.03 | 0.900 | 0.000 |
| 0.75 cm | 0.85 | 0.305 | 1.96 | 0.10 | 0.850 | 0.063 | 1.32 | 0.03 | 0.850 | 0.000 |
| | 0.80 | 0.352 | 2.07 | 0.10 | 0.800 | 0.085 | 1.60 | 0.03 | 0.800 | 0.000 |
| | 0.75 | 0.394 | 1.95 | 0.08 | 0.750 | 0.106 | 1.64 | 0.02 | 0.750 | 0.000 |
| | 0.70 | 0.431 | 1.99 | 0.08 | 0.701 | 0.127 | 1.64 | 0.02 | 0.701 | 0.000 |
| r (cm) | IRF | d (cm) | $d_T$ | $\sigma_{d_T}$ | $I_{avg}$ | $\Delta I_R$ | $d_T$ | $\sigma_{d_T}$ | $I_{avg}$ | $\Delta I_R$ |
| | 0.95 | 0.235 | 0.96 | 0.05 | 0.950 | 0.081 | 0.77 | 0.03 | 0.950 | 0.002 |
| | 0.90 | 0.332 | 0.95 | 0.05 | 0.901 | 0.162 | 1.14 | 0.03 | 0.900 | 0.004 |
| 1.00 cm | 0.85 | 0.407 | 1.11 | 0.06 | 0.851 | 0.244 | 1.30 | 0.03 | 0.850 | 0.006 |
| | 0.80 | 0.470 | 1.29 | 0.07 | 0.801 | 0.326 | 1.43 | 0.03 | 0.800 | 0.008 |
| | 0.75 | 0.525 | 1.30 | 0.07 | 0.752 | 0.406 | 1.59 | 0.03 | 0.750 | 0.010 |
| | 0.70 | 0.575 | 1.41 | 0.06 | 0.702 | 0.487 | 1.68 | 0.03 | 0.700 | 0.012 |
| r (cm) | IRF | d (cm) | $d_T$ | $\sigma_{d_T}$ | $I_{avg}$ | $\Delta I_R$ | $d_T$ | $\sigma_{d_T}$ | $I_{avg}$ | $\Delta I_R$ |
| | 0.95 | 0.294 | 0.96 | 0.07 | 0.950 | 0.220 | 1.47 | 0.09 | 0.950 | 0.036 |
| | 0.90 | 0.415 | 1.07 | 0.06 | 0.901 | 0.438 | 2.06 | 0.07 | 0.900 | 0.072 |
| 1.25 cm | 0.85 | 0.508 | 1.12 | 0.08 | 0.852 | 0.657 | 1.98 | 0.05 | 0.850 | 0.107 |
| | 0.80 | 0.587 | 1.29 | 0.08 | 0.802 | 0.877 | 1.92 | 0.06 | 0.800 | 0.143 |
| | 0.75 | 0.656 | 1.40 | 0.08 | 0.754 | 0.985 | 2.00 | 0.06 | 0.751 | 0.179 |
| | 0.70 | 0.719 | 1.42 | 0.08 | 0.713 | 0.981 | 2.06 | 0.06 | 0.700 | 0.215 |
| r (cm) | IRF | d (cm) | $d_T$ | $\sigma_{d_T}$ | $I_{avg}$ | $\Delta I_R$ | $d_T$ | $\sigma_{d_T}$ | $I_{avg}$ | $\Delta I_R$ |
| | 0.95 | 0.352 | 0.73 | 0.08 | 0.952 | 0.319 | 2.09 | 0.08 | 0.951 | 0.078 |
| | 0.90 | 0.498 | 0.67 | 0.06 | 0.905 | 0.639 | 2.29 | 0.07 | 0.901 | 0.155 |
| 1.50 cm | 0.85 | 0.610 | 0.71 | 0.04 | 0.857 | 0.959 | 2.38 | 0.06 | 0.852 | 0.233 |
| | 0.80 | 0.704 | 0.58 | 0.03 | 0.814 | 0.998 | 2.34 | 0.05 | 0.802 | 0.310 |
| | 0.75 | 0.788 | 1.05 | 0.06 | 0.780 | 0.997 | 2.48 | 0.05 | 0.753 | 0.388 |
| | 0.70 | 0.863 | 1.08 | 0.05 | 0.753 | 0.997 | 2.20 | 0.06 | 0.703 | 0.466 |

Table C.6: Metrics summary for 16 MeV at 100 cm SSD at y=0cm 20x20 half-blocked field for z=0.5cm (left) and z=2.0cm (right).

| r (cm) | IRF | d (cm) | $d_T$ | $\sigma_{d_T}$ | $I_{avg}$ | $\Delta I_R$ | $d_T$ | $\sigma_{d_T}$ | $I_{avg}$ | $\Delta I_R$ |
|---|---|---|---|---|---|---|---|---|---|---|
| | 0.95 | 0.117 | 0.81 | 0.04 | 0.950 | 0.013 | 0.60 | 0.00 | 0.950 | 0.000 |
| | 0.90 | 0.166 | 0.90 | 0.04 | 0.900 | 0.026 | 0.88 | 0.01 | 0.900 | 0.000 |
| 0.50 cm | 0.85 | 0.203 | 1.04 | 0.03 | 0.850 | 0.040 | 1.00 | 0.00 | 0.851 | 0.000 |
| | 0.80 | 0.235 | 1.22 | 0.04 | 0.800 | 0.053 | 1.00 | 0.00 | 0.800 | 0.000 |
| | 0.75 | 0.263 | 1.09 | 0.04 | 0.749 | 0.066 | 1.09 | 0.01 | 0.749 | 0.000 |
| | 0.70 | 0.288 | 1.12 | 0.03 | 0.699 | 0.080 | 1.20 | 0.00 | 0.699 | 0.000 |
| r (cm) | IRF | d (cm) | $d_T$ | $\sigma_{d_T}$ | $I_{avg}$ | $\Delta I_R$ | $d_T$ | $\sigma_{d_T}$ | $I_{avg}$ | $\Delta I_R$ |
| | 0.95 | 0.176 | 1.43 | 0.08 | 0.950 | 0.094 | 0.57 | 0.01 | 0.950 | 0.004 |
| | 0.90 | 0.249 | 1.33 | 0.05 | 0.900 | 0.189 | 0.72 | 0.01 | 0.900 | 0.008 |
| 0.75 cm | 0.85 | 0.305 | 1.30 | 0.04 | 0.850 | 0.283 | 1.11 | 0.02 | 0.850 | 0.011 |
| | 0.80 | 0.352 | 1.36 | 0.06 | 0.800 | 0.377 | 1.18 | 0.02 | 0.800 | 0.015 |
| | 0.75 | 0.394 | 1.24 | 0.06 | 0.750 | 0.473 | 1.22 | 0.02 | 0.750 | 0.019 |
| | 0.70 | 0.431 | 1.20 | 0.07 | 0.701 | 0.566 | 1.83 | 0.10 | 0.701 | 0.023 |
| r (cm) | IRF | d (cm) | $d_T$ | $\sigma_{d_T}$ | $I_{avg}$ | $\Delta I_R$ | $d_T$ | $\sigma_{d_T}$ | $I_{avg}$ | $\Delta I_R$ |
| | 0.95 | 0.235 | 0.59 | 0.03 | 0.951 | 0.202 | 0.97 | 0.04 | 0.950 | 0.031 |
| | 0.90 | 0.332 | 0.73 | 0.04 | 0.901 | 0.406 | 1.29 | 0.07 | 0.900 | 0.061 |
| 1.00 cm | 0.85 | 0.407 | 0.83 | 0.04 | 0.852 | 0.606 | 1.53 | 0.08 | 0.850 | 0.025 |
| | 0.80 | 0.470 | 0.87 | 0.04 | 0.802 | 0.808 | 1.61 | 0.07 | 0.800 | 0.123 |
| | 0.75 | 0.525 | 0.90 | 0.04 | 0.754 | 0.978 | 1.49 | 0.07 | 0.751 | 0.153 |
| | 0.70 | 0.575 | 0.93 | 0.04 | 0.709 | 0.974 | 1.58 | 0.07 | 0.701 | 0.184 |
| r (cm) | IRF | d (cm) | $d_T$ | $\sigma_{d_T}$ | $I_{avg}$ | $\Delta I_R$ | $d_T$ | $\sigma_{d_T}$ | $I_{avg}$ | $\Delta I_R$ |
| | 0.95 | 0.294 | 0.78 | 0.07 | 0.951 | 0.323 | 1.47 | 0.08 | 0.950 | 0.081 |
| | 0.90 | 0.415 | 0.71 | 0.06 | 0.902 | 0.643 | 1.45 | 0.08 | 0.900 | 0.162 |
| 1.25 cm | 0.85 | 0.508 | 0.64 | 0.06 | 0.852 | 0.963 | 1.43 | 0.09 | 0.851 | 0.243 |
| | 0.80 | 0.587 | 0.87 | 0.06 | 0.808 | 0.998 | 1.55 | 0.07 | 0.801 | 0.324 |
| | 0.75 | 0.656 | 0.85 | 0.05 | 0.773 | 0.998 | 1.62 | 0.07 | 0.751 | 0.405 |
| | 0.70 | 0.719 | 0.99 | 0.06 | 0.745 | 0.998 | 1.65 | 0.08 | 0.701 | 0.486 |
| r (cm) | IRF | d (cm) | $d_T$ | $\sigma_{d_T}$ | $I_{avg}$ | $\Delta I_R$ | $d_T$ | $\sigma_{d_T}$ | $I_{avg}$ | $\Delta I_R$ |
| | 0.95 | 0.352 | 0.67 | 0.07 | 0.953 | 0.463 | 1.65 | 0.08 | 0.951 | 0.130 |
| | 0.90 | 0.498 | 0.68 | 0.09 | 0.906 | 0.927 | 1.59 | 0.05 | 0.902 | 0.279 |
| 1.50 cm | 0.85 | 0.610 | 0.55 | 0.06 | 0.865 | 1.000 | 1.68 | 0.07 | 0.853 | 0.419 |
| | 0.80 | 0.704 | 0.70 | 0.05 | 0.835 | 1.000 | 1.60 | 0.08 | 0.804 | 0.558 |
| | 0.75 | 0.788 | 0.85 | 0.06 | 0.813 | 1.000 | 1.57 | 0.08 | 0.755 | 0.700 |
| | 0.70 | 0.863 | 0.94 | 0.05 | 0.793 | 1.000 | 1.57 | 0.09 | 0.706 | 0.839 |

Table C.7: Metrics summary for 20 MeV at 100 cm SSD at y=0cm 20x20 half-blocked field for z=0.5cm (left) and z=2.0cm (right).

| r (cm) | IRF | d (cm) | $d_T$ | $\sigma_{d_T}$ | $I_{avg}$ | $\Delta I_R$ | $d_T$ | $\sigma_{d_T}$ | $I_{avg}$ | $\Delta I_R$ |
|---|---|---|---|---|---|---|---|---|---|---|
| | 0.95 | 0.117 | 0.94 | 0.03 | 0.950 | 0.042 | 0.52 | 0.01 | 0.950 | 0.000 |
| | 0.90 | 0.166 | 0.96 | 0.04 | 0.900 | 0.084 | 0.65 | 0.01 | 0.900 | 0.001 |
| 0.50 cm | 0.85 | 0.203 | 0.91 | 0.03 | 0.850 | 0.126 | 0.82 | 0.01 | 0.851 | 0.001 |
| | 0.80 | 0.235 | 0.95 | 0.03 | 0.799 | 0.168 | 0.92 | 0.01 | 0.800 | 0.001 |
| | 0.75 | 0.263 | 0.98 | 0.03 | 0.749 | 0.211 | 0.97 | 0.01 | 0.749 | 0.002 |
| | 0.70 | 0.288 | 1.01 | 0.03 | 0.698 | 0.253 | 1.00 | 0.00 | 0.699 | 0.002 |
| r (cm) | IRF | d (cm) | $d_T$ | $\sigma_{d_T}$ | $I_{avg}$ | $\Delta I_R$ | $d_T$ | $\sigma_{d_T}$ | $I_{avg}$ | $\Delta I_R$ |
| | 0.95 | 0.176 | 0.57 | 0.05 | 0.950 | 0.164 | 0.69 | 0.03 | 0.950 | 0.019 |
| | 0.90 | 0.249 | 0.75 | 0.05 | 0.900 | 0.328 | 1.79 | 0.07 | 0.900 | 0.038 |
| 0.75 cm | 0.85 | 0.305 | 0.65 | 0.04 | 0.850 | 0.492 | 2.0 | 0.1 | 0.855 | 0.056 |
| | 0.80 | 0.352 | 0.78 | 0.07 | 0.800 | 0.655 | 1.9 | 0.1 | 0.800 | 0.075 |
| | 0.75 | 0.394 | 0.83 | 0.07 | 0.750 | 0.820 | 2.07 | 0.08 | 0.750 | 0.094 |
| | 0.70 | 0.431 | 0.84 | 0.07 | 0.701 | 0.949 | 2.04 | 0.08 | 0.701 | 0.031 |
| r (cm) | IRF | d (cm) | $d_T$ | $\sigma_{d_T}$ | $I_{avg}$ | $\Delta I_R$ | $d_T$ | $\sigma_{d_T}$ | $I_{avg}$ | $\Delta I_R$ |
| | 0.95 | 0.235 | 0.31 | 0.04 | 0.951 | 0.306 | 1.08 | 0.05 | 0.950 | 0.076 |
| | 0.90 | 0.332 | 0.42 | 0.03 | 0.902 | 0.612 | 1.04 | 0.06 | 0.901 | 0.152 |
| 1.00 cm | 0.85 | 0.407 | 0.49 | 0.04 | 0.852 | 0.919 | 1.18 | 0.07 | 0.851 | 0.228 |
| | 0.80 | 0.470 | 0.44 | 0.03 | 0.807 | 0.998 | 1.33 | 0.07 | 0.801 | 0.304 |
| | 0.75 | 0.525 | 0.45 | 0.03 | 0.771 | 0.997 | 1.39 | 0.07 | 0.751 | 0.380 |
| | 0.70 | 0.575 | 0.49 | 0.03 | 0.742 | 0.997 | 1.48 | 0.06 | 0.702 | 0.455 |
| r (cm) | IRF | d (cm) | $d_T$ | $\sigma_{d_T}$ | $I_{avg}$ | $\Delta I_R$ | $d_T$ | $\sigma_{d_T}$ | $I_{avg}$ | $\Delta I_R$ |
| | 0.95 | 0.294 | 1.1 | 0.1 | 0.951 | 0.480 | 0.91 | 0.06 | 0.950 | 0.149 |
| | 0.90 | 0.415 | 0.89 | 0.07 | 0.902 | 0.957 | 1.22 | 0.08 | 0.901 | 0.297 |
| 1.25 cm | 0.85 | 0.508 | 0.78 | 0.07 | 0.860 | 1.000 | 1.38 | 0.08 | 0.851 | 0.446 |
| | 0.80 | 0.587 | 0.79 | 0.07 | 0.830 | 0.999 | 1.44 | 0.08 | 0.801 | 0.595 |
| | 0.75 | 0.656 | 0.67 | 0.06 | 0.807 | 1.000 | 1.50 | 0.08 | 0.752 | 0.743 |
| | 0.70 | 0.719 | 0.66 | 0.07 | 0.788 | 1.000 | 1.54 | 0.08 | 0.702 | 0.893 |
| r (cm) | IRF | d (cm) | $d_T$ | $\sigma_{d_T}$ | $I_{avg}$ | $\Delta I_R$ | $d_T$ | $\sigma_{d_T}$ | $I_{avg}$ | $\Delta I_R$ |
| | 0.95 | 0.352 | 0.57 | 0.06 | 0.954 | 0.689 | 0.45 | 0.05 | 0.952 | 0.226 |
| | 0.90 | 0.498 | 0.67 | 0.07 | 0.911 | 1.000 | 0.94 | 0.05 | 0.903 | 0.452 |
| 1.50 cm | 0.85 | 0.610 | 0.46 | 0.05 | 0.882 | 1.000 | 0.75 | 0.05 | 0.855 | 0.677 |
| | 0.80 | 0.704 | 0.45 | 0.05 | 0.863 | 1.000 | 0.96 | 0.06 | 0.807 | 0.902 |
| | 0.75 | 0.788 | 0.47 | 0.05 | 0.849 | 1.000 | 1.04 | 0.07 | 0.760 | 0.985 |
| | 0.70 | 0.863 | 0.44 | 0.05 | 0.837 | 1.000 | 1.01 | 0.07 | 0.721 | 0.982 |

Table C.8: Metrics summary for 7 MeV at 103 cm SSD at y=0cm 20x20 half-blocked field for z=0.5cm (left) and z=2.0cm (right).

| r (cm) | IRF | d (cm) | $d_T$ | $\sigma_{d_T}$ | $I_{avg}$ | $\Delta I_R$ | $d_T$ | $\sigma_{d_T}$ | $I_{avg}$ | $\Delta I_R$ |
|---|---|---|---|---|---|---|---|---|---|---|
| | 0.95 | 0.117 | 1.06 | 0.04 | 0.950 | 0.000 | 1.36 | 0.05 | 0.950 | 0.003 |
| | 0.90 | 0.166 | 1.49 | 0.04 | 0.900 | 0.000 | 2.19 | 0.05 | 0.900 | 0.003 |
| 0.50 cm | 0.85 | 0.203 | 1.87 | 0.03 | 0.851 | 0.000 | 2.63 | 0.04 | 0.850 | 0.002 |
| | 0.80 | 0.235 | 1.90 | 0.03 | 0.800 | 0.000 | 2.85 | 0.02 | 0.800 | 0.002 |
| | 0.75 | 0.263 | 2.07 | 0.03 | 0.749 | 0.000 | 3.04 | 0.02 | 0.749 | 0.002 |
| | 0.70 | 0.288 | 2.26 | 0.03 | 0.699 | 0.000 | 3.24 | 0.02 | 0.699 | 0.002 |
| r (cm) | IRF | d (cm) | $d_T$ | $\sigma_{d_T}$ | $I_{avg}$ | $\Delta I_R$ | $d_T$ | $\sigma_{d_T}$ | $I_{avg}$ | $\Delta I_R$ |
| | 0.95 | 0.176 | 1.05 | 0.03 | 0.950 | 0.000 | 1.51 | 0.05 | 0.950 | 0.002 |
| | 0.90 | 0.249 | 1.66 | 0.03 | 0.900 | 0.000 | 2.18 | 0.05 | 0.900 | 0.002 |
| 0.75 cm | 0.85 | 0.305 | 1.69 | 0.03 | 0.850 | 0.000 | 2.60 | 0.04 | 0.850 | 0.002 |
| | 0.80 | 0.352 | 2.07 | 0.03 | 0.800 | 0.000 | 2.84 | 0.02 | 0.800 | 0.002 |
| | 0.75 | 0.394 | 2.07 | 0.03 | 0.750 | 0.000 | 3.04 | 0.02 | 0.750 | 0.002 |
| | 0.70 | 0.431 | 2.16 | 0.03 | 0.701 | 0.000 | 3.24 | 0.02 | 0.701 | 0.002 |
| r (cm) | IRF | d (cm) | $d_T$ | $\sigma_{d_T}$ | $I_{avg}$ | $\Delta I_R$ | $d_T$ | $\sigma_{d_T}$ | $I_{avg}$ | $\Delta I_R$ |
| | 0.95 | 0.235 | 1.00 | 0.03 | 0.950 | 0.000 | 1.34 | 0.05 | 0.950 | 0.003 |
| | 0.90 | 0.332 | 1.56 | 0.03 | 0.900 | 0.000 | 2.18 | 0.05 | 0.900 | 0.002 |
| 1.00 cm | 0.85 | 0.407 | 1.79 | 0.03 | 0.850 | 0.000 | 2.61 | 0.03 | 0.850 | 0.002 |
| | 0.80 | 0.470 | 1.95 | 0.03 | 0.800 | 0.000 | 2.84 | 0.02 | 0.800 | 0.002 |
| | 0.75 | 0.525 | 2.08 | 0.03 | 0.750 | 0.000 | 3.04 | 0.02 | 0.750 | 0.002 |
| | 0.70 | 0.575 | 2.18 | 0.03 | 0.700 | 0.000 | 3.22 | 0.02 | 0.700 | 0.002 |
| r (cm) | IRF | d (cm) | $d_T$ | $\sigma_{d_T}$ | $I_{avg}$ | $\Delta I_R$ | $d_T$ | $\sigma_{d_T}$ | $I_{avg}$ | $\Delta I_R$ |
| | 0.95 | 0.294 | 0.95 | 0.03 | 0.950 | 0.001 | 1.34 | 0.05 | 0.950 | 0.003 |
| | 0.90 | 0.415 | 1.46 | 0.03 | 0.900 | 0.003 | 2.17 | 0.05 | 0.900 | 0.002 |
| 1.25 cm | 0.85 | 0.508 | 1.73 | 0.03 | 0.850 | 0.004 | 2.59 | 0.03 | 0.850 | 0.002 |
| | 0.80 | 0.587 | 1.91 | 0.03 | 0.800 | 0.005 | 2.80 | 0.02 | 0.800 | 0.002 |
| | 0.75 | 0.656 | 2.04 | 0.03 | 0.750 | 0.007 | 3.01 | 0.02 | 0.750 | 0.002 |
| | 0.70 | 0.719 | 2.13 | 0.03 | 0.700 | 0.008 | 3.05 | 0.02 | 0.700 | 0.002 |
| r (cm) | IRF | d (cm) | $d_T$ | $\sigma_{d_T}$ | $I_{avg}$ | $\Delta I_R$ | $d_T$ | $\sigma_{d_T}$ | $I_{avg}$ | $\Delta I_R$ |
| | 0.95 | 0.352 | 0.91 | 0.04 | 0.950 | 0.008 | 1.33 | 0.04 | 0.950 | 0.003 |
| | 0.90 | 0.498 | 1.33 | 0.04 | 0.900 | 0.016 | 2.12 | 0.05 | 0.900 | 0.003 |
| 1.50 cm | 0.85 | 0.610 | 1.98 | 0.04 | 0.850 | 0.024 | 2.52 | 0.03 | 0.850 | 0.003 |
| | 0.80 | 0.704 | 2.61 | 0.06 | 0.800 | 0.032 | 2.77 | 0.02 | 0.800 | 0.002 |
| | 0.75 | 0.788 | 3.23 | 0.07 | 0.750 | 0.040 | 2.98 | 0.02 | 0.750 | 0.002 |
| | 0.70 | 0.863 | 2.98 | 0.08 | 0.700 | 0.048 | 3.11 | 0.02 | 0.700 | 0.002 |

Table C.9: Metrics summary for 9 MeV at 103 cm SSD at y=0cm 20x20 half-blocked field for z=0.5cm (left) and z=2.0cm (right).

| r (cm) | IRF | d (cm) | $d_T$ | $\sigma_{d_T}$ | $I_{avg}$ | $\Delta I_R$ | $d_T$ | $\sigma_{d_T}$ | $I_{avg}$ | $\Delta I_R$ |
|---|---|---|---|---|---|---|---|---|---|---|
| | 0.95 | 0.117 | 0.83 | 0.02 | 0.950 | 0.000 | 1.05 | 0.04 | 0.950 | 0.000 |
| | 0.90 | 0.166 | 1.23 | 0.02 | 0.900 | 0.000 | 1.85 | 0.04 | 0.900 | 0.000 |
| 0.50 cm | 0.85 | 0.203 | 1.43 | 0.02 | 0.851 | 0.000 | 2.25 | 0.03 | 0.851 | 0.000 |
| | 0.80 | 0.235 | 1.62 | 0.02 | 0.800 | 0.000 | 2.28 | 0.03 | 0.800 | 0.000 |
| | 0.75 | 0.263 | 1.63 | 0.02 | 0.749 | 0.000 | 2.47 | 0.03 | 0.749 | 0.000 |
| | 0.70 | 0.288 | 1.82 | 0.02 | 0.699 | 0.000 | 2.48 | 0.03 | 0.699 | 0.000 |
| r (cm) | IRF | d (cm) | $d_T$ | $\sigma_{d_T}$ | $I_{avg}$ | $\Delta I_R$ | $d_T$ | $\sigma_{d_T}$ | $I_{avg}$ | $\Delta I_R$ |
| | 0.95 | 0.176 | 0.82 | 0.02 | 0.950 | 0.000 | 1.21 | 0.04 | 0.950 | 0.000 |
| | 0.90 | 0.249 | 1.23 | 0.02 | 0.900 | 0.000 | 1.67 | 0.04 | 0.900 | 0.000 |
| 0.75 cm | 0.85 | 0.305 | 1.43 | 0.00 | 0.850 | 0.000 | 2.08 | 0.03 | 0.850 | 0.000 |
| | 0.80 | 0.352 | 1.62 | 0.02 | 0.800 | 0.000 | 2.28 | 0.03 | 0.800 | 0.000 |
| | 0.75 | 0.394 | 1.62 | 0.02 | 0.750 | 0.000 | 2.47 | 0.03 | 0.497 | 0.000 |
| | 0.70 | 0.431 | 1.66 | 0.02 | 0.701 | 0.000 | 2.48 | 0.03 | 0.701 | 0.000 |
| r (cm) | IRF | d (cm) | $d_T$ | $\sigma_{d_T}$ | $I_{avg}$ | $\Delta I_R$ | $d_T$ | $\sigma_{d_T}$ | $I_{avg}$ | $\Delta I_R$ |
| | 0.95 | 0.235 | 0.80 | 0.02 | 0.950 | 0.001 | 1.13 | 0.04 | 0.950 | 0.001 |
| | 0.90 | 0.332 | 1.21 | 0.02 | 0.900 | 0.003 | 1.77 | 0.04 | 0.900 | 0.000 |
| 1.00 cm | 0.85 | 0.407 | 1.34 | 0.02 | 0.850 | 0.004 | 2.07 | 0.03 | 0.850 | 0.000 |
| | 0.80 | 0.470 | 1.52 | 0.02 | 0.800 | 0.006 | 2.27 | 0.03 | 0.800 | 0.000 |
| | 0.75 | 0.525 | 1.64 | 0.02 | 0.750 | 0.007 | 2.43 | 0.03 | 0.750 | 0.000 |
| | 0.70 | 0.575 | 1.70 | 0.02 | 0.700 | 0.008 | 2.48 | 0.03 | 0.700 | 0.000 |
| r (cm) | IRF | d (cm) | $d_T$ | $\sigma_{d_T}$ | $I_{avg}$ | $\Delta I_R$ | $d_T$ | $\sigma_{d_T}$ | $I_{avg}$ | $\Delta I_R$ |
| | 0.95 | 0.294 | 0.67 | 0.02 | 0.950 | 0.011 | 1.13 | 0.03 | 0.950 | 0.000 |
| | 0.90 | 0.415 | 1.41 | 0.04 | 0.900 | 0.022 | 1.71 | 0.03 | 0.900 | 0.000 |
| 1.25 cm | 0.85 | 0.508 | 2.25 | 0.07 | 0.850 | 0.033 | 2.05 | 0.02 | 0.850 | 0.001 |
| | 0.80 | 0.587 | 2.33 | 0.06 | 0.800 | 0.044 | 2.23 | 0.02 | 0.800 | 0.001 |
| | 0.75 | 0.656 | 2.53 | 0.07 | 0.750 | 0.055 | 2.35 | 0.02 | 0.750 | 0.001 |
| | 0.70 | 0.719 | 2.49 | 0.07 | 0.700 | 0.067 | 2.47 | 0.02 | 0.700 | 0.001 |
| r (cm) | IRF | d (cm) | $d_T$ | $\sigma_{d_T}$ | $I_{avg}$ | $\Delta I_R$ | $d_T$ | $\sigma_{d_T}$ | $I_{avg}$ | $\Delta I_R$ |
| | 0.95 | 0.352 | 1.50 | 0.06 | 0.950 | 0.034 | 1.07 | 0.04 | 0.950 | 0.002 |
| | 0.90 | 0.498 | 2.30 | 0.10 | 0.901 | 0.068 | 1.69 | 0.04 | 0.900 | 0.004 |
| 1.50 cm | 0.85 | 0.610 | 2.53 | 0.09 | 0.851 | 0.102 | 1.95 | 0.03 | 0.850 | 0.006 |
| | 0.80 | 0.704 | 2.60 | 0.10 | 0.801 | 0.136 | 2.20 | 0.03 | 0.800 | 0.009 |
| | 0.75 | 0.788 | 2.60 | 0.10 | 0.751 | 0.171 | 2.34 | 0.03 | 0.750 | 0.011 |
| | 0.70 | 0.863 | 2.50 | 0.10 | 0.701 | 0.205 | 2.41 | 0.03 | 0.700 | 0.013 |

Table C.10: Metrics summary for 10 MeV at 103 cm SSD at y=0cm 20x20 half-blocked field for z=0.5cm (left) and z=2.0cm (right).

| r (cm) | IRF | d (cm) | $d_T$ | $\sigma_{d_T}$ | $I_{avg}$ | $\Delta I_R$ | $d_T$ | $\sigma_{d_T}$ | $I_{avg}$ | $\Delta I_R$ |
|---|---|---|---|---|---|---|---|---|---|---|
| | 0.95 | 0.117 | 0.63 | 0.02 | 0.950 | 0.000 | 1.05 | 0.03 | 0.950 | 0.000 |
| | 0.90 | 0.166 | 1.03 | 0.02 | 0.900 | 0.000 | 1.66 | 0.03 | 0.900 | 0.000 |
| 0.50 cm | 0.85 | 0.203 | 1.42 | 0.02 | 0.851 | 0.000 | 1.87 | 0.03 | 0.851 | 0.000 |
| | 0.80 | 0.235 | 1.42 | 0.02 | 0.800 | 0.000 | 2.07 | 0.03 | 0.800 | 0.000 |
| | 0.75 | 0.263 | 1.43 | 0.02 | 0.749 | 0.000 | 2.26 | 0.03 | 0.749 | 0.000 |
| | 0.70 | 0.288 | 1.62 | 0.02 | 0.699 | 0.000 | 2.27 | 0.03 | 0.699 | 0.000 |
| r (cm) | IRF | d (cm) | $d_T$ | $\sigma_{d_T}$ | $I_{avg}$ | $\Delta I_R$ | $d_T$ | $\sigma_{d_T}$ | $I_{avg}$ | $\Delta I_R$ |
| | 0.95 | 0.176 | 0.79 | 0.02 | 0.950 | 0.000 | 1.15 | 0.03 | 0.950 | 0.000 |
| | 0.90 | 0.249 | 1.16 | 0.02 | 0.900 | 0.000 | 1.67 | 0.03 | 0.900 | 0.000 |
| 0.75 cm | 0.85 | 0.305 | 1.22 | 0.02 | 0.850 | 0.000 | 2.02 | 0.03 | 0.850 | 0.000 |
| | 0.80 | 0.352 | 1.42 | 0.02 | 0.800 | 0.000 | 2.07 | 0.03 | 0.800 | 0.000 |
| | 0.75 | 0.394 | 1.58 | 0.02 | 0.750 | 0.000 | 2.81 | 0.03 | 0.750 | 0.000 |
| | 0.70 | 0.431 | 1.62 | 0.02 | 0.701 | 0.001 | 2.44 | 0.02 | 0.701 | 0.000 |
| r (cm) | IRF | d (cm) | $d_T$ | $\sigma_{d_T}$ | $I_{avg}$ | $\Delta I_R$ | $d_T$ | $\sigma_{d_T}$ | $I_{avg}$ | $\Delta I_R$ |
| | 0.95 | 0.235 | 0.67 | 0.02 | 0.950 | 0.004 | 1.04 | 0.03 | 0.950 | 0.000 |
| | 0.90 | 0.332 | 1.03 | 0.02 | 0.900 | 0.007 | 1.61 | 0.03 | 0.900 | 0.000 |
| 1.00 cm | 0.85 | 0.407 | 1.24 | 0.02 | 0.850 | 0.011 | 1.53 | 0.08 | 0.850 | 0.000 |
| | 0.80 | 0.470 | 1.30 | 0.02 | 0.800 | 0.015 | 2.03 | 0.03 | 0.800 | 0.000 |
| | 0.75 | 0.525 | 1.47 | 0.03 | 0.750 | 0.019 | 2.17 | 0.03 | 0.750 | 0.000 |
| | 0.70 | 0.575 | 1.64 | 0.03 | 0.700 | 0.022 | 2.26 | 0.03 | 0.700 | 0.000 |
| r (cm) | IRF | d (cm) | $d_T$ | $\sigma_{d_T}$ | $I_{avg}$ | $\Delta I_R$ | $d_T$ | $\sigma_{d_T}$ | $I_{avg}$ | $\Delta I_R$ |
| | 0.95 | 0.294 | 0.69 | 0.04 | 0.950 | 0.021 | 0.98 | 0.03 | 0.950 | 0.001 |
| | 0.90 | 0.415 | 1.98 | 0.06 | 0.900 | 0.042 | 1.59 | 0.02 | 0.900 | 0.002 |
| 1.25 cm | 0.85 | 0.508 | 2.27 | 0.07 | 0.850 | 0.063 | 1.78 | 0.03 | 0.850 | 0.002 |
| | 0.80 | 0.587 | 2.20 | 0.06 | 0.800 | 0.084 | 2.02 | 0.02 | 0.800 | 0.003 |
| | 0.75 | 0.656 | 2.24 | 0.05 | 0.750 | 0.104 | 2.12 | 0.02 | 0.750 | 0.004 |
| | 0.70 | 0.719 | 2.26 | 0.05 | 0.700 | 0.125 | 2.19 | 0.02 | 0.700 | 0.005 |
| r (cm) | IRF | d (cm) | $d_T$ | $\sigma_{d_T}$ | $I_{avg}$ | $\Delta I_R$ | $d_T$ | $\sigma_{d_T}$ | $I_{avg}$ | $\Delta I_R$ |
| | 0.95 | 0.352 | 2.5 | 0.1 | 0.950 | 0.053 | 0.95 | 0.03 | 0.950 | 0.006 |
| | 0.90 | 0.498 | 2.51 | 0.08 | 0.901 | 0.106 | 1.43 | 0.04 | 0.900 | 0.011 |
| 1.50 cm | 0.85 | 0.610 | 2.65 | 0.07 | 0.851 | 0.159 | 1.94 | 0.05 | 0.850 | 0.017 |
| | 0.80 | 0.704 | 2.50 | 0.08 | 0.802 | 0.212 | 2.18 | 0.04 | 0.800 | 0.022 |
| | 0.75 | 0.788 | 2.42 | 0.09 | 0.752 | 0.266 | 2.61 | 0.05 | 0.750 | 0.028 |
| | 0.70 | 0.863 | 2.45 | 0.09 | 0.702 | 0.319 | 2.74 | 0.07 | 0.700 | 0.034 |

Table C.11: Metrics summary for 11 MeV at 103 cm SSD at y=0cm 20x20 half-blocked field for z=0.5cm (left) and z=2.0cm (right).

| r (cm) | IRF | d (cm) | $d_T$ | $\sigma_{d_T}$ | $I_{avg}$ | $\Delta I_R$ | $d_T$ | $\sigma_{d_T}$ | $I_{avg}$ | $\Delta I_R$ |
|---|---|---|---|---|---|---|---|---|---|---|
| | 0.95 | 0.117 | 0.63 | 0.02 | 0.950 | 0.000 | 1.06 | 0.04 | 0.950 | 0.000 |
| | 0.90 | 0.166 | 1.02 | 0.02 | 0.900 | 0.000 | 1.49 | 0.04 | 0.900 | 0.000 |
| 0.50 cm | 0.85 | 0.203 | 1.22 | 0.02 | 0.851 | 0.000 | 1.87 | 0.03 | 0.851 | 0.000 |
| | 0.80 | 0.235 | 1.42 | 0.02 | 0.800 | 0.000 | 1.88 | 0.03 | 0.800 | 0.000 |
| | 0.75 | 0.263 | 1.42 | 0.02 | 0.749 | 0.000 | 2.07 | 0.03 | 0.749 | 0.000 |
| | 0.70 | 0.288 | 1.42 | 0.02 | 0.699 | 0.000 | 2.08 | 0.03 | 0.699 | 0.000 |
| r (cm) | IRF | d (cm) | $d_T$ | $\sigma_{d_T}$ | $I_{avg}$ | $\Delta I_R$ | $d_T$ | $\sigma_{d_T}$ | $I_{avg}$ | $\Delta I_R$ |
| | 0.95 | 0.176 | 0.68 | 0.02 | 0.950 | 0.000 | 0.88 | 0.95 | 0.950 | 0.000 |
| | 0.90 | 0.249 | 1.02 | 0.02 | 0.900 | 0.001 | 1.58 | 0.03 | 0.900 | 0.000 |
| 0.75 cm | 0.85 | 0.305 | 1.22 | 0.02 | 0.850 | 0.001 | 1.68 | 0.03 | 0.850 | 0.000 |
| | 0.80 | 0.352 | 1.22 | 0.02 | 0.800 | 0.001 | 2.01 | 0.03 | 0.800 | 0.000 |
| | 0.75 | 0.394 | 1.36 | 0.02 | 0.750 | 0.002 | 2.07 | 0.03 | 0.750 | 0.000 |
| | 0.70 | 0.431 | 1.48 | 0.02 | 0.701 | 0.002 | 2.08 | 0.03 | 0.701 | 0.000 |
| r (cm) | IRF | d (cm) | $d_T$ | $\sigma_{d_T}$ | $I_{avg}$ | $\Delta I_R$ | $d_T$ | $\sigma_{d_T}$ | $I_{avg}$ | $\Delta I_R$ |
| | 0.95 | 0.235 | 0.59 | 0.03 | 0.950 | 0.008 | 0.97 | 0.04 | 0.950 | 0.000 |
| | 0.90 | 0.332 | 1.28 | 0.03 | 0.900 | 0.016 | 1.48 | 0.03 | 0.900 | 0.000 |
| 1.00 cm | 0.85 | 0.407 | 1.40 | 0.03 | 0.850 | 0.024 | 1.74 | 0.03 | 0.850 | 0.000 |
| | 0.80 | 0.470 | 1.69 | 0.04 | 0.800 | 0.031 | 1.85 | 0.03 | 0.800 | 0.000 |
| | 0.75 | 0.525 | 1.99 | 0.06 | 0.750 | 0.039 | 1.99 | 0.03 | 0.750 | 0.001 |
| | 0.70 | 0.575 | 2.13 | 0.07 | 0.700 | 0.047 | 2.10 | 0.03 | 0.700 | 0.001 |
| r (cm) | IRF | d (cm) | $d_T$ | $\sigma_{d_T}$ | $I_{avg}$ | $\Delta I_R$ | $d_T$ | $\sigma_{d_T}$ | $I_{avg}$ | $\Delta I_R$ |
| | 0.95 | 0.294 | 1.4 | 0.1 | 0.950 | 0.034 | 0.90 | 0.03 | 0.950 | 0.002 |
| | 0.90 | 0.415 | 2.10 | 0.08 | 0.900 | 0.067 | 1.39 | 0.03 | 0.900 | 0.005 |
| 1.25 cm | 0.85 | 0.508 | 2.02 | 0.05 | 0.850 | 0.101 | 1.67 | 0.03 | 0.850 | 0.007 |
| | 0.80 | 0.587 | 2.02 | 0.06 | 0.800 | 0.135 | 1.78 | 0.03 | 0.800 | 0.009 |
| | 0.75 | 0.656 | 2.12 | 0.07 | 0.751 | 0.169 | 1.93 | 0.03 | 0.750 | 0.011 |
| | 0.70 | 0.719 | 2.09 | 0.06 | 0.700 | 0.202 | 2.04 | 0.03 | 0.700 | 0.014 |
| r (cm) | IRF | d (cm) | $d_T$ | $\sigma_{d_T}$ | $I_{avg}$ | $\Delta I_R$ | $d_T$ | $\sigma_{d_T}$ | $I_{avg}$ | $\Delta I_R$ |
| | 0.95 | 0.352 | 2.1 | 0.1 | 0.951 | 0.074 | 0.81 | 0.04 | 0.950 | 0.011 |
| | 0.90 | 0.498 | 2.30 | 0.07 | 0.901 | 0.149 | 1.39 | 0.03 | 0.900 | 0.005 |
| 1.50 cm | 0.85 | 0.610 | 2.33 | 0.07 | 0.852 | 0.223 | 2.66 | 0.09 | 0.850 | 0.034 |
| | 0.80 | 0.704 | 2.50 | 0.06 | 0.802 | 0.297 | 3.04 | 0.07 | 0.801 | 0.046 |
| | 0.75 | 0.788 | 2.75 | 0.06 | 0.752 | 0.372 | 3.22 | 0.08 | 0.750 | 0.057 |
| | 0.70 | 0.863 | 2.37 | 0.07 | 0.703 | 0.446 | 3.58 | 0.06 | 0.700 | 0.069 |

Table C.12: Metrics summary for 13 MeV at 103 cm SSD at y=0cm 20x20 half-blocked field for z=0.5cm (left) and z=2.0cm (right).

| r (cm) | IRF | d (cm) | $d_T$ | $\sigma_{d_T}$ | $I_{avg}$ | $\Delta I_R$ | $d_T$ | $\sigma_{d_T}$ | $I_{avg}$ | $\Delta I_R$ |
|---|---|---|---|---|---|---|---|---|---|---|
| | 0.95 | 0.117 | 0.60 | 0.00 | 0.950 | 0.000 | 0.86 | 0.03 | 0.950 | 0.000 |
| | 0.90 | 0.166 | 1.00 | 0.00 | 0.900 | 0.000 | 1.26 | 0.03 | 0.900 | 0.000 |
| 0.50 cm | 0.85 | 0.203 | 1.02 | 0.00 | 0.851 | 0.000 | 1.46 | 0.03 | 0.851 | 0.000 |
| | 0.80 | 0.235 | 1.05 | 0.01 | 0.800 | 0.000 | 1.65 | 0.03 | 0.800 | 0.000 |
| | 0.75 | 0.263 | 1.20 | 0.00 | 0.749 | 0.000 | 1.84 | 0.03 | 0.749 | 0.000 |
| | 0.70 | 0.288 | 1.26 | 0.01 | 0.699 | 0.000 | 1.83 | 0.02 | 0.699 | 0.000 |
| r (cm) | IRF | d (cm) | $d_T$ | $\sigma_{d_T}$ | $I_{avg}$ | $\Delta I_R$ | $d_T$ | $\sigma_{d_T}$ | $I_{avg}$ | $\Delta I_R$ |
| | 0.95 | 0.176 | 0.57 | 0.01 | 0.950 | 0.002 | 0.86 | 0.03 | 0.950 | 0.000 |
| | 0.90 | 0.249 | 0.80 | 0.00 | 0.900 | 0.004 | 1.26 | 0.03 | 0.900 | 0.000 |
| 0.75 cm | 0.85 | 0.305 | 1.01 | 0.00 | 0.850 | 0.006 | 1.56 | 0.03 | 0.850 | 0.000 |
| | 0.80 | 0.352 | 1.09 | 0.01 | 0.800 | 0.009 | 1.65 | 0.03 | 0.800 | 0.000 |
| | 0.75 | 0.394 | 1.17 | 0.01 | 0.750 | 0.011 | 1.65 | 0.03 | 0.750 | 0.000 |
| | 0.70 | 0.431 | 1.20 | 0.00 | 0.701 | 0.013 | 1.75 | 0.03 | 0.701 | 0.000 |
| r (cm) | IRF | d (cm) | $d_T$ | $\sigma_{d_T}$ | $I_{avg}$ | $\Delta I_R$ | $d_T$ | $\sigma_{d_T}$ | $I_{avg}$ | $\Delta I_R$ |
| | 0.95 | 0.235 | 0.62 | 0.03 | 0.950 | 0.022 | 0.84 | 0.03 | 0.950 | 0.001 |
| | 0.90 | 0.332 | 1.68 | 0.06 | 0.900 | 0.044 | 1.24 | 0.03 | 0.900 | 0.002 |
| 1.00 cm | 0.85 | 0.407 | 1.90 | 0.06 | 0.850 | 0.067 | 1.38 | 0.03 | 0.850 | 0.003 |
| | 0.80 | 0.470 | 1.82 | 0.07 | 0.800 | 0.089 | 1.58 | 0.03 | 0.800 | 0.004 |
| | 0.75 | 0.525 | 1.89 | 0.07 | 0.750 | 0.111 | 1.69 | 0.03 | 0.750 | 0.005 |
| | 0.70 | 0.575 | 1.85 | 0.07 | 0.701 | 0.133 | 1.75 | 0.03 | 0.700 | 0.006 |
| r (cm) | IRF | d (cm) | $d_T$ | $\sigma_{d_T}$ | $I_{avg}$ | $\Delta I_R$ | $d_T$ | $\sigma_{d_T}$ | $I_{avg}$ | $\Delta I_R$ |
| | 0.95 | 0.294 | 1.65 | 0.09 | 0.950 | 0.066 | 0.73 | 0.03 | 0.950 | 0.009 |
| | 0.90 | 0.415 | 1.38 | 0.08 | 0.900 | 0.132 | 1.35 | 0.04 | 0.900 | 0.019 |
| 1.25 cm | 0.85 | 0.508 | 1.60 | 0.08 | 0.851 | 0.197 | 1.90 | 0.04 | 0.850 | 0.028 |
| | 0.80 | 0.587 | 1.62 | 0.08 | 0.801 | 0.264 | 2.34 | 0.05 | 0.800 | 0.037 |
| | 0.75 | 0.656 | 1.58 | 0.08 | 0.751 | 0.329 | 2.47 | 0.06 | 0.750 | 0.047 |
| | 0.70 | 0.719 | 1.66 | 0.07 | 0.701 | 0.395 | 2.71 | 0.06 | 0.700 | 0.056 |
| r (cm) | IRF | d (cm) | $d_T$ | $\sigma_{d_T}$ | $I_{avg}$ | $\Delta I_R$ | $d_T$ | $\sigma_{d_T}$ | $I_{avg}$ | $\Delta I_R$ |
| | 0.95 | 0.352 | 1.95 | 0.08 | 0.951 | 0.120 | 1.49 | 0.06 | 0.950 | 0.030 |
| | 0.90 | 0.498 | 2.00 | 0.06 | 0.902 | 0.024 | 2.5 | 0.1 | 0.900 | 0.061 |
| 1.50 cm | 0.85 | 0.610 | 1.85 | 0.05 | 0.853 | 0.360 | 2.81 | 0.09 | 0.851 | 0.091 |
| | 0.80 | 0.704 | 1.86 | 0.06 | 0.804 | 0.479 | 2.7 | 0.1 | 0.801 | 0.121 |
| | 0.75 | 0.788 | 1.90 | 0.07 | 0.754 | 0.600 | 2.8 | 0.1 | 0.751 | 0.152 |
| | 0.70 | 0.863 | 1.82 | 0.07 | 0.705 | 0.720 | 2.7 | 0.1 | 0.701 | 0.182 |

Table C.13: Metrics summary for 16 MeV at 103 cm SSD at y=0cm 20x20 half-blocked field for z=0.5cm (left) and z=2.0cm (right).

| r (cm) | IRF | d (cm) | $d_T$ | $\sigma_{d_T}$ | $I_{avg}$ | $\Delta I_R$ | $d_T$ | $\sigma_{d_T}$ | $I_{avg}$ | $\Delta I_R$ |
|---|---|---|---|---|---|---|---|---|---|---|
| | 0.95 | 0.117 | 0.56 | 0.01 | 0.950 | 0.042 | 0.63 | 0.02 | 0.950 | 0.000 |
| | 0.90 | 0.166 | 0.61 | 0.01 | 0.900 | 0.007 | 1.03 | 0.02 | 0.900 | 0.000 |
| 0.50 cm | 0.85 | 0.203 | 0.94 | 0.01 | 0.851 | 0.001 | 1.22 | 0.02 | 0.851 | 0.000 |
| | 0.80 | 0.235 | 1.00 | 0.00 | 0.800 | 0.000 | 1.42 | 0.02 | 0.800 | 0.000 |
| | 0.75 | 0.263 | 1.00 | 0.00 | 0.749 | 0.001 | 1.42 | 0.02 | 0.749 | 0.000 |
| | 0.70 | 0.288 | 1.00 | 0.00 | 0.699 | 0.001 | 1.42 | 0.02 | 0.699 | 0.000 |
| r (cm) | IRF | d (cm) | $d_T$ | $\sigma_{d_T}$ | $I_{avg}$ | $\Delta I_R$ | $d_T$ | $\sigma_{d_T}$ | $I_{avg}$ | $\Delta I_R$ |
| | 0.95 | 0.176 | 0.44 | 0.01 | 0.950 | 0.024 | 0.68 | 0.02 | 0.950 | 0.000 |
| | 0.90 | 0.249 | 0.73 | 0.02 | 0.900 | 0.031 | 1.03 | 0.02 | 0.900 | 0.001 |
| 0.75 cm | 0.85 | 0.305 | 1.38 | 0.08 | 0.850 | 0.033 | 1.22 | 0.02 | 0.850 | 0.001 |
| | 0.80 | 0.352 | 1.55 | 0.10 | 0.800 | 0.044 | 1.25 | 0.02 | 0.800 | 0.001 |
| | 0.75 | 0.394 | 2.35 | 0.09 | 0.750 | 0.056 | 1.39 | 0.02 | 0.750 | 0.001 |
| | 0.70 | 0.431 | 1.90 | 0.06 | 0.700 | 0.067 | 1.48 | 0.02 | 0.701 | 0.002 |
| r (cm) | IRF | d (cm) | $d_T$ | $\sigma_{d_T}$ | $I_{avg}$ | $\Delta I_R$ | $d_T$ | $\sigma_{d_T}$ | $I_{avg}$ | $\Delta I_R$ |
| | 0.95 | 0.235 | 1.17 | 0.06 | 0.950 | 0.056 | 0.59 | 0.03 | 0.950 | 0.007 |
| | 0.90 | 0.332 | 0.86 | 0.06 | 0.900 | 0.113 | 1.23 | 0.04 | 0.900 | 0.014 |
| 1.00 cm | 0.85 | 0.407 | 1.43 | 0.08 | 0.850 | 0.169 | 1.37 | 0.03 | 0.850 | 0.021 |
| | 0.80 | 0.470 | 1.68 | 0.07 | 0.800 | 0.226 | 1.55 | 0.03 | 0.800 | 0.029 |
| | 0.75 | 0.525 | 1.50 | 0.09 | 0.751 | 0.282 | 1.90 | 0.05 | 0.750 | 0.036 |
| | 0.70 | 0.575 | 1.50 | 0.07 | 0.701 | 0.338 | 2.21 | 0.07 | 0.700 | 0.043 |
| r (cm) | IRF | d (cm) | $d_T$ | $\sigma_{d_T}$ | $I_{avg}$ | $\Delta I_R$ | $d_T$ | $\sigma_{d_T}$ | $I_{avg}$ | $\Delta I_R$ |
| | 0.95 | 0.294 | 1.19 | 0.08 | 0.950 | 0.122 | 1.07 | 0.07 | 0.950 | 0.032 |
| | 0.90 | 0.415 | 1.29 | 0.08 | 0.901 | 0.243 | 2.09 | 0.07 | 0.900 | 0.064 |
| 1.25 cm | 0.85 | 0.508 | 1.43 | 0.08 | 0.851 | 0.363 | 1.98 | 0.05 | 0.850 | 0.095 |
| | 0.80 | 0.587 | 1.50 | 0.09 | 0.801 | 0.485 | 2.10 | 0.05 | 0.800 | 0.127 |
| | 0.75 | 0.656 | 1.55 | 0.08 | 0.752 | 0.606 | 2.17 | 0.06 | 0.751 | 0.159 |
| | 0.70 | 0.719 | 1.56 | 0.08 | 0.702 | 0.728 | 2.17 | 0.06 | 0.700 | 0.191 |
| r (cm) | IRF | d (cm) | $d_T$ | $\sigma_{d_T}$ | $I_{avg}$ | $\Delta I_R$ | $d_T$ | $\sigma_{d_T}$ | $I_{avg}$ | $\Delta I_R$ |
| | 0.95 | 0.352 | 0.67 | 0.07 | 0.951 | 0.191 | 2.2 | 0.1 | 0.951 | 0.071 |
| | 0.90 | 0.498 | 0.69 | 0.05 | 0.903 | 0.382 | 2.48 | 0.07 | 0.901 | 0.143 |
| 1.50 cm | 0.85 | 0.610 | 0.97 | 0.06 | 0.854 | 0.573 | 2.40 | 0.07 | 0.852 | 0.214 |
| | 0.80 | 0.704 | 0.97 | 0.06 | 0.806 | 0.763 | 2.60 | 0.06 | 0.802 | 0.285 |
| | 0.75 | 0.788 | 0.99 | 0.06 | 0.757 | 0.955 | 2.54 | 0.06 | 0.752 | 0.357 |
| | 0.70 | 0.863 | 0.98 | 0.06 | 0.712 | 0.967 | 2.41 | 0.08 | 0.703 | 0.428 |

Table C.14: Metrics summary for 20 MeV at 103 cm SSD at y=0cm 20x20 half-blocked field for z=0.5cm (left) and z=2.0cm (right).

| r (cm) | IRF | d (cm) | $d_T$ | $\sigma_{d_T}$ | $I_{avg}$ | $\Delta I_R$ | $d_T$ | $\sigma_{d_T}$ | $I_{avg}$ | $\Delta I_R$ |
|---|---|---|---|---|---|---|---|---|---|---|
| | 0.95 | 0.117 | 0.44 | 0.03 | 0.950 | 0.016 | 0.60 | 0.00 | 0.950 | 0.000 |
| | 0.90 | 0.166 | 0.64 | 0.03 | 0.900 | 0.003 | 0.89 | 0.01 | 0.900 | 0.000 |
| 0.50 cm | 0.85 | 0.203 | 0.68 | 0.05 | 0.850 | 0.005 | 1.00 | 0.00 | 0.851 | 0.000 |
| | 0.80 | 0.235 | 0.73 | 0.08 | 0.800 | 0.007 | 1.00 | 0.00 | 0.800 | 0.000 |
| | 0.75 | 0.263 | 1.0 | 0.1 | 0.749 | 0.008 | 1.13 | 0.01 | 0.749 | 0.000 |
| | 0.70 | 0.288 | 0.89 | 0.07 | 0.699 | 0.010 | 1.20 | 0.00 | 0.699 | 0.000 |
| r (cm) | IRF | d (cm) | $d_T$ | $\sigma_{d_T}$ | $I_{avg}$ | $\Delta I_R$ | $d_T$ | $\sigma_{d_T}$ | $I_{avg}$ | $\Delta I_R$ |
| | 0.95 | 0.176 | 1.24 | 0.05 | 0.950 | 0.037 | 0.57 | 0.01 | 0.950 | 0.003 |
| | 0.90 | 0.249 | 1.42 | 0.05 | 0.900 | 0.075 | 0.73 | 0.01 | 0.900 | 0.007 |
| 0.75 cm | 0.85 | 0.305 | 1.26 | 0.07 | 0.850 | 0.112 | 1.12 | 0.02 | 0.850 | 0.010 |
| | 0.80 | 0.352 | 1.76 | 0.09 | 0.801 | 0.149 | 1.18 | 0.02 | 0.800 | 0.013 |
| | 0.75 | 0.394 | 1.79 | 0.09 | 0.750 | 0.187 | 1.23 | 0.01 | 0.750 | 0.017 |
| | 0.70 | 0.431 | 1.64 | 0.07 | 0.701 | 0.224 | 1.28 | 0.01 | 0.701 | 0.020 |
| r (cm) | IRF | d (cm) | $d_T$ | $\sigma_{d_T}$ | $I_{avg}$ | $\Delta I_R$ | $d_T$ | $\sigma_{d_T}$ | $I_{avg}$ | $\Delta I_R$ |
| | 0.95 | 0.235 | 0.78 | 0.01 | 0.948 | 0.113 | 0.94 | 0.03 | 0.950 | 0.028 |
| | 0.90 | 0.332 | 1.19 | 0.01 | 0.900 | 0.226 | 1.27 | 0.07 | 0.900 | 0.057 |
| 1.00 cm | 0.85 | 0.407 | 1.33 | 0.01 | 0.850 | 0.339 | 1.53 | 0.08 | 0.850 | 0.085 |
| | 0.80 | 0.470 | 1.50 | 0.01 | 0.800 | 0.453 | 1.54 | 0.07 | 0.800 | 0.114 |
| | 0.75 | 0.525 | 1.62 | 0.01 | 0.750 | 0.565 | 1.54 | 0.07 | 0.751 | 0.142 |
| | 0.70 | 0.575 | 1.69 | 0.01 | 0.700 | 0.678 | 1.61 | 0.07 | 0.701 | 0.171 |
| r (cm) | IRF | d (cm) | $d_T$ | $\sigma_{d_T}$ | $I_{avg}$ | $\Delta I_R$ | $d_T$ | $\sigma_{d_T}$ | $I_{avg}$ | $\Delta I_R$ |
| | 0.95 | 0.294 | 0.69 | 0.06 | 0.950 | 0.199 | 1.51 | 0.08 | 0.950 | 0.078 |
| | 0.90 | 0.415 | 0.97 | 0.07 | 0.901 | 0.397 | 1.45 | 0.09 | 0.900 | 0.155 |
| 1.25 cm | 0.85 | 0.508 | 1.30 | 0.08 | 0.852 | 0.594 | 1.52 | 0.09 | 0.851 | 0.232 |
| | 0.80 | 0.587 | 1.40 | 0.07 | 0.802 | 0.794 | 1.56 | 0.07 | 0.801 | 0.309 |
| | 0.75 | 0.656 | 1.46 | 0.08 | 0.753 | 0.977 | 1.63 | 0.07 | 0.751 | 0.386 |
| | 0.70 | 0.719 | 1.47 | 0.08 | 0.707 | 0.973 | 1.66 | 0.08 | 0.701 | 0.464 |
| r (cm) | IRF | d (cm) | $d_T$ | $\sigma_{d_T}$ | $I_{avg}$ | $\Delta I_R$ | $d_T$ | $\sigma_{d_T}$ | $I_{avg}$ | $\Delta I_R$ |
| | 0.95 | 0.352 | 0.72 | 0.08 | 0.952 | 0.291 | 1.80 | 0.08 | 0.951 | 0.135 |
| | 0.90 | 0.498 | 0.88 | 0.07 | 0.904 | 0.582 | 1.79 | 0.05 | 0.902 | 0.270 |
| 1.50 cm | 0.85 | 0.610 | 0.65 | 0.05 | 0.856 | 0.874 | 1.79 | 0.06 | 0.853 | 0.405 |
| | 0.80 | 0.704 | 1.13 | 0.06 | 0.811 | 0.996 | 1.75 | 0.07 | 0.804 | 0.539 |
| | 0.75 | 0.788 | 0.74 | 0.04 | 0.773 | 0.995 | 1.69 | 0.08 | 0.755 | 0.675 |
| | 0.70 | 0.863 | 0.74 | 0.04 | 0.745 | 0.994 | 1.66 | 0.09 | 0.706 | 0.810 |

# VITA

Erin Chambers grew up in rural Byrdstown, Tennessee. She graduated from Tennessee Technological University with a Bachelor of Science in Physics. An interest in contributing to the medical field led her to the graduate program for medical physics at Louisiana State University, from which she expects to receive her Master of Science in 2016. After attaining her degree, Erin will be joining the medical physics residency program at Rhode Island Hospital in Providence, RI.